Experiments on Cold Molecules Produced via Stark Deceleration

by

Eric R. Hudson

B.S., Morehead State University, 2000

M.S., University of Colorado - Boulder, 2004

A thesis submitted to the

Faculty of the Graduate School of the

University of Colorado in partial fulfillment

of the requirements for the degree of

Doctor of Philosophy

Department of Physics

2006

This thesis entitled:
Experiments on Cold Molecules Produced via Stark Deceleration
written by Eric R. Hudson
has been approved for the Department of Physics

———————————————————————

Jun Ye

———————————————————————

Eric A. Cornell

Date ————————————

The final copy of this thesis has been examined by the signatories, and we find that both the content and the form meet acceptable presentation standards of scholarly work in the above mentioned discipline.

Hudson, Eric R. (Ph.D., Physics)

Experiments on Cold Molecules Produced via Stark Deceleration

Thesis directed by Prof. Jun Ye

The work described in this thesis is the construction and operation of a Stark deceleration apparatus. Specifically, this work represents only the second successful implementation of the method[1] and the first deceleration of the hydroxyl radical (OH) and the formaldehyde molecule (H_2CO). Experimentally, much of the work in the beginning of our experiments was the construction of a suitable molecular beam. Though molecular beams have been used for decades in physical chemistry, the design goals of the typical physical chemistry experiment are very different than ours, and as such, much work was required to adapt these sources for Stark deceleration. Since the maximum-attainable, decelerated molecular density is set at this stage, the importance of a good molecular beam source cannot be understated. Once a stable decelerated beam became routine in our laboratory, we performed the first precision measurement on cold molecules leading to the best ever values for the frequencies of the main lines in the lowest OH Λ-doublet. These measurements, when coupled with the appropriate astrophysical measurements, can be used to put the most stringent constraints on the variations of the fundamental constants. Excitingly, we have recently been informed that the required astrophysical measurements may be performed as early as the latter part of this year.

Our most recent work, not covered in this thesis,[2] has been the construction and implementation of a magnetic trap for OH molecules. To prepare decelerated molecules for loading into this trap we have built a second-generation decelerator, which has more stages than our first, to provide a higher flux of decelerated molecules. In the construction of this decelerator, several interesting phenomena, which currently limit

---

[1] The Berlin group, whose collaboration has been fruitful (for both sides, I hope), was first.

[2] This topic will likely be the crux of the dissertation of Brian Sawyer.

the decelerator efficiency, have come to our attention. Specifically, these are transverse over-focussing of the decelerated molecular packets in the decelerator and the possibility of Majorana type transitions during deceleration. These effects (especially transverse over-focussing) extremely limit the number of molecules decelerated to below 15 m/s in our apparatuses. Since molecules of this speed or less are required for proper loading into our magnetic trap, both of these phenomena **must** be addressed in order for the optimal deceleration performance to be reached. Currently, as detailed in this thesis, experiments are already underway to learn how to eliminate them. Thus, it is my opinion that the technique of Stark deceleration is very close to blossoming into the best technique for producing cold molecules,[3] since addressing these issues will lead to several orders of magnitude gain in decelerated molecule number. Furthermore, with ideas for further cooling of trapped samples being developed, *e.g.* cavity-assisted Doppler cooling, the possibilities for cold molecule physics are staggering.

---

[3] Perhaps this argument could already be made.

Dedication

For Natasha

Acknowledgements

As anyone who has worked in a research environment will tell you, success requires a large number of great people working together. I have been fortunate enough to work at JILA in Prof. Jun Ye's group, which can be defined as a 'large number of great people working together'. In some sense, I feel I was in an environment where it was impossible to fail because the people around me would not allow it to happen, and as such, I am indebted to many. The help I received from the JILA electronics shop (Terry Brown, Mike Whitmore, James Fung-a-Fat, Paul Beckingham, Carl Sauer, and David Tegart) was instrumental in both the production and detection of our cold molecules. Likewise, without the aid of the JILA instrument shop (Alan Pattee, Hans Green, Kim Hagen, Tom Foote, Tracey Keep, and Blaine Horner), our decelerator would never have been constructed. These individuals are more than engineers and excellent technicians, they are artisans who have mastered their craft. In the laboratory I have had the pleasure of working with many great scientists. I still remember my first visit to the lab (to see the empty table) when I met Jason Bochinski, the project's first postdoc. Together, Jason and I navigated the perils of switching high voltages and making a molecular beam, and though Jason was clearly the leader, he never belittled my contributions and for that I am grateful. Almost two years later Heather Lewandowski joined the effort as a postdoc, and it was from a series of fruitful discussions with her that the work that comprises Chapter 6 sprung forth. Brian Sawyer was next on the scene as the graduate student who would take over my position. I have thoroughly enjoyed every moment I have worked

with Brian, especially the construction of our second decelerator. His relaxed attitude and sharp mind have greatly accelerated the progress of the project. At the beginning of the year Benjamin Lev started working with us as a postdoc. Benjamin quickly took over the high resolution spectroscopy experiment, and I am completely impressed with his wit and attention to detail. Last to join our group was Ben Stuhl, a graduate student. While Ben and I have only worked together for a few short weeks, he has already taught me much about coding, and I expect only the best things from him in the future. Outside of the cold molecule laboratory I have had the benefit of a close relationship with the theory group of John Bohn. John, his posdocs, and his students (Alexander Avdeenkov, Chris Ticknor, and Ed Meyer) have taught me molecular physics. I have also been fortunate to have a close relationship with the group of Gerard Meijer in Berlin. The friendly competition/collaboration with this group, the originators of the Stark deceleration technique, has not only accelerated the development of the field, but has left me with many wonderful friends (Rick Bethlem, Floris Crompvoets, Bas van der Meeraker, Joop Gilijamse, Steven Hoekstra, Nicolas Vanhaecke, Joost Bakker, Jacqueline van Vandhoven, and Gerard Meijer). Of course, none of this work would be possible without the guidance of Prof. Jun Ye. It is impossible to overstate the importance of Jun to the success of the experiment. In the difficult times Jun always seems to know the right way to proceed. Furthermore, working for Jun is a joy because he is as committed to the growth of his students as he is to doing excellent science. Jun has allowed me to travel around the globe to further my development as a scientist, and I cannot begin to explain how important those trips have been to me. If I ever have my own laboratory, I can only hope to approach the excellent leadership Jun has demonstrated.

Beyond the amazing people at JILA and in Jun's group, there is another element to how easy it is to succeed here. This element, which is somewhere between an ideal and an attitude, – maybe Zeitgeist is the right word – is a sense of family that pervades

the institution. Whether it is loaning equipment or taking the time to talk with someone about a problem on their experiment, this approach greatly decreases the time it takes for good science to be done. More importantly though, it makes for a non-stressful work environment. I am not sure how this culture comes to prevail at an institution. Perhaps the foundation was laid by the early Fellows, or it has to do with living in such a beautiful place as Boulder, e.g. even if the laser breaks, you can still go skiing on the weekend. Regardless, it is, in my opinion, the gold standard for any working environment and I hope to help recreate wherever I work.

I am extremely indebted to my parents, Raymond and Christine. Though they knew the importance of education, they never pushed me into anything, preferring to let me find my own way. I credit this relaxed atmosphere as the reason I was able to make it this far. Because I enjoyed what I was doing, I was never 'bogged-down' by the work. Nonetheless, the most important gift I received from my parents was a strong faith in Christ. In retrospect, it was my beliefs as a Christian that led me to physics. In my opinion, there are scarce better ways to know God than to study his creation, and the beauty and symmetry I have found in physics have only strengthened my faith. And any reader who thinks that things like religion or prayer have no place in a laboratory has never applied 30 kV across a couple of millimeters.

And thank Tasha for all the rest.

<div style="text-align: right">

Eric R. Hudson
Boulder, 2006

</div>

Contents

Chapter

Tables

Table

Figures

Figure

Chapter 1

Introduction to Cold Molecules

The study of cold and ultra-cold atoms has led to some of the most interesting discoveries in the last quarter of the twentieth century. From the onset of the use of laser cooling and magneto-optical trapping, the field has produced many of the most precise and fascinating results in all of physics, culminating in the production of degenerate Bose and Fermi gases. Thus, it is not surprising that a new effort has begun to extend these studies to molecules, whose rich ro-vibrational spectra and lack of spherical symmetry promise even more scientific reward. At present cold molecule research is poised to revolutionize the face of molecular physics, as cold samples of molecules are becoming available for study.

The topic of this dissertation is work which produced the first cold samples of hydroxyl radicals (OH) and formaldehyde molecules (H_2CO) for study by Stark deceleration of molecular beams. In this thesis, the motivation for studying cold molecules is detailed followed by a quick summary of the other successful techniques for producing cold polar molecules. Next, a brief introduction to molecular structure is given before the technique of Stark deceleration is discussed. The remainder of this work details our results for production of cold polar molecules, culminating in a high-resolution spectroscopy measurement of the Λ-doublet splitting in OH, which has important implications for constraining the fundamental constants. The final chapter contains outlines of several ideas for future experiments that we have had over the course of this work.

It is the aim of this thesis to be accessible to the atomic physicist, and as such, the first four chapters provide an introduction to many of the ideas and techniques of molecular physics. For those already familiar with these ideas, the remaining six chapters describe our work on Stark deceleration, though chapters 3 and 4 may still deserve attention since we have implemented several improvements to the standard molecular detection and beam techniques.

1.1   Motivation

There are many compelling reasons for producing cold samples of polar molecules, ranging from high-resolution spectroscopy and molecular clocks to long-range, collective quantum effects and ultra-cold chemistry to the possibility for quantum computation. The underpinning theme of nearly all these interesting areas of study is that they are facilitated by the anisotropic electric dipole-dipole interaction present in polar molecules, namely:

$$V_{dd} = \frac{1}{4\pi\epsilon_o r^3}\left(\mu_\mathbf{1}\cdot\mu_\mathbf{2} - \frac{3(\mu_\mathbf{1}\cdot\mathbf{r})(\mu_\mathbf{2}\cdot\mathbf{r})}{r^2}\right), \tag{1.1}$$

where μ_i is the electric dipole moment of the colliding molecules and $\mathbf{r}$ is the vector connecting the two molecules. This interaction is fundamentally different from the types of interaction studied in ultra-cold atom research, where the interaction is isotropic and comparatively short-ranged.

Theoretical work, pioneered by the group of John Bohn [18, 19, 122], has predicted new collision dynamics specific to polar molecules. Representative results of their calculations are shown in Fig.1.1, where the total scattering rate for OH molecules in the weak-field-seeking state is shown. The hallmark features of cold polar molecules collisions are evident in this graph; the collision rate rises by nearly three orders of magnitude and then undergoes several large modulations with only a modest change in electric field. Because the dipole-dipole interaction is anisotropic, molecules can either
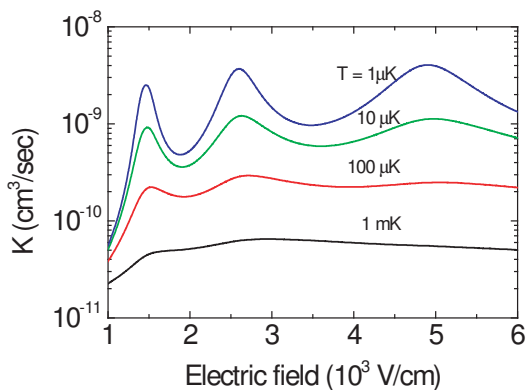
Figure 1.1: Total collision rate of weak-field-seeking OH molecules as a function of electric field. Courtesy of John Bohn.

repel or attract each other during a collision depending on their relative orientation. Furthermore, the strength of the interaction is directly proportional to the dipole moment of the colliding molecules, and since the dipole moment is a function of the electric field, the interaction is electric field dependent. Thus, the salient features of Fig. 1.1 can be understood as due to bound states forming at threshold, *i.e.* scattering resonances, in the attractive part of the inter-molecular potential curve as the strength of the interaction increases with electric field.

Though currently there has been no experimental observation of cold polar molecule collisions, there is considerable effort towards this goal and it will soon be realized. The first detailed experiments will be extremely important since little is known about the short-range structure of the inter-molecular potential curves and a better understanding would afford more precise knowledge of chemical reaction dynamics, a necessary step towards control of chemical reactions at the quantum level.

Other, possibly monumental, experiments are the investigation of the weak interaction in chiral molecules [106, 77] and the search for an electric dipole moment of the electron [74]. A chiral (or handed) molecule is one that is not superposable on its mirror image. A chiral molecule and its mirror image are classified as enantiomers.

While the usual physical properties of enantiomers such as density, melting point, and boiling point are identical within experimental error, the enantiomers of a given chiral molecule can exhibit noticeable differences. For example, nature seems to prefer one handedness to the other, *e.g.* all amino acids are left-handed chiral molecules. The question then naturally arises as to why one mirror image is preferred over another. The parity violating weak interaction could produce an energy difference between the two enantiomers leading to the selection observed in nature [106, 77]. With a cold sample of chiral molecules, experiments may become sensitive enough to see this energy difference (up to present such experiments have failed [40]). The existence of an electron permanent electric dipole moment (EDM) would be equally interesting. If an electron possesses an EDM this leads to a time reversal symmetry violation [74]. It is necessary that any electron EDM would be fixed relative to the electron's spin axis. Otherwise, a separate quantum number is needed and twice as many electrons as observed could be stored in each atomic shell. Thus, in an external electric and magnetic field, the EDM is manifested as an energy shift equal to the electric dipole moment multiplied by the local electric field value. Preliminary work indicates that experiments with polar molecules can be far more sensitive than current atom experiments, due to the larger internal electric fields and ease of orientation in the lab frame [105, 63]. With a cold sample of polar molecules, the sensitivity of the measurement can be enhanced and the results used to filter the appropriate theories [49].

With the promise of enormous gain with molecule experiments and the considerable success of atom cooling and trapping, one may wonder why so little work has been focused on creating cold molecular samples. The reason for minimal development in molecule cooling is simply that molecules are a much more complicated system, and thus harder to control than atoms. Simply put, the techniques developed for atoms cannot be easily applied in the production of cold molecules. For example, laser cooling, the foundation of cold atom research, is not amenable to molecules because of their

complicated energy structure. Therefore new approaches are being developed to provide physicists with samples of cold molecules. Currently there are only four techniques that have been realized experimentally; buffer gas loading, association of cold atoms, slow molecule filtering, and Stark deceleration - the topic of this dissertation. The implementation of these methods (save Stark deceleration) as well as their inherent advantages, disadvantages, and outstanding issues will be discussed in the following sections.

1.2   Buffer Gas Loading

The loading of thermal molecules into a magnetic trap via cooling with a cold Helium buffer gas, buffer gas loading, represents the conceptually simplest of all techniques for cold molecule production. Thermal molecules are sympathetically cooled via collisions with a Helium gas to cryogenic temperatures and subsequently trapped in a minimum of an applied magnetic field. Because the collision cross-section of the molecules with the Helium buffer gas is essentially independent of the molecular energy level pattern and generally increases with decreasing temperature, the technique is applicable to many species and should be successful for any molecule with a sufficient magnetic dipole to be trapped at cryogenic Helium temperatures ($\sim$250mK) [41]. Because at these low temperatures only Helium has an appreciable vapor pressure, it is necessary to introduce the 'molecule-to-be-trapped' at thermal temperatures. The subsequent decrease of the molecule's temperature can be easily modeled by hard sphere elastic scattering of two masses. From conservation of energy and momentum with averaging over a thermal velocity distribution it is easy to show the temperature change of the 'molecule-to-be-trapped' due to one collision with the buffer gas is given as [41]:

$$\Delta T = \frac{-(T_i - T)}{\kappa}, \kappa = \frac{(M_{Mol} + m_{He})^2}{2M_{Mol}m_{He}} \tag{1.2}$$

with T_i = initial temperature of the molecule, T = initial buffer gas temperature, and M_{Mol} and m_{He} the mass of the 'molecule-to-be-trapped' and the helium, respectively.
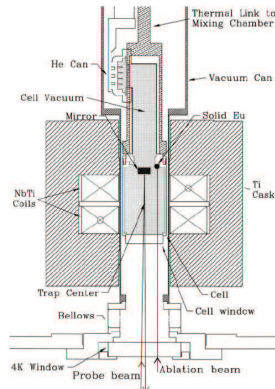
Figure 1.2: Typical buffer gas loading experiment set-up. Taken from [41].

Integrating for the molecule temperature as a function of the number of collisions yields:

$$\frac{T_n}{T} = (\frac{T_i}{T} - 1)e^{-\frac{n}{\kappa}} + 1, \tag{1.3}$$

where T_n is the molecule temperature after n collisions. In order for the thermal molecules to be cooled enough to fall below the trap edge before they collide with the chamber walls, it is necessary for the buffer gas density to be sufficient to provide enough collisions to lower the temperature below the trap edge in a volume on the order of the chamber size (i.e. cm scale). Ultimately, this constraint sets the minimum attainable temperature since the buffer gas density is a strong function of temperature. If we assume the molecules are introduced at 1000 K (common for laser ablation) and have a typical mass of $M_{Mol} = 50 \ m_{He}$, for the molecules' temperature to fall within 10% of the that of the buffer gas we see from equation 1.3 that approximately 300 collisions are required. Assuming hard sphere elastic collisions the cross-section can be estimated as 10^{-14} cm^2, the required buffer gas density to thermalize the 'molecule-to-be-trapped' over the dimensions of the system is then $3(10^{16})$ cm^3. From the vapor pressure of ^{3}He, the minimum buffer gas temperature is then 250 mK.

Experimentally, buffer gas cooling is achieved in a system similar to the one depicted in Fig. 1.2. The two main parts of the apparatus are the super-conducting

magnetic field coils and the science cell where molecules are trapped. The two NbTi super-conducting coils are arranged in an anti-Helmholtz configuration and are immersed in ^{4}He at 4 K and can provide a magnetic field up to 3 T deep. The coils are held within a Titanium cask that compensates the 10^5 N (11 tons!) repulsive force between them. The science cell is thermally isolated from the relatively warm 4 K walls of the chamber and is connected to the mixing chamber of a dilution refrigerator at the top. Its temperature can be adjusted from 100 mK up to 800 mK via resistive heaters. Inside the science chamber is a mirror that reflects the molecule detection laser beams, which enter through the bottom of the cell. Typically, near the mirror is a solid precursor to the 'molecule-to-be-trapped'. In all buffer gas loading experiments to date, the 'molecule-to-be-trapped' was introduced into the buffer gas environment by laser ablation of a metal precursor. To load the magnetic trap, the science chamber is filled with a sufficient amount of Helium (typically 10^{17} cm^{-3} at 300 mK) for the sympathetic cooling process, and the temperature reduced to $\sim$100 mK. This causes the Helium to condense to the sides of the science cell. Next, the temperature of the cell is raised via the resistive heaters to the appropriate temperature for the required Helium number density (typically $\sim$250 mK), and the laser ablation pulse is fired, introducing the 'molecule-to-be-trapped' into the science chamber. The molecules thermalize with the buffer gas and those in the weak field seeking state are trapped in the magnetic field, while those whose energy decrease with increasing field (strong-field seekers) are pushed towards the science cell walls where they are lost. Simultaneously, the temperature of the science cell is reduced to begin the cryo-pumping of the Helium buffer gas to minimize its effect on the trap lifetime of the molecules. While this technique has been used to cool several atomic species, it has to date only been implemented on one molecular species: Calcium Monohydride (CaH). Laser ablating a CaH$_2$ metal precursor, it was observed that the strong-field seeking molecules were expelled from the trap, while the weak field seeking molecules were pulled toward the trap center. Approximately, 10^8

CaH molecules were trapped at a temperature of 400 ± 50 mK with a density of $8(10^7)$ cm^{-3} [138]. These trapped weak-field seeking molecules can be observed in the trap for approximately 2 s and decay from the trap exponentially with a time constant of 0.5 s. Further reduction of the CaH temperature by standard evaporative cooling was not possible because the Helium buffer gas, which could not be pumped away quickly enough, would warm the molecules.

1.3   Cold Atom Association

The association of cold atoms to make cold molecules has had several successful manifestations including photo-association [79, 86], Feshbach resonance association [46, 117], and three-body collision combination processes [118]. Of these, three-body collision processes resulting in the formation of cold molecules has seen the least amount of experimental work and will be neglected here. However, it should be noted that recent theoretical work holds much promise for this technique and new experiments may soon follow [30]. Historically, the work in cold atom association started with one-color photo-association, then two-color photo-association was developed with the aim of populating only one ground ro-vibrational state. Feshbach resonance association was the latest of the three to see use in producing cold molecules, but its result are certainly some of the most exciting of the entire cold molecule field. One-color photo-association of cold atoms aims to excite two colliding atoms to an excited, bound molecular state that will hopefully spontaneously decay to a bound, electronic ground state molecule. The basic ideas of photo-association were already apparent in the 1960s [47] in the context of free-bound spectroscopy and were evidenced early in cold atom trapping where the process was manifested as trap loss [67]. Photo-association of alkali atoms, as seen in Fig. 1.3, occurs when two colliding S state atoms with total energy above the dissociation limit are excited to a bound state of the S + P potential curve by the photo-association laser ω_P. Subsequent decay from this excited state is either to unbound S state atoms with

the emission of a photon of frequency ω_F, or decay to a bound, electronic ground state molecule with emission of a photon of frequency ω_B.

To date, this technique has been demonstrated for the homonuclear molecules Li_2 [12], Na_2 [79], K_2 [135], Rb_2 [86], Cs_2 [51], Sr_2 [89, 145], and Ca_2 [146], and for the heteronuclear molecules NaCs [55], KRb [134] and RbCs [72]. These ground state molecules usually have a temperature on the order of their parent atom's temperature ($\sim 100~\mu K$). The production rates of ground state molecules can be estimated by first finding the rate, R_{pa}, at which the atoms in the colliding S state are photo-associated into bound excited molecules, which will roughly be: R_{pa} = Atom Density×Laser Intensity×Photo-association probability. Pillet et al. [96], treat this problem from a perturbative approach by calculating the overlap of approximate initial and final state nuclear wave functions (essentially Franck-Condon factors) with an approximate dipole matrix element for the electronic transition. They report the maximum value of the photo-association rate as:

$$R_{pa} \approx \frac{N}{V} \Big(\frac{\pi^2 \Gamma^2}{2} \frac{I}{I_o} \Big) \frac{\mu^{J-1/2} T^{J-1} C_3^{(2J+2)/3}}{\Delta^{(4J+7)/3}} \tag{1.4}$$

Where N/V is the atomic density, Γ is the atomic spontaneous emission rate, I is the laser intensity, I_o is the transition saturation intensity, μ is the reduced mass, J is the angular momentum of excited molecular state, C_3 characterizes the long-range potential of the excited molecule state (*i.e.* $-C_3/R^3$), and Δ is the binding energy of photo-associated state. From this result it is trivial to estimate the rate of production of ground state molecules, R_{gm}, as:

$$R_{gm} = R_{pa} \sum_f P_{i \to f}, \tag{1.5}$$

where $P_{i \to f}$ is the probability of spontaneous emission to a final bound-state f, which depends on the usual dipole matrix element, as well as the Franck-Condon factors introduced by the nuclear overlap integrals. While typical values for R_{pa} can be substantial,
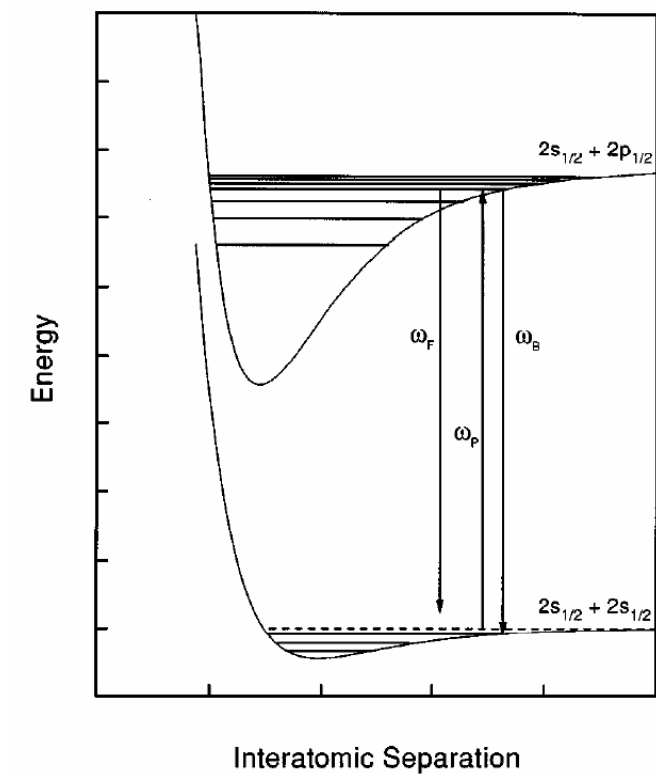
Figure 1.3: Representative potential curves for colliding alkali atoms along with the photon frequencies involved in one-color photo-association. The laser field, ω_P, excites the colliding atoms to a bound state of the excited potential curve, which hopefully decays by ω_B to a bound, ground state molecule. Taken from [12].

the values of $P_{i \to f}$ are quite small leading to small molecular formation rates [96][1] . Because colliding atoms do not spend much time near each other the absorption of the associating photon, ω_L, must occur at large intermolecular separation and thus the Franck-Condon factors are only significant to states of high vibration. Furthermore, the subsequent decay to the bound, electronic ground state is typically to high vibrational levels because, again, the Franck-Condon factors are only significant to high vibrational levels of the ground state. The Franck-Condon factors do not provide strict transition rules, and in the case of high vibrational level transitions they are usually quite weak. This leads to the population of many different high-lying vibrational levels and the observed low molecule production rate (typically 10^3 molecules/sec).

Since both high vibrational level molecules and a distribution of population complicate most experiments, two-color photo-association has been developed to circumvent the problems inherent to one-color photo-association. In two-color photo-association a second laser field is applied with the aim of primarily populating a single, low vibrational level in the ground state. As seen in Fig. 1.4 there are two general types of two-color photo-association. The more common type, shown in Fig. 1.4(a), is a stimulated Raman process. Here the two atoms absorb a photon from the laser field, ω_1, and emit a photon into a second laser field, ω_2, leaving the atoms as a bound, ground state molecule. Because $(\omega_2 - \omega_1)$ is only resonant with one vibrational level in the molecular ground state, stimulated Raman photo-association only populates a single vibrational state. Most notably, a variation of this process has been used to produce RbCs molecules in the absolute ground state [72]. An important variation of this method, stimulated Raman adiabatic passage photo-association (STIRAP PA), uses a counterintuitive pulse sequence to provide near unit transfer of the initial free atoms to molecules in a single vibrational state. By first applying the ω_2 field, the ground and excited molecule states

---

[1] Notable exceptions to this are the homonuclear alkaline earths and heteronuclear molecules, where for the resonant dipole-dipole interaction (C_3) is negligible and the overlap between the excited and ground vibration wavefunctions can be large.
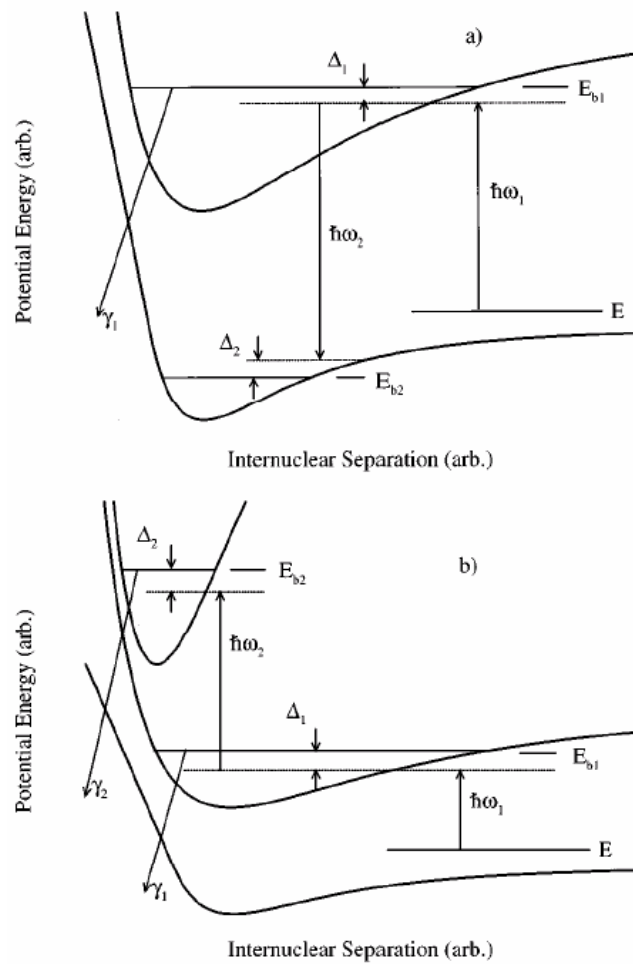
Figure 1.4: Two types of two-color photo-association. In panel (a), two-color photo-association by a stimulated Raman process is shown, which populates a single vibrational level. In panel b, two-color photo-association by a short range Rydberg state is shown, which populates several deeply bound vibrational levels in the ground electronic state. Taken from [29].

are coupled before the application of the ω_1 field, which can then transfer the atoms into a coupled state that, after the removal of ω_2, is parallel to the ground molecule state [21]. Unfortunately, it has been predicted that this type of photo-association should be absent in all cold atom samples except a condensate [82]. One drawback to the stimulated Raman process (not STIRAP PA) is that the laser fields can excite the ground state molecule back into free atoms. To combat this loss of molecules a variant of this two-color photo-association was developed. As seen in Fig. 1.4b, this method relies on the irreversible process of spontaneous emission rather than the reversible process of stimulated emission to populate the ground molecular states. The goal of this process is to excite the free atoms to an excited bound molecule state that is then excited to a short range molecular Rydberg state that will subsequently, primarily (the short range Rydberg state has appreciable Franck-Condon overlap with the lower vibrational states) decay by spontaneous emission to the low vibrational levels of the ground state molecule [20]. Using this technique researchers have been able to produce up to 10^5 molecules/sec per vibrational level [91]. This method produces deeply bound ground state molecules (v < 10), but because it relies on spontaneous emission, and the Franck-Condon factors do not provide strict transition rules, it populates many different vibrational levels.

The most recent method, Feshbach resonance association, used to produce cold molecules is conceptually similar to the stimulated Raman photo-association in that the interaction between atoms are drastically altered by the coupling of specific initial and final quantum states by an applied field. Fig. 1.5 represents the relevant information in Feshbach resonance scattering, which occurs when the relative kinetic energy of two colliding atoms is close to the energy of a bound molecule state. These bound molecular states arise from the potential energy curve of a different hyperfine configuration of the colliding atoms. Since the different hyperfine configurations of the atoms experience different energy shifts in a magnetic field, the tuning of an external magnetic field can bring the colliding atoms in and out of resonance with the bound molecular state. As

seen in Fig. 1.5(a) (for the specific case of ^{85}Rb) when the magnetic field is tuned towards 155 Gauss (the position of a Feshbach resonance) the energy of the colliding atoms moves towards that of the bound molecular state, and the scattering length diverges (Fig. 1.5(b)) [46]. During a Feshbach resonance scattering event, atoms colliding on the open channel can make a transition to the closed channel and thus cold molecules are formed. To date the technique of Feshbach resonance association has been used to produce ultra-cold Li_2 [117], Na_2 [140], K_2 [104], Rb_2 [46], and Cs_2 [58] molecules. Furthermore, heteronuclear molecules formed with feshbach resonance association should become available in the near future as recent experiments have observed heteronuclear feshbach resonances between K and Rb [65] and between Li and Na [115]. Typical experiments produce 10^3-10^5 molecules at $\sim$100 nK, with the higher molecule production numbers belonging to the experiments that employ fermions due to the suppression of molecule decay by Fermi statistics. The most notable success of these experiments is the creation of a coherent atom-molecule superposition [46]. In this experiment, two magnetic field pulses, slightly detuned from the Feshbach resonance, and separated by a constant but variable magnetic field significantly detuned from the resonance, B_{evolve}, were applied. The first pulse converted some of the atoms to molecules and the second pulse transformed the molecules back into atoms. Observations of the atom number remaining in the condensate after the second pulse revealed dramatic oscillations as a function of the time between the two pulses as seen in Fig. 1.6. This was interpreted as evidence of a coherent superposition of atom and molecule states. The first pulse is believed to provide a rapid perturbation that leads to non-adiabatic mixing of the atom and molecule states that then evolves at the energy given by the magnetic field, B_{evolve}. Thus, in analogy to Ramsey's method of separated, oscillatory fields [102], the conversion of molecules back to atoms by the second pulse exhibits remarkable dependence on the time between the two pulses.

The future of cold atom association is indeed bright with new ideas, such as
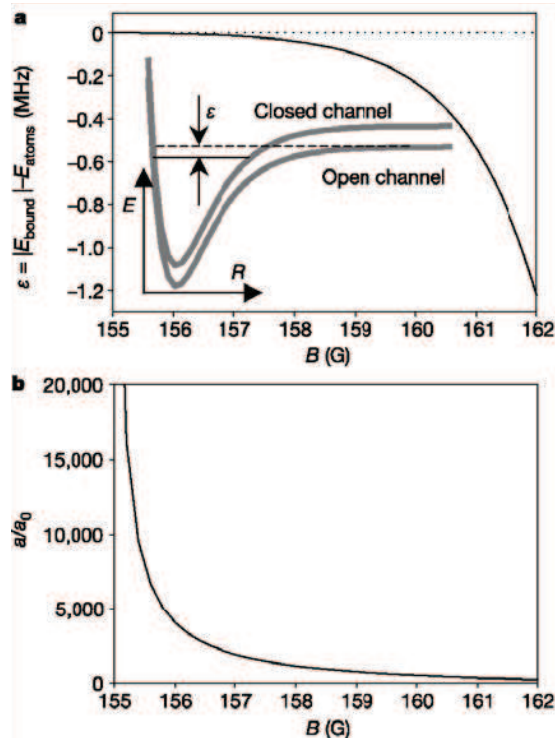
Figure 1.5: The relevant information for Feshbach resonance association is shown. As the magnetic field is tuned towards the resonance the scattering length diverges, and it becomes possible to make a transition to the bound molecule state (closed channel) from the initial atom states (open channel). Taken from [46].
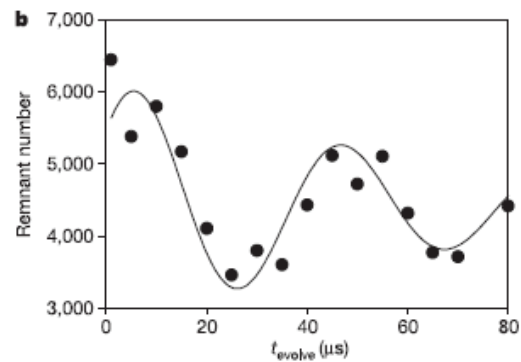
Figure 1.6: The oscillation in remaining condensate number is shown after the second magnetic field pulse, the frequency of the Rabi oscillations match well with the energy of a bound molecule state indicating the production of a coherent superposition of atom and molecule states. Taken from [46].
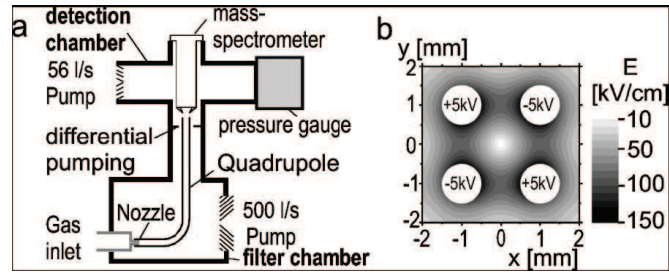
Figure 1.7: (a) Slow molecule filter experimental set-up. (b) Quadrupolar electric field contour plot. Taken from [103].

association with coherent population accumulation via pulse shaping of a femtosecond laser [32] and optical Feshbach resonances [145] being developed, the field may prove to be the method of choice for cold molecule production – though it will likely always be limited to molecules composed of atoms that can be laser cooled.

1.4   Slow Molecule Filtering

The underlying principle behind slow molecule filtering is quite similar to the operation of slow molecule spectroscopy in a cavity [141], namely: Slow molecules already exist in a room temperature distribution. Thus, slow, cold molecules can be obtained by distilling them out of a room temperature distribution. This idea was already apparent as early as 1956 [101], when it was (unsuccessfully) attempted to filter slow atoms from a hot beam using gravity. The first successful implementation of the method came in 1999 [53], when slow Li atoms were selected out of a thermal source by a curved magnetic guide that only the slowest atoms could follow.

The realization of this technique for polar molecules is nearly identical to that of Ref. [53], except that the Stark effect associated with polar molecules is used for the guiding force instead of the Zeeman effect. The basic experimental set-up, along with a contour plot of the guiding, quadrupole electric field, is shown in Fig. 1.7. The molecule of choice (to-date H_2CO and ND_3) is introduced into the electric-quadrupole

guide through an effusive nozzle, *i.e.* gas inlet. The molecules are transversely guided by the quadrupole field until they reach a bend in the guide. The bend serves to limit the maximum longitudinal velocity since fast molecules will not be guided around the bend and consequently, exit the guide. Typical molecular fluxes at the exit of the guide are 10^9 molecules/s and are composed of several rotational states since the gas inlet is near room temperature. The quadrupole guide has also been operated in an alternate gradient manner, opening the door for production of cold strong-field seeking molecules [68]. Recently, an electrostatic trap was placed at the exit of the quadrupole guide, which held a sample of ND_3 at a density of 10^8 cm^{-3} with an average lifetime of 130 ms [107].

Chapter 2

Molecular Structure: A Primer

2.1 The Basics

Unlike an atom, whose fine structure is completely determined by the behavior of its electrons, a molecule's structure largely depends on the degrees of freedom of the nuclei. The ability of molecules to rotate and vibrate makes their spectra fundamentally different than that of atoms. Because of these extra degrees of freedom, the internal energy of a molecule, E_M, is the sum of three parts; rotation (E_R), vibration (E_V), and electronic (E_E):

$$E_M = E_R + E_V + E_E. \tag{2.1}$$

The relative scale of these energies is shown in Fig. 2.1. As seen in the figure, the three energy contributions represent three distinct energies scales - rotation, the smallest scale, adds energies on the order of 10 cm^{-1}, vibration contributes energies on the order of 1000 cm^{-1}, and the electronic energy is on the order of 10,000 cm^{-1}. For this reason, it is acceptable to treat vibration as a perturbation to the electronic energy and rotation as a perturbation to vibration.

The electronic contribution to the energy, E_E, is the same as for atoms. Namely, it is the energy of the molecule's electrons moving in the potential created by the nuclei and the other electrons. While this contribution is considerably more difficult to calculate for molecules than atoms, it is conceptually no different and all of one's intuition from atoms can be properly applied.
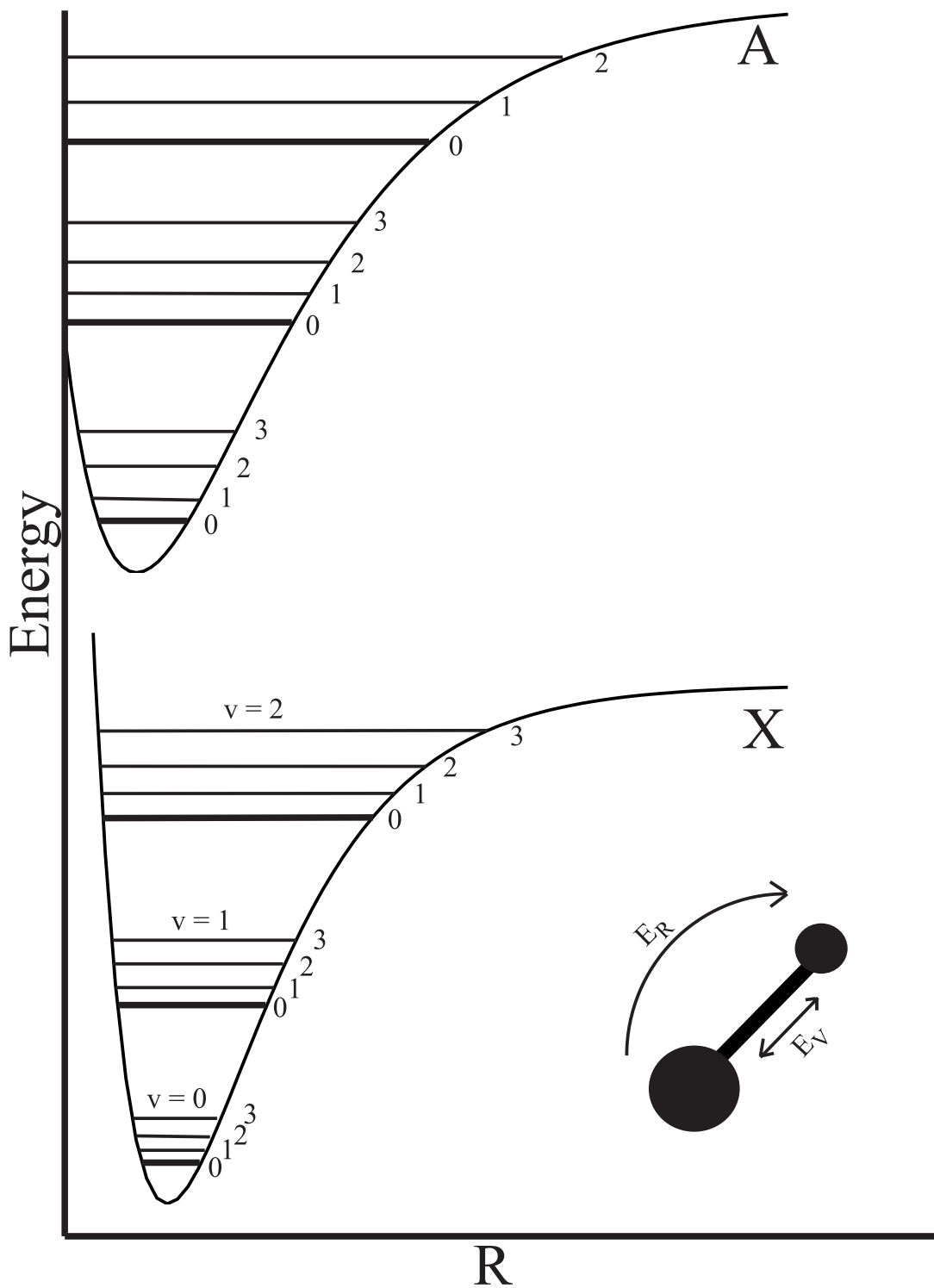
Figure 2.1: Schematic energy level structure of a molecule. The vibrational and rotational structure is drawn in the internuclear (Morse) potential for a ground (X) and excited (A) electronic state. Labels to the right of the potential curves are the rotational quantum number, R.

For low vibration and rotation, the intermolecular potential of Fig. 2.1 is sufficiently approximated as a harmonic oscillator [59]. Thus, the expected vibrational splittings are simply:

$$E_V = h\omega(v + 1/2), \tag{2.2}$$

where ω is the oscillator frequency and v is the vibrational quantum number. Clearly, as the molecule is excited in rotation and vibration this approximation breaks down, *i.e.* the vibrational potential becomes substantially anharmonic. To treat this, one typically expresses the vibrational energy of the molecule as a power series of harmonic oscillator energies with different oscillator frequencies,

$$E_V = \sum_n h\omega_n(v + 1/2)^n. \tag{2.3}$$

Retaining the first three terms of Eq. 2.3 is typically enough to be accurate within 1 cm^{-1}. Though the values of the ω_n's can be calculated, they are usually derived from spectroscopic data.

The molecular rotation of a diatomic molecule can be approximated quite well by a rigid rotor model, which describes two masses m_1 and m_2 separated by a fixed distance, r. Solution of the rigid rotor Schrödinger equation yields the molecular rotation energies as:

$$E_R = \frac{h^2}{8\pi^2 I} R(R + 1), \tag{2.4}$$

where I is the molecule's moment of inertia and R is the rotational quantum number. The prefactor of Eq. 2.4 is called the rotational constant and is usually written as B for diatomic molecules. For a real vibrating molecule, the rigid rotor model breaks down since the average internuclear distance depends on v. However, by defining a value of B for each vibrational level, *i.e.* B_v, it is possible to use Eq. 2.4 to predict reasonably accurate values for the rotational energy spacing.

2.2 The Structure of OH

The neutral hydroxyl free radical (OH), though extremely chemically reactive, is a stable, diatomic molecule. For low rotational levels, the angular momentum coupling of the $^2\Pi$ electronic ground state of the OH molecule is sufficiently described by Hund's case (a) [59] as seen in Fig. 2.2. Under this interaction scheme, both the electron orbital angular momentum L and electron spin S are coupled to the intramolecular axis, leading to the definition of the total electron angular momentum as $\Omega = \Lambda + \Sigma$, where $|\Lambda| = 1$ ($|\Sigma| = 1/2$) represents the projection of L (S) onto this axis. This coupling results in two spin-orbit states, where the $^2\Pi_{3/2}$ state lies ~ 126 cm^{-1} below the $^2\Pi_{1/2}$ state as shown in Fig. 2.4(a). Strong spin-orbit coupling (A_{SO} = -139 cm^{-1}) is responsible for the observed large splitting between the two Ω branches. The molecular angular momentum, J, in the laboratory frame is defined as $J = L + S + R$, where R represents the nuclear rotation angular momentum. The allowed values of J in the laboratory frame are given as $J = \Omega, \Omega + 1, \Omega + 2, \ldots$

The fine structure energy in Hund's case (a) for a diatomic molecule is primarily given by the sum of the rotational energy described by the Hamiltonian H_{Rot} and the fine-structure energy described by the Hamiltonian H_{FS}. The rotational Hamiltonian is clearly given as

$$
\begin{aligned}
H_{Rot} &= B\vec{R}^2 \\
&= B[(J^2 - J_z^2) + (L^2 - L_z^2) + (S^2 - S_z^2) + (L^+S^- + L^-S^+) \\
&\quad -(J^+L^- + J^-L^+) - (J^+S^- + J^-S^+)],
\end{aligned}
\tag{2.5}
$$

where subscript-z denotes the projection onto the space-fixed axis z (see Fig. 2.2). While the fine-structure Hamiltonian is the sum of two parts describing the spin-orbit and the spin-rotation coupling [144]

$$
H_{FS} = A_{SO}\vec{L} \cdot \vec{S} + \gamma_{SR}\vec{R} \cdot \vec{S}
$$
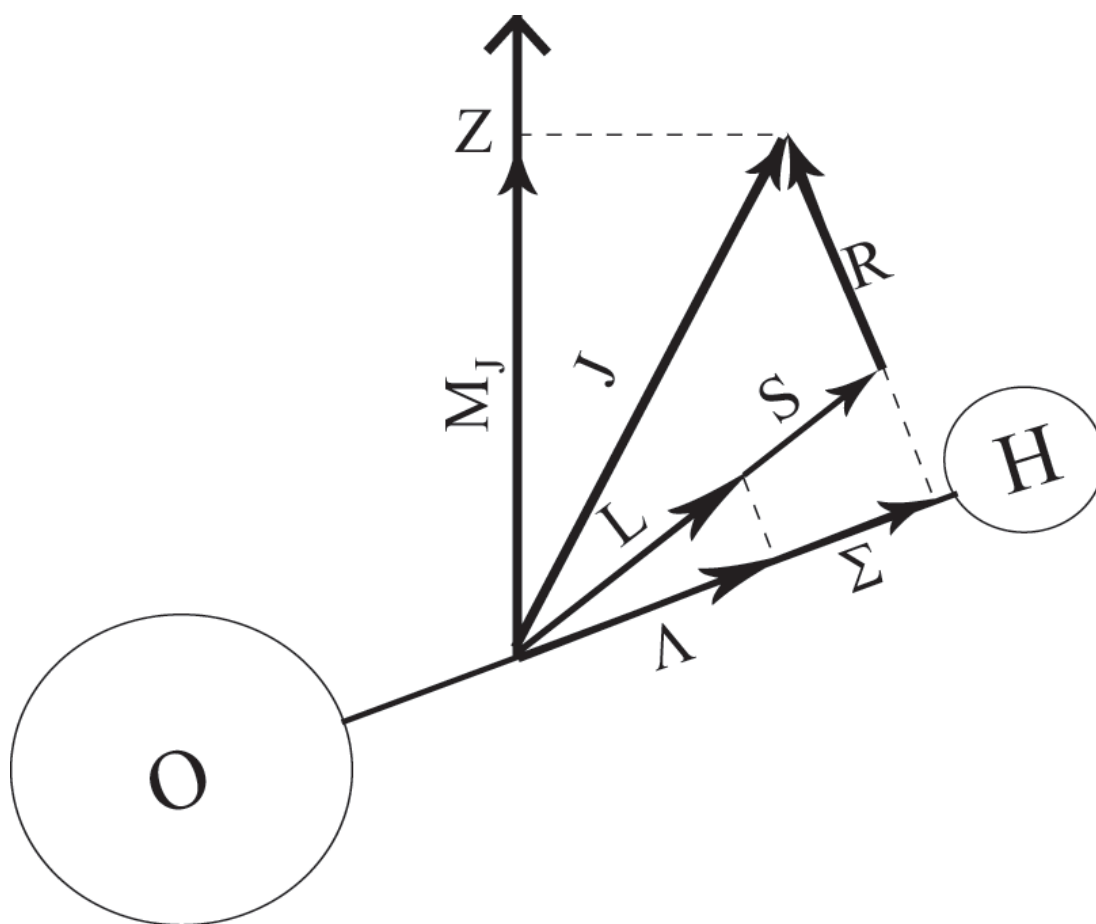
Figure 2.2: Hund's case (a) angular momentum coupling scheme for OH.

$$= A_{SO}L_z S_z + \frac{1}{2}A_{SO}(L^+ S^- + L^- S^+)$$

$$+ \gamma_{SR}(\vec{J} - \vec{L} - \vec{S}) \cdot \vec{S}, \tag{2.6}$$

where γ_{SR} is the spin-rotation constant. The total Hamiltonian can efficiently be written in a Hund's case (a) basis that respects parity

$$|JM|\Omega|\epsilon\rangle = \frac{1}{\sqrt{2}}[|JM|\Omega|\rangle|\Lambda\Sigma\rangle + \epsilon|JM - |\Omega|\rangle| - \Lambda - \Sigma\rangle], \tag{2.7}$$

with the rotational part of the wavefunction given by the Wigner rotation matrix elements [31]

$$|JM\Omega\rangle = \left(\frac{2J+1}{8\pi^2}\right)^{\frac{1}{2}} D_{M\Omega}^{J*}(\theta, \phi, \chi). \tag{2.8}$$

In this basis, the matrix elements of the rotational Hamiltonian are given as

$$
\begin{aligned}
E_{11}(J,\epsilon) &= \langle JM\frac{1}{2}\epsilon|H_{Rot}|\langle JM\frac{1}{2}\epsilon\rangle = -\frac{1}{2}A_{SO} + B(J+\frac{1}{2})^2 \\
&\quad + \frac{1}{2}(1 - \epsilon(J+\frac{1}{2}))[p + q(1 - \epsilon(J+\frac{1}{2}))] \tag{2.9} \\
E_{22}(J,\epsilon) &= \langle JM\frac{3}{2}\epsilon|H_{Rot}|\langle JM\frac{3}{2}\epsilon\rangle = \frac{1}{2}A_{SO} + B((J+\frac{1}{2})^2 - 2) \\
&\quad + \frac{1}{2}q((J+\frac{1}{2})^2 - 1) \tag{2.10} \\
E_{12}(J,\epsilon) &= \langle JM\frac{1}{2}\epsilon|H_{Rot}|\langle JM\frac{3}{2}\epsilon\rangle = \\
&\quad -\frac{1}{4}[4B + p + 2q(1 - \epsilon(J+\frac{1}{2}))]\sqrt{(J+\frac{1}{2})^2 - 1}, \tag{2.11}
\end{aligned}
$$

where p and q are the Λ-doubling parameters. Diagonalizing this Hamiltonian leads to an intermediate Hund's case, *i.e.* mixture of Hund's case (a) states, with eigenstates

$$|\Psi^-\rangle = -b(J)|JM\frac{1}{2}\epsilon\rangle + a(J)|JM\frac{3}{2}\epsilon\rangle \tag{2.12}$$

$$|\Psi^+\rangle = a(J)|JM\frac{1}{2}\epsilon\rangle + b(J)|JM\frac{3}{2}\epsilon\rangle \tag{2.13}$$

$$a(J) = \left[\frac{\sqrt{4(J+\frac{1}{2})^2 + \frac{A_{SO}}{B}(\frac{A_{SO}}{B} - 4)} + (\frac{A_{SO}}{B} - 2)}{2\sqrt{4(J+\frac{1}{2})^2 + \frac{A_{SO}}{B}(\frac{A_{SO}}{B} - 4)}}\right]^{1/2} \tag{2.14}$$

$$b(J) = \left[\frac{\sqrt{4(J+\frac{1}{2})^2 + \frac{A_{SO}}{B}(\frac{A_{SO}}{B} - 4)} - (\frac{A_{SO}}{B} - 2)}{2\sqrt{4(J+\frac{1}{2})^2 + \frac{A_{SO}}{B}(\frac{A_{SO}}{B} - 4)}}\right]^{1/2}. \tag{2.15}$$

In Fig. 2.3, the values for the mixing coefficients, $a(J)$ and $b(J)$, are shown. At low J, $b(J)$ is nearly 1 and $a(J)$ is nearly 0, and thus $|\Psi^+\rangle \approx -|JM\frac{1}{2}\epsilon\rangle$ and $|\Psi^-\rangle \approx |JM\frac{3}{2}\epsilon\rangle$, which means that for low rotation OH is sufficiently described by a Hund's case (a) basis. For this reason, it is customary to label the OH states using a Hund's case (a) basis – though it is technically correct only for the lowest J levels where Ω is still a reasonable quantum number.

The energies of these eigenstates are given from the diagonalization of the 2×2 matrix of Eq. 2.11 as

$$E^{\pm}(J,\epsilon) = \frac{E_{11}(J,\epsilon) + E_{22}(J,\epsilon)}{2} \pm \frac{1}{2}\sqrt{(E_{11}(J,\epsilon) + E_{22}(J,\epsilon))^2 - 4(E_{11}(J,\epsilon)E_{22}(J,\epsilon) - E_{12}(J,\epsilon)^2)},$$

(2.16)

where the $\pm$ is the energy of the corresponding eigenstate in Eq. 2.15. From Eq. 2.16 the energies of the rotational states of OH can be calculated and are shown in Fig. 2.4. The relatively large energy splitting between J states is due to the small moment of inertia of the molecule and subsequent large rotational constant, B. The coupling between the nuclear rotation and the electron angular momentum (projection of L along the internuclear axis) results in Λ-type splitting (Ω-doubling) of each state, denoted as f and e states or in terms of the case a symmetry index as $\epsilon = +1$ and $\epsilon = -1$ (the parity of a state is given as $\epsilon(-1)^{J-1/2}$). In Fig. 2.4(b), these energy separations are exaggerated for clarity. For the most abundant isotopomer (^{16}OH) with an intrinsic nuclear spin, I of 1/2, the free radical molecule is a boson. The total angular momentum is given by $F = I + J$. Each Λ-doublet component is split into hyperfine states that are characterized by a symmetry index p that defines the state's parity ($\pm$). The hyperfine energy separations have also been exaggerated for clarity of presentation in Fig. 2.4(b).

The vibrational structure of OH is the familiar spectrum of a diatomic molecule, which can be calculated from Eq. 2.3 using the values shown in Tab. 2.1.

The $^2\Sigma^+_{1/2}$ first electronic excited state of the OH molecule has an electron spin

Eigenstate Composition
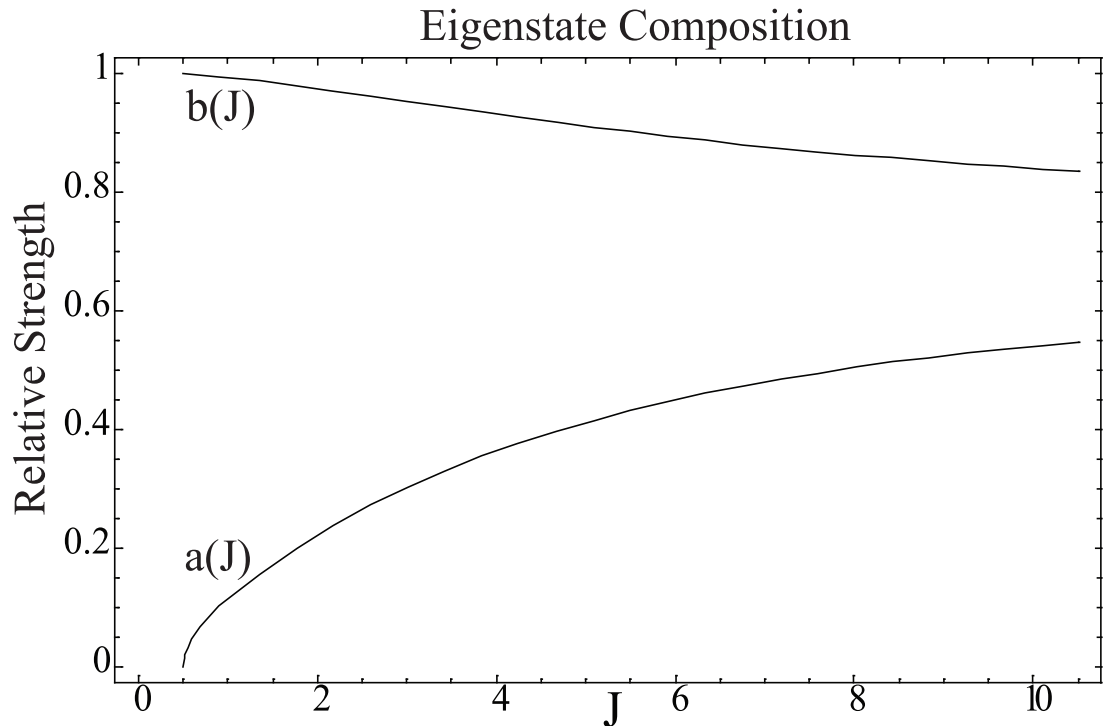
Figure 2.3: Mixing of the Hund's case (a) basis. At low J, $b(J)$ is nearly 1 and $a(J)$ is nearly 0 making it possible to label the states in the Hund's case (a) basis.

Table 2.1: Relevant molecular constants in units of cm^{-1} for calculating the ro-vibrational spectrum of OH. Taken from Refs. [36, 83].

	v = 0	v = 1	v = 2
B	18.531041	17.820121	17.118694
p	0.235214756	0.22462668	0.21387549
q	$3.86786223(10^{-2})$	$3.692540(10^{-2})$	$3.516101(10^{-2})$
ω_1	3737.7613		
ω_2	-84.881297		
ω_3	0.54090394		
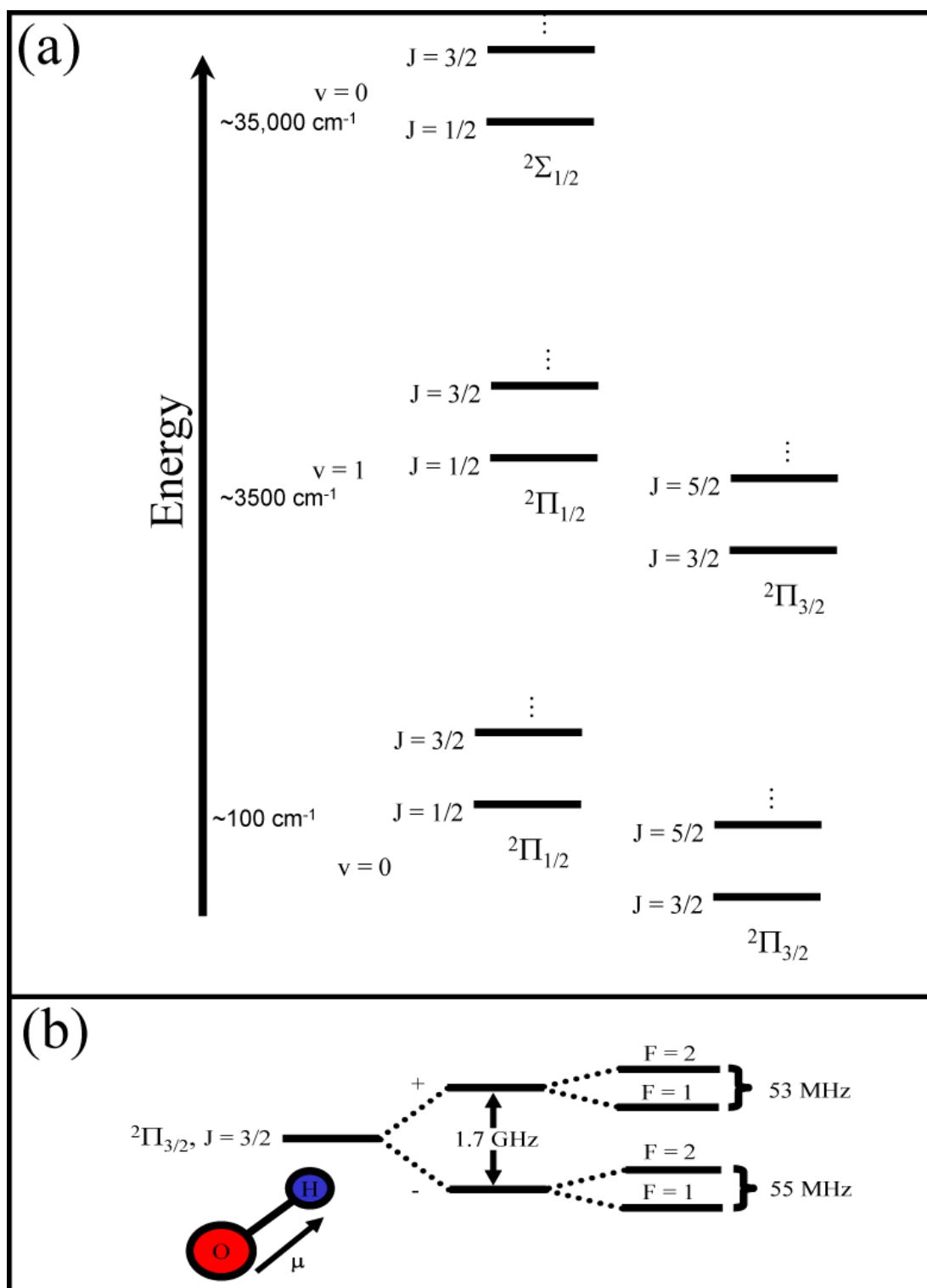
Figure 2.4: (a) Basic OH energy structure with both Λ- and ρ-doubling suppressed for clarity. The relative energy scale is given on the left. (b) Energy structure of $^2\Pi_{3/2}$ ro-vibrational ground state of OH.

of 1/2 but no electron angular momentum; thus, the appropriate couplings are well-described by Hund's case (b) [59]. For this angular momentum configuration, the only important interaction is between the nuclear rotation of the molecule R and the electron spin S – so-called ρ-doubling. This coupling separates every J state that has non-zero R into two states of the same parity and like the Λ-doubling of the Π state has been suppressed in Fig. 2.4(a) for clarity.

Because the Λ-doublet states possess opposite parity and small energy separations, adjacent levels of the ground state OH readily mix under the interaction of the molecule's permanent electric dipole ($\mu = 1.67$ D) with an external electric field. Since the electric dipole moment, μ, must lie along the intermolecular axis, its projection on the space fixed axis z, $i.e.$ the electric field, is given as

$$\mu_{eff} = \mu \cos(\Omega, J) \cos(J, z) = \mu \frac{\Omega}{\sqrt{J(J+1)}} \frac{M_J}{\sqrt{J(J+1)}} = \frac{\mu \Omega M_J}{J(J+1)}, \qquad (2.17)$$

where $cos(a, b)$ is the is the interior angle between vectors $\vec{a}$ and $\vec{b}$. The matrix elements of this dipolar coupling for a linear electric field, transformed into a hyperfine basis, are given by [87]

$$\langle JI|\Omega|FM_F\epsilon|\vec{\mu} \cdot \vec{\mathbf{E}}|J'I'|\Omega'|F'M_F'\epsilon'\rangle = -\frac{\mu E}{2}[1 + (-1)^{J+J'}\epsilon\epsilon'](-1)^{F+F'+M_F'+I-|\Omega|+1}$$

$$\times \sqrt{[J][J'][F][F']} \begin{pmatrix} J & 1 & J' \\ -|\Omega| & 0 & |\Omega| \end{pmatrix} \begin{pmatrix} F' & 1 & F \\ -M_F' & 0 & M_F \end{pmatrix} \begin{Bmatrix} J & 1 & J' \\ -|\Omega| & 0 & |\Omega| \end{Bmatrix}.$$

Inspection of the above equation reveals the convenient fact that only states of the same Ω and M_F are coupled. With the large spin-orbit and rotational splittings present in OH, this means that the Stark shifts of the relevant states are accurately calculated with a basis containing only the lowest Λ-doublet. For example, the Stark shift of four of the main states of interest, $|2 \pm 2\pm\rangle$ ($|FM_Fp\rangle$) (the stretched states), is given from the Hamiltonian:

$$H^{Stark} = \begin{pmatrix} 0 & -\frac{3}{5}\mu E \\ -\frac{3}{5}\mu E & \Delta_\Lambda \end{pmatrix}, \qquad (2.18)$$
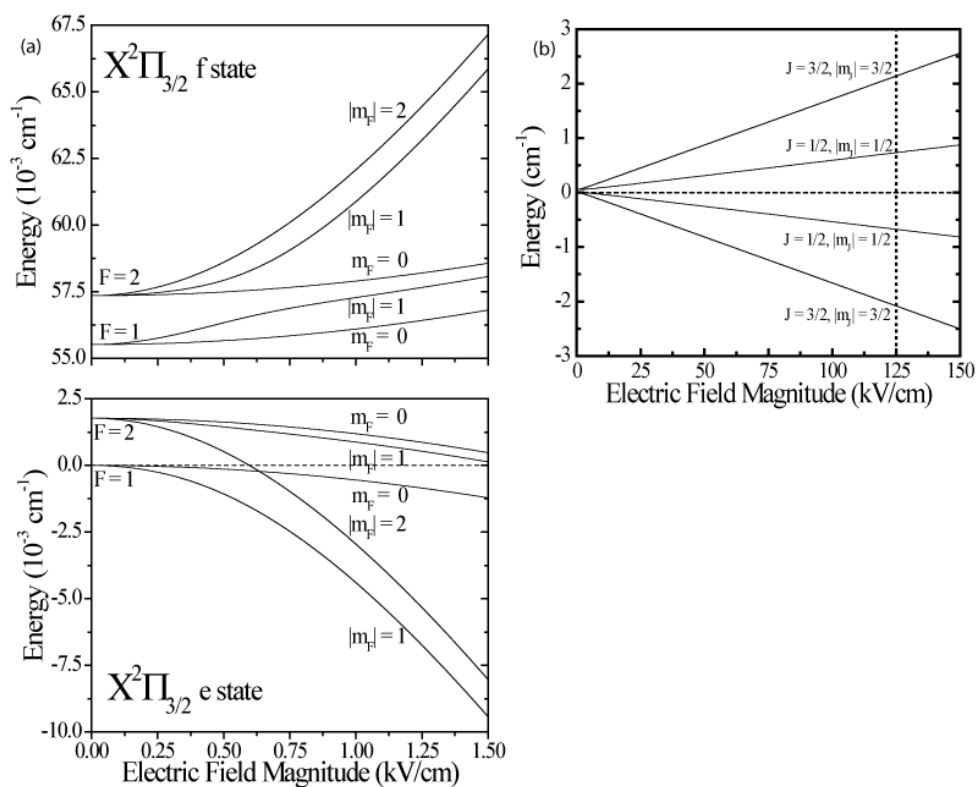
Figure 2.5: (a) The Stark energy shift for ground state OH molecules in low electric fields. The initial e (f) state is shown in the lower (upper) panel, where the hyperfine levels are indicated next to the traces. (b) The Stark shift for ground state OH molecules in high electric fields. The vertical dotted line indicates the regime where the Stark decelerator operates; the dashed horizontal line denotes zero energy.

written in the basis

$$\Psi = \begin{pmatrix} |2 \pm 2-\rangle \\ |2 \pm 2+\rangle \end{pmatrix}. \tag{2.19}$$

And thus, the Stark shift of these state is $E_{Stark}^{\pm} = \frac{\Delta_\Lambda}{2} \pm \sqrt{(\frac{\Delta_\Lambda}{2})^2 + (\frac{3}{5}\mu E)^2}$ and the eigenvectors are given as

$$|\chi^{\pm}\rangle = \frac{1}{\sqrt{(\frac{3}{5}\mu E)^2 + (E_{Stark}^{\pm})^2}} \left(\left(\frac{-3}{5}\mu E\right)|2 \pm 2-\rangle + E_{Stark}^{\pm}|2 \pm 2+\rangle \right). \tag{2.20}$$

The energy of these mixed states increases (weak-field seeking states) or decreases (strong-field seeking states) as a function of the electric field strength, as shown for the ro-vibrational ground state of OH in Fig. 2.5. The Stark energy shift evolves from quadratic to linear when the energy change due to the applied field exceeds the Λ-doublet splitting value of 0.055 cm^{-1}. The ground state shift is unaffected by the next higher rotational state due to the large energy separation of $\sim$84 cm^{-1}.

In the high electric field regime, the complex energy levels depicted in Fig. 2.5(a) emerge as four distinct fine-structure families. As shown in Fig. 2.5(b), for the Stark slowing experiment discussed here, the weak-field seeking states are most relevant, with the $^2\Pi_{3/2}$ F = 2, —m$_F$— = 2,1 states experiencing approximately three times the Stark energy shift of the $^2\Pi_{3/2}$ F = 2, m$_F$ = 0 and $^2\Pi_{3/2}$ F = 1, m$_F$ = 0,1 states. The horizontal dashed line corresponds to the zero energy level while the vertical dotted line represents the peak electric field magnitude under the normal operating voltages of the Stark decelerator. We note molecules in strong-field seeking states do not survive the first state-selection device, namely the hexapole acting as a molecular focusing lens, and therefore do not contribute to any observed signals thereafter.

From the eigenstates of Eq. 2.20 we calculate the expectation value for the electric dipole moment as a function of an electric field as

$$\langle \chi^{\pm}|\mu|\chi^{\pm}\rangle = \frac{-1}{(\frac{3}{5}\mu E)^2 + (E_{Stark}^{\pm})^2} \left(\left(\frac{3}{5}\mu E\right) E_{Stark}^{\pm}\langle 2 \pm 2 + |\mu|2 \pm 2-\rangle \right.$$
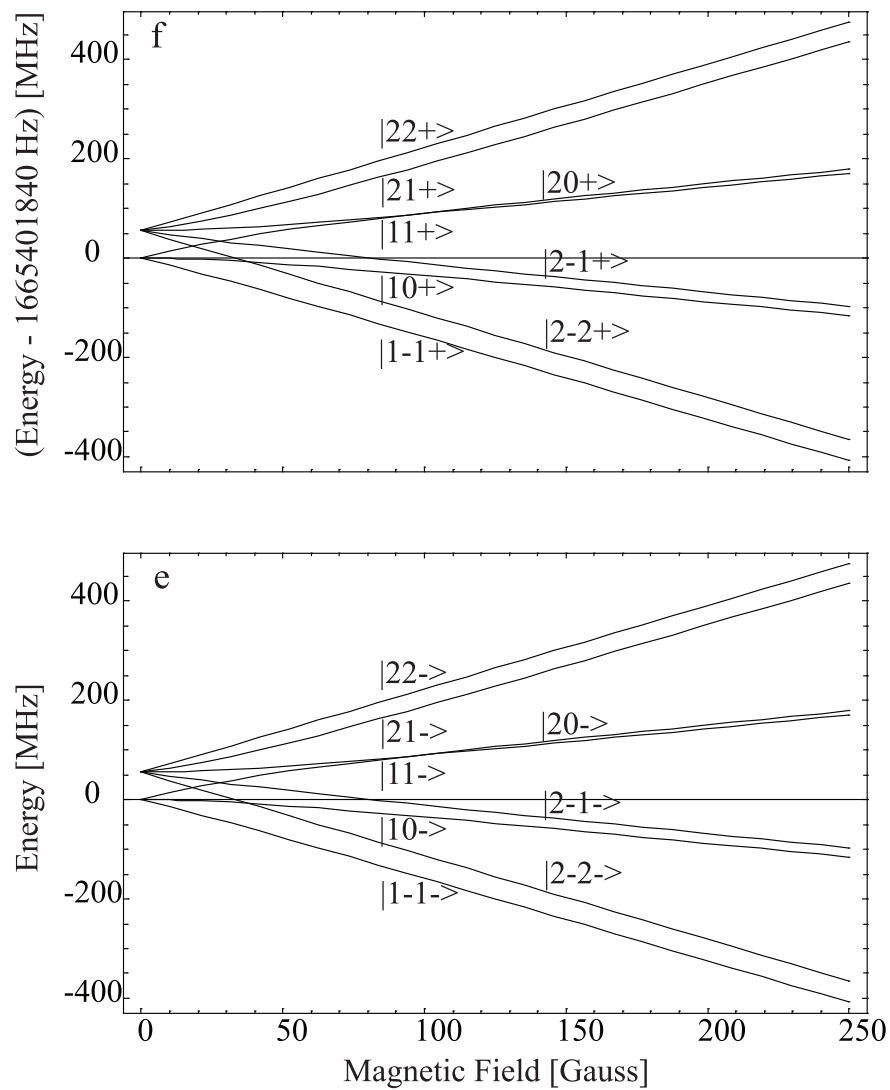
Figure 2.6: (a) The Zeeman energy shift for ground state OH molecules in low magnetic fields. The initial e (f) state is shown in the lower (upper) panel, where the hyperfine levels are indicated next to the traces.

$$+ \left(\frac{3}{5}\mu E\right) E_{Stark}^{\pm} \langle 2 \pm 2 - |\mu| 2 \pm 2+\rangle \Big)$$

$$= -\frac{18}{25} \left(\frac{(\mu E) E_{Stark}^{\pm}}{(\mu E)^2 + (E_{Stark}^{\pm})^2}\right) \mu. \tag{2.21}$$

A graph of the OH dipole moment according to this equation is shown in Fig. 2.7. The signature of a 'permanent-electric dipole moment' is evident; as the field is increased from zero the dipole moment increases from zero until it reaches its asymptotic value. At this point the dipole moment is said to be saturated, and the Stark shift becomes linear. Since the dipole-dipole potential, which depends on μ, is the dominant interaction between colliding polar molecules this leads to electric field dependent collision properties as detailed in Chap. 10.

Similarly, the Zeeman shift of the lower Λ-doublet in OH can be calculated by considering a basis that contains only the lowest Λ-doublet states. Since a Hund's case (a) molecule's electronic spin and orbital angular momentum are strongly coupled to the intermolecular axis, OH posses a magnetic dipole moment along its intermolecular axis of $\mu_{Bo} = \mu_b(\Lambda + g_e\Sigma)$ (μ_b is the Bohr magneton and $g_e = 2.002$). Like the case of an electric dipole moment this leads to a projection on the space-fixed axis, $i.e.$ magnetic field, of

$$\mu_{Bo,eff} = \frac{\mu_b(\Lambda + g_e\Sigma)\Omega M_J}{J(J+1)}. \tag{2.22}$$

The matrix elements of this dipolar coupling for a linear magnetic field, transformed into a hyperfine basis, are given by [122]

$$\langle JI|\Omega|FM_F\epsilon|\vec{\mu}\cdot\mathbf{B}|J'I'|\Omega'|F'M_F'\epsilon'\rangle = -\frac{(\Lambda+g_e\Sigma)B}{2}[1+(-1)^{J+J'+2|\Omega|}\epsilon\epsilon'](-1)^{J+J'+F+F'-M_F+I-|\Omega|+}$$

$$\times\sqrt{[J][J'][F][F']} \begin{pmatrix} J & 1 & J' \\ -|\Omega| & 0 & |\Omega| \end{pmatrix} \begin{pmatrix} F' & 1 & F \\ M_F' & 0 & -M_F \end{pmatrix} \begin{Bmatrix} F & F' & 1 \\ J' & J & I \end{Bmatrix}.$$

Conveniently, the magnetic dipole operator does not couple states of the opposite parity and the upper and lower Λ-doublet have essentially the same Zeeman shift as shown in Fig. 2.6.
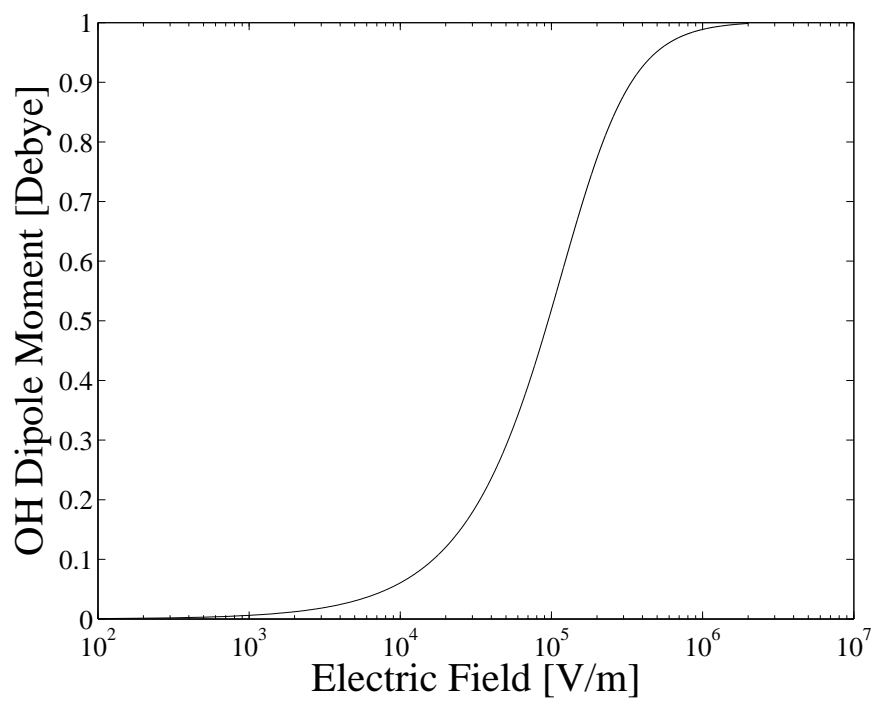
Figure 2.7: The absolute value of the of the OH dipole moment for the $|2 \pm 2\pm\rangle$ state.
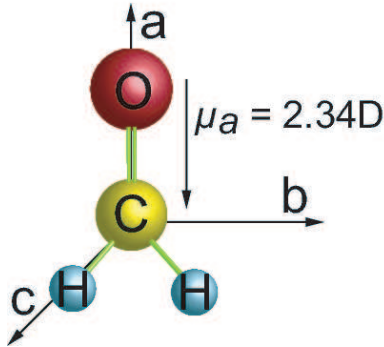
Figure 2.8: Structure of formaldehyde (H_2CO).

2.3   The Structure of H_2CO

As shown in Fig. 2.8, H_2CO is a near-symmetric prolate top molecule, with nearly degenerate rotations about the b- and c- axes. The dipole moment, μ_a, along the a-axis causes these nearly degenerate, opposite parity states to experience a large Stark shift with an applied electric field. Calculations of the Stark shift are quite intense since there is no analytical expression for the zero-field energies of asymmetric top molecules. The rotational Hamiltonian for the asymmetric rotor can be written as [56]:

$$H = A\mathbf{J}_a^2 + B\mathbf{J}_b^2 + C\mathbf{J}_c^2, \tag{2.23}$$

where A, B, and C are the rotational constants for rotation about the respective axes and $\mathbf{J}_i^2$ is the angular momentum operator for the ith axis. Since the rotational energy of a symmetric top molecule is well known [123], it is convenient to recast Eq. 2.23 into two terms – one of which is diagonal in the symmetric top basis and one that couples different symmetric top states:

$$H = 1/2(A+C)\mathbf{J}^2 + 1/2(A-C)(\mathbf{J}_a^2 + \frac{2B-A-C}{A-C}\mathbf{J}_b^2 - \mathbf{J}_c^2). \tag{2.24}$$

Thus, the problem of calculating the rotational energies of an asymmetric top molecule has been reduced to diagonalizing Eq. 2.24 in the symmetric top molecule basis of

Table 2.2: Parameters for calculating the off-diagonal rotational contribution for an asymmetric top molecule.

Principal axis	a	b	c
F	$\frac{1}{2}(\frac{2B-A-C}{A-C} - 1)$	0	$\frac{1}{2}(\frac{2B-A-C}{A-C} + 1)$
G	1	$\frac{2B-A-C}{A-C}$	-1
H	$-\frac{1}{2}(\frac{2B-A-C}{A-C} + 1)$	1	$\frac{1}{2}(\frac{2B-A-C}{A-C} - 1)$

$|JKM\rangle$, where K is the projection of J onto the symmetric top molecule's symmetry axis. Schematically, the rotational energy and eigenstates of the assymetric top molecule in the $|J_\tau M\rangle$ ($\tau = K_a - K_c$) basis may now be written as:

$$E_{J_\tau M} = \frac{1}{2}(A+C)J(J+1) + \frac{1}{2}(A-C)\widetilde{E}_{J_\tau M} \tag{2.25}$$

$$|J_\tau M\rangle = \sum_K a_K^{J_\tau M}|JKM\rangle, \tag{2.26}$$

where both the values $a_K^{J_\tau M}$ and $\widetilde{E}_{J_\tau M}$ are found from the eigenvalues and eigenvectors of the non-diagonal part of Eq. 2.24. The matrix elements of this part of the Hamiltonian can be found in several reviews [56, 123], and are given as:

$$\langle JKM|\mathbf{J}_a^2 + \tfrac{2B-A-C}{A-C}\mathbf{J}_b^2 - \mathbf{J}_c^2|JKM\rangle = F[J(J+1) - K^2] + GK^2$$

$$\langle J(K \pm 2)M|\mathbf{J}_a^2 + \tfrac{2B-A-C}{A-C}\mathbf{J}_b^2 - \mathbf{J}_c^2|JKM\rangle =$$

$$H\sqrt{\tfrac{1}{4}[J(J+1) - K(K \pm 1)][J(J+1) - K(K \pm 1)(K \pm 2)]},$$

where the values of F, G, and H depend on the molecule's principal axis, *i.e.* the molecule's axis of symmetry in the symmetric top limit, and are given in Tab. 2.2. As seen in Fig. 2.8, H_2CO is a type-a molecule and the appropriate values for F,G, and H are taken from the first column of Tab. 2.2.

Once the zero-field energies and eigenstates of the asymmetric top rotor are found, *i.e.* once eqns. 2.25 and 2.26 are solved, the Stark effect of an electric field, E, may be calculated from the Hamiltonian:

$$H_{Stark} = E\sum_i \mu_i \Phi_i, \tag{2.27}$$

Table 2.3: Direction cosine reduced matrix elements

Matrix Element	$J' = J+1$	J	$J' = J-1$
$\langle J\|\Phi_i\|J'\rangle$	$\frac{1}{4(J+1)\sqrt{(2J+1)(2J+3)}}$	$\frac{1}{4J(4J+1)}$	$\frac{1}{4J\sqrt{4J^2-1}}$
$\langle JM\|\Phi_i\|J'M\rangle$	$2\sqrt{(J+1)^2 - M^2}$	$2M$	$-2\sqrt{J^2 - M^2}$
$\langle JK\|\Phi_i\|J'K\rangle$	$2\sqrt{(J+1)^2 - K^2}$	$2K$	$-2\sqrt{J^2 - K^2}$

where μ_i is the dipole moment along the ith axis and Φ_i is the direction cosine between the electric field direction and the ith axis. The direction cosine matrix elements are given in the $|J_\tau M\rangle$ basis as:

$$\langle J_\tau M|\Phi_i|J'_{\tau'}M\rangle = \langle J|\Phi_i|J'\rangle\langle JM|\Phi_i|J'M\rangle \sum_K a_K^{J_\tau M} a_K^{J'_{\tau'}M} \langle JK|\Phi_i|J'K\rangle, \qquad (2.28)$$

with the values of the reduced matrix elements given in Tab. 2.3.

For H_2CO only the a-axis supports a dipole moment, and thus the Stark effect is conceptually similar to a diatomic molecule like OH. However, unlike the OH case, where different Λ-doublet states are coupled by the electric field, different J states are coupled in H_2CO and thus a large basis of states is required to accurately approximate the Stark shift. The results of a calculation that included up to J = 3 (16 basis states) are shown in Fig. 2.9. Here, the states are labeled by their zero-field identity in the $|J_\tau m_J\rangle$ basis. Of particular interest to this work is the $|1_1 1\rangle$ state, which is the upper component of the lowest J level of ortho-formaldehyde and is hence well populated in our supersonic expansion. This state experiences a large Stark shift (1.32 cm^{-1} at 125 kV/cm), making it excellent for Stark deceleration. There are other states accessible via, for example, stimulated Raman adiabatic passage that offer an improved Stark deceleration efficiency ($|2_2 2\rangle$) or a good candidate for implementing an AC Stark trap ($|0_0 0\rangle$) [129].
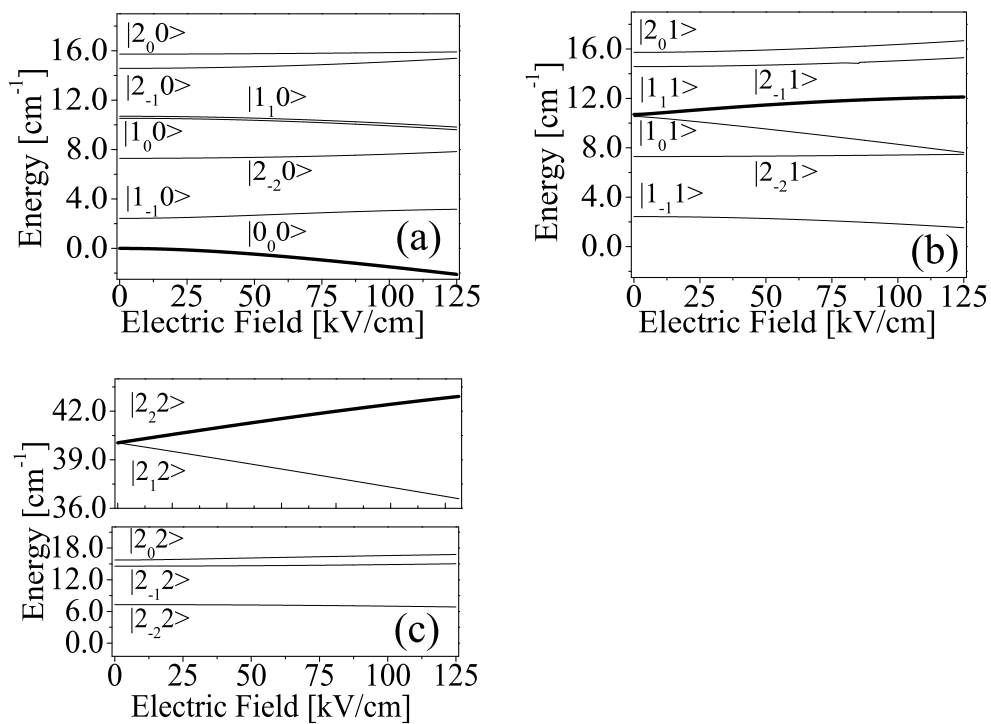
Figure 2.9: Stark shifts of the low-lying rotational states of H_2CO. States of interest for Stark deceleration and trapping are shown in bold.

Chapter 3

Molecular Detection

3.1   Laser Induced Fluorescence Detection

Potentially, background-free laser induced fluorescence (LIF) is a highly sensitive technique for detecting small numbers of molecules. In analytical chemistry and biology, resonance fluorescence is used extensively for efficient detection and identification of single molecules. The sensitivity of the fluorescence detection technique depends upon the characteristics of the decay channels of the excited states, namely that the radiative branching ratios are favorable and quenching processes are not significant. Further, for maximum detected signal, the decay photons should be collected over as large a solid angle as possible; in our experiment, intra-vacuum optics provide solid angle efficiencies of 0.5-4.5%, depending on the specific spatial location. With quantum efficiencies in the range of 10% for the cathode surfaces of modern photomultiplier tubes (PMT), one then expects a photoelectron event for every $\sim$1000 fluorescent decays. The dark current of the quantum detector is a few to a few tens of counts per second. However, various phenomena may degrade the signal-to-noise ratio. Even with careful baffling and shielding, the most severe limitation on the detection sensitivity is often the scattered excitation laser photons, which may dominate stray background light, even after careful imaging and spatial filtering.

To combat this scattered light noise, we have developed several useful techniques. The most substantial of these is a PMT whose gain can be suppressed by 10^4 in 100 ns.

The key to switching the PMT's gain is to reverse-bias several of the dynodes in the electron multiplier chain. Experimentally, we have found that for most PMTs (circular and linear geometries) reverse biasing the dynodes 1, 3, and 5 by -20 V provided the most suppression (see Fig. 3.1). Note, that because of the tube geometry linear PMTs usually exhibit a larger gain suppression. Another advantage of switching a small number of dynodes is that the capacitive load of the switches is greatly reduced, thus speeding up the attainable switching time. Typically, the gated photo-multiplier, which is normally in the suppressed gain state, is turned 'on' $\sim$100 ns after the excitation laser fires and remains on for 5 to 20 μs, depending on the molecule's fluorescence lifetime. Thus, the PMT and subsequent electronics do not 'see' the majority of the scattered excitation laser light. This is particularly advantageous in situations when the scattered light noise dominates over the LIF signal, *e.g.* imaging within the decelerator array which consist of highly polished stainless steel rods. Also, because the PMT is gated 'on' only for a few microseconds the contribution of dark counts is completely negligible. Another useful technique for suppressing scattered light has been to coat the inside of the vacuum chamber with a flat-black vacuum compatible paint, originally developed for use in satellites [2]. This paint prevents multiple reflections of the scattered light and can decrease the stray light signal as much as an order of magnitude, while still allowing vacuum pressures of 10^{-9} torr. One final useful technique, which is often over-looked in LIF detection experiments, is the use of a 'red' filter. The typical LIF experiment utilizes an optical filter whose goal is to attenuate at the excitation laser frequency as much as possible (typically OD $\geq$ 5), while transmitting as much as possible at the fluorescence wavelength (typically 50%). However, when using an ultra-violet wavelength for the excitation frequency, as is required for most molecular detection schemes, the scattered light can cause objects in its path (windows, vacuum chamber walls, etc.) to fluoresce. This fluorescence is almost always red-shifted and can usually passes through the filter used to block the excitation laser, leading to substantial noise backgrounds. By placing
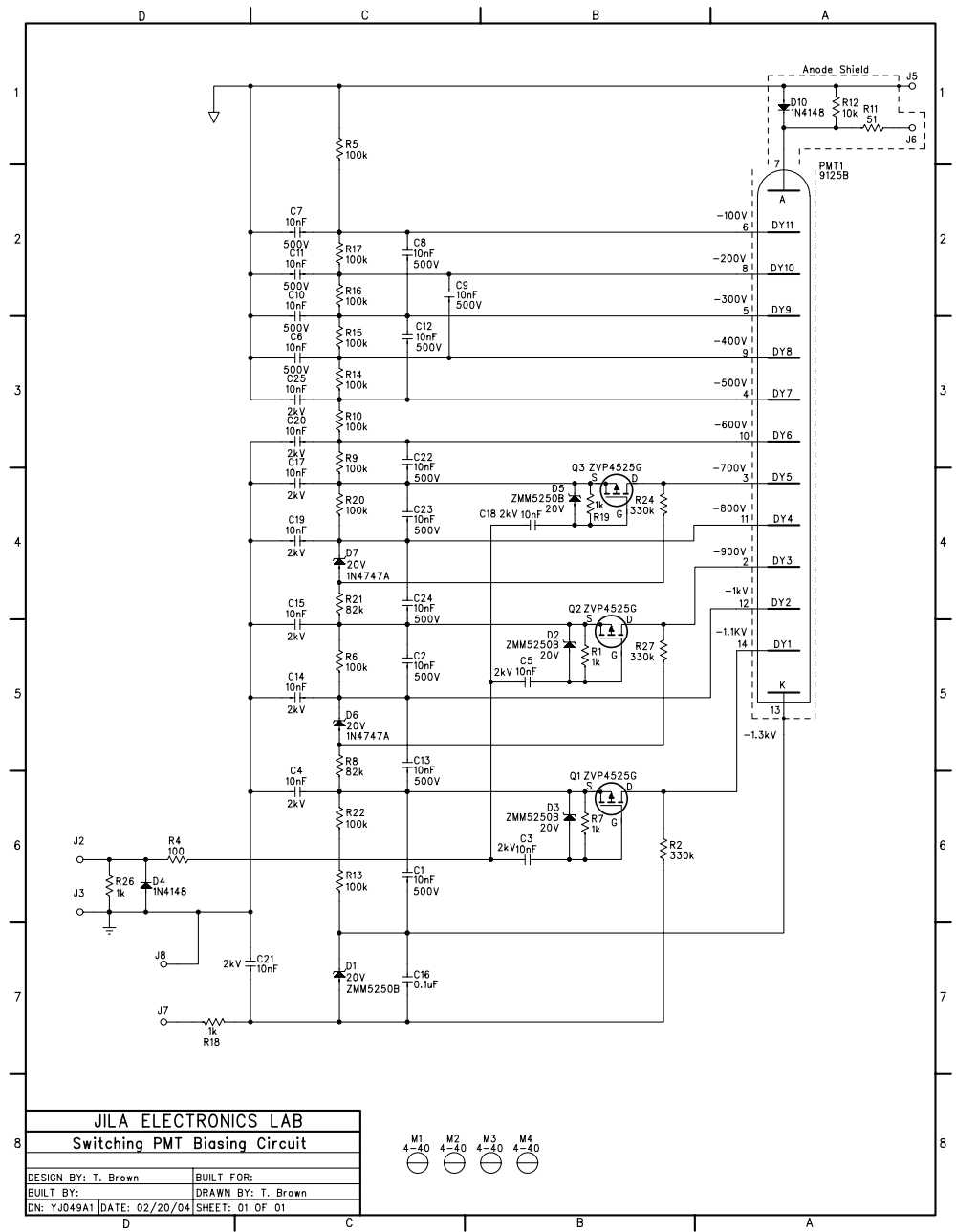
Figure 3.1: Gated photomultiplier schematic. The voltages on dynodes 1, 3, and 5 are reverse biased by -20 V shutting off the electron cascade.

a filter in the fluorescence collection path, which blocks frequencies to the red of the laser (but obviously not the fluorescence wavelength) this source of noise can be completely eliminated.

Using these three techniques, along with careful imaging and spatial filtering of the collected fluorescence, we reduce the noise signal due to scattered/stray light to a negligible level. In optimum situations, we register $\sim$0.03 noise photons per pulse of the excitation laser, while a typical bunching peak, containing of order 10^6 molecules, registers 10 signal photons in a single pulse.

A key benefit of utilizing fluorescence detection, besides its relative ease of implementation, is, as opposed to a spatially fixed ionization-based scheme, the ability to detect in situ molecules at multiple locations within the decelerator, greatly increasing the experimental flexibility and level of understanding. OH signals are measured within the decelerator during the actual slowing process, giving insight into the active longitudinal phase-space manipulation of the molecules by the pulsed, inhomogeneous electric fields. Specifically, in the experiment we employ LIF detection to monitor the molecules after the valve, observe the focusing effects of the hexapole on the molecules, measure the molecular packet spectra at various positions within the Stark decelerator, and finally, detect the molecules at the decelerator exit.

3.2 Hydroxyl Radical Detection

A relatively favorable branching ratio ($\sim$70%), a large difference between the excitation and decay wavelengths, and a reasonable quantum efficiency in fluorescence detection make laser induced fluorescence (LIF) a versatile approach for detecting the hydroxyl radical. The excitation source is tuned resonant with the $A^2\Sigma^+_{1/2}$ (v $=$ 1) $\leftarrow$ $^2\Pi_{3/2}$ (v $=$ 0) electronic transition at 282 nm for subsequent detection of the red-shifted radiative decay around 313 nm $A^2\Sigma^+_{1/2}$ (v $=$ 1) $\rightarrow$ $^2\Pi_{3/2}$ (v $=$ 1). The separation in wavelength allows effective optical filtering to reduce the background scattering. The

characteristic fluorescence 750 ns decay lifetime provides a distinctive signature of the presence of OH molecules.

Using a beta barium borate (BBO) crystal to frequency-double a 564 nm dye laser output (∼10 ns pulse duration) creates the ultraviolet excitation light at 282 nm with high peak intensity. The excitation laser is counter-propagated to the molecular pulse traveling down the central axis of the Stark decelerator. The relatively spectrally broad light source (∼2 GHz) encompasses any Doppler-induced frequency shifts in the OH resonance as the molecular longitudinal velocity changes during the deceleration process. As aforementioned, reduction of the laser scatter is paramount for optimized signal collection. First, due to the separation of the excitation and fluorescence wavelengths, the carefully selected photomultiplier tube (PMT) has a photocathode responsivity that is severely reduced at the laser wavelength versus the fluorescence wavelength. Next, an interference filter selectively inhibits the laser light (10^5 suppression) versus the fluorescent photons (70% transmission). We also utilize a switched PMT whose dynode voltages are quickly arranged during the laser pulse so as to actively repel photoelectrons liberated by the scattered UV light on the cathode material.

The OH molecular signal is measured as a function of time at a particular spatial location in the following manner. First, immediately prior to the measurement (∼1 μs), all high voltage electrodes within the vacuum chamber are grounded to avoid Stark shifting of the OH transition frequency. Subsequently, before the molecules have had an opportunity to exit the specific detection region, the excitation laser pulse fires, generating the OH fluorescence signal. The detected photoelectrons from the PMT are then either counted with a photon counter or amplified, averaged, and integrated over a 5 μs time window to fully encompass the appropriate state decay lifetime. The laser is stepped later in time relative to when the valve opens, and the entire measurement is repeated. In this iterative manner, a spectrum consisting of the OH signal as a function of time is generated.

3.3 Formaldehyde Molecule Detection

Laser induced fluorescence detection of the formaldehyde molecule is extremely similar to the hydroxyl radical case. The molecules are excited from the $|1_1 1\rangle$ ground state by photons at 353 nm generated from a frequency-doubled, pulsed-dye laser (PDL) pumped by a Nd:YAG laser to the $\widetilde{A}^1 A_2$ electronically excited state with one quantum in the ν_4 out-of-plane bending vibrational mode. Approximately 40% of the excited H_2CO decays non-radiatively [57], while the remaining molecules emit distributed fluorescence from 353 nm to 610 nm [109]. This fluorescence is collected, filtered, and imaged onto a photo-multiplier tube. The output of the photomultiplier tube is sent to a multi-channel scalar/averager, which serves as a gated photon counter. Operating the decelerator at 5 Hz and the PDL system at 10 Hz allows a "lock-in" type data-collection, such that every other signal is subtracted from the total photon counts. By scanning the delay between the PDL system and the triggering of the valve, a time-of-flight (ToF) curve is generated. A single data point is generated by collecting photon counts for 30 s to 2400 s (depending on required signal to noise).

Chapter 4

Sourcery: Supersonic Molecular Beams

Supersonic expansion in molecular beam experiments is a widely used technique. Under proper operating conditions, rotational and vibrational temperatures are significantly lowered along with the benefit of a reduced translational velocity spread in the molecular frame. Within the present experiments, collisions during the expansion represent the only true cooling mechanism. The maximum phase-space density achievable in the experiment is determined at this stage since during the subsequent deceleration process the phase-space distribution of the molecules undergoes conservative rotation without any enhancement in density. Therefore, as long as the relatively large translational speed of the molecular beam can be removed by the slowing capability of the Stark decelerator, a supersonic expansion provides a very useful initial source for creation and experimentation of cold molecules.

Anyone who has ever felt a leaky tire, and noticed the cool area around the leak, is familiar with the basic idea of a supersonic expansion. Namely, as a gas expands from
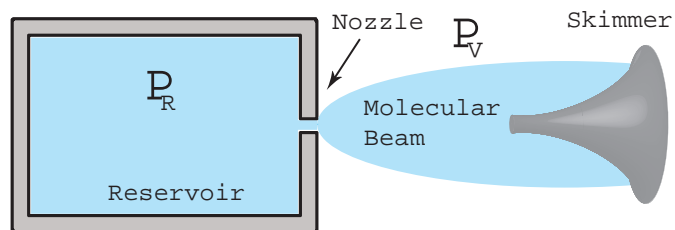
Figure 4.1: Schematic of skimmed, supersonic molecular beam.

high to low pressure, it cools. This is akin to the adiabatic expansion process in a heat engine, where the gas cools by doing work on the piston. In this case, the piston is the gas itself[1] . Furthermore, because the rotational and vibrational energies will equilibrate through collisions with this local (moving frame) temperature, they are cooled as well. Interestingly, the pressure differential necessary for the expansion accelerates the gas as it expands, *i.e.* the piston is accelerated, leading to a beam of molecules with a high mean velocity and low spread about that mean. Therefore, one might expect that as the pressure of the reservoir (see Fig. 4.1) is increased the final speed of the molecular beam increases. While this is true at low differential pressure, once the pressure difference reaches a critical value the molecular beam is accelerated to the local velocity of sound and can no longer respond to the local boundary conditions. Thus, the pressure at the nozzle exit is no longer given by the pressure in the vacuum chamber, P_V, but is rather some fraction of the pressure in the reservoir, P_R, and further increase in the reservoir pressure does not result in any increase in the beam velocity. This final beam velocity, v_∞, can easily be approximated from conservation of energy [11]. Conservation of energy for the expanding gas takes the form:

$$Nk_BT_o = \frac{1}{2}Mv^2 + Nk_BT, \tag{4.1}$$

where N is the number of molecules, k_B is the Boltzman constant, T_o is the reservoir temperature, M is the total mass of the expanding molecules, v is the speed of the molecular beam, and T is the final temperature of the expanded gas. Dividing Eq. 4.1 by M, utilizing the ideal gas law and the definition of enthalpy we have:

$$h_o = \frac{v^2}{2} + h, \tag{4.2}$$

where h_o and h are the enthalpy per unit mass of the gas in the reservoir and after expansion, respectively. Assuming the specific heat, C_p, is constant with temperature

---

[1] Perhaps more precisely, the piston is the gas in front of the expanding gas

and using its relation with enthalpy, *i.e.* $dh/dT = Cp$, the final beam velocity is given as:

$$v_\infty = \sqrt{2C_p(T - T_o)}. \tag{4.3}$$

For an ideal gas the specific heat can be expressed as $C_p = (\gamma/(\gamma - 1))(R/m)$, where γ is the ratio of the specific heats of constant pressure and volume ($\gamma = 5/3$ for an ideal gas), R is the universal gas constant, and m is the mass of the expanding molecule. Thus, the final beam velocity from a supersonic expansion can be written as:

$$v_\infty = \sqrt{2\frac{\gamma}{\gamma - 1}\frac{R}{m}(T - T_o)}. \tag{4.4}$$

From this equation it is evident that typical beam velocities are on the order of 10^3 m/s,[2] and depend on the mass of the expanding molecule and the reservoir temperature. Since the kinetic energy of a molecule is quadratic in velocity it is advantageous for deceleration experiments to start with a molecular beam speed that is as low as possible. Clearly, this can be accomplished by lowering the reservoir temperature or choosing a large mass. Lowering the reservoir temperature is experimentally trivial and is usually only limited by the vapor pressure of the expanding molecules. Choosing a large mass for the expanding gas is often not possible since the choice of molecule is usually made based on the desired experiment. Furthermore, the kinetic energy is linearly proportional to the mass, so that overall decrease in beam energy is not substantial. Fortunately, it is possible to dilute the molecule of interest into a heavy carrier gas, like Xenon (131 amu), which sets the speed of the expansion. In Eq. 4.4 this requires replacing m by the average mass of the mixture, $\overline{m} = \sum_i X_i m_i$, where X_i and m_i are the molar fraction and mass of the ith species of the gas mixture. Typical experiments use a mixture of heavy carrier gas to molecule-of-interest on the order of 99:1, so that the final speed is essentially that of a beam of the carrier gas.

As aforementioned, the ability of a supersonic molecular beam to provide a beam

---

[2] The approximation $T_o \approx 0$ is usually sufficient in Eq. 4.4

Table 4.1: Working formulas for $T_\parallel$ [1].

Molecule	γ	$T_\parallel$ working formulas
He	5/3	$T_\parallel = \frac{T_o}{6.1}(P_o d)^{-12/11}$
Ne	5/3	$T_\parallel = \frac{T_o}{10.4}(P_o d)^{-12/11}$
Ar	5/3	$T_\parallel = \frac{T_o}{24.3}(P_o d)^{-12/11}$
Kr	5/3	$T_\parallel = \frac{T_o}{31.2}(P_o d)^{-12/11}$
Xe	5/3	$T_\parallel = \frac{T_o}{40.8}(P_o d)^{-12/11}$
O_2	7/5	$T_\parallel = \frac{T_o}{6.1}(P_o d)^{-0.706}$
HBr	7/5	$T_\parallel = \frac{T_o}{8.4}(P_o d)^{-0.7061}$
CH_3F	1.278	$T_\parallel = \frac{T_o}{4.3}(P_o d)^{-0.509}$
	8/6	$T_\parallel = \frac{T_o}{6.5}(P_o d)^{-0.6}$
SF_6	1.094	$T_\parallel = \frac{T_o}{1.5}(P_o d)^{-0.182}$
	8/6	$T_\parallel = \frac{T_o}{6.7}(P_o d)^{-0.6}$

of molecules with a low velocity spread is crucial for Stark deceleration experiments. Calculating the expected temperature, $T_\parallel$, is non-trivial and calculations rarely agree with experiments. Therefore, it is more beneficial to compare to empirical formulas for the expected final temperature, like those shown in Tab. 4.1 [1]. The predictions of these formulas should be taken only as rough estimates of what to expect in an actual apparatus. Nonetheless, it is clear the longitudinal beam temperature is usually on the order of 1 K and as such, supersonic molecular beams are a good source of molecules for input into a Stark decelerator, which can accept spreads up to a few 100 mK.

As anyone who has ever worked with molecular beams can attest, there is an art (or perhaps more correctly, a magic) to making a good molecular beam source. Real life complications such as pumping speed, valve opening time, nozzle construction, skimmer location, and velocity slip [11] can completely change the pulse speed and temperature. Furthermore, as most modern molecular beams are pulsed to accommodate higher beam intensities, the beam characteristics can be quite different than those predicted by the above analysis, which, strictly speaking, is valid only for a continuous beam. In the following sections, the pulsed molecular beam sources used in our Stark deceleration experiments are detailed. It is important to remember, that these sources have been

optimized for producing a beam suitable for input into a Stark decelerator under the conditions imposed by our vacuum system and as such, should be thought of only as a starting point for future molecular beam use.

4.1 Hydroxyl Radical Discharge Source

There are several different techniques to produce a molecular beam of OH radicals. The four main methods for creating OH molecules are photolysis [15, 112], radio-frequency discharge [13], DC discharge [124, 64], and chemical reactions [121]. We chose DC discharge because, of all of the methods, it is the simplest and most cost-effective technique. As presented below, the system we have developed fulfills the goal of producing a large sample of cold molecules with a high phase-space density. We report several key improvements to the standard DC discharge system, including a pulsed high-voltage discharge to reduce heating of the molecular packet and to allow for control of the mean speed of the molecular packet. Also, the introduction of a hot filament into the source chamber allows the discharge to operate more stably and at a lower voltage, thus reducing the heating of the OH molecules during their production. Through controlled application of a high voltage discharge pulse, we are able to create packets of OH molecules at reasonable densities that vary in mean speed from 265 to 470 m/s with full-width half-maximum (FWHM) velocity spread as low as 16%[3] . The results of an initial test experiment to characterize our pulsed-discharge source are presented below.

A diagram of the test apparatus and discharge assembly is shown in Fig. 4.2. The vacuum system consists of two chambers separated by a mechanical skimmer, which maintains a differential pressure between the chambers. During operation the source (hexapole) chamber is at a pressure of 4×10^{-4} torr (1×10^{-6} torr). A current loop

---

[3] More recent work utilizing a Piezo transducer actuated valve produces spreads of 10%, as detailed in a later subsection

actuated valve, commercially available from R. M. Jordan Company Inc., operates at 5-10 Hz to create a gas pulse ~100 μs long. Directly in front of the 0.5 mm diameter valve nozzle is a set of stainless steel disc electrodes, electrically isolated from one another as well as from the valve body by Boron nitride spacers. The relevant dimensions are shown in Fig. 4.2. The electrode closest to the valve has a 0.5 mm diameter hole to match the valve nozzle. The downstream electrode has an inner diameter of 4 mm to allow the gas to expand as it travels between the electrodes. For the test experiment, the valve nozzle is placed ~8 cm away from the downstream wall of the vacuum chamber to ensure carrier gas atoms scattered from the wall do not interfere with the supersonic expansion and beam propagation.

In the second chamber, a 13 cm long electric focusing hexapole is centered along the beam path. The hexapole is used as a tool to determine the transverse velocity spread of the molecular beam. The hexapole is formed by six, stainless steel, cylindrically shaped rods with rounded ends. They are 3.18 mm in diameter and set at every 60° at a center-to-center radius of 4.6 mm. Alternate rods are charged to equal magnitude but opposite polarity high voltage.

The experimental procedure begins with the pulsed valve opening for ~100 μs, thus creating a supersonically cooled pulse of Xenon (Xe) carrier gas seeded with a few percent water. The typical backing pressure of Xe is one to three atmospheres. Xe is used instead of a lighter noble gas because of the resulting lower mean speed of the molecular beam, which is advantageous for our Stark-decelerator application. At a variable time after the valve opens, a high-voltage pulse is applied to the disc electrodes. The duration of the high-voltage pulse can be varied from 1 to 200 μs. A discharge duration greater than 150 μs is considered to be essentially DC because the discharge duration is longer than the gas pulse. The polarity of the voltage applied is such that electrons are accelerated against the molecular beam propagation direction, which results in a more stable discharge than the opposite polarity. During the discharge
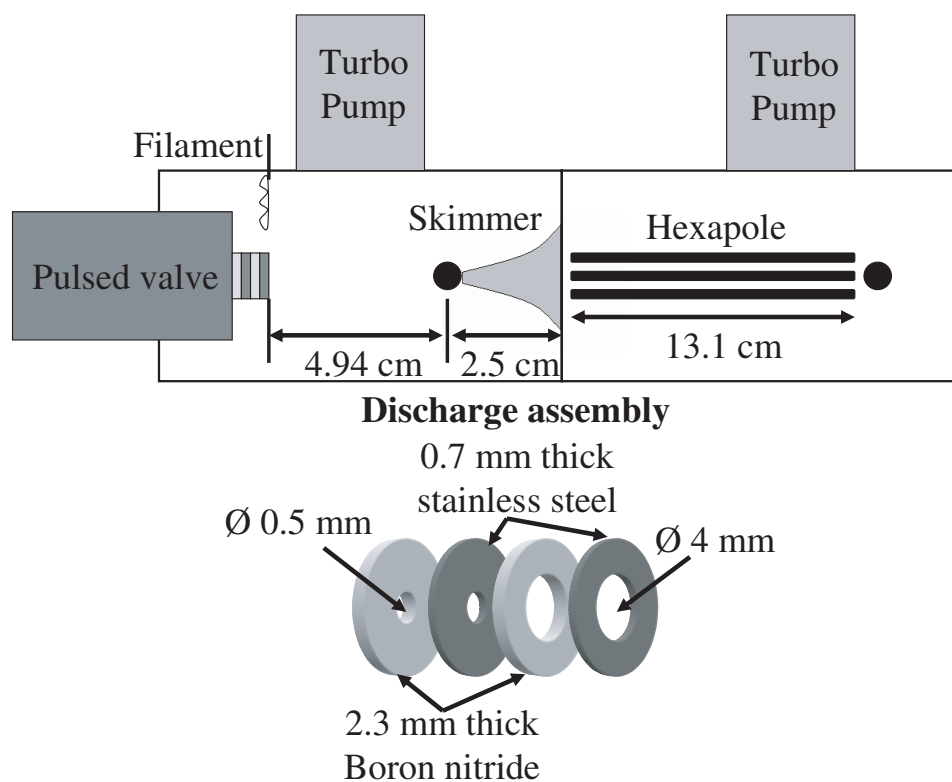
Figure 4.2: Diagram of the experimental apparatus and discharge assembly (not to scale). The system consists of two chambers individually pumped by 300 L/s turbo pumps. A differential pressure is maintained between the chambers by a mechanical skimmer. A discharge assembly is mounted directly onto a pulsed current loop actuated valve in the source chamber. The discharge assembly consists of two disc electrodes separated by insulating spacers. The second chamber contains an electric hexapole. Molecule detection, by laser induced fluorescence, takes place in two regions marked by black circles.

operation, ~3 mA of DC current is passed though a tungsten filament, which is located inside the source chamber. The positive ions created by the filament are accelerated towards the outer electrode and help to initiate a stable discharge at lower electrode voltages and shorter discharge pulse durations, ultimately leading to a colder molecular beam.

After the OH molecules are produced in the discharge, they are allowed to fly to one of two detection regions, which are illustrated by black dots in Fig. 4.2. The density of OH molecules in the detection region is determined by laser-induced fluorescence (LIF). The OH molecules are excited by a frequency-doubled pulsed dye laser on the $A^2\Sigma_{1/2}(v = 1) \leftarrow X^2\Pi_{3/2}(v = 0)$ transition at 282 nm. The fluorescence from the $A^2\Sigma_{1/2}(v = 1) \rightarrow X^2\Pi_{3/2}(v = 1)$ transition at 313 nm (with a lifetime of 750 ns) is then imaged onto a gated photomultiplier tube (PMT). An interference filter is placed in front of the PMT to reduce the transmission of the excitation laser photons by $> 10^3$, while still allowing 15% of the fluorescence photons to pass.[4] . This spectral discrimination, along with careful spatial filtering and imaging, greatly reduces the background signal from scattered laser light. The signal from the PMT is averaged 300 times and integrated over a 3 μs time window on a digital oscilloscope. The time from the discharge to the detection is varied to obtain a time-of-flight (TOF) profile of the OH molecular packet (see Fig.4.3(a)).

Creating OH using a high-voltage discharge pulse shorter than the gas pulse significantly reduces the translational and the rotational temperature, as well as permits control of the mean speed of the OH packet. In our system, the applied voltage between the discharging disc electrodes is controlled by a high-voltage MOSFET switch produced by Behlke Electronics GmbH. This device can switch up to 5 kV in well under 1 μs. Using

---

[4] After this work the fluorescence filter was improved to 10^5 suppression at the excitation frequency and 70% transmission at the fluorescence frequency through the combination of a colored glass filter (UG11 from Melles-Griot) and a bandpass filter centered at the fluorescence frequency (31BP10 from Omega Optical)

this switch to pulse the discharging voltage, the velocity spread of the OH molecular packet is greatly reduced. The TOF profiles in Fig. 4.3(a) show a dramatic narrowing of the longitudinal velocity distribution by reducing the duration of the discharge pulse from DC to 2 μs. Also, the measured rotational temperature of the OH beam decreases from 195 K to 28 K. The voltage on the electrodes is increased from 1.4 kV, for the short discharge duration, to 1.9 kV for the DC case. For a DC discharge, very few OH molecules are produced at 1.4 kV. To make a reasonable comparison between the two modes of operation, we increased the voltage for the DC case until the peak signal of the OH packet was approximately equal to that of the short discharge duration case. When the discharge is allowed to occur during the entire gas pulse, there is a large amount of heating from the violent discharge process. Thus, shortening the discharge pulse duration greatly reduces the temperature of the OH molecular packet and significantly increases the molecular phase-space density. This effect can be understood as heating only a small fraction of the expanding molecules, which then cool to a lower temperature by collisions with the remaining (unheated) pulse.

A short discharge pulse duration also gives the freedom to produce OH molecules at different stages during the supersonic expansion. OH molecular packets created at different times in the expansion process are shown to have differing mean speeds and velocity widths. Figure 4.3(b) is a plot of several example TOF profiles taken just before the skimmer where the discharge durations is 2 μs for all the data. The time between the signal triggering the valve to open and the discharge pulse, defined as "ignition time," for each trace is listed in the legend. There is an $\sim$50 μs time delay between the valve trigger and the valve opening. By timing the discharge correctly, OH molecular packets can be created with a mean speed up to 465 m/s with the discharge ignition at 80 μs or down to 275 m/s with the discharge ignition at 190 μs. The mean speed of the packet as a function of the discharge ignition time is summarized in Fig. 4.3(c) .

A likely explanation for this discharge ignition-time dependent beam velocity is
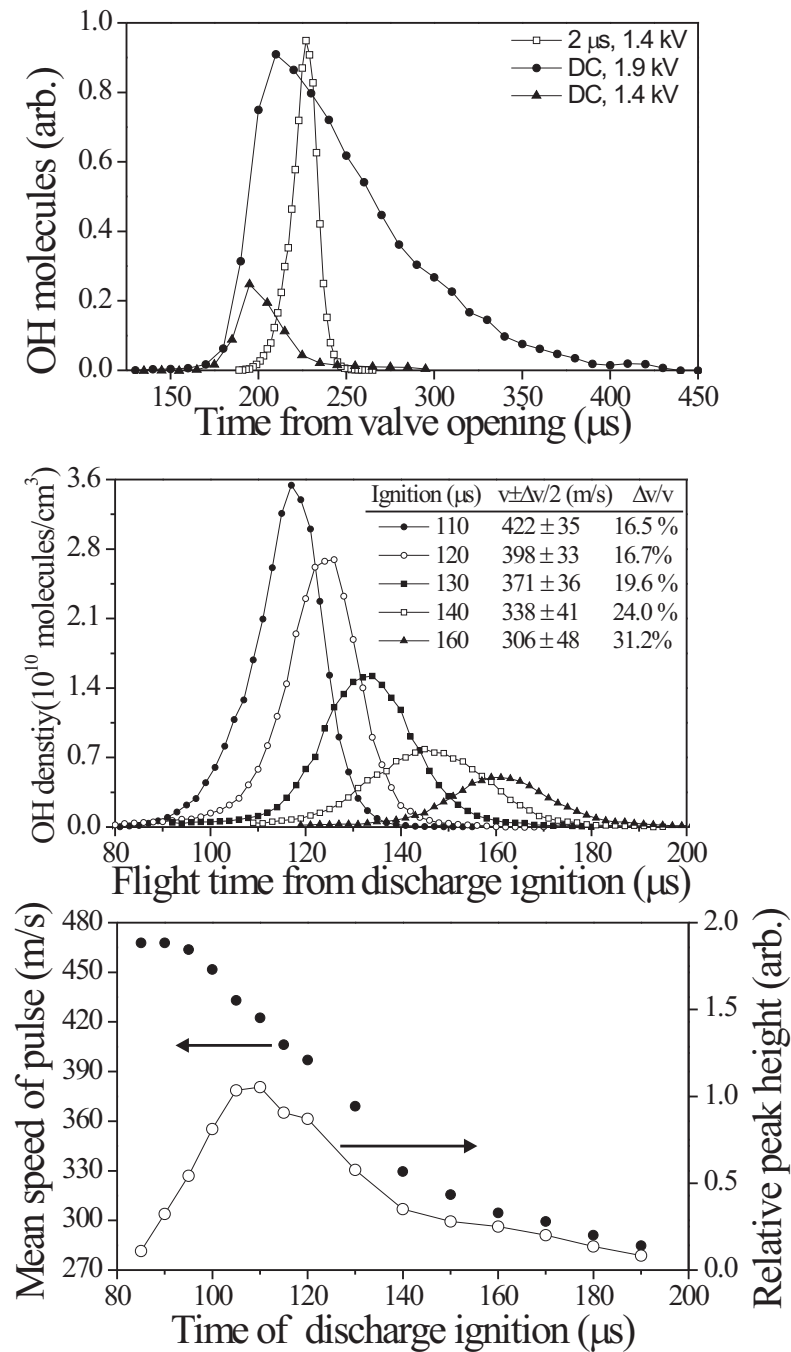
Figure 4.3: (a) Longitudinal time-of-flight (TOF) profiles, acquired in the detection region before the skimmer, for a pulsed discharge and a DC discharge at 1.4 kV and 1.9 kV. (b) TOF profiles, acquired in the detection region before the skimmer, as a function of the time from the filament-assisted discharge ignition to the LIF detection. The discharge duration is 2 μs for all the data. The discharge ignition time, mean longitudinal packet speed, and velocity width are listed in the legend for each trace. The velocity width, Δv, is the full-width half-max of the velocity distribution, which is determine from the TOF profiles taken at both detection locations. (c) Mean longitudinal speed (solid circles) and relative peak height (open circles) of the TOF profiles as a function of time from the valve trigger to the discharge ignition. For all traces, the lines serve as visual guides.

that our current-loop actuated valve heats the gas in an asymmetric way. The valve opens by passing a few thousand amperes of current through two copper leaves for several microseconds, the leaves subsequently repel one another allowing gas to escape through a small hole in one of the leaves. Presumably, this high current pulse initially heats the leaves, and since molecules must collide with these leaves before escaping through the small hole the expanding gas is heated. However, since the copper leaves have a small thermal mass and are in good contact with the rest of the valve, they quickly cool down. Thus, the later in the pulse a molecule exits the valve, the less it is heated. We see evidence of this asymmetric operation of the valve using our pulsed discharge to sample different parts of the expanding gas pulse. As seen in Fig. 4.3(c), the gas speed is large and constant over the first 15 μs of the pulse when the supersonic expansion has reached a steady-state beam velocity while the number of molecules in the beam is still steadily increasing. The speed of the gas gradually decreases as the valve remains open. We note the peak signal size is reached (at $\sim$110 μs) only after the mean speed of the supersonic expansion beam has already decreased. However, the FWHM longitudinal velocity spread is still only 16.6%.

For the application of a cooled molecular beam as an input to a Stark decelerator, we require a packet of OH molecules with a high phase-space density propagating at a low mean speed. Choosing to create the OH molecules towards the end of the gas pulse, for example at an ignition time of 160 μs, produces a packet moving at an attractive mean speed of only 306 m/s. However the amplitude of the packet is significantly smaller and the velocity width is significantly larger than a packet created at 110 μs. The variation of OH packet amplitudes for different ignition times can be seen in Fig. 4.3(c) . The optimum discharge ignition time for our application is around 110 μs. For different applications, *e.g.* reactive collision dynamics, the tunability of the mean speed of the molecular packet could be advantageous.

The other important component in the improved discharge-based system is a

hot filament in the source chamber. The hot filament has two major effects on the discharge. First, it allows the discharge to occur reliably and reproducibly even at the shortest discharge pulse duration of 1 μs. The improvements from a short discharge pulse duration are demonstrated in the previous section. Second, the hot filament allows a stable discharge to occur at lower voltages on the disc electrodes. Without the hot filament, the discharge is either not stable or does not even occur at an electrode voltage less than 3 kV; using the hot filament, the discharge is stable down to 0.7 kV, which results in a significantly colder molecular packet.

The longitudinal TOF profile and rotational temperature of the OH molecular packet are measured for different discharge voltages (Fig. 4.4). For discharge voltages below 1.9 kV, a single peak is observed in the TOF profile. However, for voltages at or above 1.9 kV, the TOF profile starts to develop two distinct maxima and indicates a considerably larger velocity spread. We expect this heating arises from the higher energy electrons created by a larger potential difference between the electrodes. As the voltage is lowered from 1.6 kV to 1.2 kV, the velocity spread remains nearly constant, but the peak number of molecules decreases as the electrons' energy decreases and thus creates OH molecules less efficiently. The rotational temperature also elucidates the heating effect from the higher discharge voltages. The rotational temperature is determined by measuring the ratio of OH molecules produced in the J = 3/2 and 5/2 states. The introduction of the hot filament permits the reduction of the discharge voltage from 3 kV to an optimized voltage of 1.4 kV, leading to almost a factor of four reduction in rotational temperature (Fig. 4.4(b)).

A Stark decelerator benefits from a molecular beam that has both a high phase-space density and a low mean longitudinal speed. The optimum configuration of the source for this application uses a 2 μs discharge duration that is ignited 110 μs after the valve is triggered to open. The filament-assisted discharge is created using a potential difference between the electrodes of 1.4 kV. A molecular packet created under these
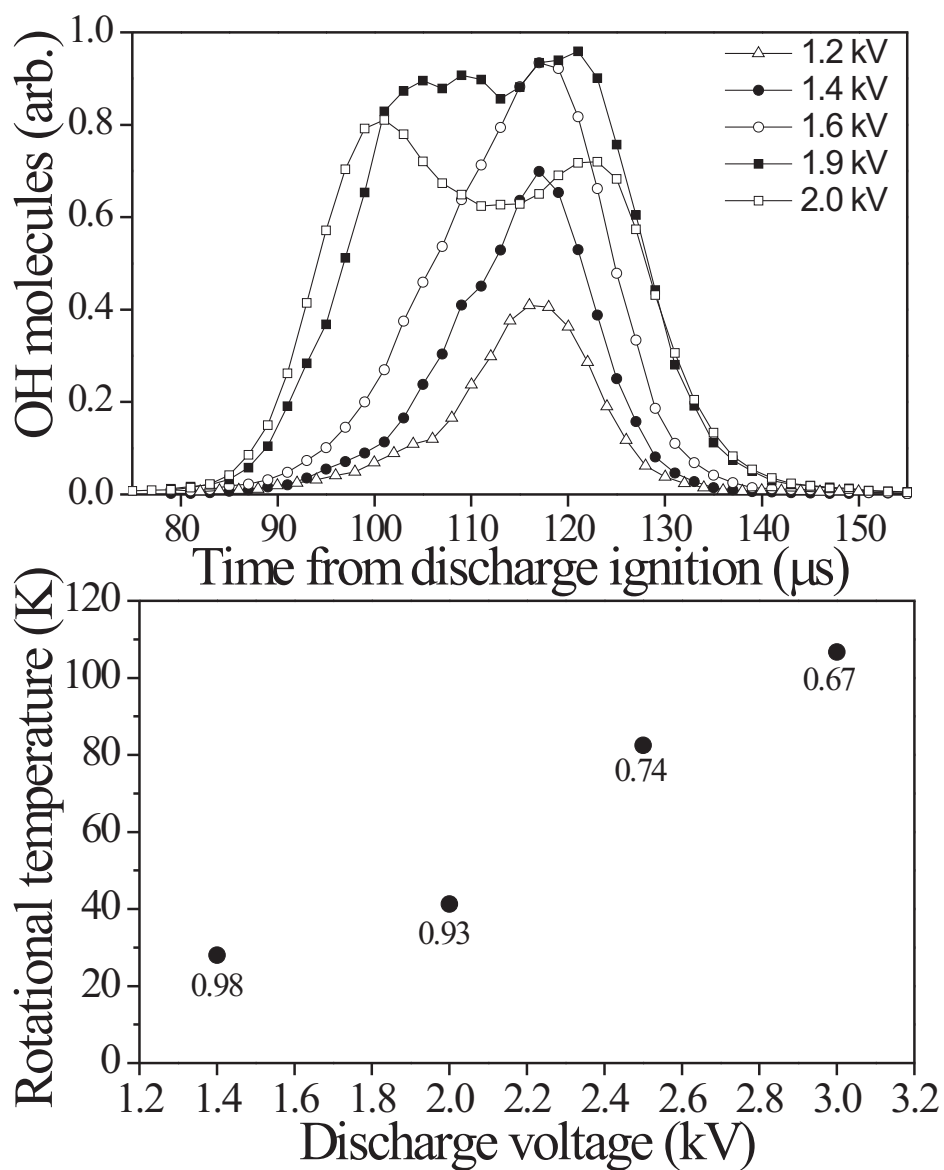
Figure 4.4: (a) TOF profiles, acquired in the detection region before the skimmer, for several discharge voltages. The discharge pulse duration is 2 μs. The solid lines are visual guides. (b) Rotational temperatures for different discharge voltages. The number associated with each point is the fraction of the molecules in the lowest rotational state (J = 3/2).

conditions has a mean velocity of 422 m/s and a longitudinal velocity spread of 16.6%, which corresponds to a translational temperature of 5 K. This is a significantly colder translational temperature than was reported by [124] of 26 K and [64] of 29 K.

The transverse velocity spread is determined through the use of the hexapole focusing effect and detailed numerical simulations. The density of OH is measured 2 mm downstream of the hexapole for different hexapole voltages, thus producing a focusing curve. From the comparison of the numerical simulations to the hexapole focusing data the full-width transverse velocity spread is estimated to be 35 m/s, which corresponds to a transverse temperature of $\sim$1.3 K.

The density of OH molecules just before the skimmer tip is determined from the calibrated LIF signal. The peak density of molecules in the $\Omega = 3/2$, J = 3/2, f-component state created under these conditions is $3.5 \times 10^{10} \text{cm}^{-3}$ measured at a distance of 5 cm from the valve nozzle. To compare with the density quoted in [124], we assume $1/r^2$ position dependence, where r is the distance from the nozzle, and an equal population in e and f parity states. Our calculated density at r = 2.3 cm in both parity states is $\sim 3 \times 10^{11} \text{cm}^{-3}$, which is a factor of 2 less than [124]. This lower molecular density can be attributed to a longer flight time using Xenon versus Argon. The longer flight time allows the molecular packet to spread in both the longitudinal and transverse directions reducing the density detected at a specific location. To accurately compare our results with the work of [124] and [64], we also performed the same experiments using Argon as a carrier gas and measured a factor of five improvement in the number of OH molecules produced.

In conclusion, we have developed and characterized a controllable discharge-based source of cooled OH free radicals. Through the use of a pulsed discharge we can tune the mean velocity of the OH beam from 465 m/s down to 275 m/s, with a FWHM longitudinal velocity spread as small as 16.6%. Also, the implementation of a hot filament in the source chamber allows a stable discharge to occur for short discharge

pulse durations and at low discharge voltages. We have shown that decreasing the discharge pulse duration and voltage creates a colder packet of OH molecules.

4.1.1 Piezo-electric Transducer Actuated Valve

Though the current-loop valve offers an extremely reliable, stable source it presents one large disadvantage for use with a Stark decelerator. Because the valve heats the gas before it expands, the molecular beams produced by these valves are moving considerably faster than expected for a room temperature expansion making the deceleration process harder. Thus, we have put forth a considerable effort in developing a beam source that is as reliable and stable as the current-loop actuated valve, but does not heat the expanding gas. Our early efforts focused on using solenoid type valves (General Valve Series 9 and 99), while these valves did not heat the pulse and resulted in lower mean speeds ($v_{OH} \approx 360$ m/s) these valves are notoriously unreliable in both pulse-to-pulse and long-term molecule production. More recently, we have implemented a piezo-electric actuated valve like the one shown in Fig. 4.5, and is basically identical to the original design of Ref. [98]. By applying a few hundred volt pulse (600 V typically) for a few hundred microseconds, the PZT retracts (200 μm travel) the plunger, allowing the gas to escape. Typical pulse lengths are on the order of 100 μs and can be adjusted through pre-tensioning of the plunger by screwing it into or out of the plunger holder. After the gas escapes the valve, it undergoes a pulsed-electric discharge (in the case of OH discharge production) as previously described. The discharge plates used for this valve are slightly modified from that described for the current-loop valve. While the hole in the first discharge plate still has a 0.5 mm hole to match the nozzle orifice, the boron nitride spacer between the plates opens with a 40° full-angle. This nozzle design has been recently shown [60] to produce as much as factor of 8 gain in downstream beam intensities by producing a more collimated molecular beam. In our experiments with OH, we see only a factor $\sim$2 gain in post-skimmer signal, presumably because of

heating from the discharge.

For OH production, this valve produces molecular beams with a mean speed of 375 m/s with 10% longitudinal velocity spread. While, the rotational temperature is similar to that of the current-loop valve, we observe slightly larger densities (less than a factor of 3). Furthermore, the produced molecular beam is extremely stable both pulse-to-pulse and long-term (the valve has not needed adjustment since its installation approximately 6 months ago). For these reason, we have replaced the current-loop valve with the PZT valve in most of our recent experiments.

Because the PZT valve represents a capacitive load to the high voltage pulser being used to drive it, it is important to employ a push-pull switch, such that the PZT is actively charged *and* discharged, ensuring the shortest pulse. A schematic of an inexpensive home-built push-pull switch (perfected by Brian Sawyer) is shown in Fig. 4.6. This switch operates reliably up to ~1.5 kV ($V_{Max} \approx 2$ kV) and can be re-configured to support negative polarity pulses by interchanging the high voltage input port and ground on the output side of the switch.

4.2   Formaldehyde Beam Source

Because gaseous H_2CO molecules readily polymerize to most surfaces, and are thus not commercially available, it is necessary to make the H_2CO for the expansion. We produce the H_2CO molecules by cracking formaldehyde polymer to produce the monomer, which is passed through a double u-tube apparatus for distilling [114](see Fig. 4.7). We normally heat the formaldehyde powder to 110 °C, which is sufficiently above the cracking temperature of 90 °C. While the cracking process takes longer to complete at this temperature, we have found that cracking at higher temperatures leads to increase polymerization in the apparatus, presumably because of the higher local vapor pressure of H_2CO. While this polymerization does not prevent the monomer from forming, it usually leads to much less total yield. After the monomer is released from
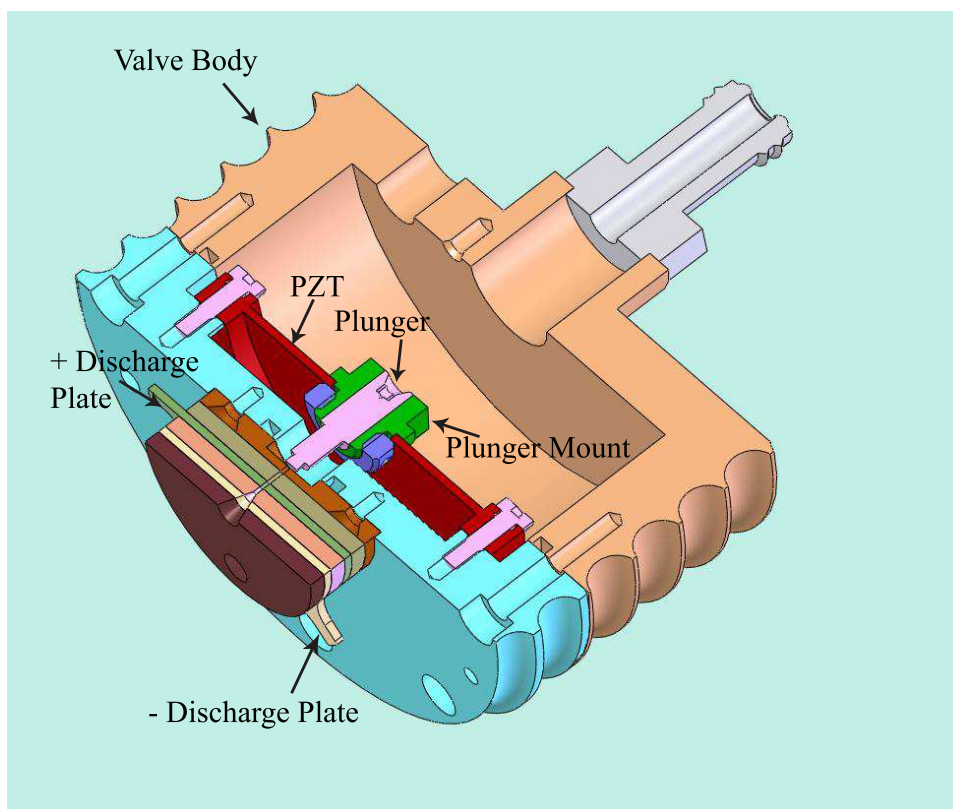
Figure 4.5: Schematic of Piezo-electric Transducer Actuated Valve. The plunger is retracted by the PZT ($\sim$200 μm travel) allowing a gas pulse (200 μs typical) to escape from the nozzle. The Xe/H_2O mixture then experiences a pulsed discharge. The discharge nozzle construction features a 40° opening angle, which produces a much more collimated beam.
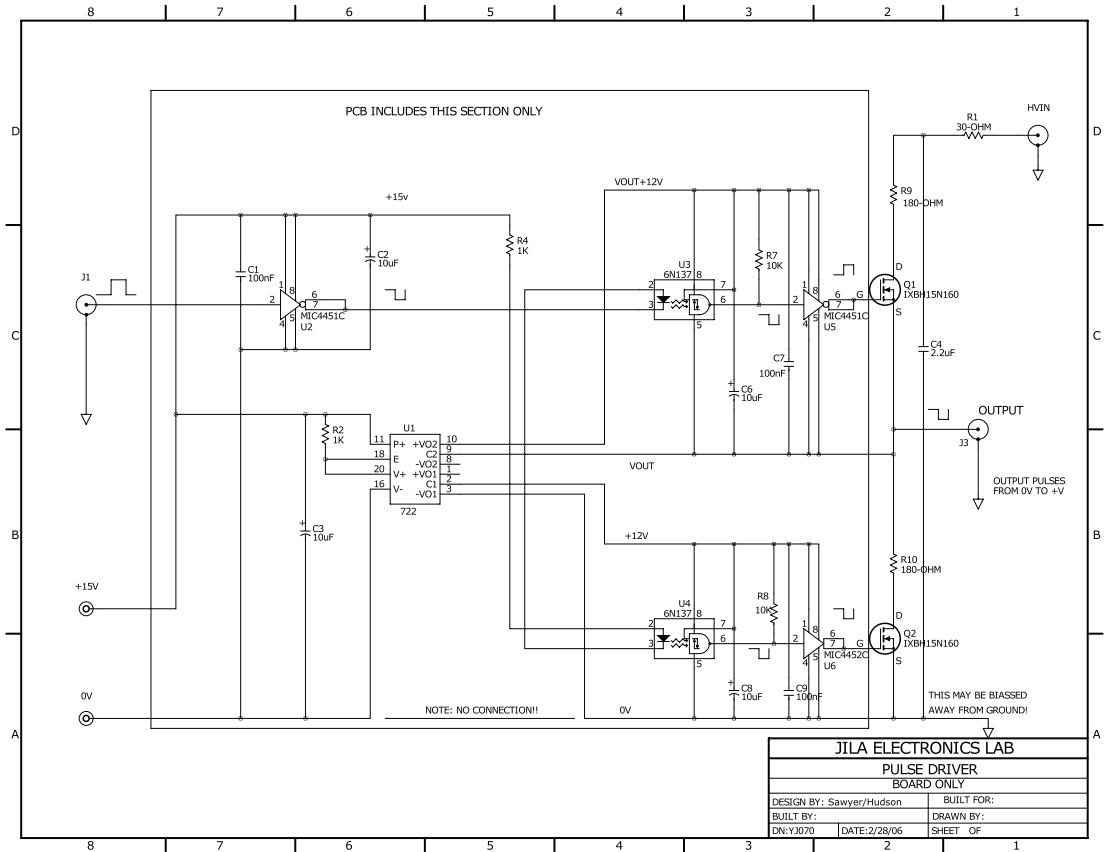
Figure 4.6: Schematic of reliable, inexpensive high voltage push-pull switch. The switch can operate reliably up to 1.5 to 2 kV.

the powder, it passes through the first u-tube, which is held at dry ice temperatures (196 K), and serves to remove contaminants such as water. The H_2CO then continues on to the second u-tube, which is held at liquid-nitrogen temperatures. At this temperature the H_2CO collects as a liquid in the bottom of the tube. Once all of the formaldehyde powder has been cracked, the valves are closed and Xenon at 2 bar pressure is flowed over the collected H_2CO, held at 196 K where H_2CO has $\sim$20 torr vapor pressure. In this work, the Xe/H_2CO mixture was expanded through either a current-loop (60 μs pulse length) or a solenoid supersonic valve (500 μs pulse length), producing beams with a mean speed (spread) of 470 m/s (10%) and 350 m/s (10%), respectively. In both cases the density of the H_2CO in the $|1_1 1\rangle$ state was approximately 10^{10} cm^{-3} measured 5 cm from the nozzle. The higher mean speed of the current-loop valve pulse is due to the aforementioned heating effects of these devices. It is interesting to note, that since H_2CO has more modes to store internal energy than OH, the heating of the current-loop valve leads to a much higher mean speed for H_2CO since this extra energy is converted into forward velocity.

In our experiments with H_2CO, we have tried several different versions of the above apparatus and have developed several practical rules for dealing with the H_2CO monomer. First, the polymerization rate to metals is much higher than to a clean glass surface. Thus, all of the distilling apparatus should be made from glass. Second, once H_2CO has polymerized to the glass the polymerization rate increases. Thus, it is important to maintain a clean distilling apparatus. The easiest and most effective way to do this is to bake the entire apparatus above the cracking temperature while pumping. Typically, we cleaned the apparatus in this way every night after we produced H_2CO. Third, as aforementioned, the highest yield in H_2CO production came when the polymer was cracked at temperatures not-too-high above the cracking temperature. Fourth, the mixture from the second u-tube was released directly into our valve reservoir for expansion and pumped away every night. This was to prevent polymerization and
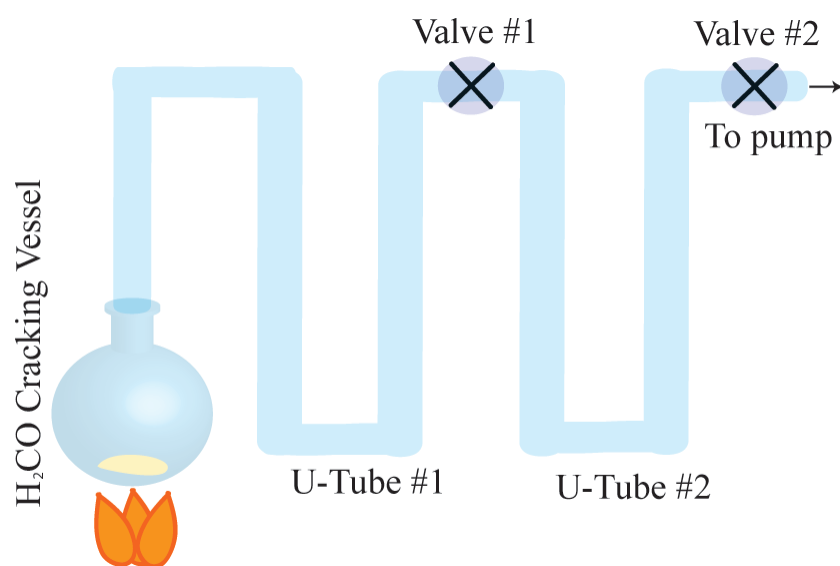
Figure 4.7: Formaldehyde cracking apparatus.

eventual clogging of the valve. For the same reason, it was not possible to store the gas for long term and we found it necessary to produce the H_2CO each day. By coating the inside of the apparatus with materials, which would reduce the polymerization rate, like Teflon, it may be possible to construct a vessel, which could store the H_2CO for longer term. Fifth, because H_2CO has a substantial vapor pressure even at low temperatures, we attempted to cool the supersonic nozzle to produce a molecular beam with lower forward velocity. While we had limited success with this technique, the polymerization rate seemed to increase at low temperatures leading to a shorter lifetime of the gas. However, a bake-able supersonic nozzle, which we did not have, should allow one to tolerate the increased polymerization rate since it could be cleaned every night. Finally, we also attempted to increase the H_2CO beam density by raising the temperature of the H_2CO reservoir (u-tube #2) which raised the H_2CO vapor pressure before the expansion. This technique showed as much as an order of magnitude improvement in beam density, however, it also led to an increased polymerization rate, which limited its usefulness in our apparatus.

4.3   Hexapole Focusing

Electrostatic hexapoles have been widely used in beam experiments to perform state-selected focusing and spatial orientation [56] of weak-field seeking, Stark-sensitive molecules. In contrast to those experiments, the hexapole utilized here is quite short in length and functions to increase the OH beam flux by matching molecules from the source into the acceptance aperture of the Stark decelerator. The hexapole is formed by six, hardened steel, 3.175 mm diameter, 50 mm long cylindrical shaped rods, set every $60°$ at a center-to-center radius of 4.39 mm, mounted to an insulated macor support disk. The rods are mechanically polished and the ends are rounded to a smooth curvature. Alternate rods are electrically connected, thus forming two sets of three rods. Each set is charged to equal magnitude but opposite polarity high voltage. The hexapolar field

distribution in the transverse plane allows a weak-field-seeking molecule to be confined and even focused in this plane, leading to transverse phase space "mode-matching" between the supersonic nozzle and the Stark decelerator.

The electric field $|\vec{E}|$ of an ideal hexapole is given as [22]:

$$|\vec{E}| = \frac{3V_o r^2}{r_o^3} \tag{4.5}$$

where V_o is the absolute value of the symmetric, opposite polarity voltages applied to each set of rods, r_o is the radius of the hexapole (from the center of the hexapole to the inner edge of the rods), and r is the radial spatial coordinate. A weak-field seeking molecule with a linear Stark shift will thus experience Stark potential energy as: $W = |\mu_{eff}\vec{E}|$. We define an "effective" dipole moment of the molecule as $|\mu_{eff}| = \mu\langle\cos\theta\rangle$, where μ is the magnitude of the electric dipole moment, θ the angle between the moment and the electric field direction, and $\langle\cos\theta\rangle$ represents the quantum mechanical expectation value. The radial force $\vec{F}$ is then written as:

$$F = -\frac{6V_o r \mu_{eff}}{r_o^3}\hat{r}. \tag{4.6}$$

This linear restoring force results in radial harmonic motion of the weak-field seeking molecules inside the hexapole field region. Thus, in analogy to ray tracing in optics, it is possible to define the focal length f of the hexapole in the thin-lens limit (for $l \to 0$ as $\sqrt{\frac{6V_o\mu_{eff}}{mr_o^3}}\frac{l}{v}$ remains constant) as:

$$f = \left(\frac{r_o^3}{6\mu_{eff}}\right)\left(\frac{mv^2}{V_o l}\right) \tag{4.7}$$

where l is the longitudinal length of the hexapole, v is the molecule's longitudinal velocity, and m is the molecular mass. Equation 4.7 demonstrates the focusing strength of a given hexapole linearly increases (decreases) with applied voltage (molecule kinetic energy). For a "real world" hexapole, the finite size of the rods can lead to deviation from Eq. 4.7 [16]. Accounting for this effect, as well as the full non-linear Stark shift as

treated in Chap. 2, detailed numerical simulations of the hexapole focusing effect are shown in Fig. 4.8. The trajectory simulations deterministically map an initial volume in phase-space to a final volume, which is then matched to the corresponding experimental data by proper weighting of initial molecular numbers. The figure shows three sets of focusing curves consisting of OH signals measured directly after the hexapole, under conditions where the applied hexapole voltage has been pulsed to match to the corresponding input molecules' velocity. Operating the hexapole in such a switched manner is designed to give maximum benefit to a particular velocity class, wherein the hexapole voltages are controlled by fast switches that rapidly charge the rods when the selected molecules enter – and then terminate the voltages to ground when the molecules exit – the hexapole region. Thus, molecules with speeds significantly different than the targeted velocity class experience less focusing power of the hexapole, minimizing the aberration effect from the distribution of velocities in the molecular pulse. Symbols in Figure 4.8 correspond to data points measured for 350 m/s (squares), 385 m/s (diamonds) and 415 m/s (triangles) velocity classes, while the solid lines joining the data represent simulation predictions. From comparison of the simulations to the hexapole focusing data, the transverse temperature of the OH beam is determined to be $\sim$4 K, consistent with a supersonically cooled molecular beam. The upper inset in the figure depicts the contributions from the two weak-field seeking states to the 385 m/s trace, where molecules in the $^2\Pi_{3/2}$ F = 2, $m_F = 0$ and $^2\Pi_{3/2}$ F = 1, $|m_F| = 0,1$ states are marginally focused (dashed line) by the hexapole fields, in contrast to the strong effect experienced by molecules populating the $^2\Pi_{3/2}$ F = 2, $|m_F| = 2,1$ states (dotted line). The two weak-field seeking states are included in the simulations with equal weighting.

This figure demonstrates the powerful molecular-focusing capability of the electric hexapole, as the OH molecules are observed only a few millimeters past the end of the hexapole rods. However, for the deceleration experiment, the hexapole is operated only to provide efficient molecular coupling into the physical opening of the slower. This task
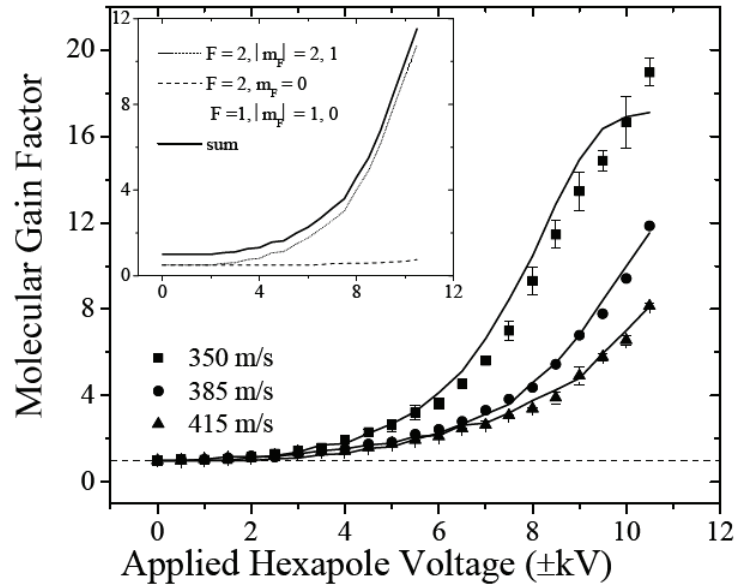
Figure 4.8: Hexapole focusing curve for different OH molecular velocities. The symbols represent the data points for molecules with velocities of 350 m/s (squares), 385 m/s (diamonds), and 415 m/s (triangles), while the solid lines represent the corresponding simulation result. The inset depicts the contribution of the $^2\Pi_{3/2}$ F = 2, $|m_F| = 2$, 1 states and the $^2\Pi_{3/2}$ F = 2, $|m_F| = 0$ and $^2\Pi_{3/2}$ F = 1, $|m_F| = 0$, 1 states to the observed signals for the 385 m/s trace.

requires simply matching the transverse velocity and spatial spreads with the decelerator cross-sectional acceptance and the subsequent requisite focal length is thus longer than that needed to bring the molecules to a sharp spatial focus. Experimentally, we find utilizing $\sim$3 kV applied voltages results in sufficient transverse coupling. This empirical result agrees well with computer simulations of the process. Unless otherwise specified, all subsequent data traces shown are taken with operating the hexapole in this described pulsed manner.

4.4   Extracting Beam Parameters from Time-of-Flight Data

The primary source of information for molecular beam measurements (and Stark deceleration experiments) is Time-of-Flight (ToF) data. Because a ToF signal observed on the data collection computer is a convolution of the true molecular pulse shape and the detection region, it is necessary to de-convolve the ToF signal to extract the relevant beam parameters, $i.e.$ spatial and velocity spreads, from the ToF signal. Though this treatment is likely done elsewhere (and is probably better done), this section details the extraction of molecular beam parameters from ToF signals produced by a Gaussian molecular pulse. The importance of this procedure cannot be understated, since analyzing the raw ToF data as an estimate of the molecular pulse always leads to an overestimate of the relevant parameters, and proper operation of a Stark decelerator relies on detailed knowledge of the input molecular beam.

If we assume that the molecular pulse in the longitudinal direction has a linear density of

$$\rho(x,t) = \rho_o e^{-\left(\frac{x-vt}{\Delta x/\sqrt{\ln 2}}\right)^2} \tag{4.8}$$

with

$$\Delta x = \sqrt{\Delta x_o^2 + (\Delta vt)^2}, \tag{4.9}$$

where Δx_o is the pulse's spatial spread at creation, Δv is the pulse's longitudinal velocity

spread x is the longitudinal coordinate, t is the time since the pulse creation, and ρ_o is the peak linear density related to the total molecule number, N, as

$$\rho_o = \frac{N}{\Delta x}\sqrt{\frac{\ln 2}{\pi}}. \tag{4.10}$$

For traditional molecular beam experiments the time of creation is when the molecule pulse is created at the nozzle (or at the discharge region), while for Stark deceleration experiments the time of creation is when the Stark decelerator voltages are extinguished and the pulse is allowed to free-fly into the detection region.

As seen in Fig. 4.9, ToF data is typically recorded in a window centered a specific distance away from the source (L) with some non-zero width (ΔL). Experimentally, L is the distance from the source to the fluorescence collection optics, and ΔL describes the width, about this center, over which fluorescence is collected. Thus, the observed ToF data is given as the integral of $\rho(x, t)$ over the detection region at time t as

$$S(t) = \rho_o \int_{(L-\Delta L/2)}^{(L+\Delta L/2)} e^{-\left(\frac{x-vt}{\Delta x/\sqrt{\ln 2}}\right)^2} dx, \tag{4.11}$$

or

$$S(t) = \sqrt{\frac{\pi}{\ln 2}}\frac{\rho_o \Delta x}{2}\left[Erf\left(\frac{L + \frac{\Delta L}{2} - vt}{\Delta x/\sqrt{\ln 2}}\right) - Erf\left(\frac{L - \frac{\Delta L}{2} - vt}{\Delta x/\sqrt{\ln 2}}\right)\right]. \tag{4.12}$$

Since there are two unknowns, *i.e.* Δx and Δv, it is necessary to measure the ToF profile at two spatially longitudinally separated locations. At each location, Eq. 4.12 is fit to the data and a value for Δx is found, *i.e.* the de-convolved spatial spread of the pulse. Using the values for Δx with Eq. 4.9, Δv is found as

$$\Delta v = \sqrt{\frac{\Delta x_2^2 - \Delta x_1^2}{t_2^2 - t_1^2}}, \tag{4.13}$$

where Δx_i and t_i are the spatial spread and peak arrival time of the pulse at detection region i. Once Δv is known, Eq. 4.9 can be used to find the initial pulse length, Δx.
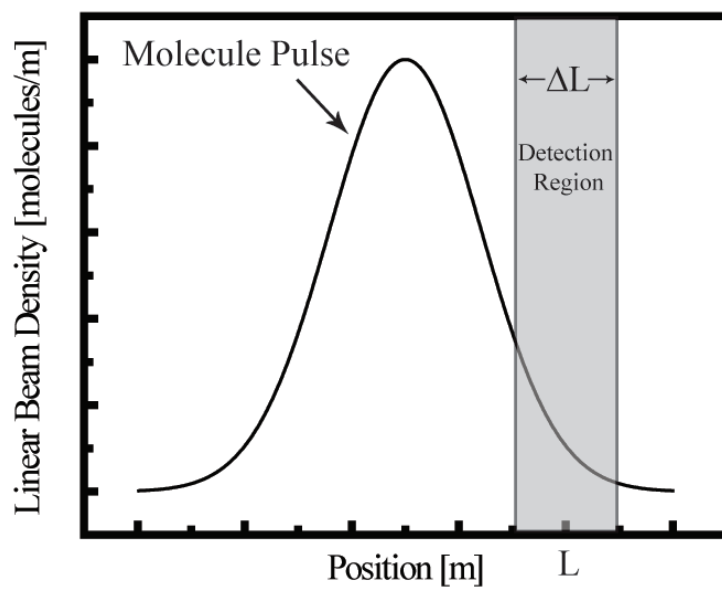
Figure 4.9: Detection of a Gaussian molecular beam pulse at a position, L, with a detection window of width ΔL.

Chapter 5

Stark Deceleration

5.1   The Basics

Strong motivation for using the Stark deceleration approach to create cold molecular samples originates from two convenient properties of supersonic expansions. Used extensively in physical chemistry experiments, beam expansions populate primarily the lowest energy molecular rotational levels and provide an intense supply of molecules with very narrow velocity widths, as compared with effusive sources. In the moving frame of the molecular pulse, the narrow velocity spread corresponds to a low temperature distribution ($\sim$1 K), *i.e.* the molecules have been cooled by the expansion versus room temperature velocity distributions. However, while the beam expansion distribution is sharper, the mean speed of the pulse is now actually faster than molecules generated by typical effusive sources – characteristically, many hundreds of meters per second in the laboratory reference frame. Stark deceleration enables reduction of the mean velocity of the pulse without disturbing the narrow velocity spread, resulting in a cold molecule distribution in the laboratory frame. In practice, given attainable electric fields, typical molecular Stark shifts, and practical numbers of slowing stages, the deceleration process is more restrictive than the velocity width of the supersonically expanded pulse, resulting ultimately in narrower velocity widths and correspondingly, colder molecular samples than few Ks, typically $<$ 100 mK. Finally, we note that the Stark deceleration technique does not require the use of supersonic expansions; it will work with effusive

sources, too, at the cost of reduced initial phase-space density and therefore, ultimately the numbers of cold molecules produced.

The conservative reduction of the pulse's mean velocity is accomplished by exploiting the Stark effect associated with weak-field-seeking molecules. As such a polar molecule moves from a low electric field into a high electric field region, its internal energy increases at the expense of its kinetic energy; thus it *slows down* as it climbs the potential energy hill created by the increasing electric field. If the electric field is rapidly extinguished, the molecule will lose this Stark energy without regaining it as kinetic energy[1] . Utilizing the appropriate field geometry, this procedure may be repeated as many times as necessary to lower molecule's speed to any arbitrary final velocity. Experimentally, this is realized in what has come to be known as a "Stark decelerator", as shown schematically in Fig. 5.1. A more complete understanding of the deceleration process is gained by careful examination of the electric field distribution produced by the spatially, alternating-oriented electrode stages. First, considering the plane perpendicular to the molecular propagation direction, the electric field minimum at any longitudinal position always lies along the central axis of the slower; thus, the alternating electrode geometry results in a stage-to-stage, on-axis focusing of the weak-field seeking molecules. The guidance similarly alters its focusing axis every other stage; thereby, molecules are always transversely guided down the slower simultaneously as their longitudinal velocity is being modified by interacting with the inhomogeneous electric fields. Second, in order to minimize the required number of expensive, fast high voltage switches, all the horizontal (vertical) electrodes of the same polarity are connected to a single switch, thus allowing four switches in total to operate the entire decelerator. A consequence of this practical switch minimization is that when the high voltage at a particular slowing stage is removed and simultaneously turned on at the

---

[1] The molecule's lost kinetic energy, which went into inducing a charge on the decelerator electrodes, is dissipated in the resistors of the switching circuit when the electrode is grounded.
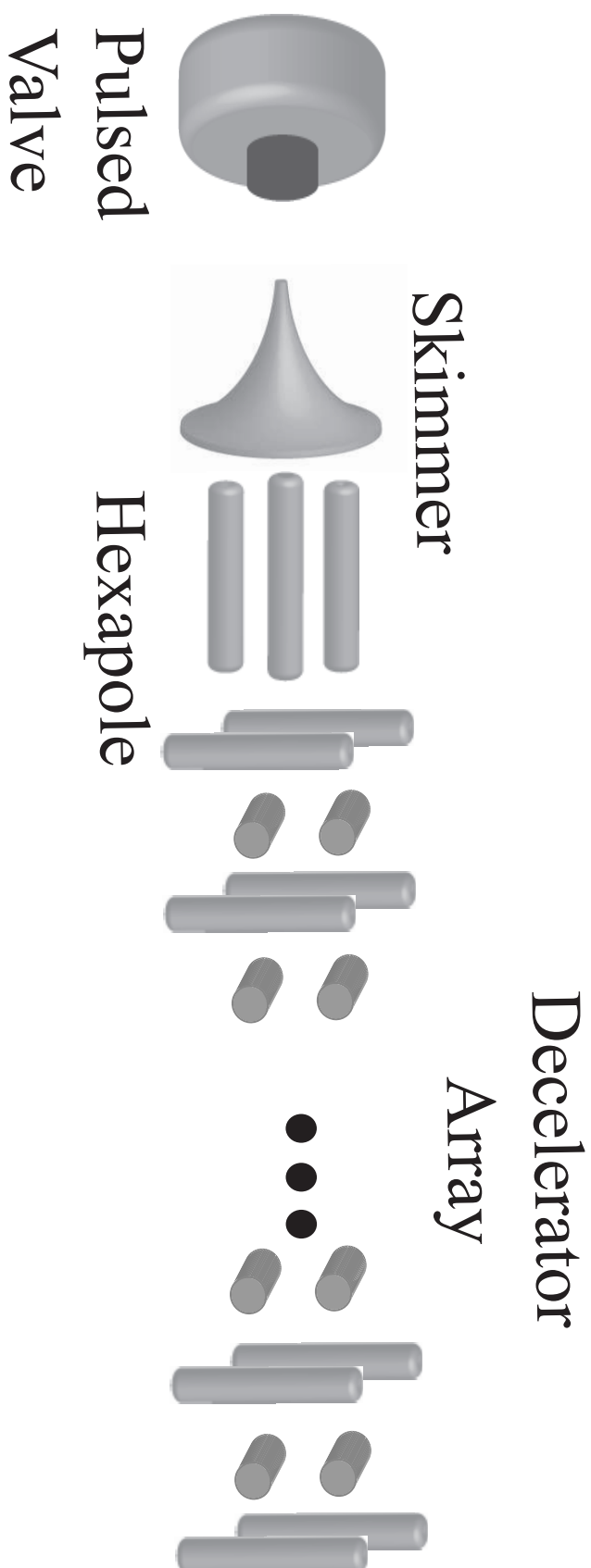
Figure 5.1: System schematic of Stark decelerator, displaying the pulsed valve, the molecular beam skimmer, the electric hexapole, and the electrode stages. The electrode stages alternate orientation (verticalto-horizontal) as shown in the figure to provide transverse guidance of the decelerated molecules.

following (and thus preceding) stage, the local electric field does not go to zero but rather to a value generated by the now active set of electrodes. While this effect detrimentally limits the maximum amount of energy per stage which can be extracted by the decelerator, it beneficially maintains the quantum mechanical state identity of the molecules, as the molecules are phase-stably slowed.

Fig 5.2(a) shows the longitudinal potential energy distribution experienced by OH molecules with our present experimental electrode geometry, generated under normal operating conditions of ± 12.5 kV. The dark line corresponds to the active set of electrodes and the dashed line indicates the other (off) set, where the horizontal axis (spatial phase angle) is defined below. Figure 5.2(b) demonstrates how switching the electric field leads to a change in the molecular kinetic energy per slowing stage that depends critically on the position of the molecules at the switching time. This dependence is conveniently characterized by utilizing a spatial coordinate ϕ_o , called the phase angle, which is defined only at the instant of electric field switching and written as:

$$\phi_o = \frac{z}{L} 180°, \tag{5.1}$$

where z is the longitudinal position of the molecule and L is the stage-to-stage separation. We define $z = 0$ ($\phi_o = 0°$) as the point midway between two adjacent stages. If a molecule has a phase angle $0° < \phi_o < 180°$ at the switching of the fields, then it will be slowed. To analyze the net effect of deceleration on a spatially distributed pulse of molecules, it is useful to define the synchronous molecule as one that is at exactly the same phase angle, ϕ_o, at the moment of each switching of the electric fields; thus, losing an identical amount of energy per stage. While the region $0° < \phi_o < 180°$ does lead to deceleration of the synchronous molecule since the kinetic energy loss ΔKE is positive, only operating in the range $0° < \phi_o < 90°$ results in phase stable deceleration of a molecular packet. This can be seen in Fig. 5.2(b), that only on the positive slope of the kinetic energy loss curve do molecules which are slightly ahead (leading - i.e. faster)
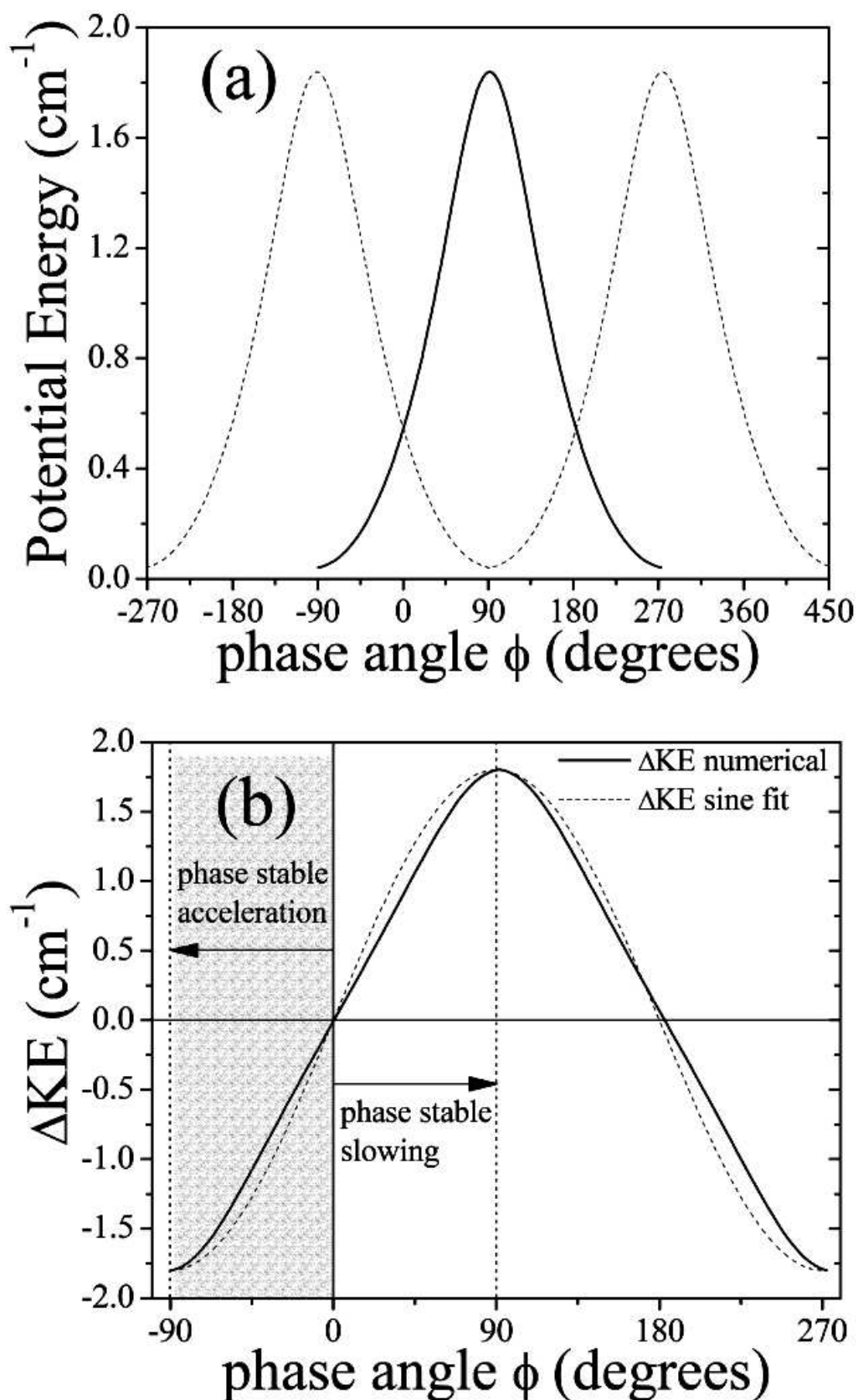
Figure 5.2: Phase stable operation of the decelerator. (a) Longitudinal Stark energy potentials generated by the two sets of electrodes, where the solid (dotted) line represents the potential from the active (grounded) set of electrodes. (b) Kinetic energy loss per stage (ΔKE) experienced by molecules from switching between the two potentials given above. Solid (dashed) line corresponds to a numerical calculation (sine function fit).

or behind (lagging - i.e. slower) the synchronous molecule experience a net restoring force towards the synchronous molecule position. Physically, a faster (slower) non-synchronous molecule travels higher (lower) up the hill than the synchronous molecule and hence, has more (less) energy removed than the synchronous molecule. Detrimentally, operating on the negative slope of the hill, *i.e.* in the range $90° \leq \phi_o < 180°$, results in faster (slower) molecules becoming progressively faster (slower) relative to the synchronous molecule, spreading the molecular pulse further and further apart. By similar arguments, phase stable acceleration of a molecular packet is only possible on the positive slope of the potential hill in the range $0° < \phi_o < -90°$. In Fig. 5.2(b), the phase stable ranges are indicated by the shaded portions. This restoring force experienced by nonsynchronous molecules, when the slower is operated in the proper regime, is the underlying mechanism for the phase stability of the molecular packet and a critical concept for understanding Stark deceleration experiments. Finally, operating the slower with $\phi_o = 0°$ represents an interesting experimental condition. As shown in Fig. 5.2(a), this point is defined spatially as exactly between two adjacent stages. While the molecules are accelerated then slowed each stage as they roll down and up the hill, these two effects cancel and result in no net change in the longitudinal velocity of a synchronous molecule; however, the molecular packet is phase stably bunched as it propagates down the slower. This so-named "bunching" condition is a good test of successful phase stable operation of the Stark decelerator.

Defining the excursion (at the switching time) of a non-synchronous molecule from the synchronous molecule position as $\Delta\phi = \phi - \phi_o$ and with the help of a sine function fit to the change of kinetic energy per stage, it is straightforward to write for the time evolution of $\Delta\phi$:

$$\frac{d^2\Delta\phi}{dt^2} + \frac{W_{max}\pi}{mL^2}\frac{d\Delta\phi}{dt}(\sin(\Delta\phi + \phi_o) - sin(\phi)) = 0 \qquad (5.2)$$

where W_{max} is the maximum work done by a slowing stage on a molecule and m is
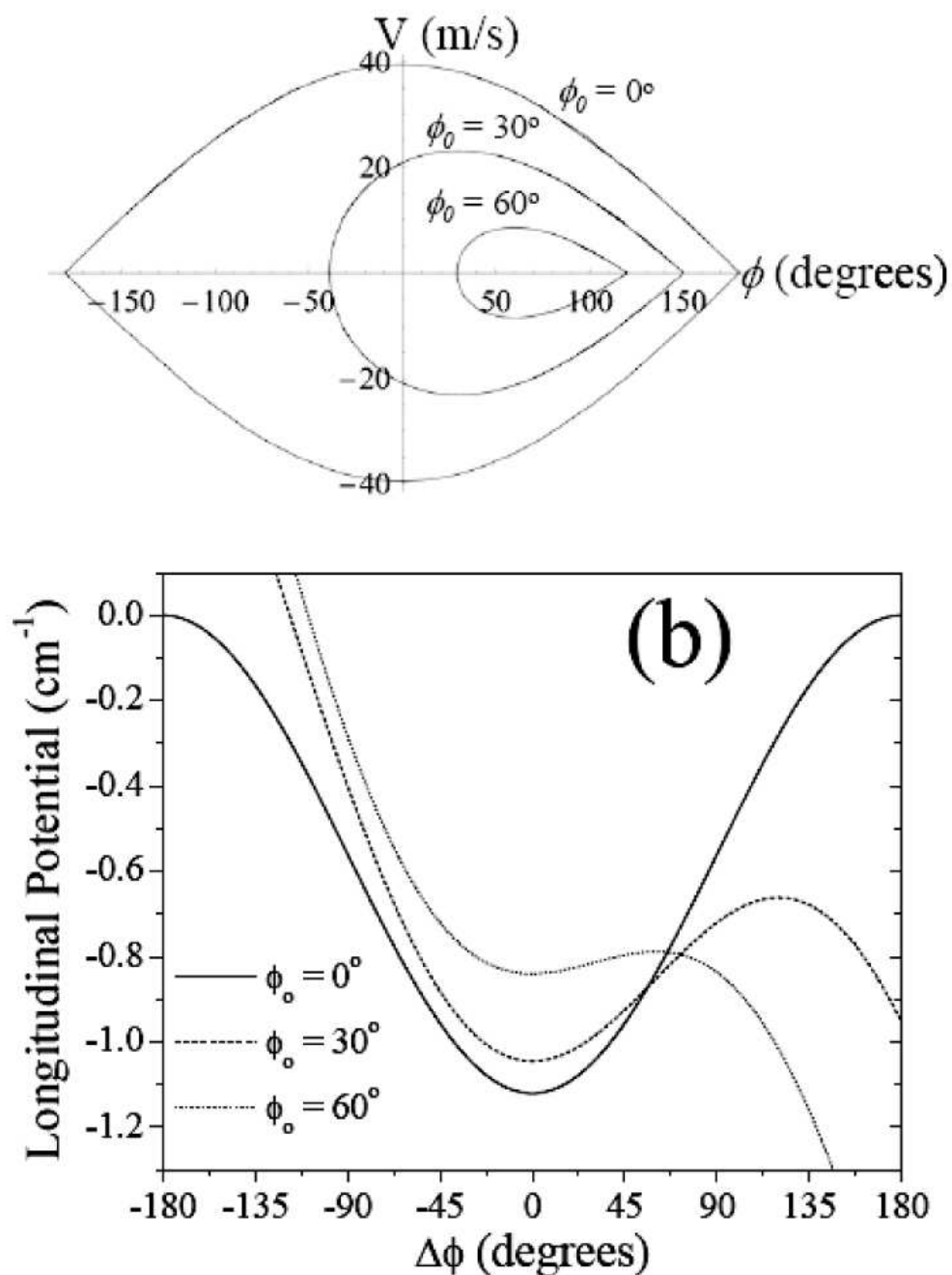
Figure 5.3: Phase stable area (separatrix area) versus phase angle for $\phi_o = 0°, 30°$, and $60°$. As the phase angle is increased, the stable area is reduced; equivalently, the stable longitudinal velocity width narrows and assuming the source completely populates the phase stable areas, decreases the numbers of molecules in the phase stable packet.

the molecular mass[2] . Thus, non-synchronous molecules will oscillate around the synchronous molecule position inside an asymmetric oscillator potential. From numerical integrations of Eq. 5.2 and the first time derivative of Eq. 5.1, solutions for the stable and unstable regions of phase-space are shown as a function of synchronous molecule phase angle ϕ_o in Fig. 5.3(a). The most interesting and relevant feature of this figure is the rapidly decreasing area of stable evolution, defined as the area inside the separatrix. This decrease in stability is easily understood by analogy to the pendulum driven by a constant torque. As the torque is increased (or equivalently, ϕ_o is increased), the equilibrium position of the pendulum is pushed toward the apex; therefore the maximum amplitude that result in stable oscillatory motion is lowered. Reasonably assuming that the molecular source homogeneously populates phase-space on the scales given here, this reduction in stable phase-space area translates to a decrease in the number of slowed molecules, setting a practical, observable limit to the ultimate temperature of the molecular packet. From Figure 5.2(b), it is seen that for molecules ahead of the synchronous molecule the maximum stable excursion, $i.e.$ the separatrix upper spatial bound, is given as:

$$\Delta\phi_{max}^{+} = 180° - 2\phi_o, \tag{5.3}$$

since any non-synchronous molecule with $\phi_o < \phi < 180° - 2\phi_o$ will be slowed more than the synchronous molecule. Furthermore, a molecule with zero velocity at this position, $i.e.$ at $\phi = \phi_o + \Delta\phi_{max}^{+}$, will have the maximum stable velocity at the $\phi = \phi_o$ position, thus the longitudinal acceptance of the slower in velocity as a function of synchronous molecule phase is given as (see the next chapter for a more detailed derivation):

$$\Delta v_{max}(\phi_o) = 2\sqrt{\frac{2C_{max}}{m\pi}\left(\cos\phi_o - \frac{\pi}{2}\left(1 - \frac{\phi}{90°}\right)\sin\phi_o\right)} \tag{5.4}$$

---

[2] This equation is the same as a harmonic oscillator with an offset equilibrium position, $e.g.$ a pendulum driven by a constant torque
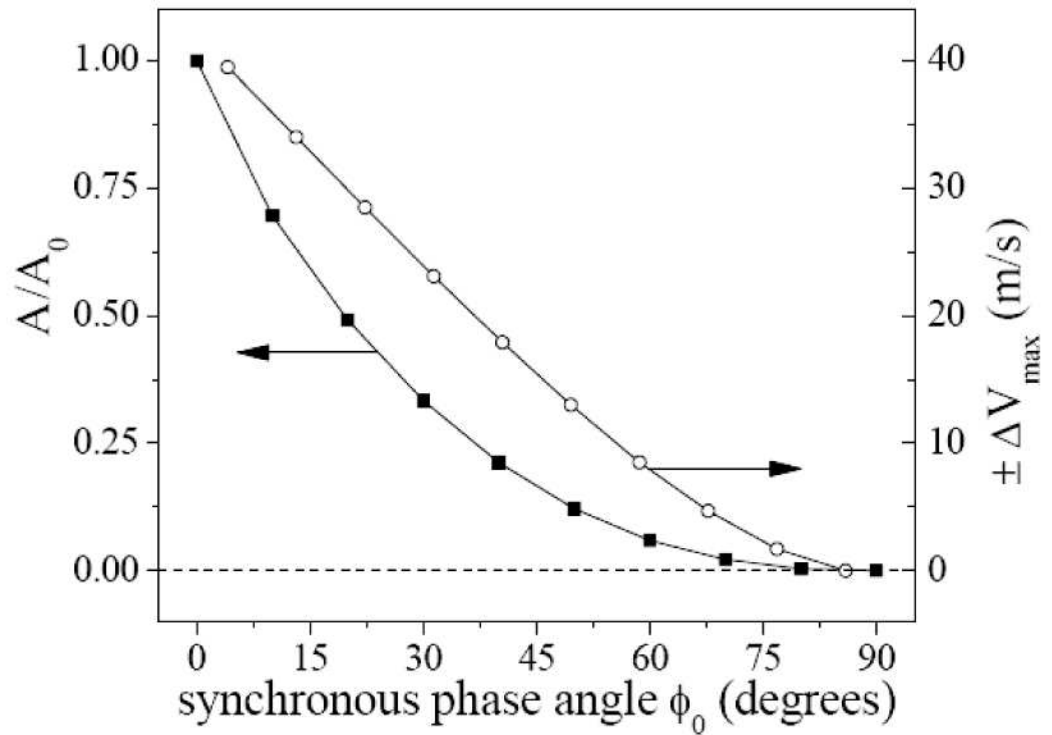
Figure 5.4: Phase stable area (separatrix area) A versus slowing phase angles ϕ_o, normalized to the phase stable area under bunching operation A_o. The subsequent maximum allowed velocity spread of the phase stable packet Δv_{max} is shown with respect to the right axis.

Figure 5.4 usefully summarizes the results of the calculation given above, giving an intuitive expectation of performance under different modes of slower operation. The solid square symbols represent stable areas, A, in phase space, plotted as a function of slowing phase angle ϕ_o and normalized to that of the bunching case A_o. The open circles are plotted along the right axis and depict the maximum longitudinal velocity spread, Δv_{max}, of the phase stable packet. As seen in the figure, operation at increasing phase angles results in fewer but also cooler molecules in the phase stable packet. Hence, with an eye toward experimental goals, a careful balance between the required number of molecules in the phase stable packet and the desired longitudinal temperature must be considered when using the Stark decelerator.

While Eq. 5.4 allows for the estimation of the longitudinal temperature of the stable molecular packet, the dependence of the transported molecule number on ϕ_o must be determined. For an initial velocity distribution of Δv_{FWHM} (full width at half maximum), the number of molecules successfully loaded into the phase stable bucket $N(\phi_o)$, normalized to that for the bunching case, is shown to be (see the next chapter for a more detailed derivation):

$$N(\phi_o) = (1 - \frac{\phi_o}{90^\circ}) \frac{Erf(\frac{\Delta v_{max}(\phi_o)}{\Delta v_{FWHM}\sqrt{\ln 2}})}{Erf(\frac{2}{\Delta v_{FWHM}}\sqrt{\frac{W_{max}}{m\pi \ln 2}})}, \tag{5.5}$$

where Erf is the Error function. In the above derivation, the area inside the separatrix is approximated as square since we are only concerned with variation relative to molecular bunching. Also, we assume that at the input of the decelerator there is no spatial variation of the molecular packet over the dimension of one slowing stage separation, as well as ignore any convolution of the input distribution due to free flight from the creation region. A more limiting assumption, made for the sake of a closed form solution, is that the lower separatrix bound relative to ϕ_o is assumed to vary in the same manner as the upper bound, i.e. $\Delta\phi_{max}^- = -\Delta\phi_{max}^+$. Nonetheless, the results of Eq. 5.5 are in good agreement with the measured molecule number as detailed in section 5.4, where a

more detailed numerical solution for Eq. 5.5 that accounts for the proper variation of $\Delta\phi_{max}^{-}$ is also shown, along with the results of a full 3D Monte Carlo simulation of the slowing process.

5.2   Decelerator Monte Carlo Simulations

The Monte Carlo simulations, presented throughout this thesis, are performed not only for comparison of the expected stable molecule number, but also for assessment of the detailed TOF spectra observed, as well as to aid in the understanding of the deceleration process. From the geometrical and electrical properties (sizes, distances, and applied voltages) of the decelerator, a three-dimensional electric field map of the slower is constructed, which when coupled with the understanding of the molecular energy structure, gives complete information on the forces experienced by molecules within the decelerator. The initial input distribution are assumed to be gaussian distributed and the parameters (centers and full-widths) are determined from both experimental dimensions (spatial parameters) and measurements on hexapole-focused, transversely guided molecular pulses (velocity parameters). The trajectories of typcially ten-million molecules sampled from the initial distribution are calculated for the appropriate Stark manipulation process, *i.e.* bunching, slowing, or accelerating starting from the skimmer entrance, then traversing the focusing hexapole and decelerator, and finally reaching the appropriate detection region. Recently, we have implemented these simulations as a C++ class that can be run in a parallel processing mode. This, ever evolving, code is freely distributed and can be obtained by contacting the author or Prof. Jun Ye.

5.3   Decelerator Construction

The most important practical issue in the construction of a Stark decelerator is the stable operation of high voltages ($\sim$25 kV) between electrodes spaced only 2 mm apart inside the decelerator. Discharge between electrodes will not only disrupt normal

operations of the decelerator, but could also inflict permanent damages to the electrodes, as well as destroy the decelerated molecules through ionization or electron attachment. There are several useful techniques for the stable application of large electric fields, including a high vacuum system, proper electrode construction, and proper electrode conditioning. This section details the methods of implementing these techniques in a Stark decelerator, as well as the implementation of the fast high-voltage switching, which is central to Stark deceleration experiments.

5.3.1   Vacuum Apparatus

Discharging between electrodes that support a high electric field occurs as an electron/ion is accelerated to sufficient energies to ionize the nearby gas. Once the electron/ion ionizes a gas molecule, both are accelerated and can also ionize more neighboring gas particles. In this way, an exponentially-growing current path is created between the high voltage electrodes by the (avalanche) gas mediated discharge. Clearly, placing the decelerator in high vacuum is helpful in terms of increasing the threshold for unwanted discharges in the apparatus. At pressures $\leq 10^{-7}$ Torr the mean free path of the gas is larger than the electrode spacing and consequently the mechanism for gas mediated discharge is removed, making the application of high voltages much easier. Nonetheless, discharging can still occur via material ablated from the electrode surface. This method of discharging, which depends on the pre-breakdown tunneling current, will be treated in the next subsection.

Additionally, high vacuum is also useful for reducing collision events between the decelerated molecules and background gas. This is especially important in the molecular beam source chamber where the beam density can be as much as 10^{12} cm^{-3}. In fact, in our first-generation decelerator we found that the volume and pumping speed (250 L/s turbo-molecular pump) in our source chamber limited our molecular beam intensity. We observed that for higher nozzle pressure and shorter nozzle to skimmer

distances scattering of the beam onto itself resulted in a collapse of the molecular beam, evidenced by a sharp reduction in post-skimmer molecule number. In our second-generation decelerator we reduced this effect by using a larger volume source chamber and higher pumping speed turbo molecular pumps (1000 L/s). While a higher pumping speed results in a lower average pressure, it does not not alleviate the problem of a molecular pulse scattering back onto itself. It is for this reason that making the source chamber larger in volume, so that molecules from the pulse cannot scatter into the beam during the pulse time-scale, is important. As aforementioned, to separate the higher pressure source chamber from the rest of the decelerator a molecular beam skimmer is used, which acts as an effective differential pumping hole. During quiescence, the source and slower chambers reach $\sim 10^{-8}$ and $\sim 10^{-9}$ Torr, respectively. Under active conditions, the source and slower chamber are at $\sim 10^{-4}$ torr $\sim 10^{-7}$, ensuring stable operation of the Stark decelerator.

5.3.2   Decelerator Electrode Construction

As aforementioned, at the pressures inside a Stark decelerator gas mediated discharge is negligible, and the mechanism for discharge is via material ablated from the electrode's surface. The process responsible for the ablation of the electrode is known as pre-breakdown tunneling current. This current is due to electrons that tunnel through the work function, ϕ, of the negative electrode and are accelerated towards the positive electrode. When these electrons strike the positive electrode they have sufficient energy to ablate some material from the electrode's surface (and sometimes produce observable fluorescence). If the pre-breakdown current is high enough that the ablated material reaches a critical local pressure, a gas mediated discharge can occur. And as such, understanding the characteristic of the pre-breakdown tunneling current is crucial to proper high voltage electrode construction.

It is generally accepted that the pre-breakdown tunneling current originates from

localized regions on the electrode surface where the electrode's work function is lower. The work function at these emitter sites is lowered either by the presence of some impurity in the metal or by the Schottky effect, *i.e.* the apparent reduction of the work function at micro-protrusions on a surface in the presence of an electric field. From the tunneling theory of Fowler and Nordheim [52] it is possible to write the value of the tunneling current as [78]

$$I = A_e j = \frac{A_e B_1 E^2}{\phi} e^{-\left(\frac{B_2 \phi^{3/2}}{E}\right)}, \tag{5.6}$$

where A_e is the total area of emitting sites, j the current density, E is the electric field magnitude, and B_1 and B_2 are constants given as $1.54 \times 10^{-6} C\Omega^{-1}$ and $6.83 \times 10^{9} C^{-1} m^{-1}$, respectively. From Eq. 5.6, we see that the parameters at the experimenters control are ϕ and E. Furthermore, the electric field in Eq. 5.6 is the electric field at the emitter site, which is typically written as $E = \beta V/d$, where V and d are the voltage across and separation of the electrodes, respectively, and β is called the geometrical enhancement factor which describes the local increase in electric field due to the surface roughness at the emitter. For these reason, most electrodes are constructed from stainless steel since it has a relatively high work function ($\phi \approx 4.5$ ev) and can be polished to high a surface quality, *i.e.* small β.

In our experiments, we first fabricated the high voltage electrodes from 304L stainless steel, or hardened steel, and subsequently mechanically polished them to the best possible surface finish we could achieve. Electron microscope pictures of these electrodes are shown in Fig. 5.5. Comparing the top two pictures at 70X magnification clearly shows the advantages of mechanical polishing as the roughness of the raw material is replaced by a much more uniform surface. At higher magnifications, however, contamination on the surface becomes visible (left-most middle picture), which is due to polishing paste that has adhered to the surface. At even higher magnification, serrations of the surface due to the ceramic beads in the polishing paste become visible (right-

Raw Hardened Stainless 70X
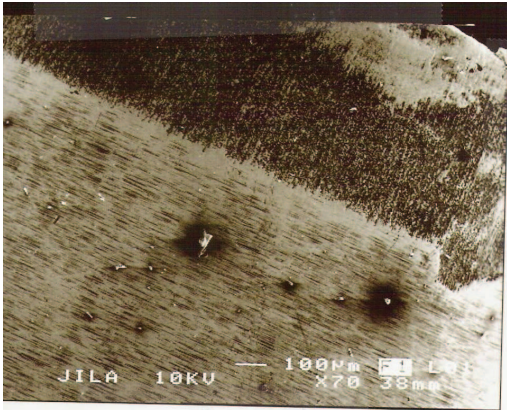
Mechanically Polished
Hardened Stainless 70X
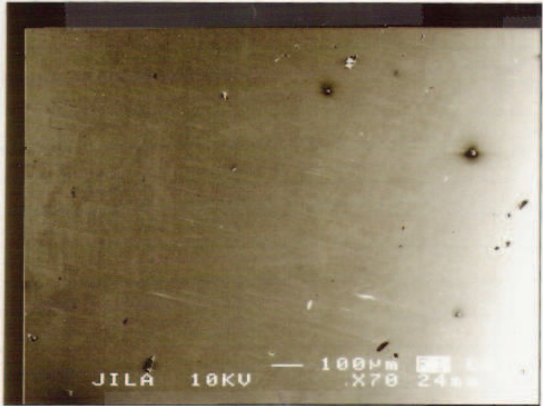
Mechanically Polished
Hardened Stainless 1800X

Mechanically Polished
Hardened Stainless 2700X
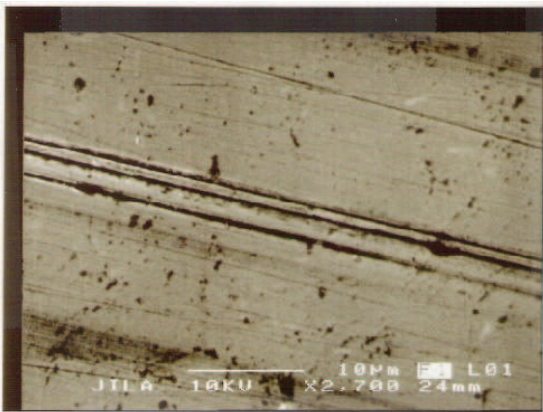
Electro-polished 3 minutes
316 Stainless 70X
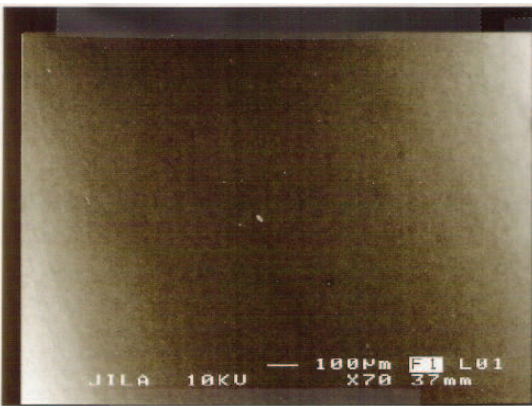
Electro-polished 3 minutes
316 Stainless 1800X
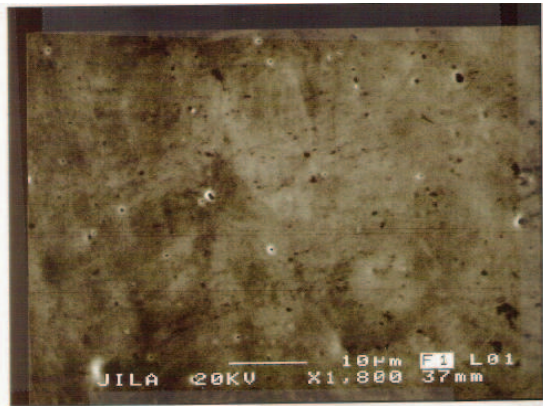
Figure 5.5: Electron microscope pictures showing the effect of material and polishing choice on surface quality.
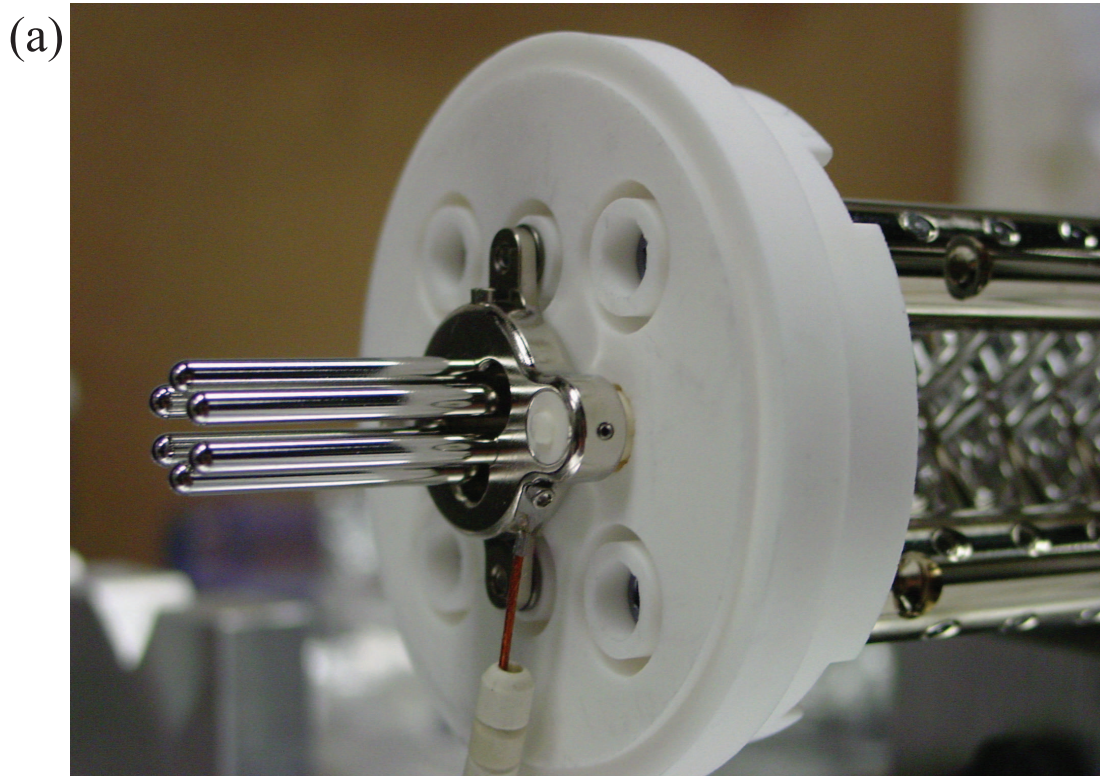
Figure 5.6: Pictures of Stark decelerator. (a) Hexapole mount. (b) Decelerator array. In both pictures notice that in the Macor mounts grooves have been cut to increase the surface path between oppositely charged electrodes.

most middle picture). Since both surface contamination and micro-roughness lead to a lowering of the electrode's work function it is clear that mechanical polishing with a polishing paste in not optimal. It should be noted that our first-generation decelerator utilizes electrodes polished in this way and they have not been problematic at current voltages. However, test of these types of electrodes have revealed they should not be used much above the current fields of 150 kV/cm.

To reach higher fields we have developed electrodes whose final polishing step is electro-polishing. These electrodes are first mechanical polished in the same way as previously described, but are then placed in an electro-polish bath, where micro-roughness features are removed atom by atom. Because 304L stainless steel does not electro-polish very well, we now use electrodes constructed from 316 stainless steel, which has the convenient property of being the least magnetic of all steels. Electrodes produced in this way are shown in the bottom two pictures of Fig. 5.5. It is clear from these pictures that the contamination and serration has been greatly reduced. Furthermore, as detailed in the next section these electrodes are stable to much higher electric fields.

With great care taken to eliminate direct discharge between opposing electrodes, surface currents and discharging to other structures become important. In our experiments, all high voltage elements are mounted on insulating materials (Macor, alumina, or boron nitride) in such a manner to avoid close proximity to ground or opposite high voltage polarities. When opposite polarity voltage elements are attached to the same insulating support, grooves were fabricated into the insulating surface in order to create longer surface path lengths to minimize current leakage between the components – a good 'rule-of-thumb' is that the surface path should be ten times longer than the vacuum gap. Shown in Fig. 5.6 are two pictures of our second-generation decelerator. In Fig. 5.6(a) the hexapole mounting structure is shown, and in Fig. 5.6(b) the decelerator array is shown. Notice that in both cases, how grooves are cut in the Macor mounts to

increase the surface path between electrodes.

5.3.3   Decelerator Electrode Conditioning

Even with highly polished decelerator electrodes and careful construction of the decelerator apparatus,[3] energizing a new decelerator to high voltage will most likely result in catastrophic discharge. This is because there are always a few emitter sites or contaminants on the decelerator array and only one is needed to start a discharge. Experimentally, this problem is rectified by the method of 'high voltage conditioning', which despite its various incarnations uses controlled 'micro-discharge' events that help clean the surfaces and prepare the electrodes for high voltage operation. Typically, once under vacuum, the electrodes are subject to a sequence of high voltage conditioning sessions to ensure stable operation. We employ two related, but distinct methods: DC current and glow-discharge conditioning modes [78].

Under DC current conditioning, all electrodes are gradually brought up to 1.2 - 2 times their nominal operating level in incremental voltage steps. A limiting resistor (~ 0.1 GΩ) in series with the high voltage power supplies limits the possible discharging current to small values ($\leq 100\mu$A) so that when discharges occur the electrodes are not damaged, *i.e.* the resistor supplies negative feedback since as the current increases more voltage drops across it and less voltage is applied to the electrodes. When a micro-discharge occurs it is always at the emitter site and works to either remove the contaminant or smooth-out the micro-roughness, thus conditioning the electrodes. It was empirically discovered that the Bayard-Alpert type ionization gauge that actively monitored the chamber pressure (which rises during a micro-discharge) was also inducing low level discharging during the conditioning process. UV lamps have also been utilized to purposefully create these beneficial micro-discharges during the current conditioning

---

[3] Because any contaminant on the decelerator, dust or otherwise, can cause discharges to occur, the decelerator should be constructed in near clean room conditions
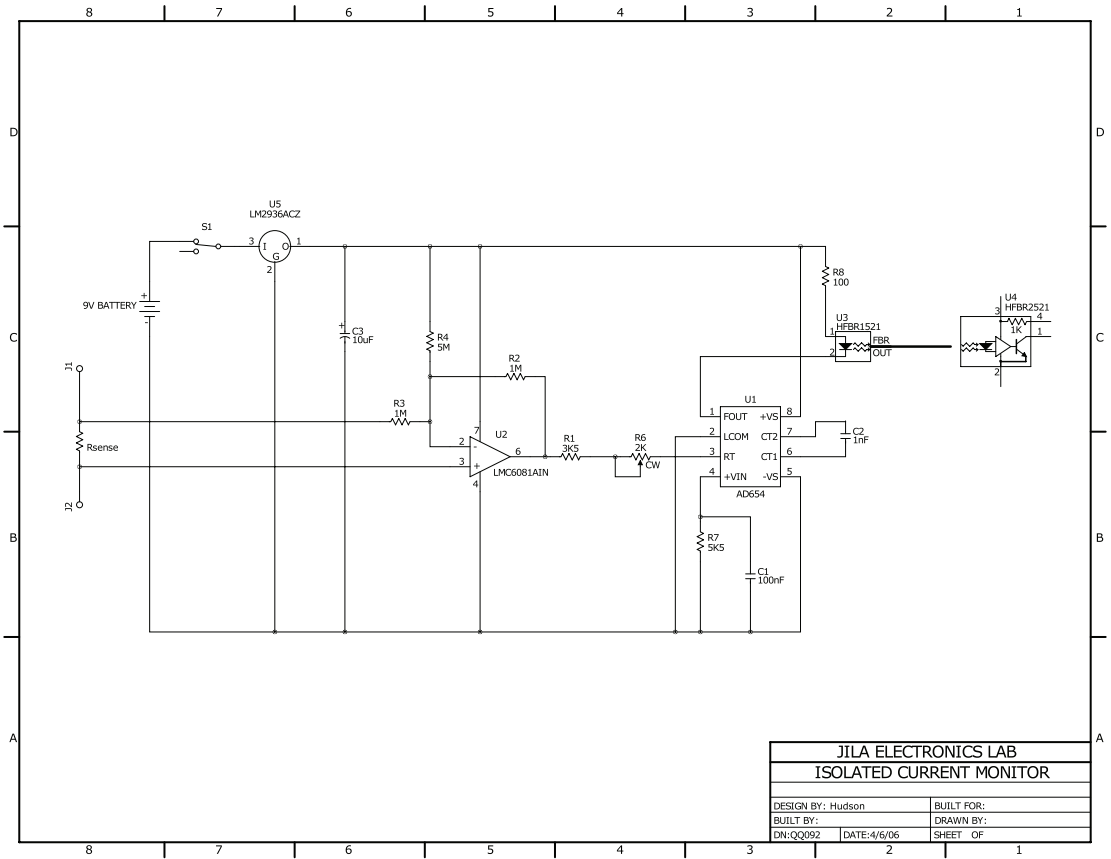
Figure 5.7: Schematic of fiber-optic isolated ammeter.

Current Conditioning
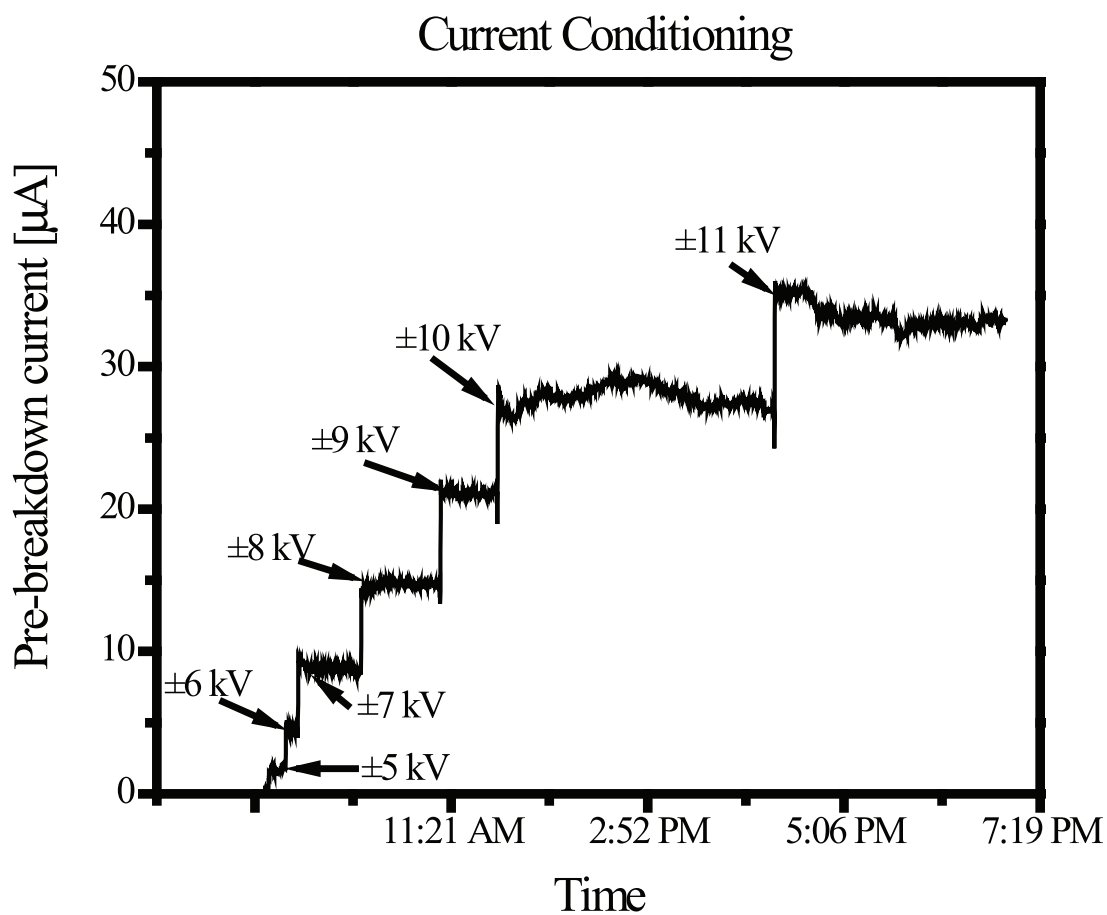
Figure 5.8: Typical current conditioning data. After each increase in voltage the observed current is usually quite 'noisy' reflecting the quasi-random nature of the microdischarges. However, after sometime the micro-discharges burn away the emitter sites and the current decreases to a steady, lower value.

process. The series current can be actively monitored by floating an analog voltmeter or by a home-made floating ammeter that uses fiber-optic isolation to allow data-logging with a computer. A schematic of this design is shown in Fig. 5.7, which uses voltage-to-frequency converting chip floating at high voltage to flash a light-emitting diode into a fiber. At the other end of the fiber a photo-diode converts the light signal back into an electrical signal that can be counted and logged on a data-taking computer. Recording the pre-breakdown current as a function of applied voltage is an extremely useful tool for diagnosing the quality of the electrodes. Shown in Fig. 5.8 is typically data for the current conditioning process. As seen in this graph, when the voltage is increased beyond a certain value the pre-breakdown current rises from zero to a few microamperes. Further increase in the voltage results in an exponential increase in the current (see Eq. 5.6). Furthermore, after each increase in voltage the observed current is usually quite 'noisy' reflecting the quasi-random nature of the micro-discharges. However, after sometime the micro-discharges burn away the emitter sites and the current decreases to a steady, lower value. After the conditioning process, measuring the current versus voltage results in graphs similar to Fig. 5.9. In Fig. 5.9(a) the current is plotted versus the voltage and the exponential behavior predicted by Eq. 5.6 is apparent. A more useful plot is given in Fig. 5.9(b), where the natural logarithm of the current divided by the square of the voltage is plotted versus the reciprocal of the voltage. Note, using $E = \beta V/d$, dividing Eq. 5.6 by V^2, and then taking the natural logarithm leads to

$$\ln(I/V^2) = \ln(\frac{A_e B_1 \beta^2}{\phi d^2}) - \frac{d B_2 \phi^{3/2}}{\beta}\frac{1}{V}. \tag{5.7}$$

If this equation is plotted versus the reciprocal voltage it is clear is should be a line with a slope proportional to the reciprocal of β. Thus, the smoothness of the electrodes can be inferred simply from the slope of the line. As seen from these graphs the glow discharge condition process produces much smoother electrode surfaces. Typically, the glow discharge conditioning process is reserved for situations when the apparatus fails
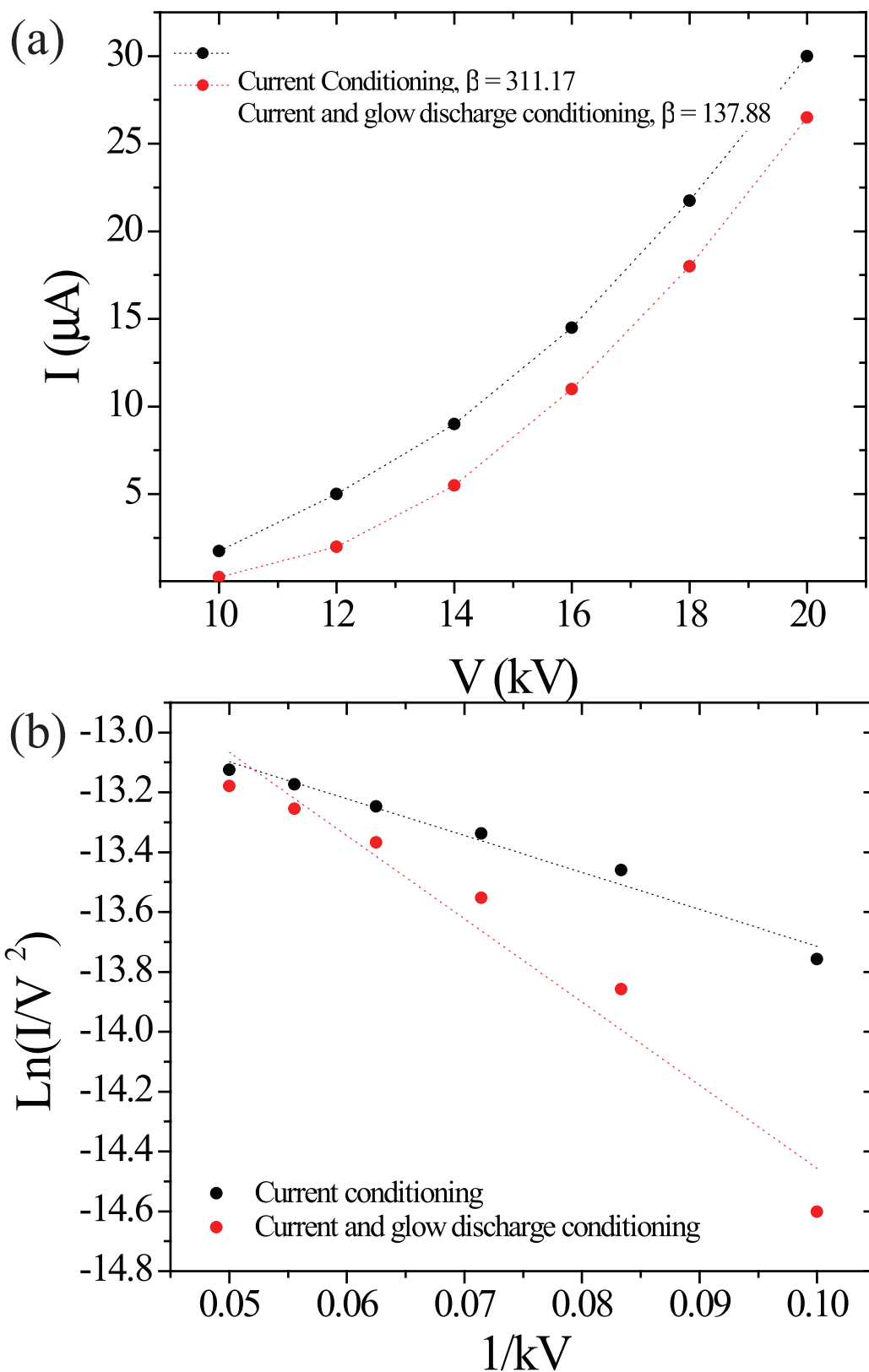
Figure 5.9: Current vs. Voltage curve after conditioning.(a) The exponential dependence of the current on the voltage is apparent, confirming the tunneling theory of Fowler and Nordheim. (b) Plotting the $\ln(I/V^2)$ versus $1/V$ reveals a line whose slope is proportional to the electrode smoothness.

to DC current condition to satisfaction. The chamber is backfilled with a few tens of milliTorr of helium gas, and a Tesla coil is used to spark a discharge between the relevant electrodes for approximately ten minutes. The system is then vented and this procedure repeated with a backfill of nitrogen gas. Subsequently, the system is DC current conditioned with significant improvements. The improved electrode quality is presumably due to the more aggressive micro-discharging induced by the Tesla coil. For this reason, glow discharging often or for more than the prescribed time can actually lead to electrode degradation [78] and it should only be used when other methods fail.

It is interesting to note that another type of electrode conditioning, Spark-gap conditioning, works by applying a high voltage, unlimited current pulse to the electrodes for a few microseconds. In this way, a micro-discharge can be initiated and the emitter site ablated, however, the voltage is removed before an avalanche discharge can be created, which would damage the electrode. Though we have never purposefully used this technique for conditioning, it is exactly how a Stark decelerator is operated. Thus, it is likely that the operation of a Stark decelerator is intrinsically stable, and perhaps may be self-healing.

5.3.4   Fast High Voltage Switching

Successful operation of the Stark decelerator relies on thorough knowledge of the initial position and velocity distribution of the molecules, as well as temporally accurate control of the inhomogeneous electric fields in order to ensure stable manipulation. We rely on machining precision in the manufacture of slower components ($< \pm 50$ μm stated tolerance) to ensure that any physical discrepancies from the specified dimensions are minimized. The applied electric fields are pulsed using commercially available, push-pull, fast high voltage switches with a specified 10 ns rise time (see Fig. 5.10). External current limiting resistors, R_L and R_{EMI}, are used both to protect the switches (Behlke HTS 151-03-GSM with high frequency burst option) from excessive current and to slow

the rise time to 500 ns to minimize the generated electromagnetic interference (EMI). The molecules are insensitive to the switching speed reduction, as even on the μs-time scale, the fastest-moving molecules in the system are almost stationary. We note the importance of reduction of the overall EMI from the system when high voltages are being switched actively. Two high voltage power supplies (one devoted to each polarity) generate the requisite high voltage for the slowing stages. Each individual power supply output is coupled in parallel with a 2 μF high voltage capacitor, C_B, on the input side of the fast switch in order to provide the large currents (12 A peak current) required for the rapid charging of the slowing electrodes. A similar arrangement generates the slightly lower high voltage and current used for the pulsed electric hexapole operation.

All high voltage cabling is constructed from a corona-discharge suppressing cable rated to 40 kV (Belden 8866 002), which is surrounded by Tygon tubing and finally enclosed in a grounded, metallic braid shield. In this way the dielectric breakdown of the cable is increased, while protecting anyone near the cable from electrical shock since the discharge current should prefer to travel down the low impedance shield.

A digital delay generator acts as the stable master-clock for the experiment, controlling the firing of the pulsed laser and the supersonic valve, as well as triggering a computer-based timing board. The timing board repetitively generates user-defined timing signals to subsequently drive the fast high voltage switches that control the OH-generating discharge, hexapole, and slowing stages. The timing pattern incorporated into the timing board is derived from computer trajectory simulations of the Stark deceleration process.

5.4   Stark Deceleration of the Hydroxyl Radical

In our experiments at JILA, we have constructed two Stark decelerators. The first-generation decelerator was similar to the design of the Berlin group [24]. The first production of cold OH radicals was achieved in this decelerator [27], as well as the
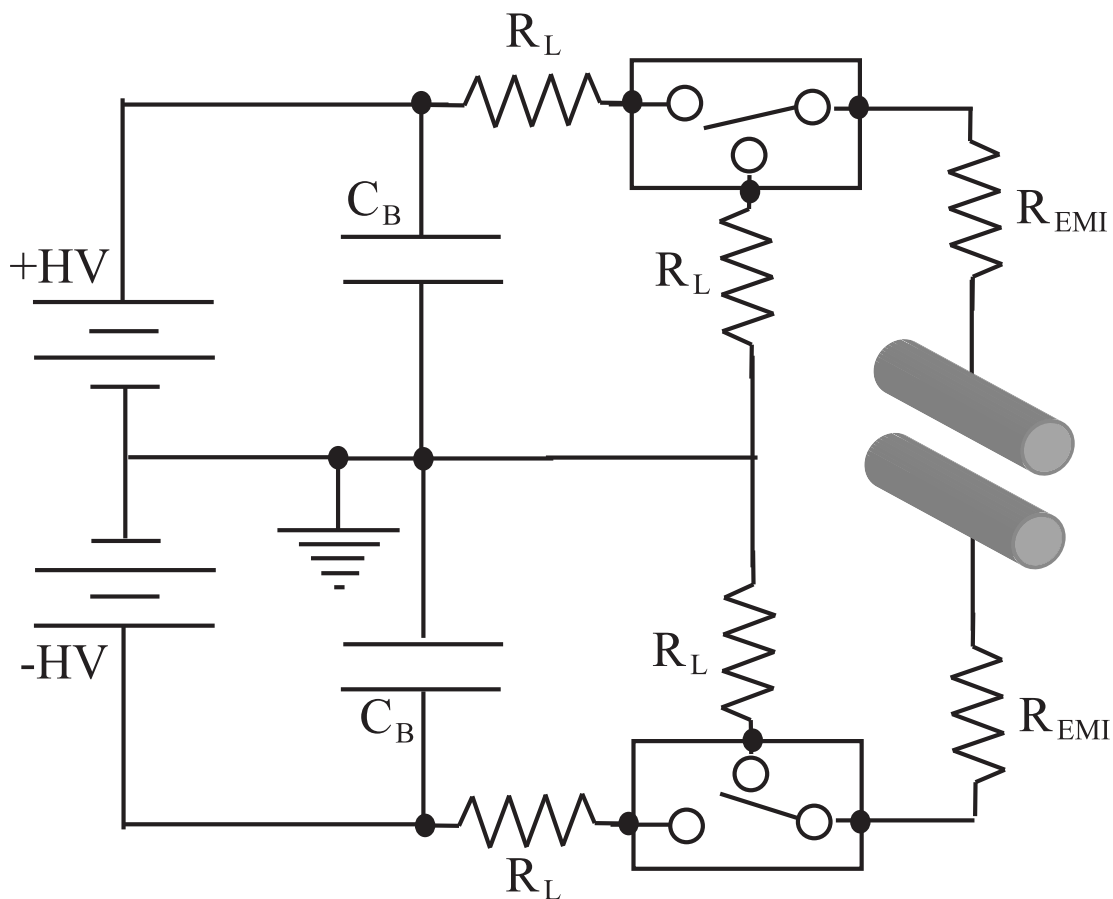
Figure 5.10: Schematic of decelerator switches. The high voltage push-pull MOSFET switches are shown schematically. The protection resistors R_L (33 Ω) are technically not needed if R_{EMI} (1kΩ) is in place, however, they provide protection in the case of a breakdown that bypasses R_{EMI}. The buffer capacitors, C_B, provide the high current necessary to quickly energize the electrodes.

measurements of the microwave transition in the lowest OH Λ-doublet. The second-generation decelerator is fundamentally similar to our earlier design with the only major design changes being twice as many deceleration stages and a more suitable vacuum chamber for making a good molecular beam. The first production of cold H_2CO molecules was achieved in this machine. Furthermore, OH has been decelerated in this machine allowing for a comparison between the two decelerators, which shows the clear advantage of a longer (but not-too-long) decelerator. The next two sections detail the deceleration of the OH molecule in these decelerators.

5.4.1   First-Generation Decelerator

In-situ experimental observations of OH molecules undergoing longitudinal phase-space manipulation inside the properly timed decelerator provide firm confirmation to the theoretical understanding. Time-of flight (ToF) spectra from three representative and distinct spatial locations – before 23 stages, before 51 stages, and at the decelerator exit – are selected to demonstrate the evolving character of the phase-stable molecular packet. Where present in all data figures that follow, a downward-pointing arrow indicates the location of the phase-stable molecular packet.

Figure 5.11 depicts the OH ToF spectra when the decelerator is operated under a phase angle $\phi_o = 0°$, *i.e.* the net longitudinal velocity of phase stable molecules is not changed but the molecular packet maintains tight spatial confinement due to bunching. ToF spectra generated under properly timed and pulsed electric fields exhibit peak and valley structures, demonstrating the velocity and spatial selectivity of the inhomogeneous electric fields acting on the evolving molecular packet. The experimental data in Fig. 5.11 (a), (b), and (c) are plotted with symbols (filled circles) while the full 3D simulation results are displayed as solid lines. The simulation traces are offset vertically for clarity of presentation. Figure 10 (a) shows the spectra before 23 stages of bunching ($\phi_o = 0°$). With such few stages of interaction, longitudinally phase unstable
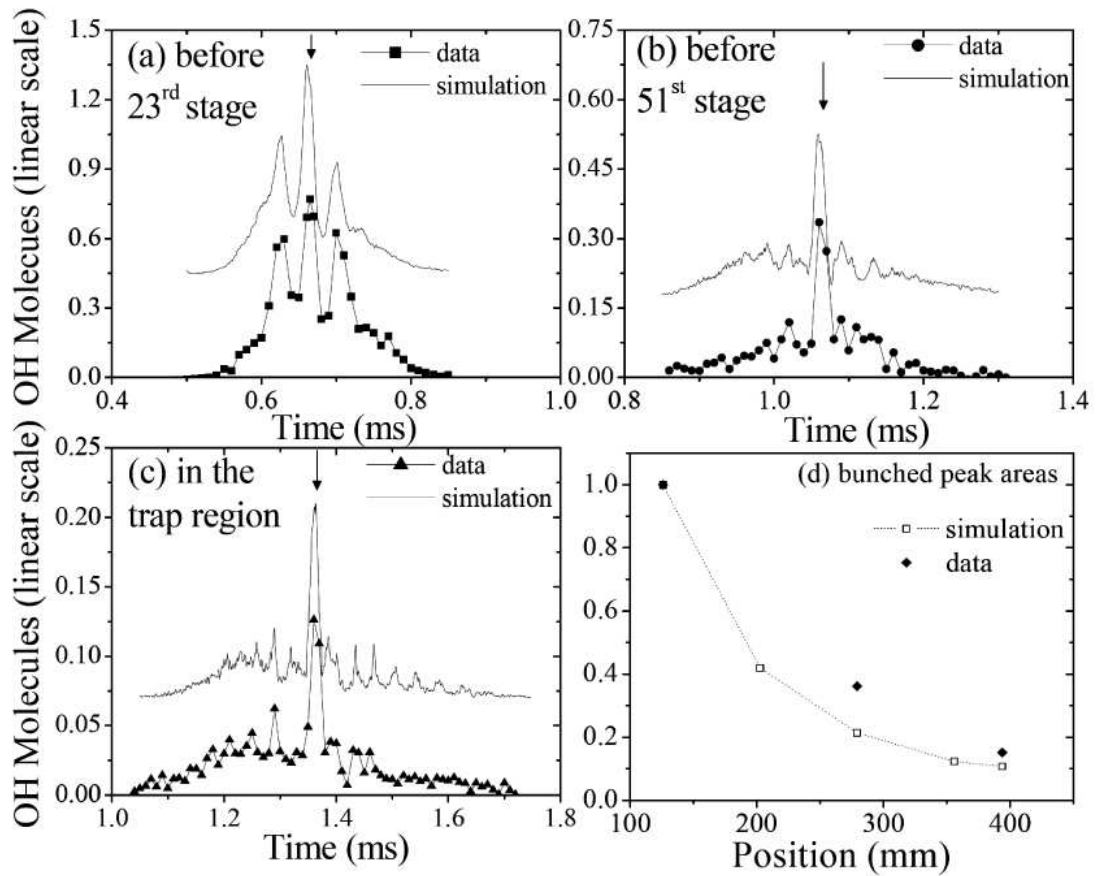
Figure 5.11: OH LIF TOF spectra under bunching ($\phi_o = 0°$) decelerator operation (a) before the 23rd stage, (b) before the 51st stage, and (d) within the electrostatic trap region. The data points are drawn as squares, circles, and triangles while the simulation results are shown as solid lines, with a vertical offset for viewing clarity. Panel (d) shows both experimental and simulation results on bunched peak areas, normalized to the 23rd stage; the reduction in peak height with position is due to longitudinally phase unstable molecules as well molecules with radial velocities ≥ 5 m/s being lost from the packet.

molecules are still dominantly present and detected by the LIF technique, generating the side peak features and contributing to the broad pedestal that the central peak sits on. By the time the molecular pulse has propagated in front of the 51st stage under the same experimental conditions, the phase stable packet has become the only distinct feature remaining, as shown in Fig. 5.11 (b). The molecules that correspond to untrapped orbits in phase-space generate the small, broad background on top of which the phase-stable peak sits. Similarly, the bunched, phase-stable packet dominates the spectrum in Fig. 5.11(c), where the molecules have exited the slower, propagated a short free-flight distance, and passed through the center of the electrostatic trap region where they are detected.

In principle, all molecules within the selected phase stable packet are transported without loss down the decelerator; the difference in peak amplitude between Fig. 5.11(b) and (c) is a result of molecular loss due to molecules with too high transverse velocities being progressively removed from the molecular pulse, inefficient coupling between the decelerator and trap region, and scattering from background gas. Figure 5.11(d) depicts the bunched packet peak areas at different spatial locations from both experimental data and simulations, normalized to the peak before the 23rd stage. This figure, along with the understanding gained from simulations, demonstrates that the apparent loss of signal is primarily due to the "boiling" away of longitudinal phase unstable molecules as they propagate down the slower, as well as molecules possessing transverse velocities $\geq$ 5 m/s slowly escapes from the phase stable packet throughout the deceleration process. Essentially, the focusing power of the hexapole is boosting the initial total number of molecules coupled into the slower. However, many of these molecules are ultimately not useful as they do not enhance the population of the phase stable packet and are subsequently lost. The simulation results provide excellent agreement with the observed spectra, confirming good understanding and control of the decelerator.

We gain more insight into the slowing process by examining in detail the ToF
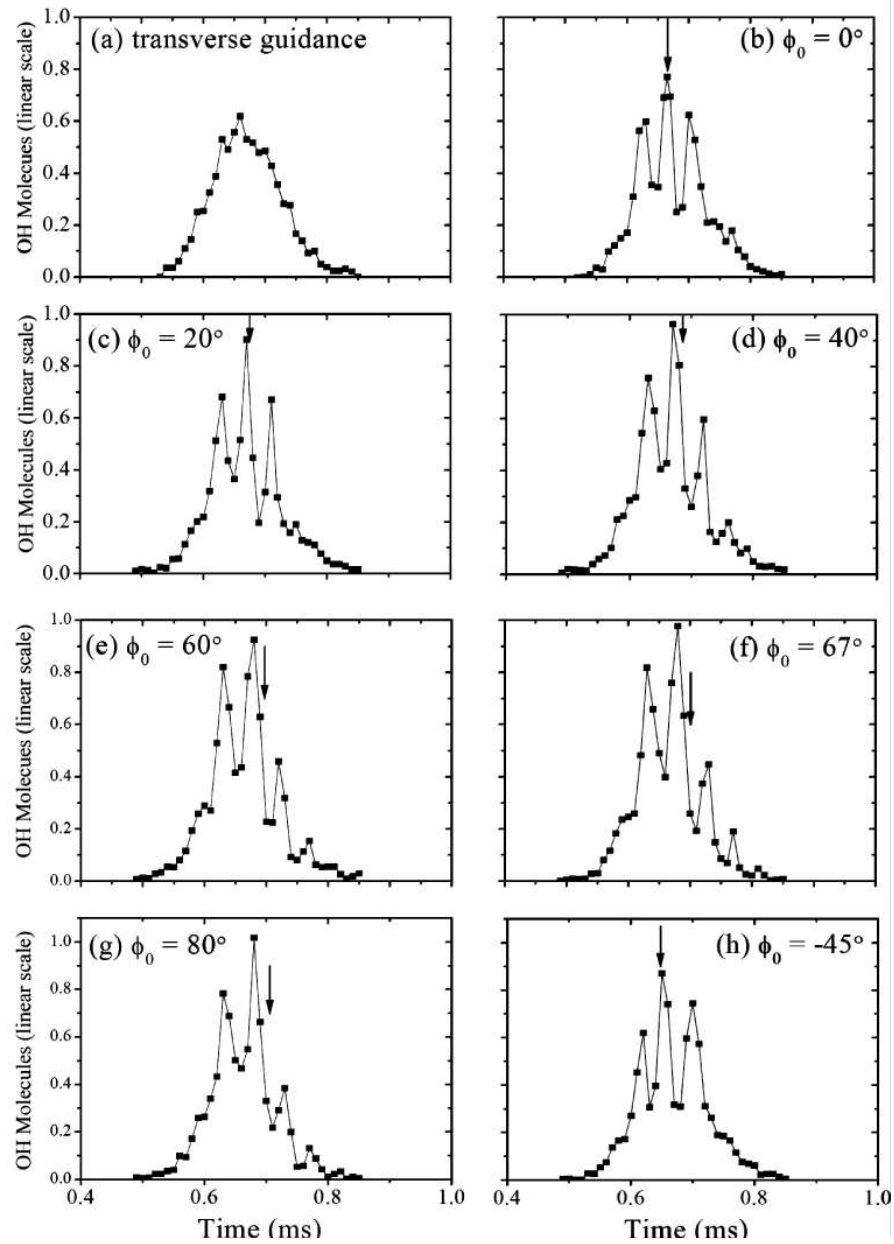
Figure 5.12: OH packet of molecules in front of the 23rd stage under (a) transverse guidance, (b) $\phi_o = 0°$ [385 m/s], (c) $\phi_o = 20°$ [365 m/s], (d) $\phi_o = 40°$ [344 m/s], (e) $\phi_o = 60°$ [323 m/s], (f) $\phi_o = 67°$ [317 m/s], (g) $\phi_o = 80°$ [309 m/s], and (h) $\phi_o = -45°$ [424 m/s], where the number in square brackets indicates the mean velocity of the phase stable packet. At this spatial location, under all operating conditions the spectra are dominated by signals from still present phase unstable molecules.
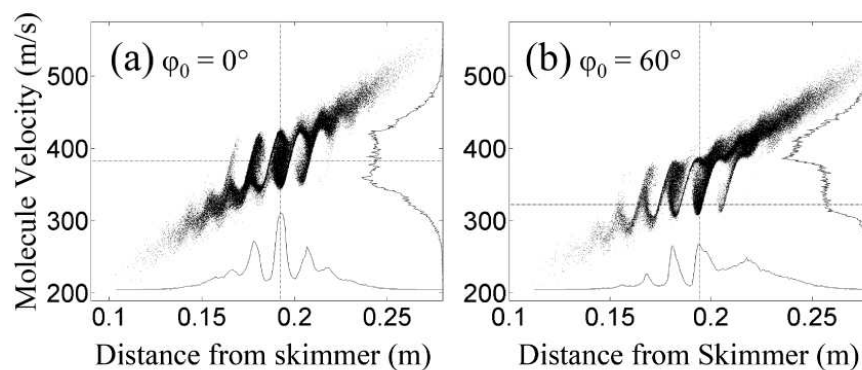
Figure 5.13: 3-D Monte Carlo simulation of the OH packet in front of the 23rd stage under the bunching and slowing (60°) conditions. Molecules are shown in longitudinal phase space as dots. Projections along the longitudinal spatial and velocity coordinates are both shown.

spectra obtained at a single specific spatial location as the phase angle is varied. Figure 5.12 focuses on LIF measurements made before the 23rd stage. Figure 5.12(a) shows the expected broad, basically featureless peak as the packet spreads longitudinally while being transversely guided down the central axis of decelerator under steady-state high voltages applied to all slowing stages. Figure 5.12(b) depicts the spectra under bunching operation (0 = 0), creating the multi-peaked structure, as also shown in Fig. 5.11(a), wherein the spatial periodicity of the high voltage stages is imprinted onto the OH pulse. The phase angle ϕ_o is then increased to 20°, 40°, 60°, 67°, and 80° in Fig. 5.12(c), (d), (e), (f), and (g), respectively.

Careful examination of the data traces reveals small changes in amplitudes and subtle time shifts in the location of the peaks as ϕ_o increases. However, the basic structure of the spectrum at this spatial location is mostly unchanged, as the signals from phase unstable molecules dominate the spectra. The downward-pointing arrow indicates the location of the phase stable packet – however, its presence is substantially masked by the signal from unstable molecules. This effect is expected and clearly seen in Fig. 5.13, where the results of a 3D Monte Carlo simulation after 22 stages

of deceleration, *i.e.* in front of 23rd stage, are shown for bunching and slowing with $\phi_o = 60°$. Figure 5.13 represents a snapshot of the longitudinal phase-space distribution of the molecular packet, with each dot corresponding to the longitudinal position and velocity of a simulated molecule. Along the horizontal (vertical) axis is shown the spatial (velocity) projection of the distribution, and a horizontal (vertical) dashed line represents the expected position (velocity) of the phase stable pulse at this instant. Figure 5.13(a) shows the result of bunching to the 23rd stage, revealing that phase unstable molecules are "boiling" away symmetrically around the stable molecule bunch. On the other hand, when $\phi_o = 60°$, Fig. 5.13(b) demonstrates that unstable molecules are lost in only one direction as the phase stable packet is pulled to lower velocities (consistent with the non-synchronous molecule potentials shown in Fig. 5.3(b)). These phase unstable molecules lead to dramatic effects in the observed ToF spectra of Fig. 5.12. In the bunching case (Fig. 5.12(b)), because the unstable molecules are lost symmetrically the bunched peak is only broadened. However, in the case of slowing or acceleration (Fig. 5.12(c) through (h)), the molecular loss is directional and the center of the observed peak is shifted from the expected location in addition to broadening. From the projection onto the horizontal axis it is evident that a peak does indeed occur at the spatial location expected for the phase stable molecule packet. However, because of convolution with the detection window this peak is unresolved in the large central peak in the ToF data. Also in Fig. 5.13(b) the manipulation of the input velocity distribution ($V_m = 385$ m/s, $\Delta v_{FWHM} \approx 75$ m/s) is beginning to become evident as molecules are moved from the central region (385 m/s) towards smaller velocities. The stable molecules have been incrementally slowed from the initial 385 m/s (Fig. 5.12(b)) to 309 m/s (Fig. 5.12 (g)), although this corresponds to only a $\sim$40 μs shift in the peak location at this position. Generally speaking, the more stages used, the more straightforward the interpretation of the spectrum will be, as contributions from the interesting though complicated dynamics of the longitudinally phase unstable molecules will be reduced.

For display purposes, Fig. 5.12(g) shows similar characteristics as we select $\phi_o = 80°$. At this aggressive slowing phase angle, the selected molecules will actually come to rest before the end of the 69-stage Stark decelerator. Finally, demonstrating the flexibility of this experimental technique, phase stable acceleration is depicted in Fig. 5.12(h), where a negative phase angle is utilized ($\phi_o = -45°$). The OH molecules have been accelerated from 385 m/s to 424 m/s. However, similar to the slowing data traces, the acceleration spectrum is complicated by signals from molecules with open trajectories (not contained inside the separatrix) in longitudinal phase-space.

We next observe molecular packets after 50 stages of operation. Similar to above, Fig. 5.14(a) shows the ToF spectrum solely under continuous, transverse guidance fields. From Fig. 5.15 it is clear that after 50 stages of operation, $i.e.$ observed in front of the 51st stage, essentially all of the phase unstable molecules have boiled out of the phase stable region. This significantly simplifies the interpretation of ToF spectra since only the well-characterized stable molecules remain in the peak of interest. Indeed, under bunching operation experimentally (i.e., $\phi_o = 0°$), Fig. 5.14(b) shows a single tall central peak representing the phase stable molecules that are maintained together with their net longitudinal velocity unchanged. The much smaller, lower-lying broad feature again arises from the phase unstable molecules. As the slowing phase angle is further increased, the behavior of the decelerated packet becomes manifestly clear in the data at this spatial location unlike after 22 stages. The slowed peak corresponding to the phase-stable packet evolves towards later arrival times, demonstrating its steadily decreasing velocity. In Fig. 5.14(c), (d), (e), (f) and (g) , the slowed peak appears at later time positions as the velocity of the OH molecules is reduced to 337 m/s, 283 m/s, 220 m/s, 198 m/s, and 168 m/s, respectively. As expected, the peak amplitude decreases as the phase angle gets larger, reflecting the reduced stable area in phase-space. Again, from Fig. 5.15(b) for $\phi_o = 60°$, we see this expected behavior in the snapshot projections of the longitudinal phase space distribution. In the horizontal projection we observe a
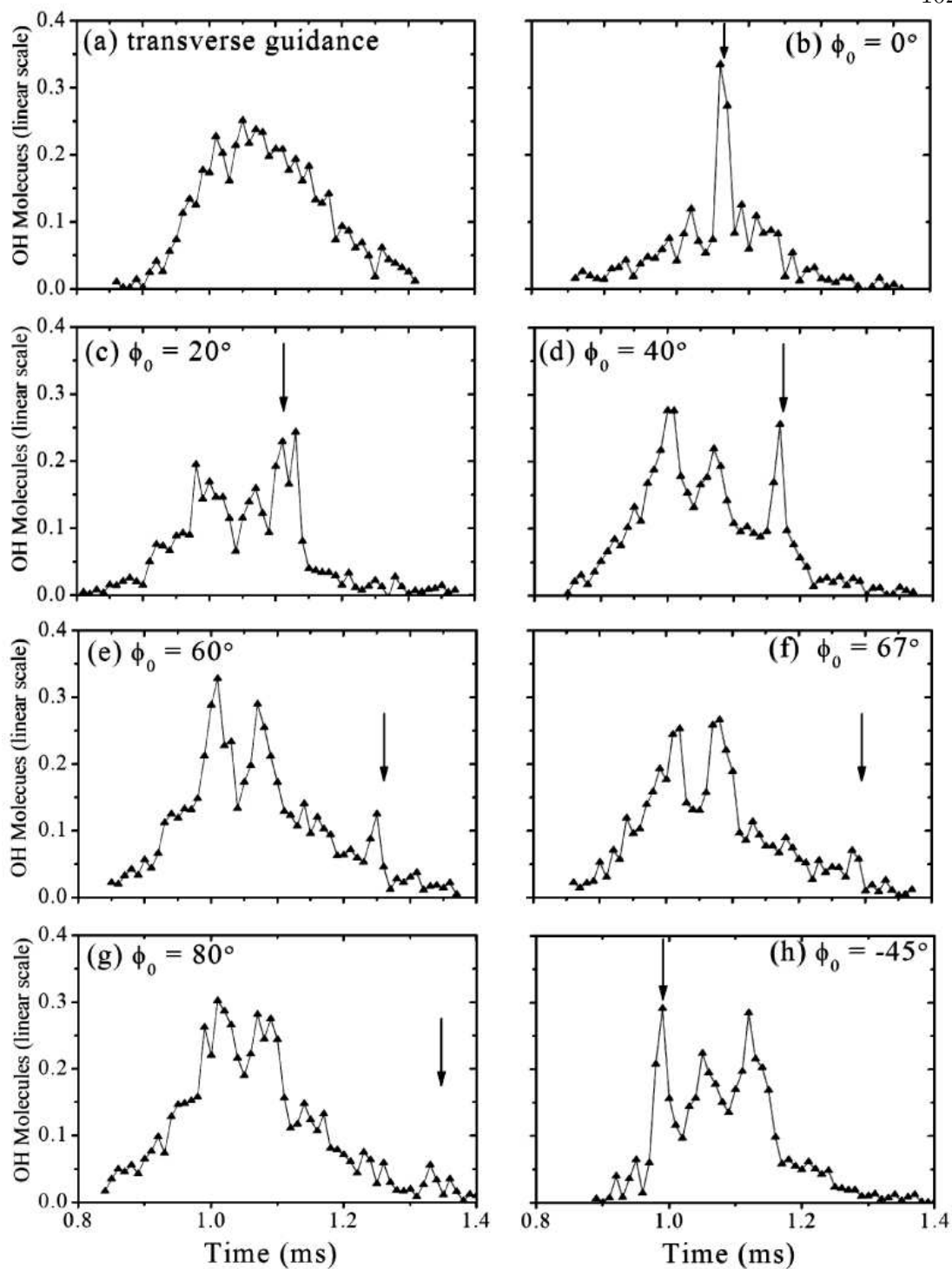
Figure 5.14: ToF LIF measurements of OH molecules before the 51st stage under (a) transverse guidance, (b) $\phi_o = 0°$ [385 m/s], (c) $\phi_o = 20°$ [337 m/s], (d) $\phi_o = 40°$ [283 m/s], (e) $\phi_o = 60°$ [220 m/s], (f) $\phi_o = 67°$[198 m/s], (g) $\phi_o = 80°$ [168], and (h) $\phi_o = -45°$ [470], where the number in square brackets indicates the mean velocity of the phase stable packet.

single phase-stable peak that has been moved towards the rear of the molecule pulse, while in the velocity projection we see that the input velocity has been significantly modified, resulting in a single packet of decelerated molecules traversing the slower.

Interestingly, there are distinctly different spectra features generated under bunching versus slowing conditions at this spatial location. In contrast to in front of the 23rd stage where the spectra maintain essentially the same characteristics at all operating phase angles, after the 50th stage at any non-zero phase angle, the spectrum changes from a single peak to a distinct triplet of peaks, where one of these structures corresponds to the phase stable packet of molecules that shifts to later (earlier) times for stable deceleration (acceleration) in the ToF observation. Within the presented data's time resolution, the other two peaks remain essentially at the same temporal locations for the same sign of phase angle, but these positions undergo a large time shift for opposite sign phase angles, as seen by comparison with Fig. 5.14(h). These structures are primarily the result of molecules being removed from the center of the free-flight ToF peak and decelerated (accelerated) to later (earlier) arrival times.

We now examine OH signals observed beyond the final (69th) stage of the decelerator. Here we present further ToF spectra of OH molecules observed moving with varying velocities at the decelerator exit. Where appropriate, the simulation results are plotted as lines that have been offset vertically from the data trace for viewing clarity. Figure 5.16(a) shows the transversely guided pulse of OH molecules in the trap region with a mean pulse velocity of 385 m/s. Under bunching conditions selected for this mean velocity, the expected narrow, single, phase-stable packet shows up as a single large peak depicted in Fig. 5.16(b), arriving at 1.37 ms. In Fig. 5.16(c) at a phase angle $\phi_o = 45°$, the slowed peak arrives later in time as the molecular speed is further slowed to 210 m/s. In fact, the peak has been moved completely off of the residual signals from phase unstable molecules that form the broad pedestal in Fig. 5.16(b). This complete separation occurs at a smaller value of ϕ_o than that for 51 stages since the entire 69
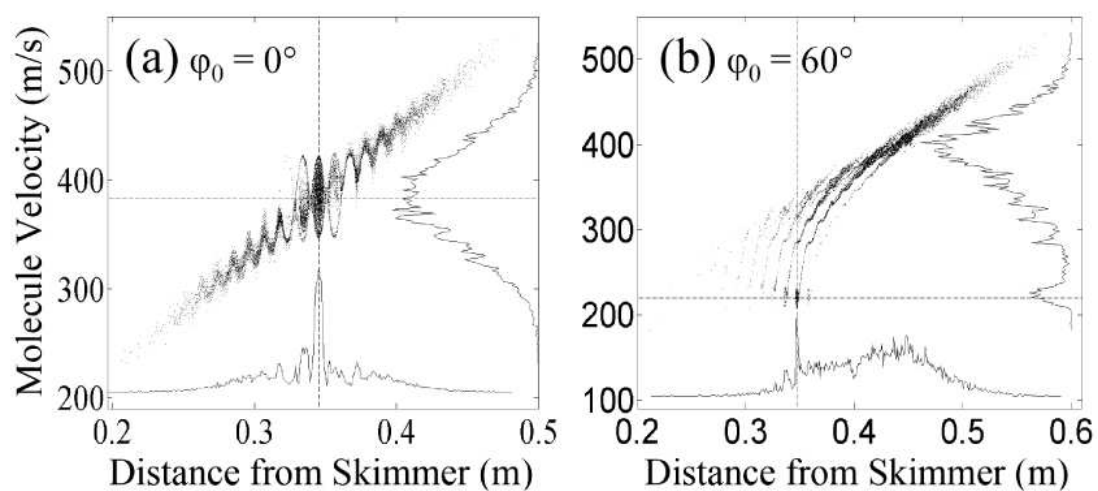
Figure 5.15: 3D Monte Carlo simulation of the OH packet in front of the 51st stage under the bunching and slowing (60°) conditions. Molecules are shown in longitudinal phase space as dots. Projections along the longitudinal spatial and velocity coordinates are both shown.
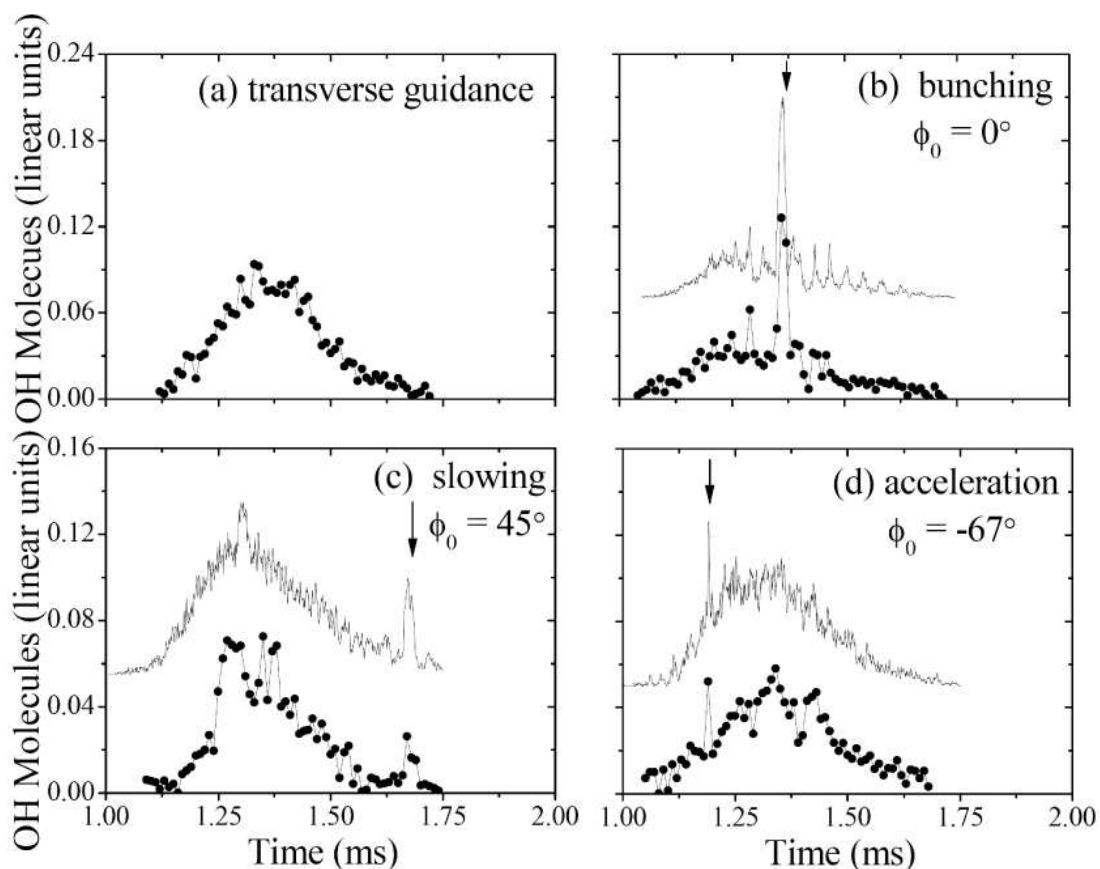
Figure 5.16: Observations of OH molecules at the decelerator exit under (a) transverse guidance, (b) bunching ($\phi_o = 0°$, v = 385 m/s), (c) slowing ($\phi_o = 45°$, v = 210 m/s), and (d) acceleration ($\phi_o = -67°$, v = 541 m/s). Monte Carlo simulation traces are plotted above the data.

stages of the decelerator are utilized for kinetic energy extraction. Finally, phase-stable acceleration is shown in Fig. 5.16(d), wherein the molecular packet is accelerated to 541 m/s, arrives correspondingly earlier in the ToF spectrum and creates the narrow peak at 1.19 ms. Above the data traces, simulation spectra with higher temporal resolution are plotted. Consistency between simulation and measurement is quite good, with locations of the phase stable packet and relative peak heights demonstrating excellent agreement.

We now focus with higher temporal resolution on measuring solely the phase stable packets generated by the decelerator moving through the trap region. Successful operation of the decelerator relies on precise knowledge of the molecular packet's velocity and location in order to be able to stably slow the packet. Hence, we can easily predict when the pulse of molecules will arrive in the trap region after it exits the decelerator. We note, that at low phase angles, when the velocity change of the molecules is not that large, the analytic expression, *i.e.* sine fit, to the potential energy hill presented in Fig. 5.2(b) enables sufficient accuracy to predict the peak arrival times. However, at higher phase angles, the deviation between the analytical calculation and the actual shape of the potential becomes a significant factor such that a numerical determination of the potential must be used to generate the proper time sequence to operate the decelerator. In fact, both simulations and measurements demonstrate that the molecular packet actually becomes phase unstable once ϕ_o becomes greater than $40°$, unless the more accurate calculation of the time sequence is used. Finally, as a minor detail, when the molecules are exiting the decelerator through the last stage, the voltage on the last electrodes is switched off, while the voltage on the preceding stage is turned on. The presence of this non-zero electric field results in a small accelerating force to the molecules. This effect needs to be taken into account to determine accurately how the molecules propagate from the last decelerator stage through the essentially field-free region into the trap.

In Fig. 5.18, we detect the molecules with 2.5 μs timing resolution per point.
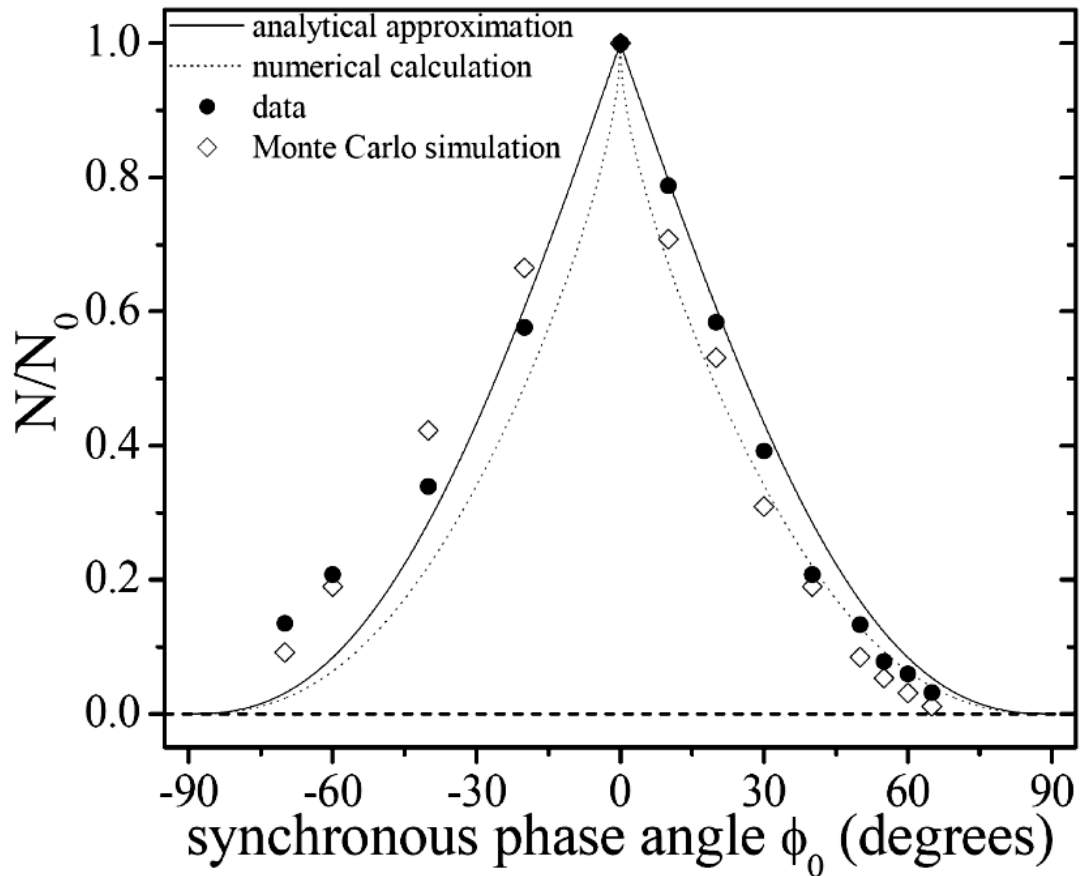
Figure 5.17: Observations at the decelerator exit: numbers of molecules in the phase stable packet N relative to the number in the bunched packet N_o, for varying slowing and accelerating phase angles. Data points (solid circles) and three-dimensional Monte Carlo simulations (open diamonds) are shown. For comparison, theory traces generated from the simple analytic expression (Eq. 5.5, solid line) and the numerical calculation (dotted line) for stable areas in phase space are shown.
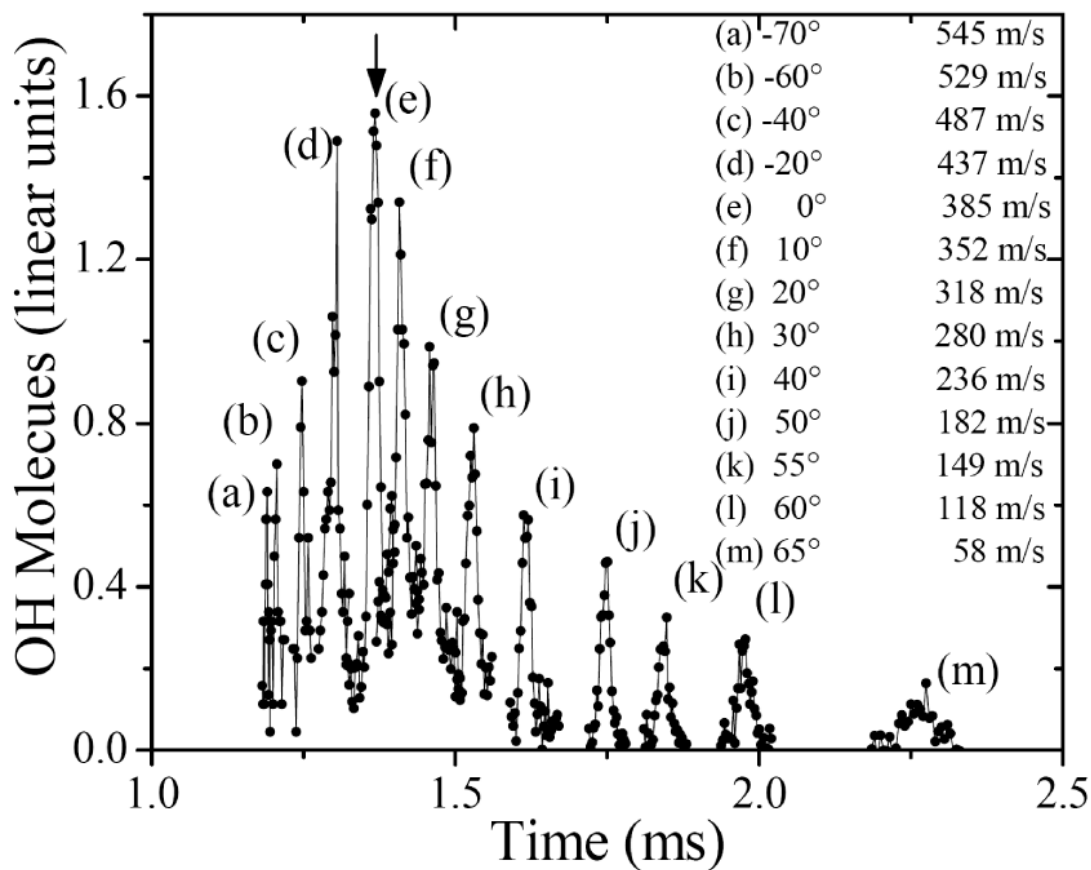
Figure 5.18: Slowed, accelerated, and bunched molecular packages at the decelerator exit under varying phase angles. Here, the downward-pointing arrow indicates solely the position of the bunched (trace (e) $\phi_o = 0°$) packet, as all observed peaks are the result of phase-stable packets. Molecular peaks arriving earlier in time result from accelerated OH packets with corresponding negative phase-angles as denoted in the figure. Peaks arriving later in time are similarly the result of slowed molecules, generated by using positive phase-angles.

Phase stable packets are measured over a broad range of operating parameters, both in acceleration, bunching, and slowing for $-70° \leq \phi_o \leq 65°$. Fig. 5.18 traces (a), (b), (c), and (d) represent OH radicals that have been accelerated from an initial velocity of 385 m/s to a maximum speed of 545 m/s. The phase stable molecules arrive earlier in time relative to the bunched peak (Fig. 5.18 trace (e)) and create the observed increasingly narrow structures. The bunched packet corresponds to $\sim 10^4$ molecules at a density of $\sim 10^6$ cm-3. Traces (f), (g), (h), (i), (j), (k), (l), and (m) show phase stable OH packets which have been decelerated to correspondingly lower velocities, as indicated in the figure. As the molecular packet is increasingly slowed, the molecules arrive progressively later in time. For $\phi_o > 40°$, the slowed peak is completely separated from the broad background signals produced by residual phase unstable molecules. In contrast to the accelerated molecules, the slowed, stable molecular packets broaden as the phase angle increases, due the reduced molecular speed.

As the molecules slow down towards rest, there is an artifact in detection of molecular numbers due to the finite spatial size of the detection window. Basically, slow molecules are counted multiple times as they move through the detection region where the LIF light pulses are shifted in fine time steps to obtain high resolution TOF spectra. When this effect is properly de-convolved from the actual underlying signal size, the number, N, of OH molecules in a phase stable packet as a function of phase angle can be determined. The measured results (filled circles), normalized to the bunching peak number N_o are plotted in Fig. 5.17. In addition, points generated under Monte Carlo simulations (open diamonds) as well as theory curves from the simple analytic expression of Eq. 5.5(solid line) and the more accurate numerical calculation (dotted line) are shown. The agreement between experimental results and simulation is quite good. The main sources of error are peak reproducibility and accurate estimation of the peak area of the bunched packet as it is temporally coincident with signals from phase unstable molecules. Disagreement between the measured data points and the simulation
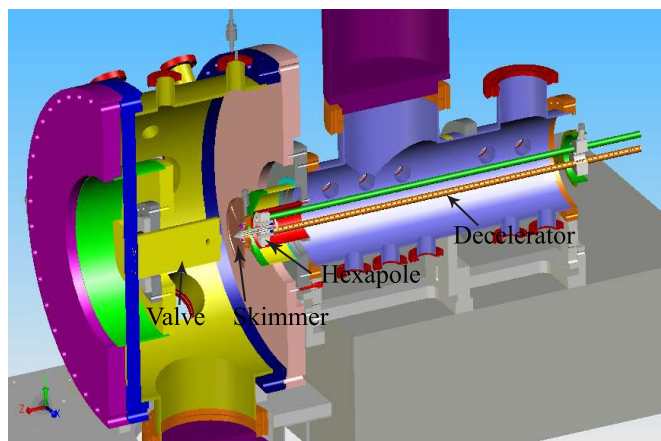
Figure 5.19: Schematic of second-generation Stark decelerator, showing increase source chamber volume.

results are within experimental error. Deviation of the data points under acceleration conditions ($\phi_o < 0°$) are primarily due to insufficient time resolution in the data points, making peak area estimates difficult.

5.4.2 Second-Generation Decelerator

As briefly mentioned, our second-generation Stark decelerator contains roughly twice the number of stages as our first (143 in all) and a more suitable vacuum chamber for producing a good molecular beam as seen in Fig. 5.19. From the discussion in the previous subsection and in Chap. 7, the advantages of a longer decelerator are clear. With a longer decelerator one can take out less energy per stage, $i.e.$ use a smaller ϕ_o, and thus decelerate with a larger phase space acceptance, leading to an increase in decelerated molecule number. For example, the second-generation decelerator can decelerate a beam of OH from 380 m/s to rest (produced by the PZT valve) with ϕ_o = 30°, while the first-generation decelerator would require $\phi_o = 60°$. From Fig. 5.4 we see this constitutes an order of magnitude gain in decelerated molecule number.

However, with a longer decelerator the slowed molecule number becomes more sensitive to transverse focusing effects. As was seen in Fig. 5.11(d), the molecule number

in the bunching peak decrease monotonically as the pulse travels down the slower. While initially this is mostly due to longitudinally un-stable molecules, the contribution from transverse loss is non-negligible, especially at the end of the decelerator when the molecules are moving more slowly (in the case of slowing). Simulations for the second-generation decelerator show that for bunching after about 70 stages of deceleration of OH very few molecules are lost transversely, and the molecule number per stage stabilizes [4] . It is important to note that this result depends on the Stark shift of the molecule being decelerated. Specifically, molecules like OH and NH whose Stark shift becomes linear at small fields are transversely guided significantly better than molecules like H_2CO whose dipole moment requires a higher field to saturate, *i.e.* reach the linear Stark shift regime. The improved guidance is because the transverse guidance comes in front of the electrodes where the fields are often small. Thus, building a long decelerator to decelerate molecules with a weak Stark effect will probably lead to extreme transverse losses.

Shown in Fig. 5.20 are ToF spectra taken at several phase angles at the decelerator exit. Comparing the signal-to-noise ratio of this data with similar data in the first-generation decelerator shows the obvious molecule number enhancement. Simulation results, also shown in these figures, agree reasonably well with the observed data. Specifically, all the modulations of observed signal are reproduced in the simulations, showing that the deceleration dynamics are understood. For these graphs the simulations are normalized by a numerical factor, which matches the non-bunched molecule number, *i.e.* the background pedestal, to the observed signal for $\phi_o = 0°$. This same numerical factor is used for all subsequent simulations. From the panels of Fig. 5.20 it is clear that the simulations properly predict the non-decelerated molecular pulse, but overestimate the number of decelerated molecules. While this could be due to the

---

[4] For deceleration the situation is more complicated, as detailed in the next section, and a small decrease of the number of molecules with stage number is observed for the entire deceleration process.
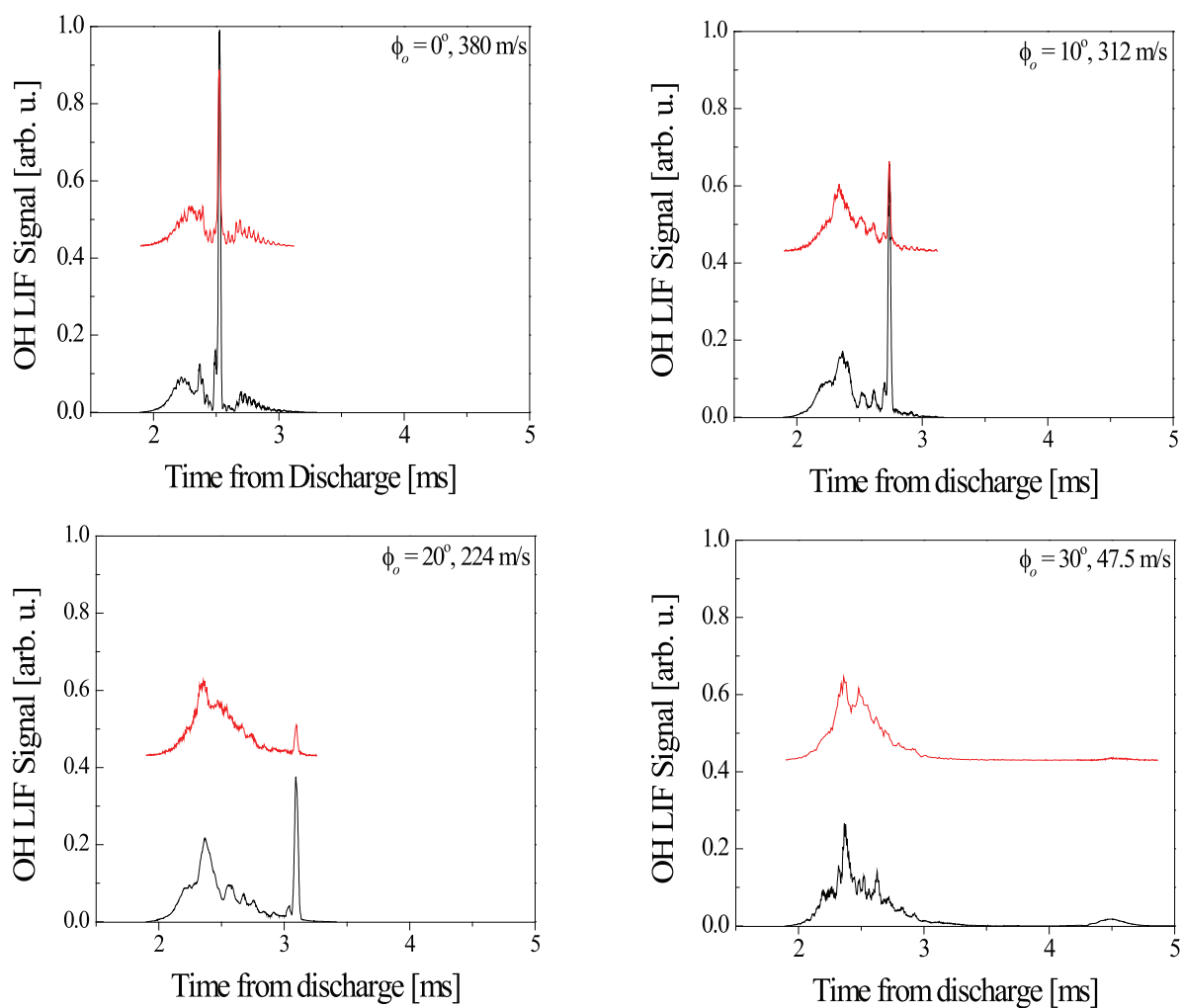
Figure 5.20: OH ToF Data (offset) taken at the exit of the second-generation Stark decelerator. The results of 3D Monte Carlo simulations are also plotted. All simulations are normalized by a numerical factor, which matches the simulations results to the bunching pedestal.

poor modeling of the initial molecule distribution at the skimmer or improper modeling of transverse motion, similar simulations correctly predict the relative heights of the decelerated peaks for our first-generation decelerator. Furthermore, comparison of ToF data to simulation at location inside our second-generation decelerator (after 31 and 106 stages of deceleration, where we have optical access) do not show the same discrepancies. For these reasons we suspect the decelerated molecule number discrepancy, plotted in Fig. 5.21, is due to an experimental effect present in the longer decelerator and not an artifact of simulation.

There are several possible explanations for the unexplained molecule number loss, such as collisions (background or OH-OH), discharge or other decelerator construction problems, switching problems, and transitions to non-decelerated quantum states. Of all these, transitions to non-decelerated quantum states appear the most likely since we have verified proper construction and operation of the decelerator, and estimation of collision effects put the effect many orders of magnitude below the observed loss. Furthermore, as seen in Fig. 5.21 the discrepancy between simulation and experiment initially increases with deceleration, but becomes less at higher phase angles and all of these effects (except transitions) should be worse at slower speeds. There are two types of transitions to non-decelerated states possible inside the decelerator; those that are driven by the radiation generated at the switching of the fields and non-adiabatic (Majorana) transitions that occur when the molecules are in the relatively low fields or quickly changing fields present directly after and during a deceleration event. Because the Λ-doublet splitting is so large for OH these transition most likely occur between the hyperfine components of the upper doublet. Specifically, a transition between any of the strongest weak-field seeking states, $e.g.$ $|2 \pm 2, +\rangle$ and $|2 \pm 1, +\rangle$, to any of the less strongly decelerated states, $e.g.$ $|20, +\rangle$ and $|1 \pm 1, +\rangle$, and $|10, +\rangle$, will lead to the observed loss. With current experimental data it is difficult to determine, which type of transition (or if both) is responsible for the decrease in decelerated molecule number.
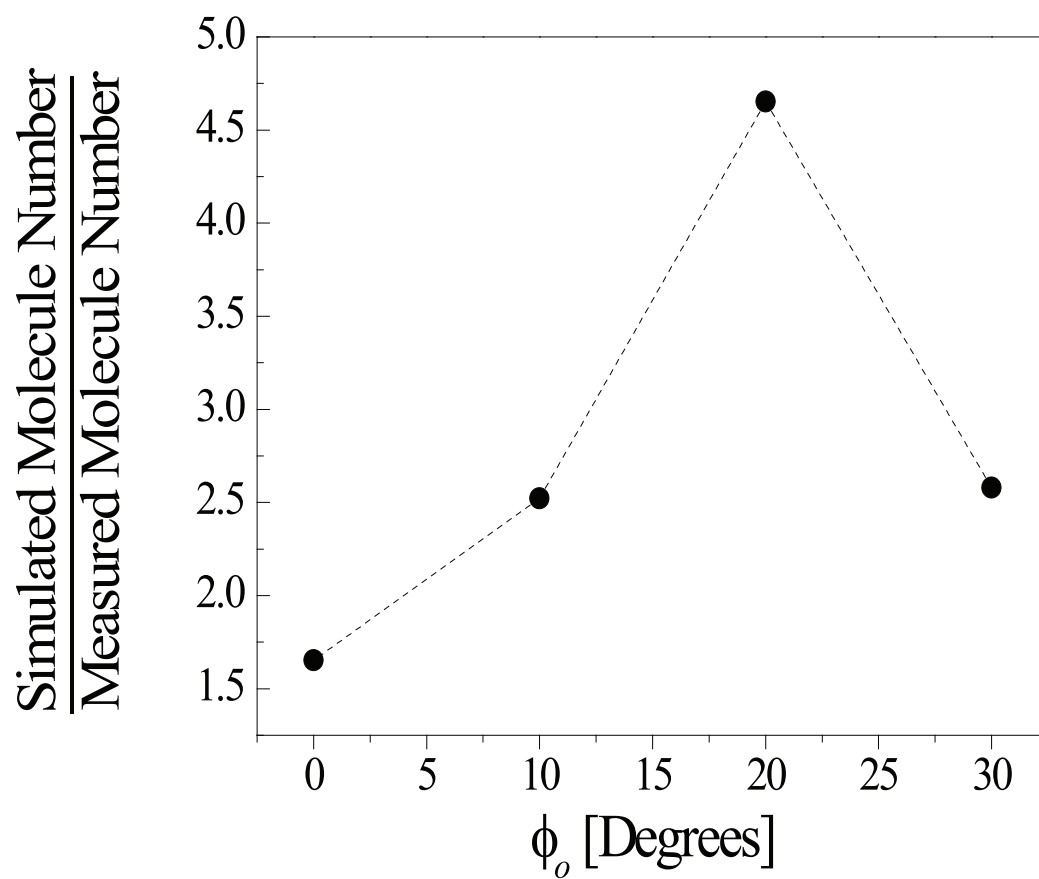
Figure 5.21: Molecule Number Discrepancy between simulation and experiment.

Thus, two experiments are underway. One will test the contribution of Majorana flips by observing the decelerated molecule number when switching the deceleration electrodes between an adjustable voltage, V, and high voltage at 12.5 kV $+ V$, instead of between ground and 12.5 kV. In this way, the OH will remain completely polarized (for high enough V) and any contribution from Majorana flips can be ruled out. The second experiment will be to observe the decelerated molecule number for different switching speeds. Currently, the high voltage is removed and applied to the electrodes in 500 ns. By slowing down the switching speed via a charging resistor the frequency bandwidth of the generated radiation can be reduced below the minimum state separation.

5.4.3   Transverse over-focussing

As will be detailed in a later chapter (see Chap. 7) the transverse guiding motion inside the Stark decelerator can play a large role in the total number of decelerated molecules. One effect, detailed in Fig. 5.22, is the transverse over-focussing of a slow molecular beam. In this figure, the number of phase-stable molecules predicted by simulation is shown as function of stage number [5] for increasing phase angle. Here we see that as expected a higher phase angle leads to a smaller number of decelerated molecules. While initially the behavior more or less follows what is expected from the longitudinal phase space dynamics at the highest phase ($\phi_0 = 30.45°$, 10 m/s) there is a sharp loss of molecules in the last several deceleration stages. This loss is attributed to transverse over-focussing. That is, because the molecular beam is moving very slowly in the last few deceleration stages the transverse guiding fields of the decelerator electrodes have a greater focussing effect on the molecules (see Sect. 4.3) and focus the molecules so tightly that they collide with the next deceleration stage and are lost. In the case of

---

[5] The phase-stable molecule number is determined by counting the number of molecules inside the box determined by the maximum stable position and velocity excursion as defined in the next chapter. Since the box does not exactly represent the phase-stable area, the increase in number shown early in the decelerator is artificial and one expects the phase-stable number to be monotonically decreasing with stage number.

our second-generation decelerator this leads to loss of 20% in the decelerated molecule number between $\phi_o = 30°(48m/s)$ and $\phi_o = 30.45°(10m/s)$, which is significantly more than the expected difference. Furthermore, this number is calculated directly after the decelerator is switched-off and is thus the 'best-case scenario', since experimentation or trapping requires the molecules to fly out of the decelerator where transverse losses can be dramatic. This sudden decrease in molecule number has been experimentally observed in our experiments as well as in the work of the Berlin group [3] and is extremely detrimental since trapping of polar molecules requires these low speeds.

To remove this undesired effect from deceleration the transverse focussing of the last several decelerators stages needs to be reduced. This may be accomplished by changing the electrode geometry, *i.e.* altering the electrode radius or moving the rods transversely further apart, or lowering the voltage on the last deceleration stages. Furthermore, it may be possible to insert focussing elements into the deceleration beam line, whose voltage can be dynamically controlled to compensate, for the over-focussing. These ideas are discussed in detail in Chap. 7.
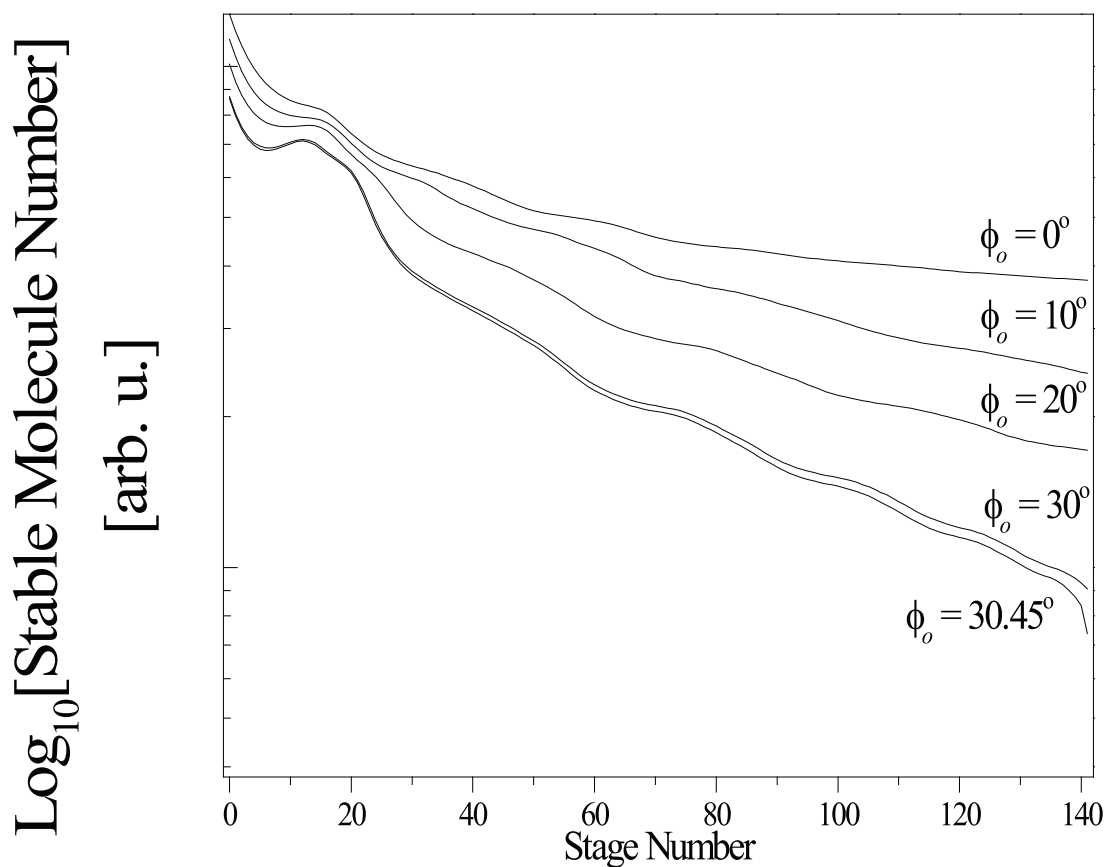
Figure 5.22: Simulations of the phase-stable molecule number as a function of stage number in our second-generation decelerator. Note the dramatic decrease in number in the last several stages for $\phi_o = 30.45°$. This decrease is due to transverse over-focussing of these slow (10 m/s) molecules.

Chapter 6

Acceptance Theory of a Stark Decelerator

6.1   Introduction

The study of ultra-cold polar molecules is a rapidly emerging field as evidenced by the large number of new experiments being undertaken [138, 24, 27, 72, 68, 119]. The permanent electric dipole moment, μ, possessed by polar molecules allows for a new type of interaction in the ultra-cold environment. This electric dipole-dipole interaction (and control over it) should give rise to unique physics and chemistry including novel cold collision dynamics [18], quantum information processing [42], and a second order phase transition analogous to spontaneous magnetization of a ferromagnet. When the translational energy of colliding polar molecules becomes comparable to their dipole-dipole interaction energy, the molecules can dramatically influence each other's trajectory. Lack of spherical symmetry in the interaction causes colliding molecules to be attracted or repelled depending on their relative orientation. Thus, an external electric field, which orients the molecules, may have a profound effect on the molecular interactions leading to large changes in observed scattering rates [18]. Another interesting possibility is the observation of criticality in a two or three (3D) dimensional lattice of dipolar molecules. For a typical polar molecule ($\sim$2 Debye) in a 3D optical lattice with 1 μm spacing, the critical temperature for the second order phase transition (spontaneous polarization) is estimated by a 3D Ising model as $\mathrm{T}_c \sim 3\mu^2/(2\pi\epsilon_0 k_B R^3) = 200$ nK, where R is the dipole-dipole separation, ϵ_0 is the permittivity of free space, and k_B is

Boltzmann's constant [94]. By using extremely polar molecules such as those predicted to occur from photo-association of free radicals with Rubidium ($\mu \sim$10 Debye) [111], or by decreasing the dipole-dipole separation through simply trapping polar molecules at a sufficient density, the critical temperature may be raised by at least one order of magnitude. It is interesting to note that at temperatures significantly higher than this regime an analog to adiabatic demagnetization refrigeration [97] may become possible, leading to a new method for further cooling polar molecules, so-called "paraelectric cooling" [71].

The technique of Stark deceleration is especially well-suited for production of cold polar molecules since it utilizes the Stark shift associated with polar molecules to remove the mean translational energy from a supersonic beam of molecules. Supersonic molecular beams, utilized extensively in physical chemistry, are capable of producing intense pulses of molecules with mean velocities of a few hundred meters per second and a small velocity spread about this mean. Therefore, in the moving frame of the molecular pulse the associated velocity spread corresponds to a low temperature distribution ($\sim$ 1 K). Stark deceleration conservatively removes this mean velocity, leaving behind a cold molecule distribution in the laboratory frame. To date this technique has been employed to produce slow, cold beams of CO [24], OH [27, 127], H_2CO [62] and ND_3 [23]. Slowing of YbF in an alternate-gradient decelerator has also been demonstrated in a proof of principle experiment [119].

Due to practical limitations of both the physical dimensions of a Stark decelerator and the applicable electric fields, only molecules within a specific range of velocities and positions can be efficiently slowed and trapped. These constraints result in a restricted phase space acceptance of the decelerator in directions both transverse and parallel to the molecular beam axis. Thus, for efficient operation care must be taken to match the phase space distribution of the supersonic beam source (emittance) to the phase space acceptance of the Stark decelerator. This chapter details work from both experiment

and model, describing the process of phase space matching between the supersonic beam source and the molecular decelerator. The focus of the current chapter is to present a clear understanding of the decelerator efficiency and describe explicitly the experimental requirements for maximizing it. For the sake of the completeness, there is some intentional overlap between this chapter and Chap. 5, though greater detail is given in the derivations of this chapter. For experimenters new to this field, this chapter will serve as a useful and practical guide for the design of future Stark deceleration experiments.

Our experiment centers on the deceleration of the neutral hydroxyl radical, OH. For low rotational levels the $^2\Pi$ electronic ground state of OH is sufficiently described by Hund's case (a). Spin-orbit coupling results in the $^2\Pi_{3/2}$ state lying $\sim$139 cm^{-1} below the $^2\Pi_{1/2}$ state. Because of the non-zero orbital angular momentum of the unpaired electron in OH each total angular momentum, J, state is λ-type doubled, resulting in two closely spaced ($\sim$1.5 GHz), opposite parity levels in the ro-vibrational ground state. The application of an electric field readily mixes these states and for the symmetric f state results in an increase in energy with electric field [23]. The most polarized sub-level of this state, denoted as $|^2\Pi_{3/2}, J = 3/2, m_J = 3/2, f \rangle$, is decelerated by our Stark decelerator. We detect the presence of OH molecules through the technique of laser induced fluorescence. A pulsed excitation laser tuned to 282 nm promotes the molecules along the $A^2\Sigma_{1/2}(v = 1, J = 3/2) \leftarrow X^2\Pi_{3/2}(v = 0, J = 3/2)$ electronic transition. The excited molecules subsequently decay primarily (73%) back to the ground electronic state along the $A^2\Sigma_{1/2}(v = 1) \rightarrow X^2\Pi_{3/2}(v = 1)$ pathway at 313 nm. This fluorescence is collected and imaged onto a photomultiplier tube. By varying the time of the laser pulse, we sample the OH molecules at a single location at different times to extract time-of-flight (ToF) information. Careful measurements of the total molecule numbers before and after the Stark decelerator, and thus determination of the overall decelerator efficiency as a function of decelerator/supersonic beam operation parameters, provides

information pertaining to the phase space matching of the source to the decelerator. We have developed a simple model and Monte Carlo simulations that provide excellent agreement with the observed behavior. The remainder of the chapter is organized as follows. Section 2 briefly describes the operation of a Stark decelerator (for a more complete review of Stark deceleration see [25, 28]) as well as develops a simple intuitive model for phase space matching. Section 3 details our experimental results and compares them to the model of Section 2 to provide confidence in using it for optimization, while Section 4 is reserved for conclusions and suggestions for optimal operation of a Stark decelerator.

6.2   Stark Deceleration

Figure 6.1 shows a schematic diagram of our Stark decelerator, which has been described elsewhere [28]. Hydroxyl radical molecules produced by the discharge of H_2O in Xenon ($\sim$1:99 mixture) undergo a supersonic expansion and are subsequently skimmed to separate the low vacuum source region ($\sim 10^{-4}$ torr) from the high vacuum region ($\sim 10^{-7}$ torr), which contains the decelerator electrodes and the applied high-voltage electric fields. After skimming, the molecules are focused by an electrostatic hexapole field to provide transverse coupling into the Stark decelerator. Once the molecules are coupled into the Stark decelerator, the slowing process begins. The Stark decelerator is constructed of 69 slowing stages spaced 5.475 mm apart with each stage comprised of two cylindrical electrodes of diameter 3.175 mm separated axially by 5.175 mm and oppositely biased at high voltage ($\pm$ 12.5 kV). Successive stages are oriented orthogonally to each other to provide guiding of the molecular beam in both transverse dimensions. The geometry of the slowing stages provides an electric field maximum between the electrodes with the field decreasing away from the electrode center. Therefore, a weak-field seeking molecule travelling longitudinally down the decelerator will be decelerated as it moves into the region between the electrodes and will remain decelerated if the high
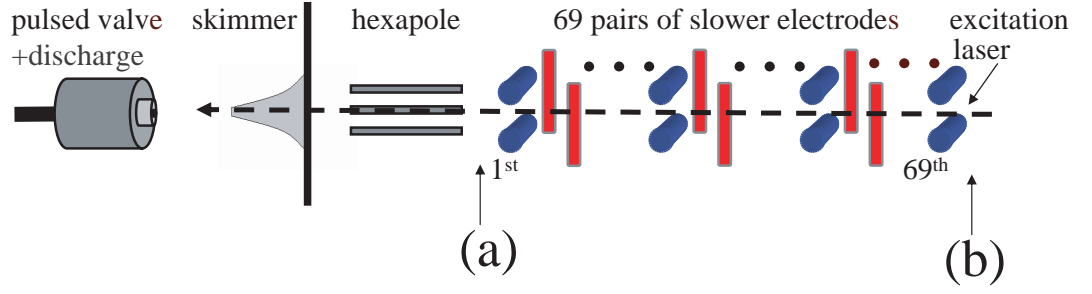
Figure 6.1: Schematic of the Stark decelerator, displaying the pulsed valve and discharge plates, the molecular beam skimmer, the electric hexapole, and the electrode stages. The electrode stages alternate orientation (vertical-to-horizontal) as shown in the figure. The spatial locations indicated by arrows correspond to the locations where molecule number is measured to determine decelerator efficiency.

voltage is removed before the molecule passes through the electrode's field. In order to minimize the number of high voltage switches used, all the like-oriented electrodes of the same polarity are connected to one switch (4 switches total for the entire decelerator).

As a consequence of this switch minimization, when the voltage at each slowing stage is grounded and the next stage is turned on, the electric field is not completely removed, but rather becomes the field generated by the alternate set of electrodes. (The potentials associated with these fields are shown in Fig. 6.2(a). Electrode pairs are centered at $\phi_0 = $ -90°, 90°, 270°) The potential energy experienced by the molecules Thus, the decrease in the molecular kinetic energy, ΔKE, is given as the difference in potential energy generated by the two sets of electrodes and is shown as a function of synchronous molecule phase angle, ϕ_0, in Fig. 6.2(b). The synchronous molecule phase angle, ϕ_0, is defined as:

$$\phi_0 = \frac{180°}{L} z,$$ (6.1)

where L is the distance between two adjacent stages and the $z = 0$ is defined to be exactly between two adjacent stages. Thus, switching at $\phi_0 = 0°$ corresponds to no net change in molecular kinetic energy, while maximum deceleration (acceleration) occurs at $\phi_0 = 90°$ (-90°). Though synchronous molecule phases between $\phi_0 = 0°$ and 180° lead
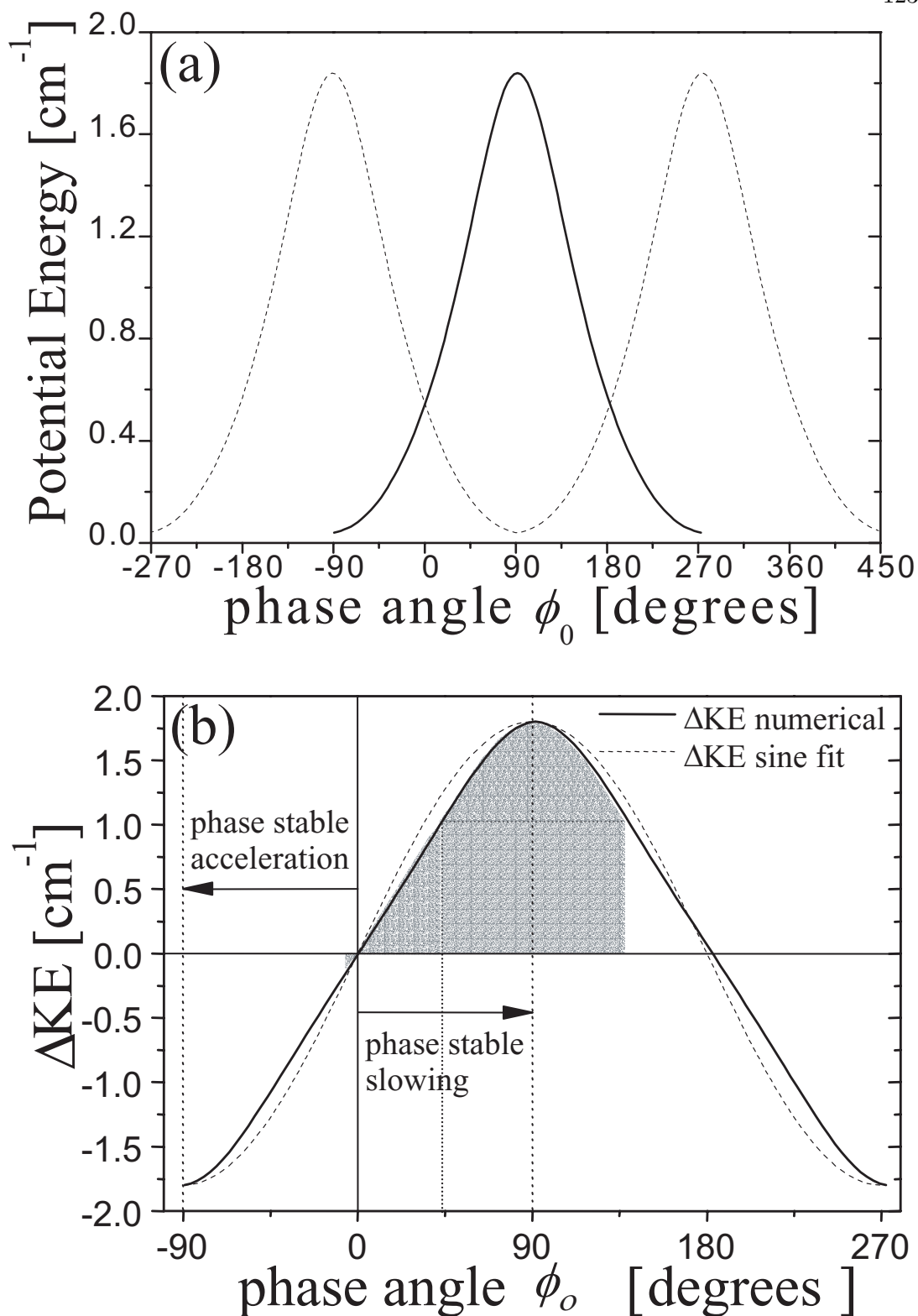
Figure 6.2: Phase stable operation of the decelerator. (a) Longitudinal Stark energy potentials generated by two sets of electrodes, where the solid line represents the potential from one set of electrodes and the dotted line from the other set. Electrode pairs are centered at $\phi_0 = $ -90, 90, 270. (b) Kinetic energy loss per stage (ΔKE) experienced by molecules due to switching between the two potentials shown in (a). The dashed line corresponds to a sine function approximation of the potential energy loss. The shaded region corresponds to the phase stable area for deceleration $\phi_0 = 45°$

to deceleration, only $0° < \phi_0 < 90°$ results in stable slowing because it is only on the positive sloping ΔKE curve that molecules ahead (behind) of the center of the bunch are decelerated more (less) than the average. To further investigate the dynamics of the molecules within this stable packet, it is useful to define the excursion of a molecule from the synchronous molecule position as $\Delta\phi = \phi - \phi_0$. Then with the use of Newton's second law and a sine function fit to the change of kinetic energy as a function of ϕ_0 (Fig. 6.2(b)) it is trivial to write [139]:

$$\frac{d^2\Delta\phi}{dt^2} + \frac{\pi C_{Max}}{mL^2}(\sin(\Delta\phi + \phi_0) - \sin(\phi_0)) = 0, \tag{6.2}$$

where C_{Max} is the maximum kinetic energy change per slowing stage, t is time, and m is the molecular mass. This equation is identical to a harmonic oscillator with its equilibrium position (represented by ϕ_0) offset from $\phi = 0$. Thus one expects non-synchronous molecules to oscillate around the synchronous molecule position inside an asymmetric oscillator potential. From numerical integration of Eq. 6.2 and the first time derivative of Eq. 6.1 one can solve for the stable and unstable regions of phase space, shown as a function of the synchronous molecule phase angle in Fig. 6.3 for OH under typical decelerator operation. The most important feature of Fig. 6.3 is the rapidly decreasing area of stable evolution (i.e. region bounded by the separatrix). This decrease in stable area is easily understood by analogy to a pendulum driven by a constant torque. As the torque is increased (*i.e.* the synchronous phase angle is increased) the equilibrium position of the pendulum is pushed toward the apex, which reduces the amplitude of oscillation that results in stable oscillatory motion. This behavior is responsible for the separatrix possessing only one cusp for non-zero ϕ_0. It is clear that the number of molecules accepted by a decelerator operating at a specific synchronous molecule phase angle is then given as an area integral inside the separatrix weighted by the supersonic beam distribution at the decelerator's entrance.

This phase space "bucket" loading is illustrated graphically in Fig. 6.4. In the

first panel of this figure, ToF data taken at the decelerator entrance (location (a) in Fig. 6.1) are shown along with a hypothetical ideal supersonic beam of OH molecules ($v_{z,center} = 300$ m/s, $\Delta v_z = 30$ m/s, where $v_{z,center}$ is the pulse mean speed and Δv_z is the full width at half maximum (FWHM) of the distribution). For this graph the supersonic molecular beam parameters were varied by tuning the discharge initiation time as described previously [80] resulting in the ability to input two vastly different molecular beams into the decelerator. The first distribution utilized has $v_{z,center} = 415$ m/s with Δv_z of $\sim$90 m/s, while the second distribution is centered about 350 m/s with a spread of $\sim$80 m/s. For these two experimental distributions and the idealized case, Monte Carlo simulation results are used to construct graphs of the longitudinal phase space occupied by the molecules in the remaining panels of the figure. Each gray point in these graphs represents the location in phase space of a sample molecule, as predicted by our simulations, at the time of loading into the decelerator. The two dashed curves on each graph are projections of the phase space distribution onto the respective axes. Overlaid on these graphs are the separatrix curves for operation at ϕ_0 = 0°, the so-called bunching condition, and for slowing the molecules to rest at the exit of the decelerator. From these graphs, the importance of creating a cold, *i.e.* small Δv, source of molecules as an input for a Stark decelerator is clear; with a smaller Δv the molecular pulse spreads less in route from generation at the source to the decelerator entrance, and thus is more efficiently coupled into the decelerator in both the spatial and velocity dimensions. The beneficial effect of lowering the pulse mean speed is also made evident; as the mean speed drops, the required phase angle for slowing is reduced and thus the separatrix area increases.

As aforementioned, the effects of supersonic beam and Stark decelerator parameters on overall efficiency can be estimated from knowledge of the separatrix overlap with the supersonic beam phase space. Approximating the area enclosed by the separatrix as that of the corresponding rectangle whose height (width) correspond to the separatrix
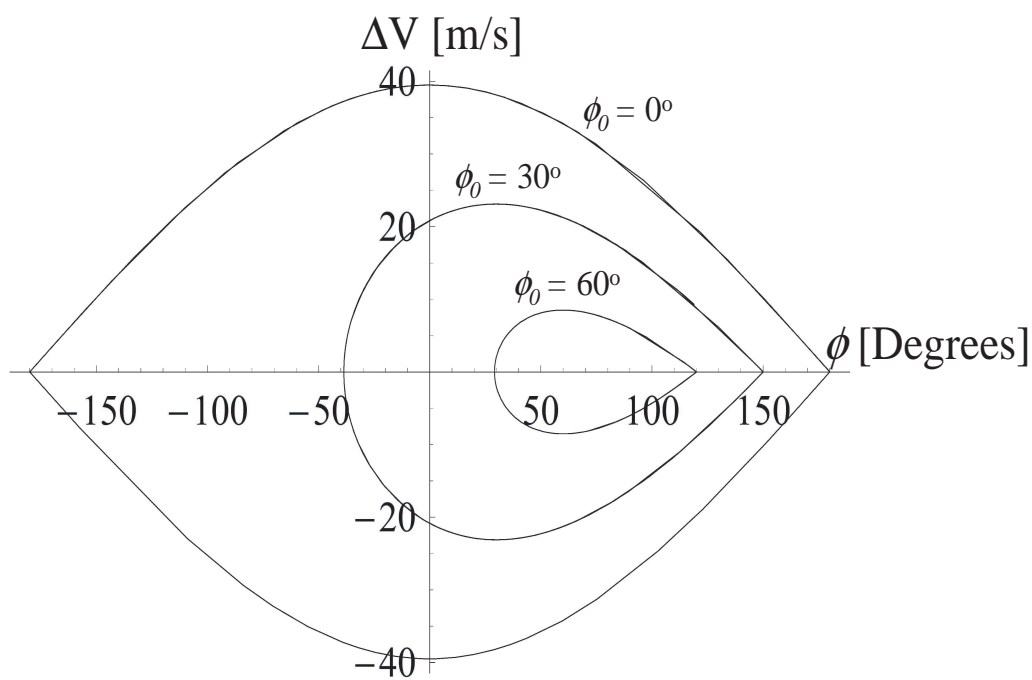
Figure 6.3: Phase stable area (separatrix area) versus phase angle for $\phi_0 = 0°$, $30°$, and $60°$. As the phase angle is increased, the stable area is reduced; equivalently, the stable longitudinal velocity width narrows, and assuming the source completely populates the phase stable region, decreases the number of molecules in the stable packet.
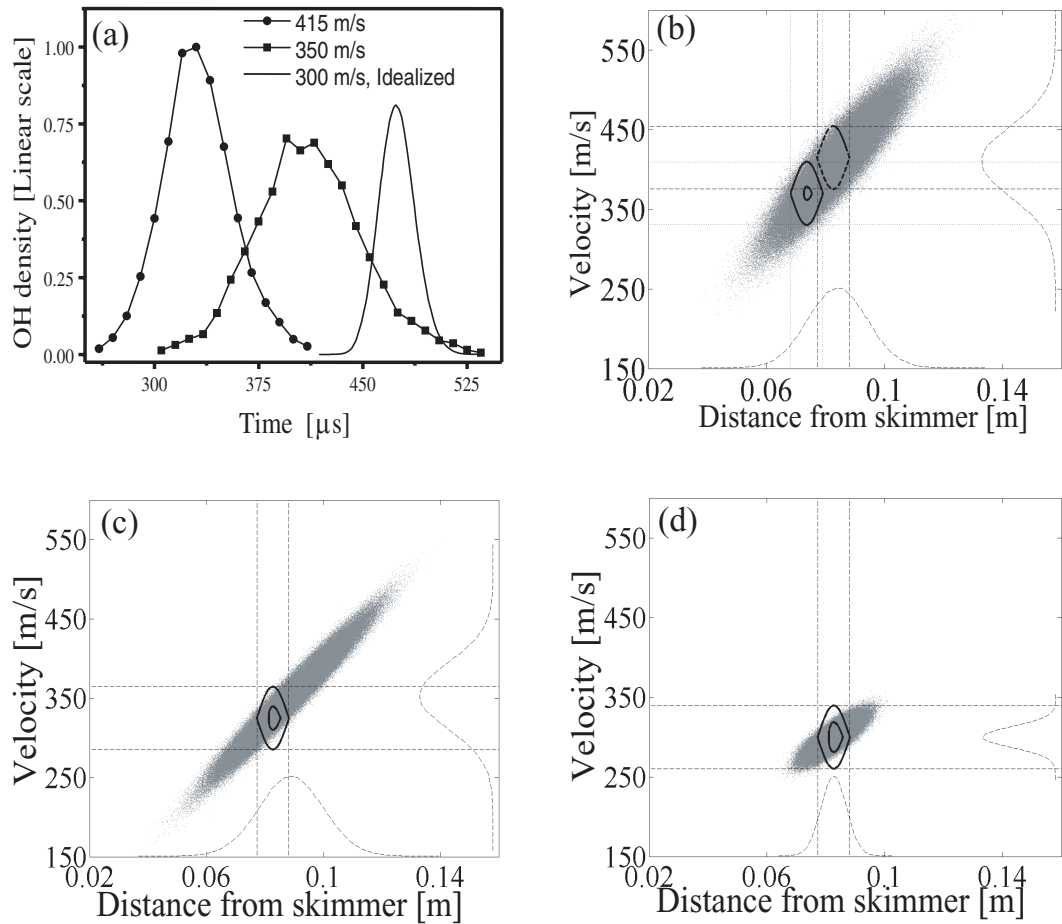
Figure 6.4: Longitudinal bucket loading. Panel (a) represents time-of-flight measurements taken at the decelerator input (location (a) in Fig. **??**) for different molecular beam operating conditions. Filled circles (filled squares) represent molecular beams with a mean speed of 415 m/s (350 m/s) and a full width at half maximum spread of 90 m/s (80 m/s). The solid line is an idealized molecular beam of 300 m/s mean speed with a 10% velocity spread. Panels (b), (c), and (d) represent the longitudinal phase space at the beginning of the Stark deceleration as derived from Monte Carlo simulations. In panel (b) the dashed separatrix represents bunching for 415 m/s, while the larger solid line is the separatrix for bunching at 370 m/s. The separatrix for slowing a packet of molecules to rest is shown inside the 370 m/s bunching separatrix. In panel (c) separatrix are shown for bunching at 325 m/s and slowing to rest molecules from the 350 m/s distribution, while panel (d) shows bunching at 300 m/s and slowing to rest for the hypothetical molecular beam.

velocity (spatial) bounds and ignoring the minimal convolution due to the short free flight of the molecules after creation, the overall longitudinal slower efficiency is given as:

$$\eta_{Longitudinal} = N[\nu_z, \Delta\nu_z, \nu_{z,Bounds}(\phi_0)] \times N[z, \Delta z, z_{Bounds}(\phi_0)], \qquad (6.3)$$

with

$$N(x, \Delta x, x_{Bounds}) = \frac{\int_{XLowerbound(\phi_0)}^{XUpperbound(\phi_0)} f(x, \Delta x)dx}{\int_{-\infty}^{\infty} f(x, \Delta x)dx}, \qquad (6.4)$$

where z refers to the dimension along the decelerator's axis (longitudinal axis) and $f(x, \Delta x)$ is the molecular distribution in the appropriate dimension. The integration bounds correspond to the separatrix maxima along their appropriate dimension and are an explicit function of the synchronous molecule phase angle. From Fig. 6.2(b) we see that for $\phi_0 = 45°$, non-synchronous molecules with phase angles between $45°$ and $135°$ will be slowed more than the synchronous molecule (shaded region). In general, the maximum stable forward excursion is then given as:

$$\Delta\phi_{Max,+}(\phi_0) = 180° - 2\phi_0 \qquad (6.5)$$

Unfortunately, a closed form solution for the maximum backwards excursion, $\Delta\phi_{Max,-}(\phi_0)$, does not exist, however, it can easily be found numerically or estimated by the negative of Eq. 6.5 since both the maximum stable forward and backward excursions have the same average derivative as a function of ϕ_0. From Eq. 6.2 we find the work done, W, in bringing a molecule starting at $\Delta\phi_{Max,+}(\phi_0)$ with the same speed as the synchronous molecule, *i.e.*at the separatrix cusp, back to the synchronous molecule position, *i.e.* $\Delta\phi = 0°$, is:

$$W = \frac{-C_{Max}}{\pi} \int_{\Delta\phi_{Max,+}(\phi_0)}^{0} (\sin(\Delta\phi + \phi_0) - \sin(\phi_0))d\Delta\phi \qquad (6.6)$$

Clearly, this molecule will possess the maximum stable velocity and we thus have the separatrix velocity bound as:

$$\Delta\nu_{Max}(\phi_0) = 2\sqrt{\frac{C_{Max}}{m\pi}(\cos(\phi_0) - (\frac{\pi}{2} - \phi_0)\sin(\phi_0))}. \tag{6.7}$$

Now, assuming the molecular distributions are adequately described by the form:

$$f(x, \Delta x) = exp\left[\left(\frac{x - x_{center}}{\frac{\Delta x}{2\sqrt{ln(2)}}}\right)^2\right] \tag{6.8}$$

where Δx refers to FWHM and x_{center} to the value at which the distribution is centered. Eq. 6.3 becomes:

$$\eta_{Longitudinal} = \frac{1}{4}[Erf\left(\frac{(v_{z,design} - v_{z,center}) + \Delta\nu_{z,Max}(\phi_0)}{\frac{\Delta\nu_z}{2}}\sqrt{ln(2)}\right) \tag{6.9}$$

$$-Erf\left(\frac{(v_{z,design} - v_{z,center}) - \Delta\nu_{z,Max}(\phi_0)}{\frac{\Delta\nu_z}{2}}\sqrt{ln(2)}\right)]$$

$$\times[Erf\left(\frac{(z_{design} - z_{center}) + \frac{L}{\pi}\Delta\phi_{Max,+}(\phi_0)}{\frac{\Delta z}{2}}\sqrt{ln(2)}\right)$$

$$-Erf\left(\frac{(z_{design} - z_{center}) - \frac{L}{\pi}\Delta\phi_{Max,+}(\phi_0)}{\frac{\Delta z}{2}}\sqrt{ln(2)}\right)]$$

Where $Erf(x)$ refers to the Error function, and $v_{z,design}$ and z_{design} have been introduced to account for the possibility of designing the decelerator pulse sequence to select molecules which are not at the peak of the molecular distribution. If molecules are loaded at the peak of the distribution, *i.e.* $v_{z,design} = v_{z,center}$ and $z_{design} = z_{center}$, and we approximate $\Delta\phi_{Max,-}(\phi_0) = -\Delta\phi_{Max,+}(\phi_0)$, we find the simple result:

$$\eta_{Longitudninal} = Erf\left(\frac{\Delta\nu_{z,Max}(\phi_0)}{\frac{\Delta\nu_s}{2}}\sqrt{ln(2)}\right) \times Erf\left(\frac{L(1 - \frac{\phi_0}{\pi/2})}{\frac{\Delta x}{2}}\sqrt{ln(2)}\right), \tag{6.10}$$

which is useful for estimating expected decelerator efficiency. Plots of Eq. 6.10 with loading at the peaks of the distributions are shown in Fig. 6.5 versus both Δv_z (Fig.

6.5(a)) and $v_{z,center}$ (Fig. 6.5(b)), where the value of $\Delta\phi_{Max,-}(\phi_0)$ has been found numerically. In these graphs the slowing phase angle was chosen to bring the molecules to rest at the decelerator's exit. Again the importance of a low central velocity and small spread about this mean is evident. The most striking feature of these graphs is the flattening of the longitudinal slower efficiency for small velocity spreads. In fact for a sufficiently narrow velocity spread the mean speed of the pulse becomes to some degree "unimportant" as the supersonic beam emittance fits entirely inside the decelerator acceptance for most operating conditions. It is important to note that similar effects can be achieved by changing the characteristics of the Stark decelerator. By increasing the stage-to-stage spacing one enlarges the spatial bounds of the separatrix resulting in more decelerated molecules; however, increasing the distance without increasing the applied electric field will result in less efficient transverse guiding and a smaller stable phase space area transverse to the molecular beam axis. In contrast, increasing the applied electric field enables deceleration of molecules with larger velocity spreads relative to the synchronous molecule speed, and thus increases the overall slower efficiency. However, the technical challenges associated with going to voltages higher than the present operating conditions are significant. Therefore a more practical alternative maybe to increase the number of slowing stages to reduce the required phase angle.

Efficient operation of a given decelerator/supersonic beam combination occurs when Eq. 6.10 is maximized at the desired final speed. Since the molecular distribution and the desired final speed are assumed fixed the only parameter which can be varied is $v_{z,design}$, the initial speed for which the decelerator pulse sequence is designed. By decreasing $v_{z,design}$ the required slowing phase angle is decreased and the separatrix area increased. However, if $v_{z,design}$ is lowered too far below $v_{z,center}$ the molecular beam phase space overlaps poorly with the decelerator input separatrix and slower efficiency suffers. Thus, the most efficient slower operation will occur for a $v_{z,design}$ below $v_{z,center}$ by an amount that depends on the Δv_z of the pulse and the desired final speed (typically
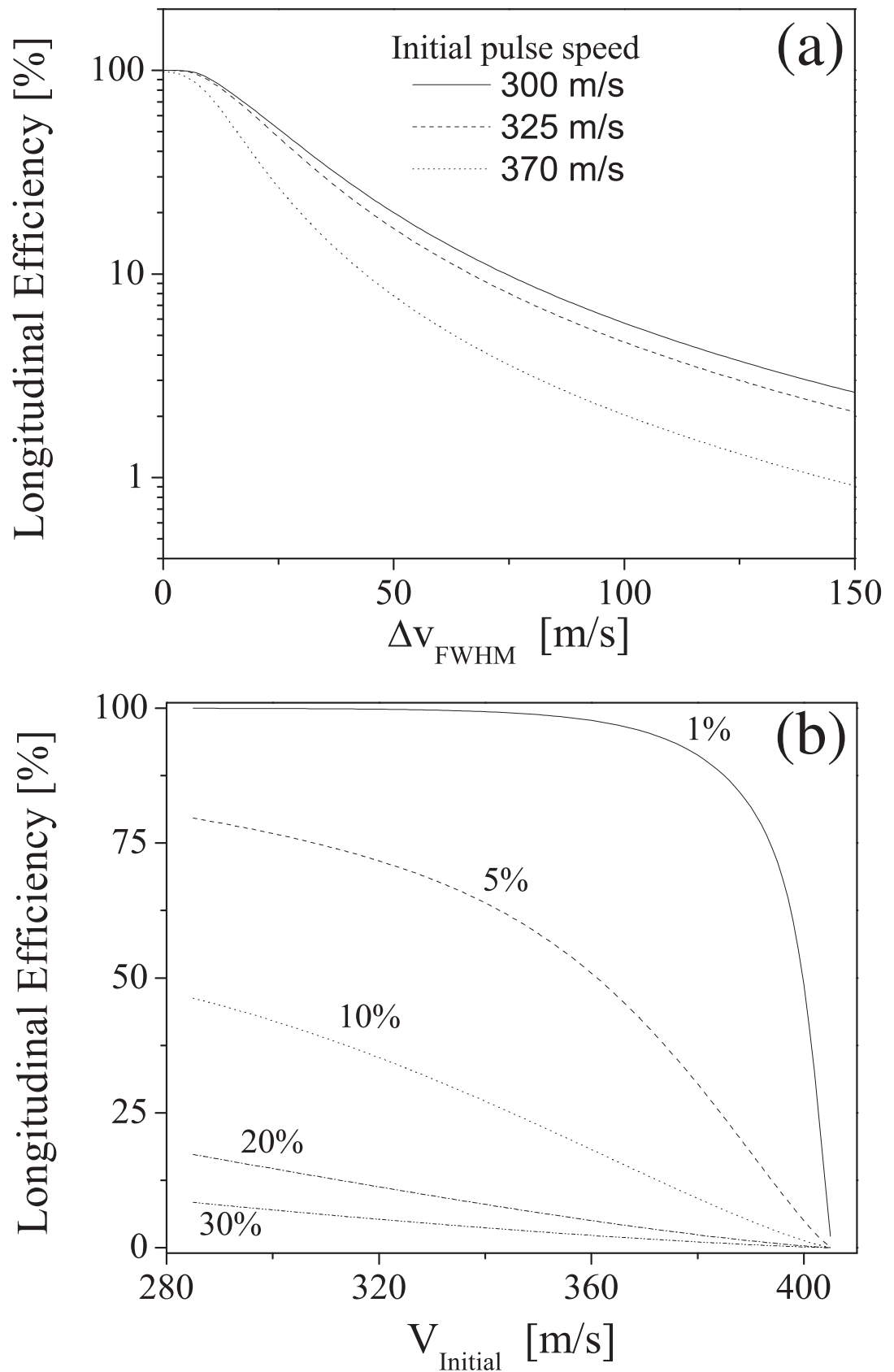
Figure 6.5: Simple model for longitudinal bucket loading. Panel (a) shows the effect of varying the supersonic beam's velocity spread on longitudinal efficiency for several initial speeds, while panel (b) shows the longitudinal efficiency as a function of initial pulse speed for several velocity spreads, where the spread is expressed as a fraction of the mean speed.

1 to 10 percent of $v_{z,center}$ for slowing to rest). Fig. 6.6 shows the result of maximizing Eq. 6.10 for the given experimental distributions as well as the idealized source. In this graph the amount of velocity detuning from $v_{z,center}$ for most efficient operation is shown as a function of desired final speed. For final packet speeds close to the initial pulse speed (right part of graph) it is most efficient to utilize a phase angle of zero (bunching) because of its large acceptance and vary $v_{z,design}$. However, as the final velocity is decreased, this procedure eventually leads to a mismatch between the supersonic beam emittance and the decelerator acceptance, and it becomes more efficient to decelerate molecules nearer the center of the supersonic beam distribution, leading to the sharp "transition" peaks. The position of this transition for our decelerator is at a detuning equal to approximately 15% of the pulse spread and is evident in the figure by the sudden drop in velocity detuning. As slower molecules are desired, the effect of the decreasing acceptance of the decelerator (with increasing ϕ_0) is combated by selecting slower initial molecules, which require less slowing. This effect is evident by the increase of detuning with slower final speeds. The gain in efficiency by optimizing decelerator operation according to Eq. 6.10 depends sensitively on both the molecular beam and decelerator parameters, but in the case of our experimental conditions ranges from only a few percent to well over a factor of 100 improvement[1] .

While Eq. 6.10 describes the efficiency of decelerator operation in the longitudinal dimension, it says nothing about evolution transverse to the decelerator axis. In this dimension the molecular distribution is centered about zero in both space and velocity thus Eq. 6.3 becomes:

$$\eta_{Transverse} = N[0, \Delta\nu_x, \nu_{x,Bounds}(\phi_0)]N[0, \Delta x, x_{Bounds}(\phi_0)]$$

---

[1] Since 415 m/s molecules cannot be slowed to rest in our decelerator, detuning the pulse design speed to decelerate molecules with 405 m/s (the maximum speed which can be brought to rest in our machine) or less initial speed would, by definition, be an infinite gain in efficiency. Thus the usefulness of this technique for hot sources is evident.

$$\times N[0, \Delta\nu_y, \nu_{y,Bounds}(\phi_0)]N[0, \Delta y, y_{Bounds}(\phi_0)], \qquad (6.11)$$

where x and y refer to the dimensions perpendicular to the decelerator axis. Assuming distributions given by Eq. 6.10 we have:

$$\eta_{Transverse} = Erf\left(\frac{\Delta\nu_{x,Max}(\phi_0)}{\frac{\Delta\nu_x}{2}}\sqrt{ln(2)}\right) Erf\left(\frac{\Delta x(\phi_0)}{\times}\frac{\Delta x}{2}\sqrt{ln(2)}\right)$$
$$Erf\left(\frac{\Delta\nu_{y,Max}(\phi_0)}{\frac{\Delta\nu_y}{2}}\sqrt{ln(2)}\right) Erf\left(\frac{\Delta y(\phi_0)}{\frac{\Delta y}{2}}\sqrt{ln(2)}\right). \qquad (6.12)$$

The spatial acceptance of the decelerator is set by the decelerator rod spacing, thus Δx and $\Delta y \sim 1$ mm. Because the transverse evolution of molecules through the Stark decelerator is a complicated dynamical process that depends sensitively on the operating conditions it is not possible to give a simple expression for $\Delta v_{x,Max(\phi_0)}$ and $\Delta v_{y,Max(\phi_0)}$. However, for most deceleration experiments to date, it can be estimated as ~ 3 m/s with minimal error [28, 37]. The behavior of Eq. 6.12 is analogous to that of Eq. 6.10. As the velocity (spatial) spread of the source is lowered or the maximum stable velocity (position) is increased by a decelerator change, the efficiency of the slower grows. It is the aim of proper hexapole focusing to "mode-match" the supersonic beam into this transverse decelerator acceptance .

6.3   Experiment

Time of flight measurements of OH molecules taken at the exit of the decelerator (location (b) in Fig. 6.1) are shown in Fig. 6.7 for various decelerator operating conditions. Open circles represent operation in transverse guidance mode, where the decelerator array is biased at high DC voltage, resulting in a potential minimum along the decelerator axis. This mode of operation does not affect the molecules' longitudinal speed, but provides transverse guidance through the length of the decelerator. The remaining traces show the stable packet of molecules produced when switching the decelerator with non-zero phase angle. As the slowing angle is increased the packets arrive
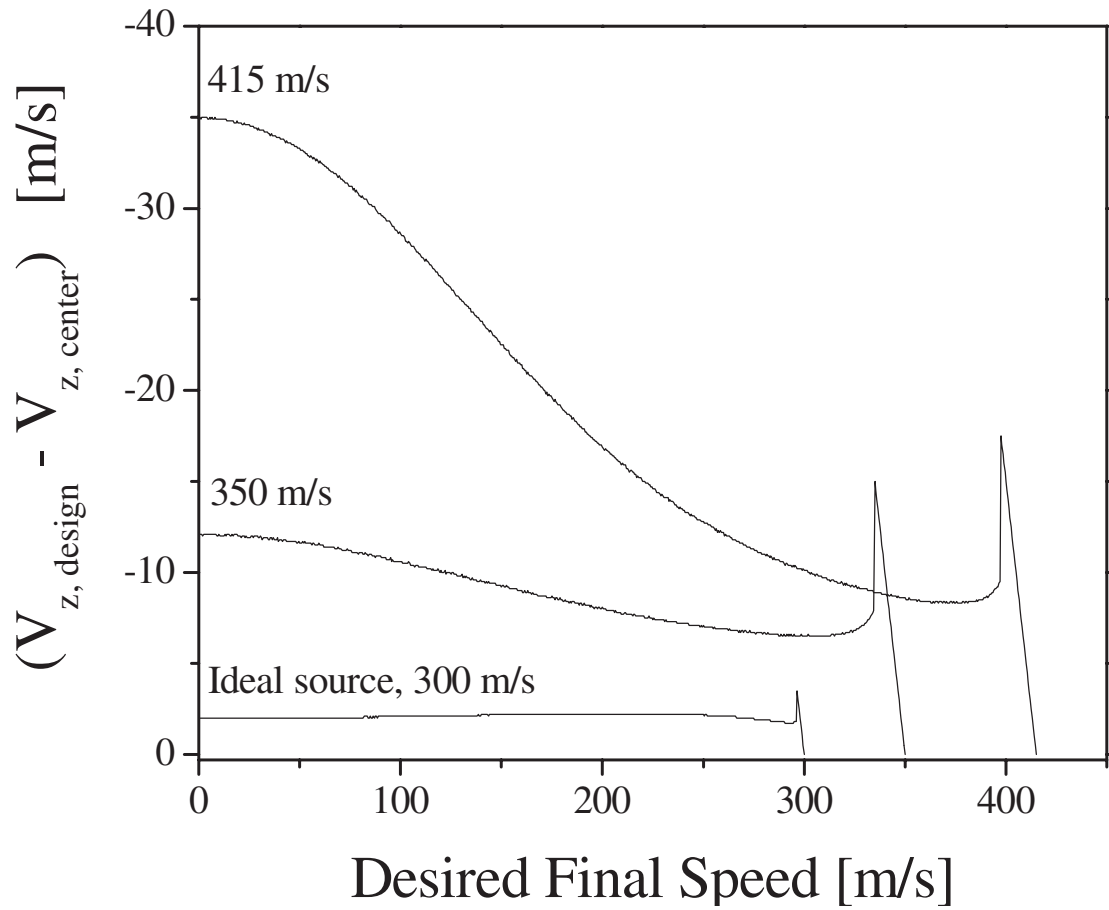
Figure 6.6: Decelerator optimization condition. The optimum detuning of the design speed from the pulse's mean speed as a function of desired final speed shown for three different supersonic beam distributions.
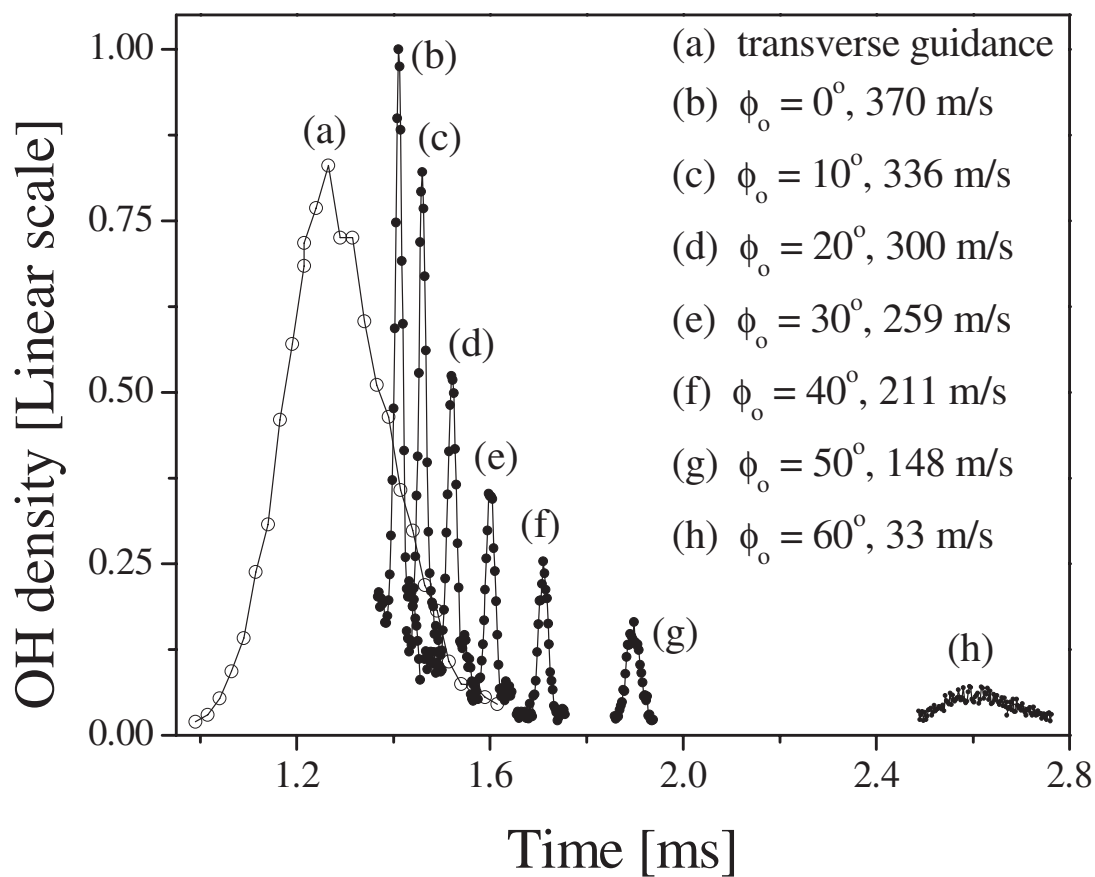
Figure 6.7: Molecular packets at the decelerator exit (location (b) in Fig. 6.1) for varying phase angles. Peaks arriving later in time are the result of slowed molecules. From comparison of the number of molecules in these packets to the total inputted molecular number, decelerator efficiency can be determined. Solid lines are to guide the eye.

later in time signifying a smaller mean speed. The spreading of the ToF pulse due to free flight and convolution with the detection window is also evident. Integration of the deconvolved ToF pulse reveals the total molecular number in each phase stable packet, and is shown in Fig. 6.8, where the data points have been normalized to the bunching condition. In this graph the total molecular number is plotted versus the final speed of the molecular bunch for the three different operating conditions represented in Fig. 6.4. The filled circles represent data taken for slowing sequences designed for an initial speed of 415 m/s. For this data the supersonic beam was operated to yield a distribution centered at 415 m/s with a 90 m/s FWHM. The filled squares in Fig. 6.8 represent loading molecules from the same distribution into a phase bucket designed for 370 m/s initial speed. For the data represented by the filled triangles, the supersonic beam was operated to yield a pulse centered at 350 m/s with an 80 m/s spread. In this data, the decelerator was operated for a 325 m/s initial speed. The solid lines in this graph represent the simple theory of Section 2, while the open points correspond to the results of our Monte Carlo simulations. Despite the assumptions made in deriving Eq. 6.10 we see the theory of Section 6.2is quite accurate. The only noticeable discrepancy occurs for the 415 m/s curve, where it appears that deviation in the experimental bunching point (which is used to normalize the graph) is responsible for the offset. From this graph we see that operation at 325 m/s is clearly more efficient at producing slow molecules. Again, the importance of developing a slow cold source as the input for efficient Stark deceleration is clear.

By comparing the total molecule number observed in each packet to the total number of molecules input into the decelerator (Fig. 6.4(a)) the overall efficiency of the Stark decelerator can be determined and is shown in Fig. 6.9 for the 370 m/s case as filled squares. Overlaid on this graph is the model of Section 2. For this theory the transverse parameters Δx and $\Delta y = 1.5$ mm and Δv_x and $\Delta v_y = 12$ m/s were used in Eq. 6.12 [?]. It is remarkable to note that this simple theory predicts the overall slowing
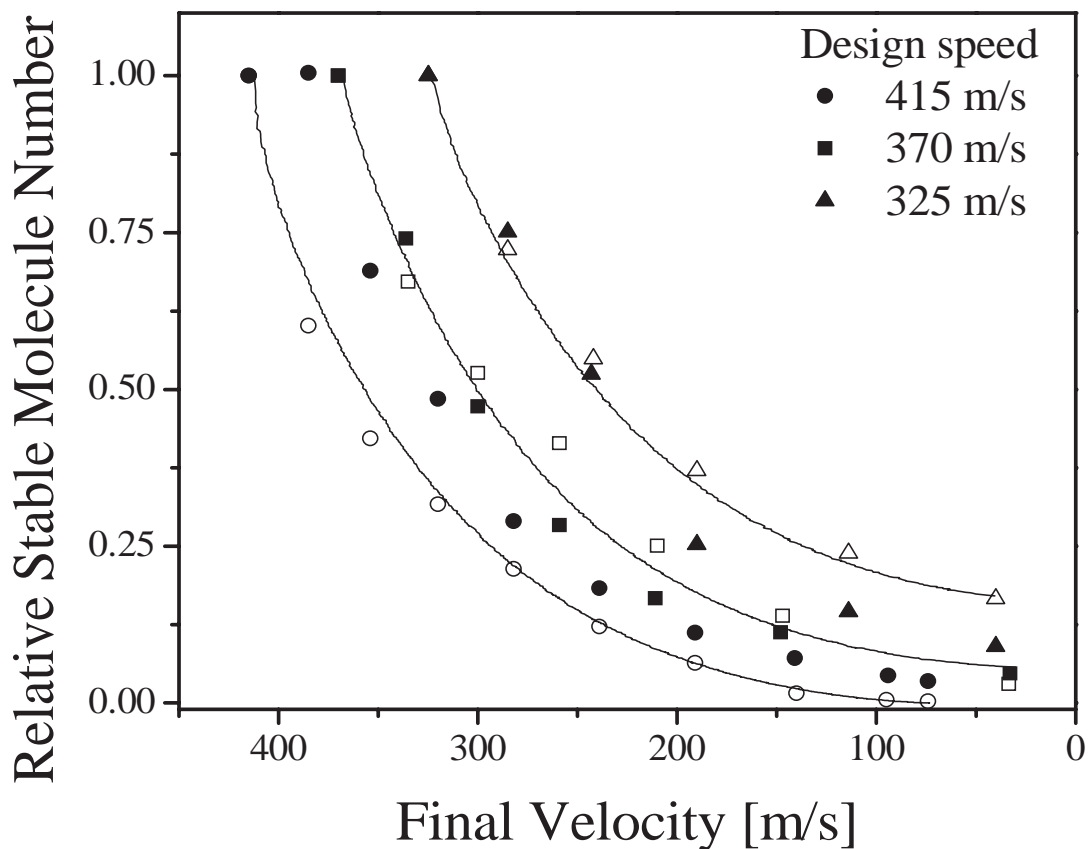
Figure 6.8: The stable molecule number normalized to $\phi_0 = 0°$ for three cases of operation. Circles represent operation with a supersonic beam centered at 415 m/s with a 90 m/s FWHM and a deceleration sequence designed for molecules at 415 m/s. Squares represent a deceleration sequence designed for 370 m/s molecules from the same beam distribution. Triangles are for deceleration designed for 325 m/s molecules from a distribution centered at 350 m/s with an 80 m/s spread. Filled points represent data, while open points represent results from the Monte Carlo simulation. The solid lines are the results of the model of Section 6.2. Typical molecule numbers per stable packet range from 10^4-10^6, depending on the ϕ_0.

efficiency quite accurately with no free parameters. Clearly, this level of agreement with our model gives confidence in using it as an optimization tool.

6.4   Conclusions

We have developed a model of the process of phase space matching between a supersonic molecular beam emittance and a Stark decelerator acceptance. The ability of this model to predict with accuracy the efficiency of the Stark deceleration process gives confidence in its use as an optimization tool. While optimization according to this model gives small gain for supersonic sources with low mean kinetic energy and small velocity spreads, it can lead to dramatic improvement for molecular beams that have either a high kinetic energy, a large velocity spread, or both. As the technique of Stark deceleration is extended to more exotic molecular species, which, because of their large mass, internal modes or process of creation result in non-ideal supersonic beams for input into a Stark decelerator, maximization of the decelerator operation efficiency will be essential.

Clearly, it is the aim of the experimenter to maximize the product of Eqs. 6.10 and 6.12 for the most efficient decelerator operation. The efficiency of the decelerator depends sensitively on both the supersonic beam and Stark decelerator parameters. The importance of developing a cold source as the input for any Stark deceleration experiment cannot be overstated since this is the only real cooling in the slowing experiment and, for a given decelerator, sets the attainable efficiency. While increasing the dimensions of slowing stages and their separations to allow deceleration of more molecules is a viable way to increase the deceleration efficiency, it is met with increasing technical challenge as the electrode voltage must also be scaled. Perhaps a more reasonable alternative is to increase the number of slowing stages, thus dropping the amount of energy removed at each stage, resulting in a larger phase space acceptance. A reasonable design goal is to include enough stages in the decelerator so that molecules can be decelerated
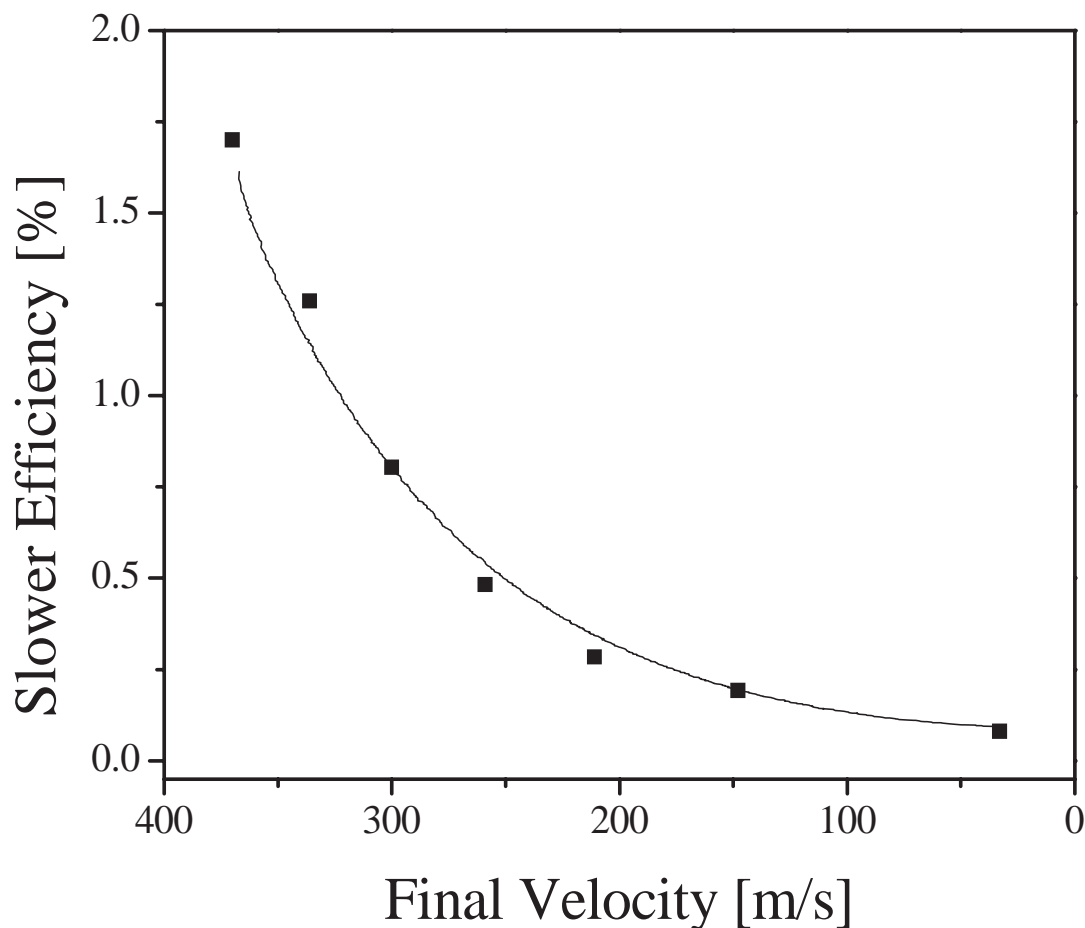
Figure 6.9: Stark deceleration efficiency. Efficiency of the Stark decelerator as a function of final speed for slowing designed for an initial speed of 370 m/s taken from the distribution centered at 415 m/s with a 90 m/s FWHM. Filled squares are data points obtained from the results of Fig. 6.8 normalized by the results of trace (a) in Fig. 6.4. The solid line is the model of Section 6.2 including both longitudinal and transverse efficiencies.

to the desired final speed with a phase angle of $\phi_0 \leq 45°$. Also, positioning the source as close as possible to the input of the decelerator provides efficient spatial coupling in the longitudinal dimension. Finally, for a given molecular beam/decelerator combination the optimum phase angle and initial pulse design speed, $v_{z,center}$, for slowing can be found from Eq. 6.10.

Chapter 7

Alternative Deceleration Techniques

In the work of previous chapters it was assumed that all motion in transverse dimensions was stable up to some maximum excursion velocity from the beam center. While this is certainly a reasonable approximation for most cases, there are several important instances where this assumption does breakdown. One of these cases is transverse over-focussing, detailed in Chap. 6, which occurs when the decelerated molecules' speed becomes so low that the decelerating electrodes focuses the molecules too tightly (transversely) and they crash into the next deceleration stage. Furthermore, transverse over-focussing appears to have a larger effect in long decelerators, where the molecules may travel at low speeds for many stages. Nonetheless, there are several motivating factors for constructing a longer decelerator. First, a longer decelerator allows less energy per stage to be removed and consequently a large longitudinal phase space acceptance. Second, a longer decelerator may allow molecules to be decelerated with an unfavorable Stark shift to mass ratio, *i.e.* molecules that have a small effective dipole moments or are heavy. Thus, it is important for future deceleration experiments that phenomenon of over-focussing (and other transverse effects) be addressed.

The fact that the transverse guidance of the molecular beam arises from the same electrodes that provide the deceleration means that the longitudinal and transverse motions are necessarily coupled. While this phenomenon is well understood in the field of accelerator physics [139], it was first pointed out in the context of Stark deceleration

in an excellent paper from the Berlin group [126]. The basic effect can be seen in the left column of Fig. 7.1, where the longitudinal phase space of a bunched OH packet in the $|2 \pm 2+\rangle$ state is shown for increasing number of deceleration stages. In these graphs the dark lines represent the separatrix, separating stable deceleration from unstable motion, as calculated from Eq. 6.2 and each dot represents the position in phase space of a simulated molecule. In the absence of coupling between the longitudinal and transverse motions, one would expect the entire area inside the separatrix to be occupied. Therefore, the structure evident in these graphs is evidence of the importance of the transverse motion.

In the left column of Fig. 7.1 the coupling of longitudinal and transverse motions is responsible for two effects[1] . First, in the center of the stable area, *i.e.* near the synchronous molecule, the density of stable molecules is less than the surrounding area. This is because molecules that spend time near the synchronous-bunched molecule experience very little of the transverse guiding forces. Clearly, this effect is by no means dramatic and is only discernable for an exceedingly large number of stages. Furthermore, this effect is even less important for phase angles typically used for deceleration, since for these switching sequences the synchronous molecule experiences more of the the transverse guiding forces than it does during bunching. Nonetheless, it can still be of moderate importance since the peak of the molecular beam is often matched to this region. The second effect, which is much more evident, is the absence of molecules at intermediate distances from the synchronous molecule as shown in the left column of Fig 7.1. This so-called 'halo' is due to parametric amplification of the transverse motion and is similar to the effects seen in cold molecule storage rings [37]. Essentially, the longitudinal oscillation frequency of a molecule in this region is matched to the transverse oscillation frequency, leading to amplification of the transverse motion, and

---

[1] It should be noted that for these phase space simulations the input molecular beam had a flat longitudinal position and velocity distribution, which helps to exaggerate the effects.

consequently, loss.

Clearly, the effects of the coupling between longitudinal and transverse motion are detrimental to efficient operation of a Stark decelerator. Furthermore, these effects, which reduce the total number of decelerated molecules, will be even more damaging for decelerating many of the interesting molecules with an unfavorable Stark shift to mass ratio. Fortunately, the transverse and longitudinal motions can essentially be decoupled by introducing a transverse focusing element to the deceleration beam line that overwhelms the transverse focusing provided by the deceleration electrodes. This technique also has the advantage of a larger stable region in the transverse phase space further enhancing the decelerated molecule number. The remainder of this chapter deals with methods of implementing a transverse focusing element to decouple the longitudinal and transverse motion. The first two subsections describe methods, which can be implemented with current decelerators with moderate success, while the last subsection present an improved design for a Stark decelerator that solves the problem of longitudinal and transverse coupling.

7.1   Decelerator Overtones

The simplest method of introducing a transverse focusing element to the decelerator beam line is to let the molecules fly through an energized deceleration stage without removing the field. In this way, molecules experience the transverse focusing of the entire stage without having their longitudinal motion affected. Because traditional longitudinal phase stability requires the switching of the fields to occur on an upward slope of the molecular potential energy, $i.e$ faster molecules are slowed more while slower molecules are slowed less than the synchronous molecule, it is necessary to de-sample the bunching switching rate by an odd factor (3,5,7...) – so called decelerator overtones [125]. For convenience we define the quantity, S, (like in Ref. [125]) given as $S = v_o/v_{Switch}$, where v_o is the synchronous molecule velocity and the switching speed,
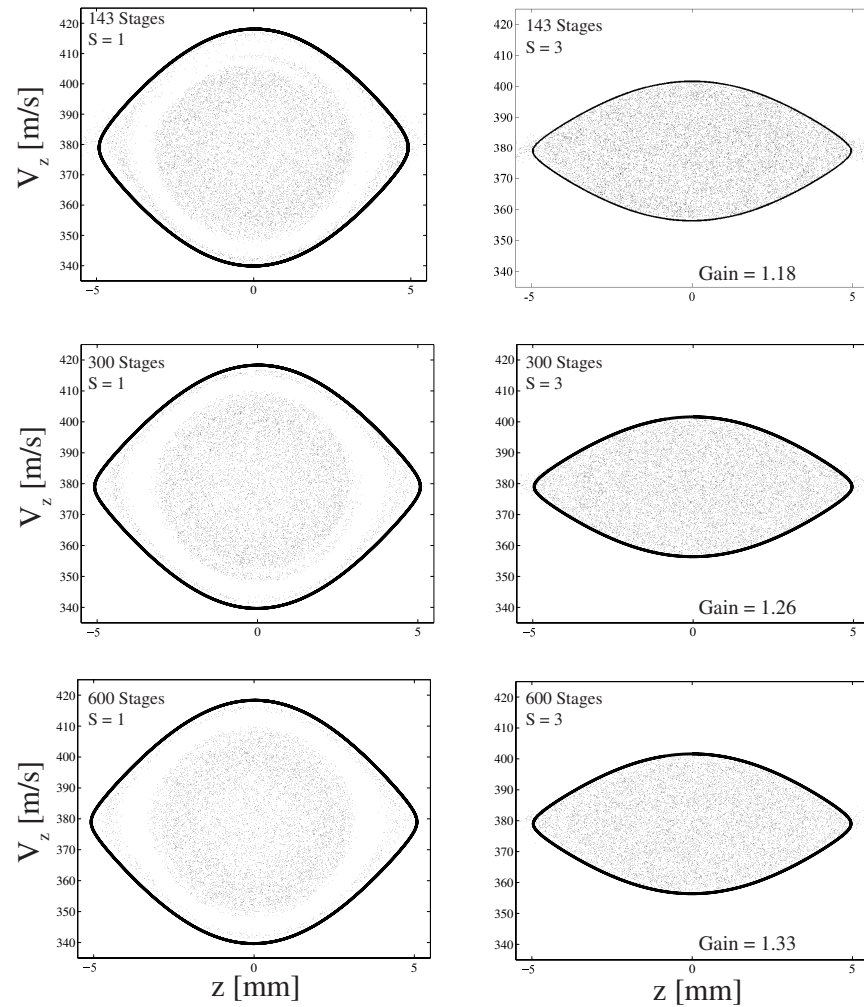
Figure 7.1: Monte Carlo results for the Longitudinal phase space of bunched molecules. The left column shows $\phi_o = 0°$ for S = 1 at several decelerator lengths, while the right column shows $\phi_o = 0°$ for S = 3 for the same decelerator lengths. In the bottom left of each S = 3 figure is the value for the molecule gain S = 3 produces over S = 1.

v_{Switch}, is given as the stage spacing, L, divided by the switching time-interval. Though, here we expand the bunching case, that was considered in Ref. [125], to include actual deceleration, the above definition of S is still valid. That is, neither v_o nor v_{Switch} is a constant for $\phi_o > 0°$ but, S is. With this definition we see that traditional deceleration can be described by $S = 1$, while the method of de-sampling the switch rate by a factor 3 is described by $S = 3$. These two methods of deceleration can be seen in Figs. 7.2 (b) and (c), where their respective switching schemes are shown for $\phi_o = 0°$. In this figure, it is seen that by switching at $1/3^{rd}$ the rate the molecule packet flies through a deceleration stage that is energized, and thus, sees the enhanced transverse guiding.

Longitudinal phase space simulations of bunching for $S = 3$ are shown in the right column of Fig. 7.1. In these graphs we see that no structure due to couplings between the longitudinal and transverse motions is present. Also evident in these simulations is that the region of longitudinal phase stability for $S = 3$ is reduced compared to $S = 1$. This is because the maximum stable velocity as calculated from Eqs. 6.2 and 6.6 depends on the spacing between deceleration stages as $L^{-1/2}$ and thus the separatrix velocity bound is reduced[2] by $\sqrt{3}$. Nonetheless, the absence of coupling to the transverse motion leads to a larger number of molecules for the $\phi_o = 0°$ case shown.

Fig. 7.3 shows time-of-flight (ToF) data (offset) taken in our second generation decelerator for $S = 3$ with increasing phase angle along with the results of 3D Monte Carlo simulations. Qualitatively, the ToF signal is no different than for $S = 1$. A decelerated packet is evidenced by a peak in the ToF data that moves later in time with a reduced amplitude that is governed by the longitudinal phase stability. Shown in Fig. 7.4(a) are the decelerated molecular packets for $S = 3$ and $S = 1$ with increasing phase angle. For each successive packet the $S = 3$ phase angle increases by $10°$ from $\phi_o = 0°$, while the $S = 1$ phase angle increases by $10/3°$ from $\phi_o = 0°$. In this way the packets

---

[2] Physically, this is because the molecules fly longer between deceleration stages, and thus, the velocity mismatch can lead to a larger accumulation of spatial mismatch
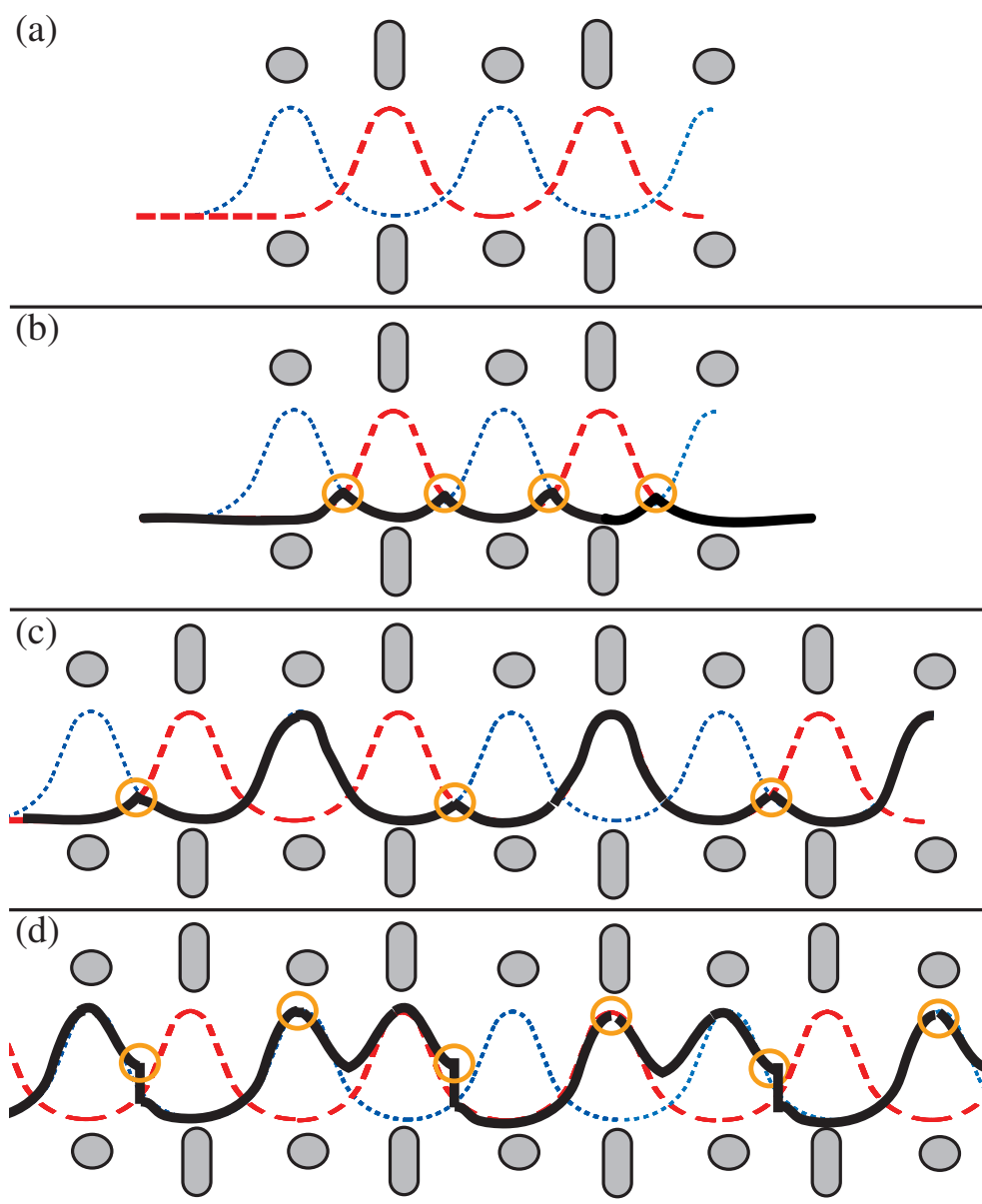
Figure 7.2: Deceleration Schemes. (a) Potential energy shift of polar molecules in the Stark decelerator. The dotted (blue) curves show the potential energy shift when the horizontal electrodes are energized, while the dashed (red) curves show the potential energy shift when the vertical electrodes are energized. Deceleration proceeds by switching between which electrodes are energized, and thus the corresponding potential energy curve. In panels (a)-(c) the thick black line indicates which of the potentials is experienced by the molecules. The (orange) circles indicates a switching event. (b) Traditional (S = 1) operation at $\phi_o = 0°$. For phase stability the switching always occurs when the molecules are on an upward slope, and as such the molecules are never directly between an energized electrode. Thus, the maximum transverse guiding is never realized. (c) First overtone operation (S = 3) at $\phi_o = 0°$. By switching at 1/3 the S = 1 rate, the molecules are allowed to fly directly between an energized stage, and thus, experience enhanced transverse guiding. (d) Optimized first overtone operation (S = 3^+) at $\phi_o = 0°$. Operation proceeds identically to S = 3, except that the grounded set of electrodes is energized when the molecules are directly between the already energized electrodes. In this way the molecules experience one more stage of maximum transverse guiding for each slowing stage. Note that the grounded-set of electrodes is switched on when the molecules are directly between the energized electrodes to minimize the un-bunching effect.

are decelerated to roughly the same velocity – there is a slight difference because the total number of stages in our decelerator is not an exact multiple of 3. In Fig. 7.4 the de-convolved total molecule number for each of these packets is plotted versus final speed. Here we see that while the $S = 3$ method dominates over $S = 1$ for small phase angles [3] it quickly falls off as the deceleration becomes more aggressive – in fact by 224 m/s the $S = 1$ molecule number is already larger than the $S = 3$. This behavior is expected since the phase angle used to decelerate to 224 m/s is $60°$, while the required $S = 1$ phase angle is only $20°$. That is, though the $S = 3$ longitudinal phase bucket does not exhibit any structure due to coupling to the transverse motion, it is so much smaller in enclosed area than the $S = 1$ that its total molecule number is less.

Since this decrease in the $S = 3$ molecule number is purely due to the longitudinal phase space, it might be expected that building a longer decelerator, which will allow operation at a lower phase angle, would allow one to enjoy the gain in molecule number produced by $S = 3$. Simulations of this kind are shown in Fig. 7.5, where the number of molecules present after deceleration at $\phi_o = 20°$ for an increasing number of stages is shown[4] . In this graph, the number next to a data point represents the number of deceleration stages used. Initially the decelerated molecule number is relatively flat with final velocity. However, after about 400 stages (224 m/s) the number of decelerated molecules begins to decreases and dramatically falls off after 550 stages (150 m/s) with very few molecules surviving below 100 m/s. This is because for $S = 3$ the decelerated molecules must fly through an entire stage without seeing any guiding force (see Fig. 7.2(c)), and once the molecules are at slower speeds they can spread out transversely or be over-focused and crash into the rods before being transversely guided again.

The transverse loss responsible for the extreme loss in molecule number for $S = 3$

---

[3] The factor of $\sim$3 gain seen in the data is not reproduced in the 3D Monte Carlo simulations, which predict a gain of roughly 1.5. The unexpected gain may be evidence of Majorana-like transitions in the decelerator since S = 3 involves less switching of the fields.

[4] In these simulations $\phi_o = 20°$ was chosen because it produced the most gain over $S = 1$ in our deceleration experiments.
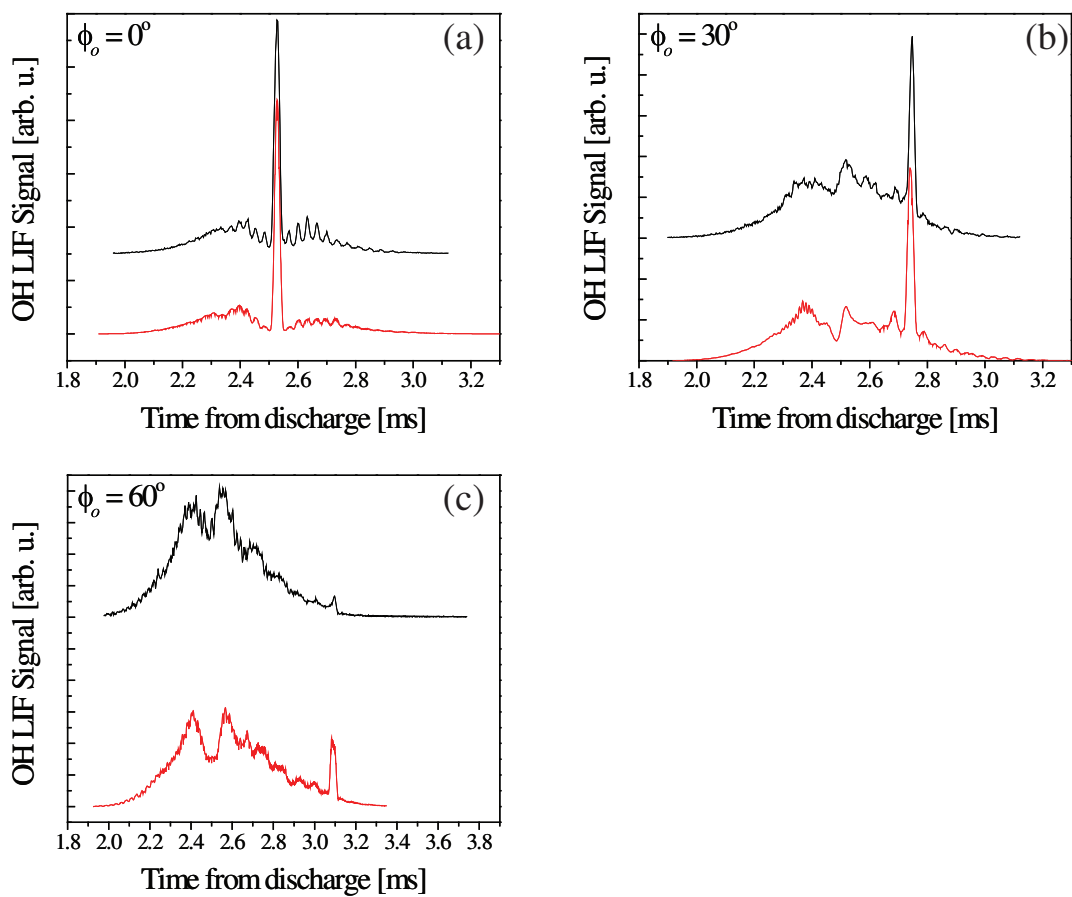
Figure 7.3: ToF data (offset) of OH molecules decelerated using S = 3. The results of 3D Monte Carlo simulations are also shown (red).
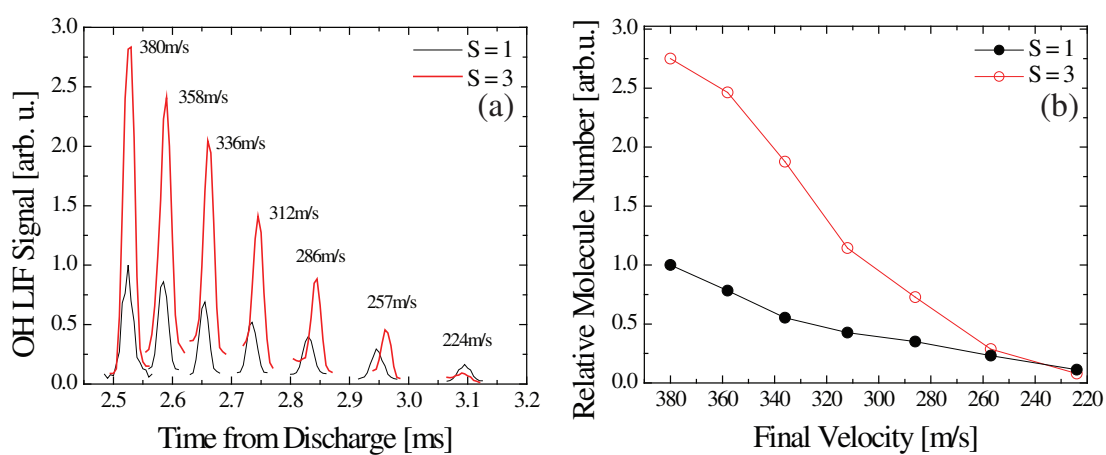
Figure 7.4: Comparison of deceleration using $S = 3$ and $S = 1$. (a) Decelerated OH packets. (b) De-convolved, integrated molecule number in the packets shown in panel (a).
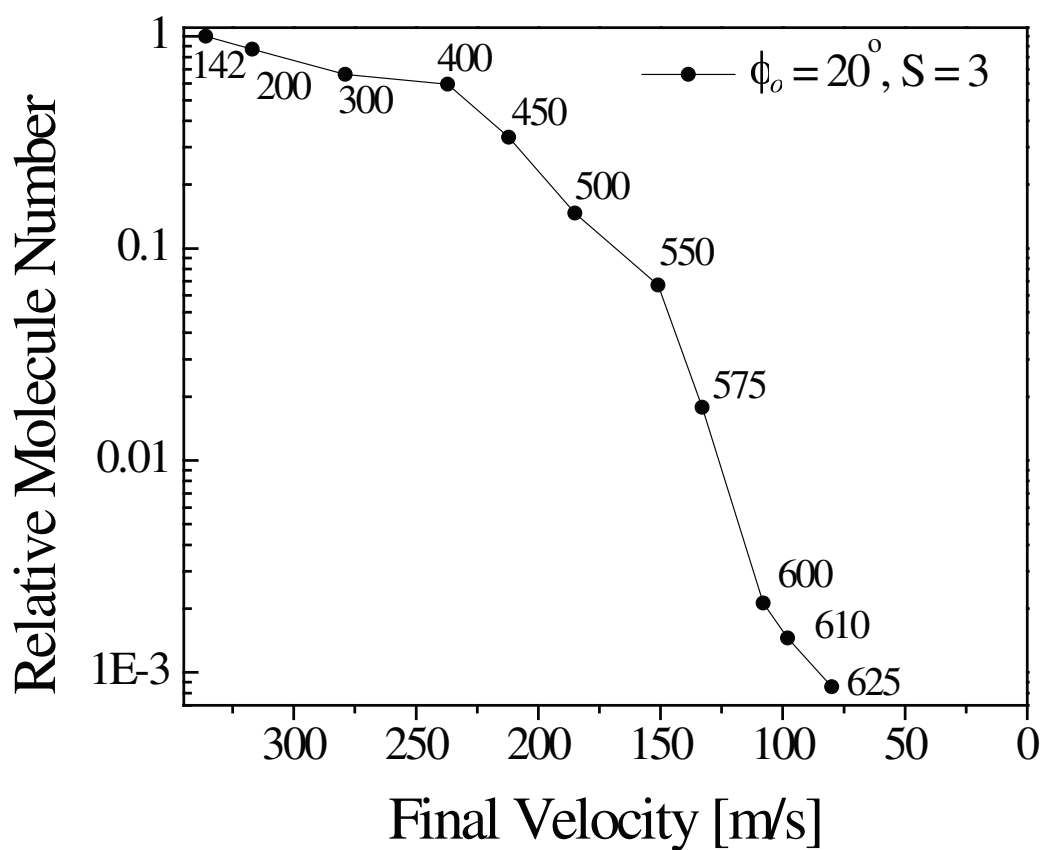
Figure 7.5: Decelerated molecule number using $S = 3$ and $\phi_o = 20°$ for increasing decelerator stage number. The number next to each data point is the number of stages used. Because of transverse over-focussing essentially no molecules survive below 100 m/s.

deceleration occurs to a lesser degree in traditional deceleration, as detailed in Chap. 5. Because of this dramatic decrease in molecule number at low speeds, the usefulness of slowing on $S = 3$ is likely limited to experiments that do not require the lowest velocities, such as microwave spectroscopy and collision experiments. Nonetheless, by using a combination of deceleration/bunching at $S = 3$ and $S = 1$ it may be possible to extend some of the gain of $S = 3$ to lower speeds.

7.2   Modified Decelerator Overtones

One possibility for extending the gain of overtone deceleration to lower speeds is the use of what we have termed a 'modified decelerator overtone', denoted by an additional plus sign, *i.e.* $S = 3+$. Deceleration in this manner is shown in Fig. 7.2(d) for $\phi_o = 0°$. In this method, deceleration proceeds identically to the regular $S = 3$ except that when the synchronous molecule is directly between the energized guiding stage the next stage is energized. While this does create a slight anti-bunching effect, *i.e.* molecules in front of the synchronous molecule gain a small amount of energy, it provides an extra stage of transverse guidance when compared to $S = 3$. Experimental results of this method of slowing are shown in Fig. 7.6 for comparison with deceleration using both $S = 1$ and $S = 3$. In Fig. 7.6(a), we see that, as consequence of the switching sequence, even operation at $\phi_o = 0°$ leads to deceleration. Also, from the comparison with the $S = 1$ bunching peak shown, we see the usual gain associated with overtone deceleration. In Fig. 7.6(b), we see that operation with $S = 3+$ provides slightly more molecules than $S = 3$, and decreases with increasing phase angle in accordance with the longitudinal phase-stability dynamics. Presumably, the increase in molecule number for $S = 3+$ over $S = 3$ is due to the extra transverse guidance, which for the higher velocities packets we measured should lead to a larger transverse acceptance.

To determine whether the extra stage of transverse guidance would combat the
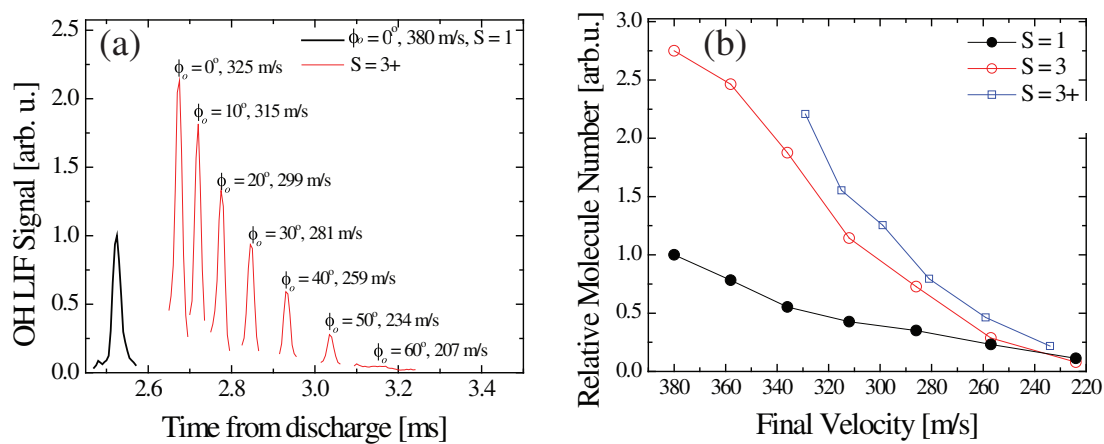
Figure 7.6: (a) Decelerated OH packets produced using the $S = 3+$ modified overtone. Also, shown for comparison is the bunching packet for operation at $S = 1$. (b) The de-convolved, integrated molecule number observed at the decelerator exit for $S = 3+$, $S = 3$, and $S = 1$.

over-focussing effects[5] we performed simulations of $S = 3+$ deceleration at $\phi_o = 20°$ for varying number of stages of deceleration. The results of these simulations, shown in Fig. 7.7, are similar to the results for $S = 3$. Namely, as the decelerator length is increased, and the molecules' speed reduced, there is a dramatic molecule number loss for velocities below 100 m/s – in fact in our simulations we could not observe any molecules below 50 m/s. Again, transverse over-focussing of the molecular packet by the deceleration electrodes is responsible for large losses in the decelerator, and it seems that more drastic measures are required to overcome the transverse focussing losses.

7.3   Quadrupole Guiding Decelerator

It may be possible to uncouple the longitudinal motion inside the Stark decelerator from the transverse motion by redesigning the decelerator electrode geometry. One of the simplest redesigns, which we call the quadrupole guiding decelerator (QGD), is shown in Fig. 7.8(a). In this decelerator, a quadrupole guiding stage (Fig. 7.8(b)) is interleaved between each deceleration stage. While it may not be necessary to have a quadrupole guiding stage between each deceleration stage (especially in the beginning of the decelerator), it simplifies the analysis and will be used here. The switching of the electric fields inside a QGD is similar to a traditional decelerator operated with $S = 1$ as shown in Fig. 7.8(c), where the potential energy experienced by a molecule decelerated at $\phi_o \approx 45°$ is shown as a thick black curve. In this figure the quadrupole guiding electrodes are omitted for clarity. Note that the quadrupole guiding stages are always energized and their center coincides with the $\phi_o = 0°$ point, while $\phi_o = 90°$ occurs between the deceleration electrodes.

Clearly, deceleration with a QGD enjoys the same longitudinal phase-stability as a traditional decelerator. However, because the decelerating electrodes are most likely

---

[5] While this may seem counter-intuitive, in some cases when the transverse over-focussing is not too strong the addition of another focussing element can change the sign of the molecules transverse velocity, keeping the beam from colliding with the electrodes.
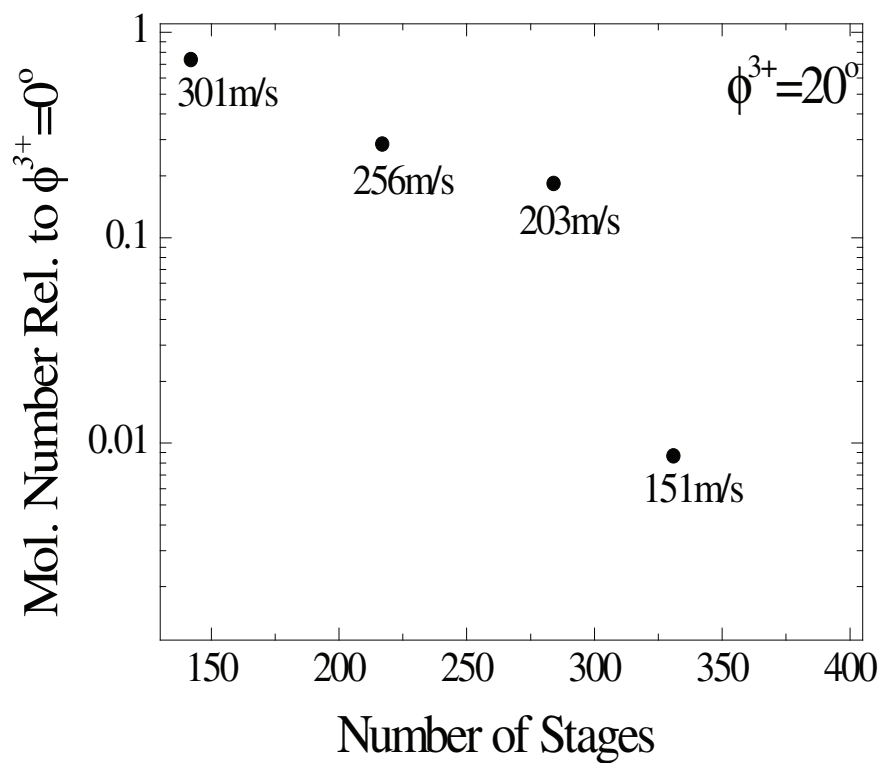
Figure 7.7: Decelerated molecule number using $S = 3+$ and $\phi_o = 20°$ for increasing decelerator stage number. The number next to each data point is the final velocity. Because of transverse over-focussing, essentially no molecules survive below 100 m/s.
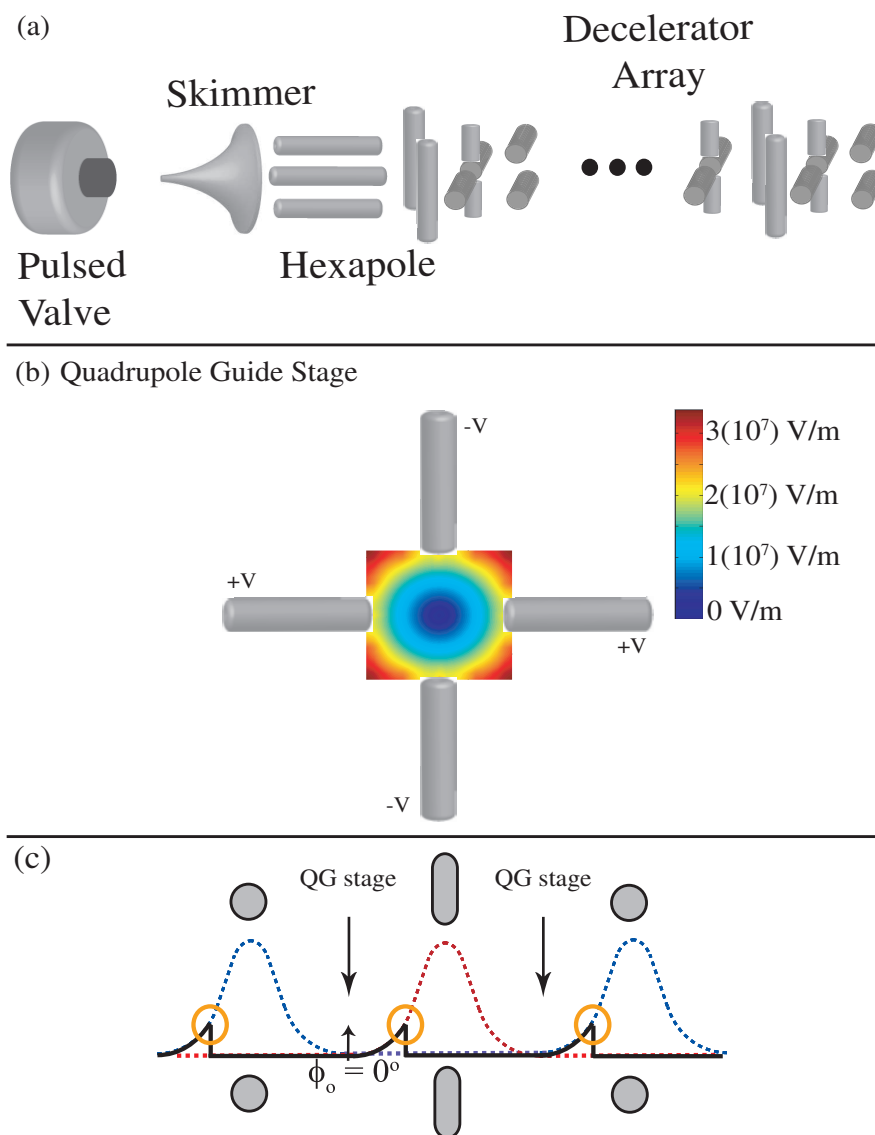
Figure 7.8: Quadrupole guiding decelerator. (a) Schematic of QGD. (b) Electric field of quadrupole guiding stage energized to ±12.5 kV. (c) Switching scheme for deceleration with the QGD.

farther apart[6] in a QGD the maximum stable excursion position, $\Delta\phi_{max}$, and velocity, Δv_{max}, will differ from that of the traditional decelerator. Furthermore, because the dependence of the decelerating force on ϕ_o is different (less steep) the shape of the stable longitudinal phase space will change. Understanding the shape of the stable longitudinal phase area is crucial to predicting the performance of the QGD, and can be derived from examining the longitudinal forces inside the QGD. Shown in Fig. 7.9(a) is the Stark shift on-axis of an OH molecule in the $|2 \pm 2+\rangle$ state inside the unit cell (3 deceleration stages) of the QGD. The solid line is the Stark shift due to the slowing stage centered at 11 mm, while the dashed line is the Stark shift of the stages which will be energized at the switching of the fields. The subtraction of these two curves, shown in Fig. 7.9(b) as a solid line, is the amount of energy removed at each switching of the fields, ΔKE. Similar to the previous section, we represent ΔKE as sum of sine-functions

$$\Delta KE(\phi) = \sum_{n=odd} a_n \sin(n\phi), \tag{7.1}$$

where we have used the definition of the phase angle $\phi = 180° z/L$. A fit of the first three terms of this equation to the actual ΔKE for deceleration stages spaced by 11 mm is shown as a dashed line in Fig. 7.9 resulting in the fit values $a_1 = 1.221$ cm^{-1}, $a_3 = 0.450$ cm^{-1}, and $a_5 = 0.089$ cm^{-1}. Using this fit, along with Newton's second law, we have the equation of motion of the molecules about the synchronous molecule position as

$$\frac{d^2\Delta\phi}{dt^2} + \frac{\pi}{mL}(\Delta KE(\Delta\phi + \phi_0) - \Delta KE(\phi_0)) = 0, \tag{7.2}$$

where we have used the excursion of the molecule from the synchronous molecule $\Delta\phi = \phi - \phi_o$. The maximum stable forward excursion of a non-synchronous molecule is exactly the same as a traditional decelerator and is given as

$$\Delta\phi_{max}^+(\phi_o) = 180° - 2\phi_o. \tag{7.3}$$

---

[6] To prevent high-voltage breakdown the quadrupole stages should be spaced from the deceleration stages by the same amount as deceleration stages are spaced in a traditional decelerator. Thus, the decelerating electrodes for a QGD will be twice as far apart as in a traditional decelerator.
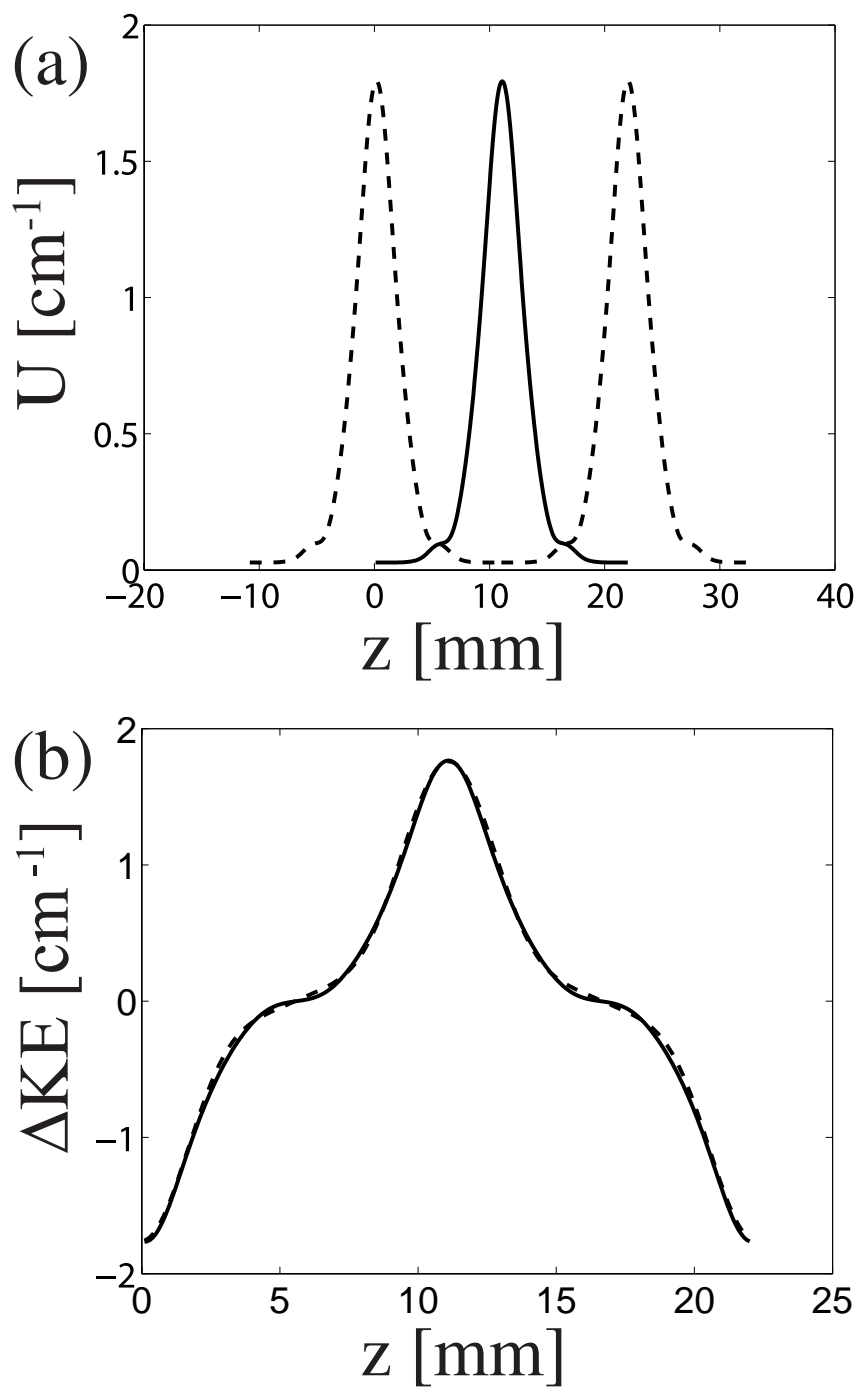
Figure 7.9: (a) The Stark shift of an OH molecule in the $|2\pm2, +\rangle$ state inside the QGD. The solid curve is the Stark shift due to the slowing electrodes, while the dashed curve is the Stark shift due to the electrodes that will be energized at the switching time. (b) The change in the molecule's kinetic energy as a function of position is shown (solid) as well as a fit of Eq. 7.1, including up to n = 3. (dashed). This graph is calculated from the subtraction of the two curves in panel (a).

Similar to the previous chapter we calculate the work done in bringing a molecule starting at this position with zero velocity to the synchronous molecule position as

$$W(\phi_o) = \int_{Start}^{End} F dx = -\frac{1}{\pi} \int_{\Delta\phi_{max}^+(\phi_o)}^{0} \sum_{n=odds} (a_n(\sin(n(\Delta\phi + \phi_o)) - \sin(n\phi_o)))d\Delta\phi.$$
(7.4)

Integrating this equation and setting it equal to the kinetic energy yields the maximum stable excursion velocity as

$$\Delta v_{max}(\phi_o) = 2\sqrt{\sum_{n=odds} \frac{a_n}{m\pi} \left(\frac{\cos(n\phi_o)}{n} - (\frac{\pi}{2} - \phi_o)\sin(\phi_o) \right)},$$
(7.5)

where ϕ_o is now in radians for convenience.

Using Eqs. 7.2-7.5 it is possible to solve for the longitudinal separatrix, which separates stable deceleration from unstable motion inside the decelerator. These separatrices are shown (thick black lines) along with the results of 3D Monte Carlo simulations of a QGD with 11 mm spacing between deceleration stages (5.5 mm spacing between deceleration and quadrupole guiding stages) in the left column of Fig. 7.10 for increasing phase angle. The longitudinal phase space is shown with each dot representing the position of a stable molecule. The lack of structure inside these separatrices is evidence of a minimization of coupling between the transverse and longitudinal modes. The right column, which shows simulated ToF curves, reveals a single stable peak arriving at later times as the ϕ_o is increased. These simulations are for only the $|2 \pm 2+\rangle$ state of OH, and thus, do not exhibit the large background contribution of the other states of OH present in experimental ToF data.

From the comparison of the 3D simulations with the separatrices, we see that the simple theory of Eqs. 7.2-7.5 is quite accurate in describing the longitudinal performance of the QGD. Thus, by numerically integrating the area inside these separatrices we can predict the longitudinal performance of the QGD relative to the traditional decelerator. As seen in Fig. 7.11(a), because the decelerator stage spacing (in this simulation) is twice that of a traditional decelerator the energy removed per stage of the QGD is
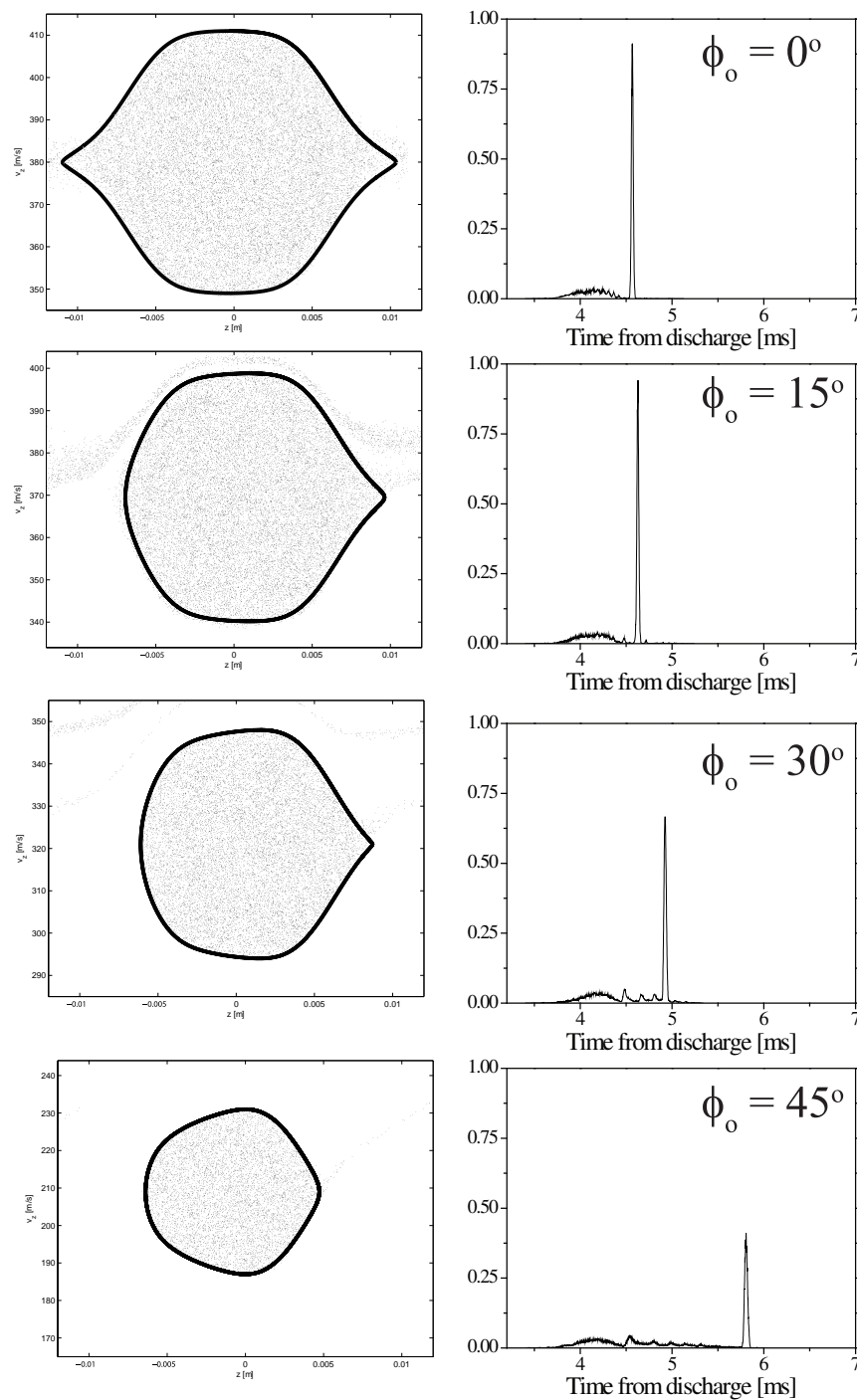
Figure 7.10: The left column is stable molecule phase space of molecules decelerated inside the QGD. The solid line is the separatrix predicted by the theory of this section, while the points represent positions of molecule in the 3D Monte Carlo simulations. The right column shows the ToF spectra of OH molecules in the $|2 \pm 2, +\rangle$ state at the exit of this decelerator which has 143 deceleration stage (286 stages in all).

less steep with ϕ_o. Therefore, QGD deceleration with the same ϕ_o as a leads to a faster beam than one produced by a traditional decelerator, given the same number of deceleration stages. Thus, when comparing the longitudinal acceptance of the two types of decelerators it is important to take the limit of high phase angles where the ΔKE's converge. Nonetheless, the QGD shows significant gain over traditional deceleration as shown in Fig. 7.11(b). This gain is primarily due to the increased physical size of the stable longitudinal phase space due to the larger deceleration stage spacing.

It is important, to note that since this graphs compares only the total area inside the separatrix and $S = 1$ deceleration does not completely fill this area (due to the coupling effects), this gain is actually an underestimate of the QGD longitudinal performance. Furthermore, these graphs do not include transverse focussing effects, which can only be properly included through detailed simulation. The results of a 3D Monte Carlo simulation, which includes these transverse effects, are shown in Fig. 7.12. In this graph, the number of decelerated molecules versus the final speed is plotted for both the traditional decelerator operating at $S = 1$ and the QGD decelerator. Here we see that while the QGD initially delivers more molecules, once the molecules are decelerated below 100 m/s the decelerated molecule number falls off abruptly. This behavior is expected since for these simulations the voltage on the quadrupole guiding stages was chosen to be ± 2.2 kV, which maximizes the bunching signal (Fig. 7.13). And, as detailed in Eq. 4.7, the focal length of a transverse guiding element is directly proportional to the molecular kinetic energy. Therefore, as the molecule speed is decreased, the molecules are over-focused and crash into the decelerator electrodes. By lowering the voltage on the quadrupole guiding stages during the deceleration process this can be prevented. A simulation of deceleration with this dynamically controlled voltage is shown in Fig. 7.12 as an open (red) circle. For this simulation, the voltages were scaled as $1/v^2$ after each deceleration stage. For ease of simulation, the transverse forces were scaled by $1/v^2$ whenever the molecules were closer to a quadrupole
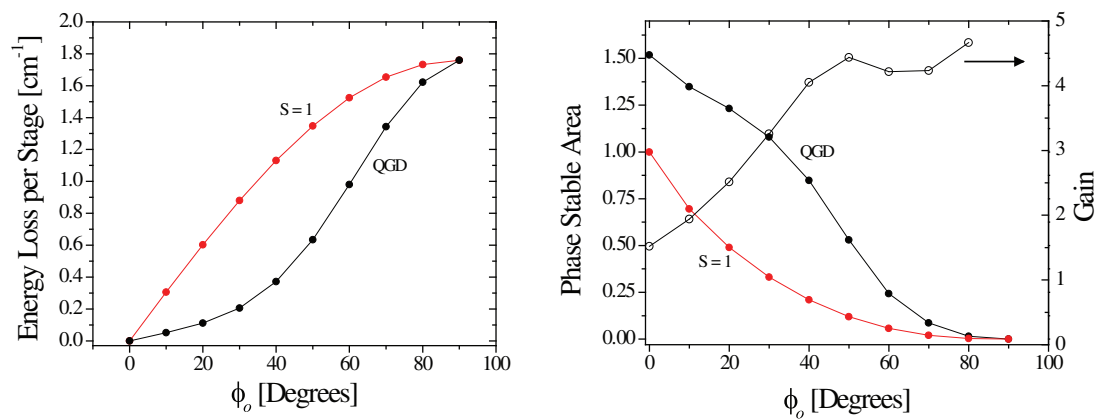
Figure 7.11: (a) The energy removed by deceleration per stage as a function of phase angle for traditional deceleration and deceleration with a QGD. Both curves are calculated for OH in the $|2 \pm 2, +\rangle$ state. (b) The phase-stable area for deceleration as a function of phase angle for traditional deceleration and deceleration with a QGD is plotted on the left axis, while the gain of the QGD over traditional deceleration is plotted on the right axis.
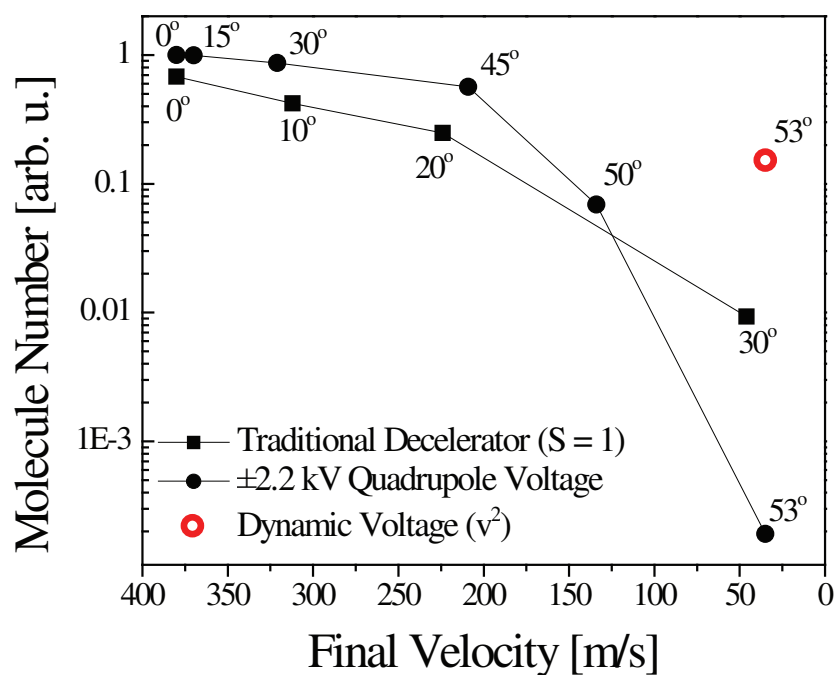
Figure 7.12: Comparison of the decelerated molecule number using traditional deceleration and deceleration using a QGD for increasing decelerator phase angle. For both curves 143 stages of deceleration were used. The number next to each data point is the phase angle used. Note that for operation of the QGD with ± 2.2 kV on the guiding stages, essentially no molecules survive below 100 m/s because of transverse over-focussing. If the voltage on the guiding stages is lowered as the molecules are decelerated this effect is removed and the QGD supplies roughly 2 times as many molecules as a traditional decelerator.
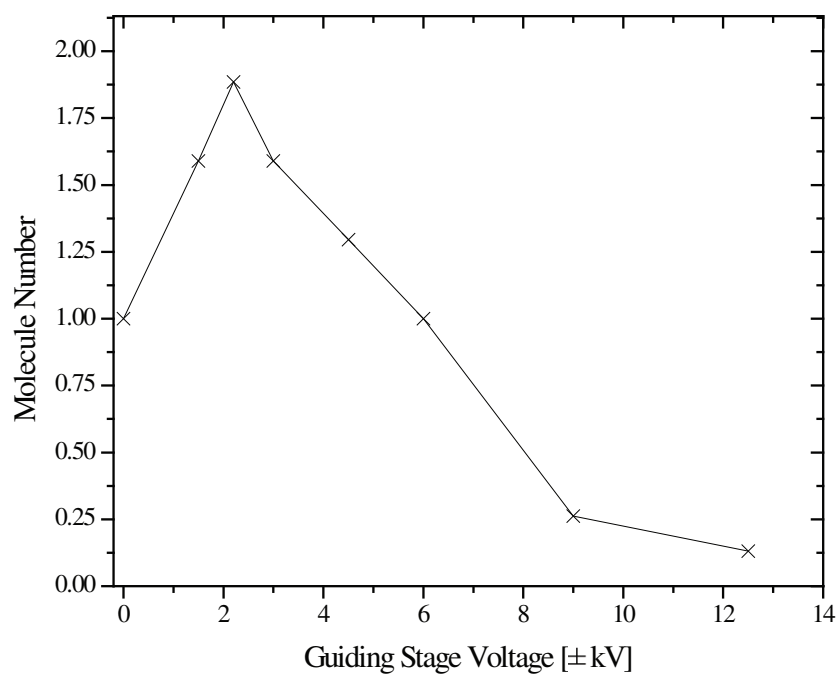
Figure 7.13: Optimization of the quadrupole guiding voltage for operation at $\phi_o = 0°$.

guiding stage than a deceleration stage. While this may be a poor approximation at the lowest speeds, it will likely lead to an underestimate of the decelerated molecule number since the transverse guidance of the quadrupole guiding stage extends beyond this regime. However, even if it leads to an overestimate, it may be that by proper control of the quadrupole voltages any over-focussing introduced by the decelerating elements can be compensated. As seen from the slowest points in Fig. 7.12, dynamically controlling the voltage of the quadrupole guiding stages leads to nearly a factor 1000 increase in decelerated number for the QGD and delivers about 20 times more decelerated molecules than traditional deceleration provides. Furthermore, because the voltages on the quadrupole guiding stages is low, dynamic control of them should be possible using an analog waveform generator and high-voltage amplifier. It should be noted that scaling the voltages as $1/v^2$ may not be the optimal scaling since the real focal length depends sensitively on the electrode construction, and at low speeds the transverse focussing of the decelerator electrodes becomes significant. In fact, simulations where the quadrupole guiding transverse forces were scaled as $1/v^{0.875}$ show a gain of 1.8 in decelerated molecule number over the $1/v^2$ scaling (see Fig. 7.14(b)). This is, presumably, because the over-focussing of the decelerator electrodes can be somewhat compensated by inputting molecules which are already slightly over-focused, *i.e.* one lens focuses, but two can make a telescope. Thus, it may be possible to use evolutionary algorithms to control the quadrupole voltage or change the design of the decelerating electrodes so that they provide less transverse focusing, and maximize the number of decelerated molecules beyond what is reported here.

One important advantage of the QGD over traditional decelerators is its inherent ability to support more deceleration stages. Because the molecules experience a tunable transverse focussing element after each deceleration stage there is little loss in extending the number of deceleration stages. In fact, as seen in Fig. 7.15, there is essentially no loss until the molecules are slowed to the slowest speeds. And since this loss is due to
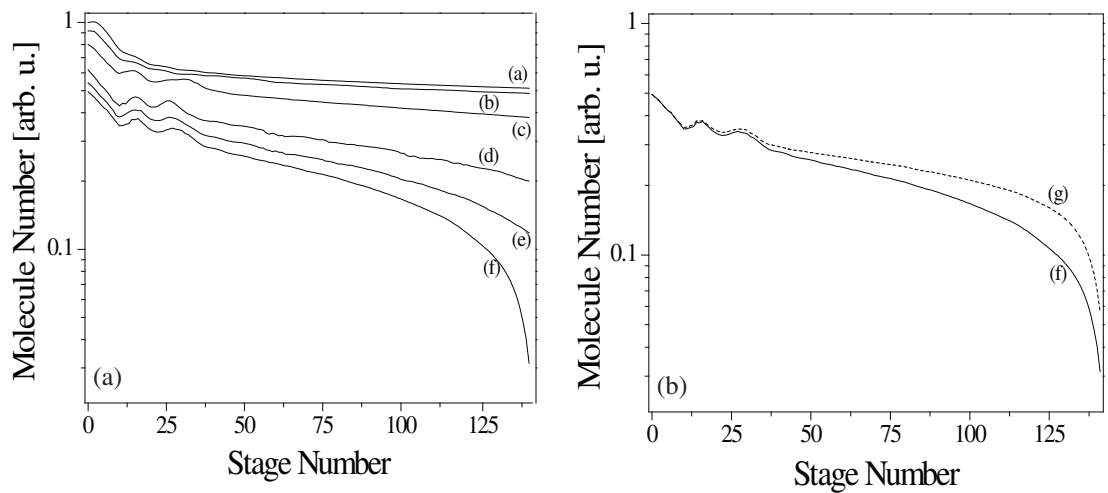
Figure 7.14: (a)Simulations of the phase-stable molecule number as a function of stage number in the QGD with the guiding voltages scaled as $1/v^2$. The traces shown are (a) $\phi_o = 0°$, (b) $\phi_o = 15°$, (c) $\phi_o = 30°$, (d) $\phi_o = 45°$, (e) $\phi_o = 50°$, and (f) $\phi_o = 53°$. Note the dramatic decrease in number in the last several stages for $\phi_o = 53°$. This decrease is due to transverse over-focussing of these slow molecules, which is still present, presumably due to the over-focussing the decelerator electrodes. (b)Comparison of deceleration at $\phi_o = 53°$ with $1/v^2$ (f) and $1/v^{0.875}$ (g) scaling of the quadrupole guiding voltage. Both panels are normalized to the $\phi_o = 0°$ case.

the aforementioned transverse over-focussing, it is not a fundamental problem. Furthermore, even with this loss the QGD enormously outperforms both $S = 3$ (Fig. 7.5)and $S = 3+$ (Fig. 7.7). Thus, the QGD seems to be an ideal decelerator for producing large numbers of currently decelerated molecules, or, perhaps more importantly, the ideal decelerator for deceleration of molecules with poor Stark shift to mass ratios like H_2O and SO_2.

In summary, the QGD solves the problem of coupling between the transverse and longitudinal motions inside a Stark decelerator by introducing transverse focusing elements. By dynamically controlling the focal length (voltage) of these guiding elements, enormous improvements in deceleration efficiency can be achieved[7] . Furthermore, it appears that with dynamic control of the guiding stage focal length there should be no limit to the length of decelerator that can be built. This opens the door for the deceleration of molecules with a poor Stark shift to mass ratio. Building upon the strong correlation between simulation and experimental results, we are confident that the simulations presented in this chapter provide a solid guideline for future implementations of Stark deceleration.

---

[7] As detailed in Chap. 5 traditional decelerators appear to suffer from over-focussing effects in their final stage. Thus, implementing dynamic voltage control ideas in current decelerators may lead to immediate improvements in decelerator efficiency.
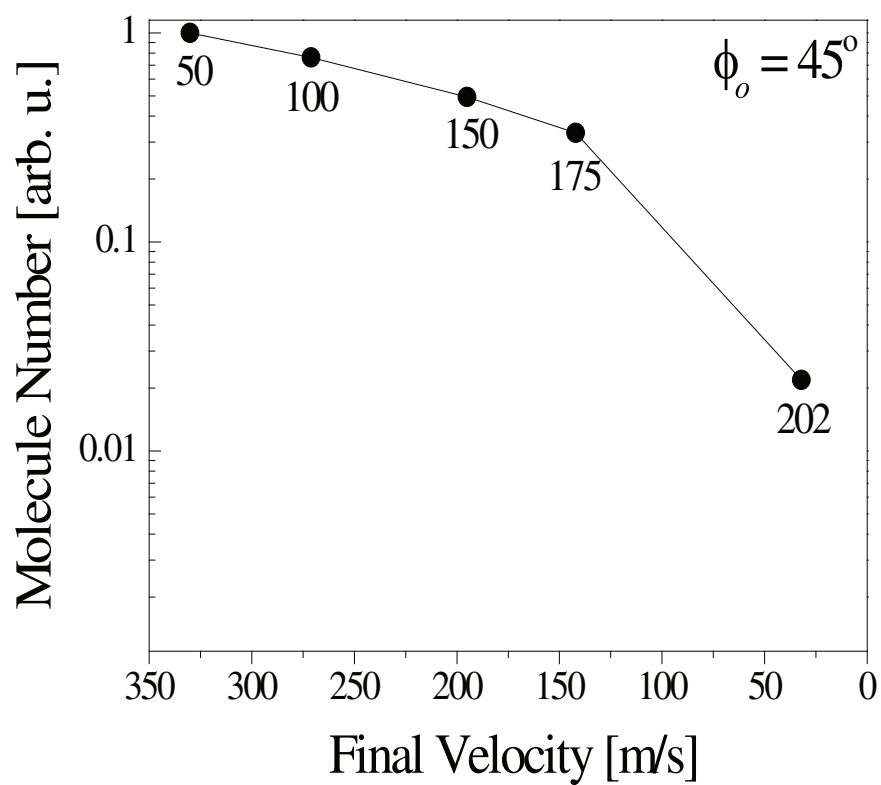
Figure 7.15: Decelerated molecule number using the QGD for increasing decelerator stage number. The number next to each data point is the number of deceleration stages used. Because of transverse over-focussing there is a sharp loss of molecules for the slowest speeds.

Chapter 8

Towards Cold Chemistry and Reaction Control: Deceleration of the Formaldehyde Molecule

8.1 Introduction

Recent exciting developments in ultracold matter research include the creation of ultracold molecules by magneto-association [46], leading to molecular Bose-Einstein condensation [4]. Despite the rich physics demonstrated in these systems, all are characterized by spherically symmetric interactions whose effect is included through one tunable parameter, namely the s-wave scattering length. By contrast, the permanent electric dipole moment possessed by polar molecules permits long-range and anisotropic interactions and enables new methods for external control in an ultra-cold environment [5]. The electric dipole-dipole interaction (and control over it) gives rise to unique physics and chemistry including novel collision and chemical reaction dynamics. Lack of spherical symmetry in the interaction causes colliding molecules to be attracted or repelled depending on their relative orientation. Thus, an external electric field, which orients the molecules, will have a profound effect on the molecular interactions [6]. Furthermore, because the transition states of a chemical reaction often involve specific orientations of the molecular dipoles, an external electric field may shift the energy barrier to reaction, making a particular reaction pathway more or less favorable. A Stark decelerator [24, 27, 28, 127] producing cold polar molecules with tunable and well-defined translational energy is thus an ideal tool for the study of low (or nega-

tive) barrier chemical reactions. We note other experiments utilizing photo-association [134, 73, 84], helium buffer gas cooling [137], and billiard ball collisions [50] have succeeded in producing cold polar molecules. Furthermore, the possibility of producing polar molecules through the use of a Feshbach resonance is also very exciting [115, 65] because of the ultra-cold temperatures possible.

Here, we present an outline of the properties and possibilities for control of the low temperature reaction of OH with H_2CO, followed by a detailed report on the production of cold H_2CO molecules via Stark deceleration, a necessary step in the study of these novel dynamics. Modeling suggests for the first time that chemical reactions and collision cross sections can be altered orders of magnitude by varying either the molecular state, or external electric field strength. We specifically consider the H-abstraction channel in the reaction of H_2CO and OH: $H_2CO + OH \rightarrow CHO + H_2O$. This reaction not only represents a key component in the combustion of hydrocarbons, but also plays an important role in atmospheric chemistry where it is the primary process responsible for the removal of the pollutant, H_2CO [88, 113, 116, 48, 90, 143, 81]. Near room temperature the rate of this reaction is weakly dependent on temperature, suggesting the barrier to the process (if any) is very low [116]. Measurements of the thermal activation energy, E_a, range from $E_a/R = 750$ K to -931 K [88, 113, 116, 48, 90, 143, 110], with the most recent measurement giving a value of -135 K [110]. Here R is the universal gas constant. The most accurate calculations [38] predict the energy of the transition state for the abstraction to lie between -700 K and +60 K relative to the reactants.

Experimentally, both OH [27, 28, 127] and H_2CO (this work) molecules have been produced at low temperatures via Stark deceleration. In the case of spontaneous reaction ($E_a < 0$) [88, 116, 90, 143], by magnetically trapping OH in the presence of a tunable bias electric field and "bombarding" the trap with decelerated H_2CO packets, the OH - H_2CO total scattering and reaction rates can be mapped as a function of collision energy and applied electric field. Thus E_a can be measured. If $E_a > 0$, as some

measurements and theory suggest [113, 48, 81, 38], the collision energy tuning afforded by the Stark decelerator provides a direct way to measure the energy barrier to reaction. Unlike thermal kinetics studies, which rely on fitting the Arrhenius formula to reaction rates, the Stark decelerator can be used to directly tune the collision energy above and below the threshold energy.

Further motivation for pursuing this particular reaction comes from the prominent position in molecular physics held by H_2CO. As a four-atom asymmetric rotor, H_2CO's rotational structure and six internal degrees of freedom give rise to the same complexities of much larger molecules. However, as a relatively light molecule, H_2CO is still tractable at a high level of theory, making it an ideal proving ground for molecular physics. Additional incentive for pursuing H_2CO was that until this work an asymmetric rotor had never been decelerated in a Stark decelerator; therefore this effort opens the door for the production of the most general class of cold molecules.

As shown in Fig. 8.1(a), H_2CO is a near-symmetric prolate top molecule, with nearly degenerate rotations about the b- and c- axes. The dipole moment, μ_a, along the a-axis causes these nearly degenerate, opposite parity states to experience a large Stark shift with an applied electric field, as shown in Fig. 8.1(b-d). Here, the states are labeled by their zero-field identity in the $|J_\tau m_J\rangle$ basis, where $\tau = K_a - K_c$ (K_i is the projection of J along the ith axis) [56]. Of particular interest to this work is the $|1_1 1\rangle$ state (Fig. 8.1(c)), which is the upper component of the lowest J level of ortho-formaldehyde and is hence well populated in our supersonic expansion. This state experiences a large Stark shift (1.32 cm^{-1} at 125 kV/cm), making it excellent for Stark deceleration. There are other states accessible via, for example, stimulated Raman adiabatic passage that offer an improved Stark deceleration efficiency ($|2_2 2\rangle$) or a good candidate for implementing an AC Stark trap ($|0_0 0\rangle$) [129].
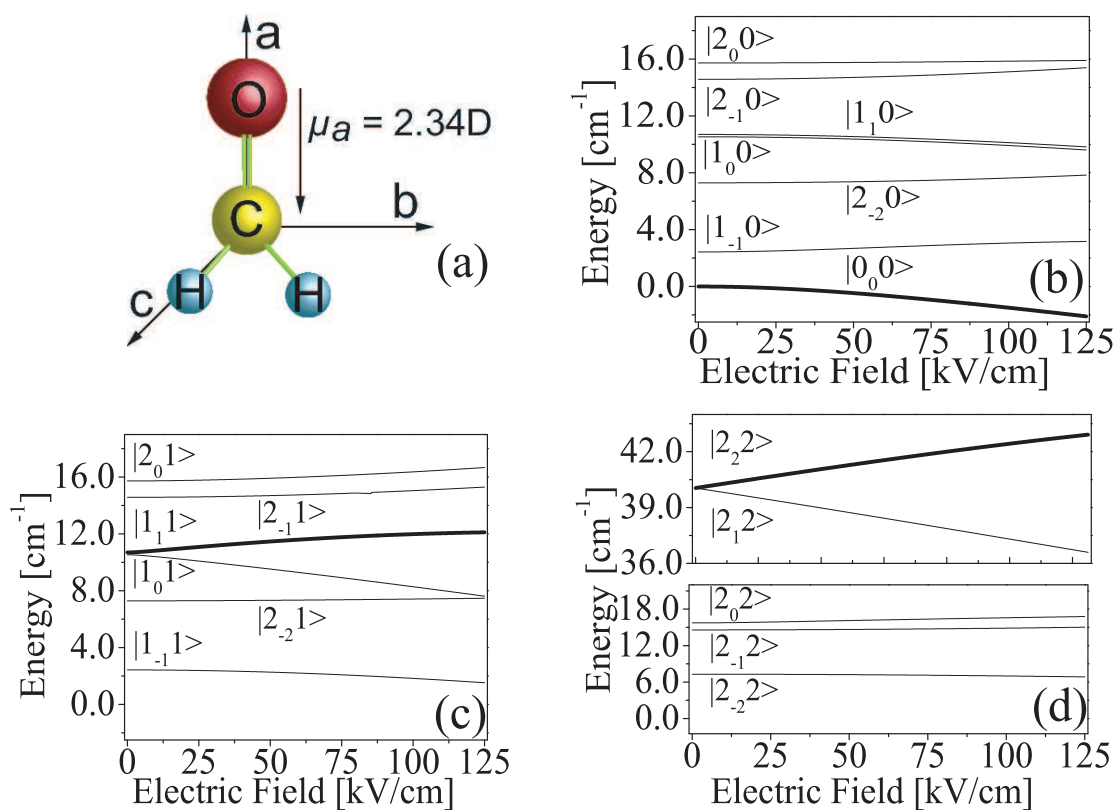
Figure 8.1: (a) (Color online) H_2CO. (b-d) Stark shifts of the low-lying rotational states of H_2CO. States of interest for this work are shown in bold.

8.2   Reaction Control

The sensitive dependence of cold molecular interactions on internal state and electric field engenders new prospects for probing and controlling chemical reactions. However, a complete theoretical model of the scattering processes is a large task. Nonetheless, simple modeling can suggest the extraordinary influence that can be exerted over the collisions by selecting appropriate initial states, or else by varying an electric field. Much of this control arises from the dipolar interaction itself, as has been stressed in the past [18, 19, 122]. We therefore construct a scattering model which is realistic with regard to the dipolar interaction, and deliberately schematic with regard to the chemical interaction dynamics. The Hamiltonian, H, used in the scattering calculations takes the following form:

$$H = T + H_{OH} + H_{H_2CO} + H_{Stark} + H_{dd} + H_{sr} + H_{chem}. \tag{8.1}$$

Here T is the kinetic energy, H_{OH} and H_{H_2CO} are the Hamiltonians of the separated molecules, and H_{Stark} describes the action of the electric field on the individual molecules. H_{dd} represents the long-range dipole-dipole interaction between the molecules, which depends on the orientations of the molecules relative to the field axis, as well as the distance R between them. This Hamiltonian will be expressed in a basis of molecular eigenstates (including the effect of the field), as was done in Ref. [18, 19]. In addition, to prevent the dipole-dipole interaction from overwhelming the short-range interaction, we replace its $1/R^3$ variation with $1/(R^3 + c_{dd})$ for an appropriate constant c_{dd} [76]. The chemical reaction dynamics are modeled in a schematic way by the terms H_{sr} and H_{chem}. The goal of H_{sr} is to mimic an anisotropic interaction with a barrier, not necessarily to characterize the OH-H$_2$CO system. This approximation is justified for the low reaction barrier where the dipole-dipole interaction dominates over internal molecular dynamics. Thus, we construct a potential as an expansion into Legendre
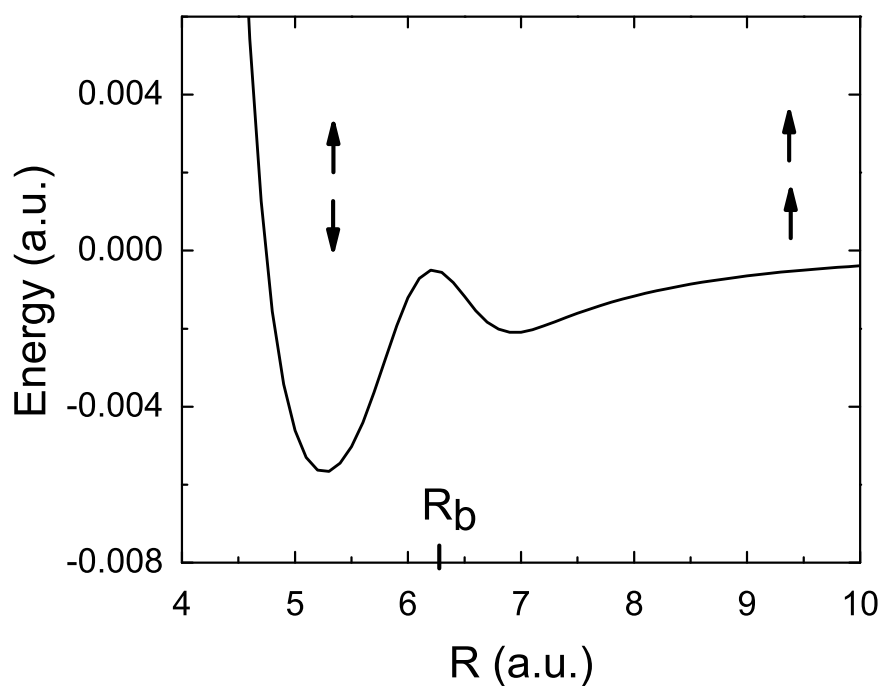
Figure 8.2: Schematic lowest-lying adiabatic potential curve for the scattering model. For intermolecular distances $R \gg R_b$, the ordinary dipole-dipole interaction holds, and the molecules attract head-to-tail. As the molecules approach a potential barrier at $R = R_b$, the potential deviates from dipolar behavior, and the sign of V_2 is switched so that, by $R < R_b$, the molecules attract in a tail-to-tail configuration to mimic chemical reaction described below. Also for $R < R_b$, the scattering channel is coupled to an artificial channel (not shown), which represents chemical reactivity.

functions,

$$H_{sr} = V_o(R) - 2V_2(R)C_{20}(\theta, \phi). \tag{8.2}$$

Here (θ, ϕ) represent the spherical angles of the relative coordinate between the molecules, referred to the electric field axis, and C_{20} is a reduced spherical harmonic [31]. The isotropic part of this potential carries the barrier at a radius $R \approx R_b$,

$$V_o(R) = \frac{C_{12}}{R^{12}} - \frac{C_6}{R^6} + D_B \exp\left(\frac{-(R - R_b)^2}{w_b}\right). \tag{8.3}$$

The height of the barrier depending on D_B is fully adjustable with w_b characterizing its range. In the following, we set the barrier height equal to the threshold energy of the incoming molecule. The resulting isotropic potential has a depth that has arbitrarily been set to 5×10^{-3} atomic units. The radial dependence of V_2 is chosen to have a magnitude comparable to V_o, but to change sign as R crosses R_b, as seen in Fig. 8.2. This is done to mimic the short-range physics responsible for the chemical reaction as depicted in Fig. 8.5 and described in the accompanying text. Thus, the polar molecules attract in a head-to-tail configuration for $R > R_b$, but attract in a tail-to-tail configuration upon crossing the barrier. Finally, chemical reactivity (H_{chem}) is modeled by coupling to a purely repulsive artificial channel. The coupling to this channel is represented by a decaying exponential in R, which is of negligible size for $R > R_b$. To complete a chemical reaction, the molecules must cross over the barrier, reverse their relative orientation, and find the artificial channel.

Collision cross sections for OH-H$_2$CO scattering in this schematic model are shown in Fig. 8.3. Here both molecules are assumed to be in spin-stretched, weak-field-seeking states: $|Fm_F, \text{parity}\rangle = |22, f\rangle$ for OH, and $|1_1 1\rangle$ for H$_2$CO. The collision cross sections are plotted as functions of electric field, with the collision energy fixed at 1 mK. The cross section for elastic (spin-changing) collisions is shown as a dashed (solid) line. These cross sections are large and comparable to one another, and exhibit strong modulations as a function of an applied electric field. Modulations of this type have
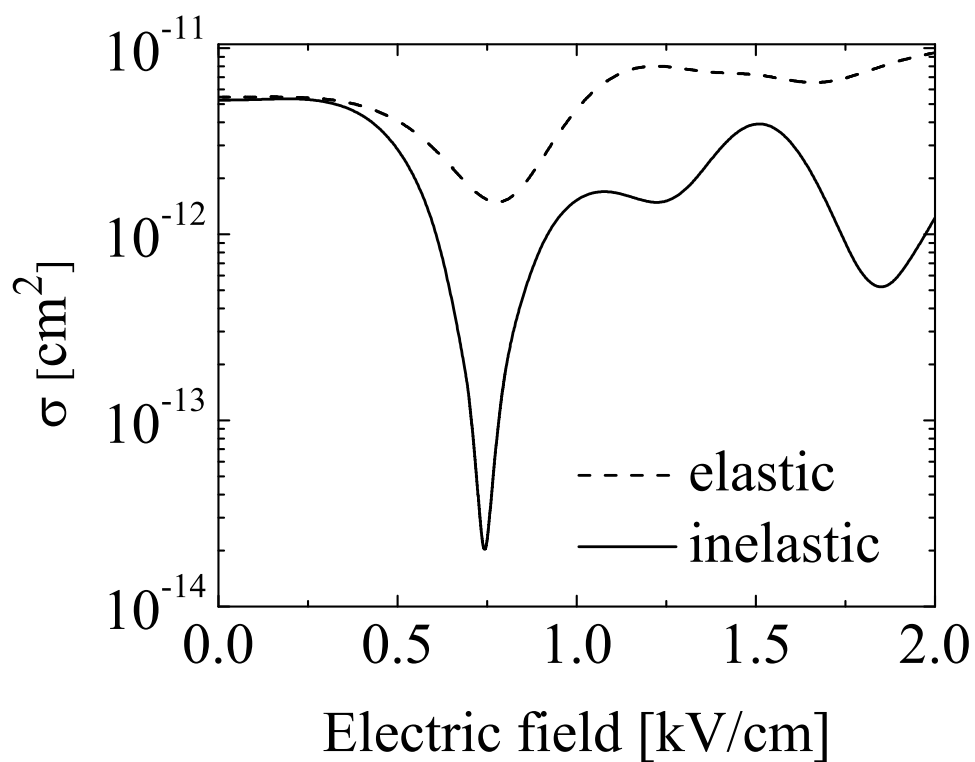
Figure 8.3: Elastic (dashed) and spin-changing inelastic (solid) cross sections for cold collisions of spin-stretched OH and H_2CO molecules. These cross sections were computed at a collision energy of 1 mK.

been discussed previously, for the OH-OH scattering system, as arising from purely long-range scattering by the dipole-dipole interaction [18, 19]. Thus, these results are relatively robust and independent of the detailed form of the short-range interaction.

The influence of long-ranged dipolar forces should also extend to the chemical reaction dynamics. To illustrate this, we show in Fig. 8.4 the chemical reaction cross section versus electric field. The collision energy is again assumed to be 1 mK. (Note that, because the reaction mechanism is schematic in our model we report only relative values for the cross sections.) The solid line is for collisions in which both OH and H_2CO molecules are in their strong-field-seeking states. At this collision energy the field has a profound influence on the reaction cross section, mostly by accessing a large number of resonant states. Considering that each resonant state likely spans a different region of configuration space, mapping out resonances such as these can in principle serve as an extremely sensitive probe to transition states. The dashed trace in Fig. 8.4 shows the reaction rate for weak-field-seeking states of the reactants. In addition to probing many resonances, this cross section rises by nearly four orders of magnitude as the field increases over a range of 2 kV/cm. This rise is also a direct consequence of the dipole-dipole interaction. In Refs [18, 19, 122], it was shown that polar molecules in weak-field-seeking states scatter at fairly long range at ultra-low energies (of order tens to hundreds of atomic units), owing to avoided crossings in the relevant adiabatic potential energy curves. In other words, the dipole-dipole interaction can "shield" these molecules from ever getting close enough to react chemically. Thus the cross section is strongly suppressed relative to that for strong-field-seekers. However, as the field is increased, the inner turning point of the relevant potential curve moves to smaller R, making the shielding less effective, and hence, the reaction more likely.

We stress that these results are by no means quantitative predictions of the expected behavior of the OH-H_2CO scattering system. However, they are qualitatively suggestive of the strong dependence of scattering on experimentally accessible parame-
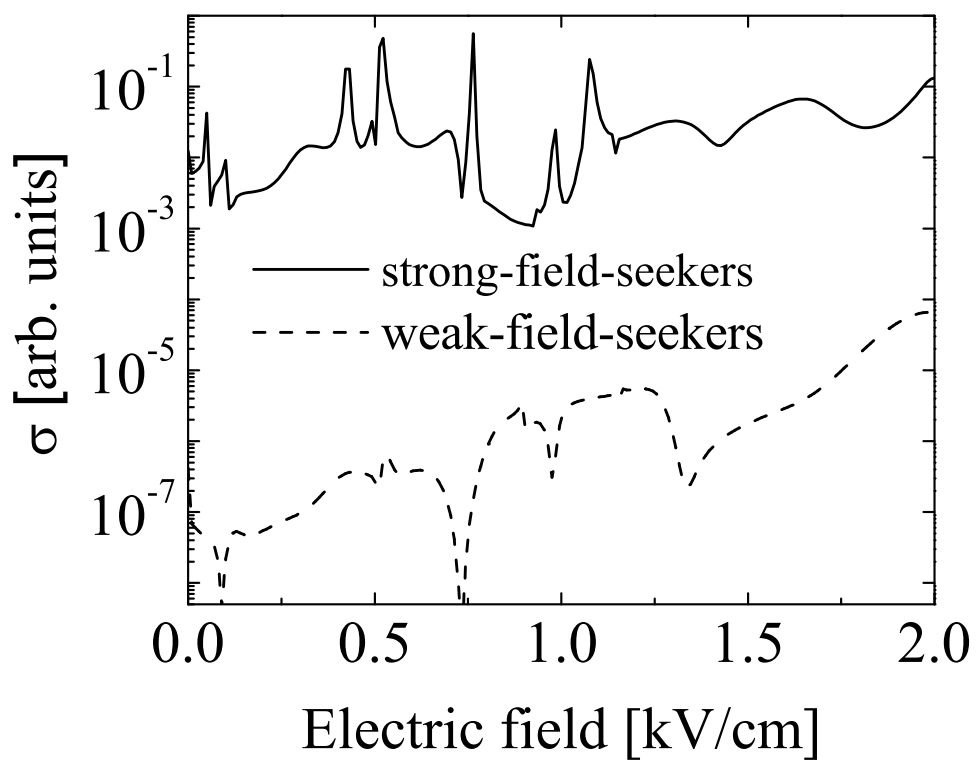
Figure 8.4: Calculated chemical reaction cross sections at a collision energy of 1 mK, versus electric field, using the model in the text.

ters such as molecular internal state and applied electric field. Our confidence in these qualitative conclusions is drawn from the fact that they originate largely in the dipolar interaction, which can be treated accurately. More detailed theoretical studies, including more realistic potential energy surfaces, are planned [7].

An important capability for current experiments (not included in our model) is the direct control of the H-abstraction reaction barrier height through the application of an external electric field. The basic H-abstraction reaction mechanism [48] is shown in Fig. 8.5. We note that Ref. [14] presents a slightly different H-abstraction configuration, but with the same end-to-end dipole coupling scheme. During the H-abstraction process, the energy required to rotate one dipole moment (OH) versus the other (H_2CO) enables our proposed control of reaction dynamics using an external electric field. Hence, the two abstraction configurations present no difference other than the magnitude of the shift we can create in the reaction barrier. The important characteristic to note is that the hydrogen-bonded complex (HBC) in the second panel (Fig. 8.5) forms along an attractive direction of the two electric dipoles, but in the transition state (TS) the OH dipole has essentially flipped its orientation relative to the H_2CO dipole. While an external electric field, which orients the molecules, would allow (and perhaps even encourage) the formation of the HBC; it would add an energy barrier to the formation of the TS, and thus the H-abstraction channel through the OH dipole-field interaction. Based on the bond geometries shown in Ref. [48], the addition to the energy barrier in going from the HBC to the TS is $\sim 1.8\mu_{OH}|\vec{E}|$, where μ_{OH} is the expectation value of the OH dipole. For a high, yet attainable, electric field of 250 kV/cm, the additional barrier energy would be 10 K. Assuming a reaction barrier at a H_2CO collision speed of 223 m/s (60 K [38]) the applied electric field would shift the required collision velocity to 234 m/s, well within the Stark decelerator resolution.
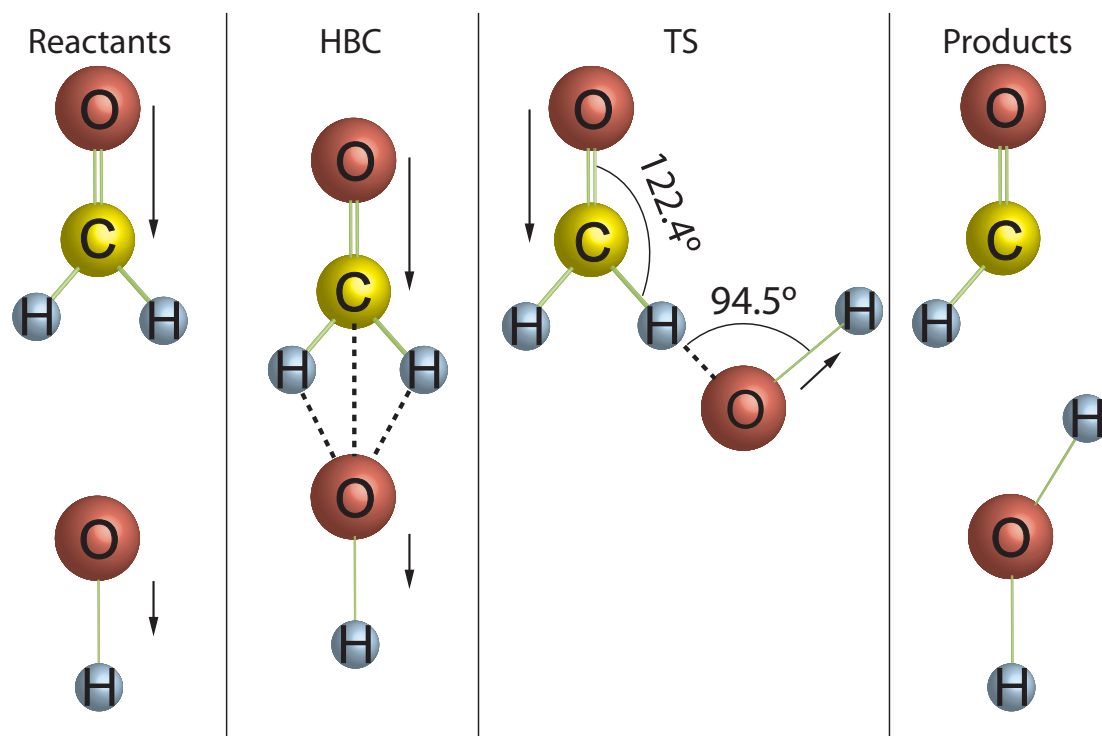
Figure 8.5: (Color online) The reaction mechanism for the H-abstraction channel following Ref [48]. The molecules initially attract in the head-to-tail configuration forming the hydrogen bonded complex (HBC). The chemical reaction proceeds via the transition state (TS) to the final reaction products.

8.3   Experiment

The decelerator used for H_2CO is similar to the apparatus in our previously described OH experiments [27, 28, 61]. Molecules in a skimmed, pulsed supersonic beam are focused by an electrostatic hexapole field to provide transverse coupling into the Stark decelerator. The Stark decelerator is constructed of 143 slowing stages spaced 5.461 mm apart with each stage comprised of two cylindrical electrodes of diameter 3.175 mm separated axially by 5.175 mm and oppositely biased at high voltage ($\pm$ 12.5 kV). Successive stages are oriented at 90° to each other to provide transverse guiding of the molecular beam. The geometry of the slowing stages provides an electric field maximum between the electrodes with the field decreasing away from the electrode center. Switching the electric field when the molecules are directly between two adjacent stages (no deceleration) is denoted by a synchronous phase angle of $\phi_o = 0^o$ (referred to as bunching), while switching the electric field when the molecules are between the electrodes (maximum deceleration, minimum stable area in phase space) is denoted by $\phi_o = 90^o$.

The H_2CO molecules are produced from the cracking of the formaldehyde polymer to produce the monomer, which is passed through a double u-tube apparatus [114]. Xenon at 200 kPa pressure is flowed over the collected H_2CO, held at 196 K where H_2CO has $\sim$2.7 kPa vapor pressure. In this work, the Xe/H_2CO mixture was expanded through either a current-loop (60 μs pulse length) or a solenoid supersonic valve (500 μs pulse length), producing beams with a mean speed (spread) of 470 m/s (10%) and 350 m/s (10%), respectively. The higher mean speed of the current-loop valve pulse is due to the documented heating effects of these devices [80].

H_2CO is detected using laser-induced fluorescence. The molecules are excited from the $|1_1 1 >$ ground state by photons at 353 nm generated from a frequency-doubled, pulsed-dye laser (PDL) pumped by a Nd:YAG laser to the $\widetilde{A}^1A_2$ electronically excited
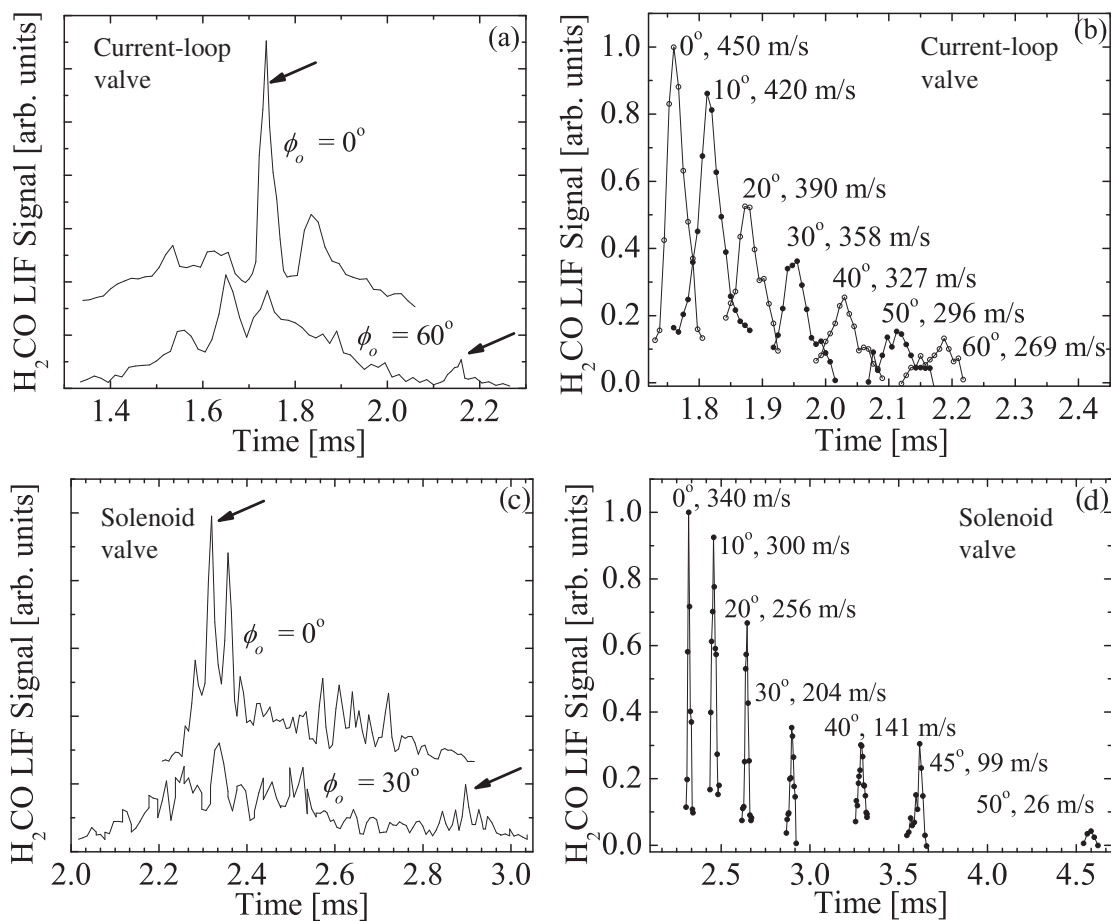
Figure 8.6: ToF data for decelerated H_2CO, showing bunching and deceleration off the main pulse (offset down for clarity) for both (a) the current-loop and (c) solenoid valves. Stark decelerated packets of H_2CO at the output of the decelerator for both the (b) current-loop and (d) solenoid valves.

state with one quantum in the ν_4 out-of-plane bending vibrational mode. Approximately 40% of the excited H_2CO decays non-radiatively [57], while the remaining molecules emit distributed fluorescence from 353 nm to 610 nm [109]. This fluorescence is collected, filtered, and imaged onto a photo-multiplier tube. The output of the photomultiplier tube is sent to a multi-channel scalar/averager, which serves as a gated photon counter. Operating the decelerator at 5 Hz and the PDL system at 10 Hz allows a "lock-in" type data-collection, such that every other signal is subtracted from the total photon counts. By scanning the delay between the PDL system and the triggering of the valve, a time-of-flight (ToF) curve is generated. A single data point is generated by collecting photon counts for 30 s to 2400 s (depending on required signal to noise).

Shown in Fig. 8.6 are ToF measurements taken ∼1 cm after the exit of the decelerator, which is ∼0.9 m down-stream from the valve. Data taken using the current-loop valve is shown in the top two panels (a,b), while data for the solenoid valve is shown in the bottom two panels (c,d). In these figures the time axis is relative to the beginning of deceleration. In Fig. 8.6(a) when the decelerator is operated at $\phi_o = 0^o$, a large peak in the ToF curve denotes the arrival (marked by an arrow) of the phase stable packet whose density is ∼10^6 cm^{-3} and contains a few million molecules. For these molecules no deceleration has occurred [?]. Also shown in Fig. 8.6(a), but offset for clarity is the ToF curve for deceleration at $\phi_o = 60^o$. Here the arrow denotes the arrival of a slowed, isolated H_2CO packet with a mean velocity of 269 m/s. In this curve the signal of deceleration is unmistakable, a peak in the ToF data arriving later than the main pulse. Displayed in Fig. 8.6(b) are ToF curves for only the slowed molecular packets as a function of ϕ_o. The effect of deceleration is evident, as ϕ_o increases and more energy per stage is removed, the phase stable packets arrive later in time signifying the reduction in velocity. For $\phi_o \leq 50^o$ the phase stable packets have not been decelerated off the main pulse and therefore their baseline values differ from that of the higher ϕ_o.

While the solenoid type valve is much less stable in pulse-to-pulse molecule num-
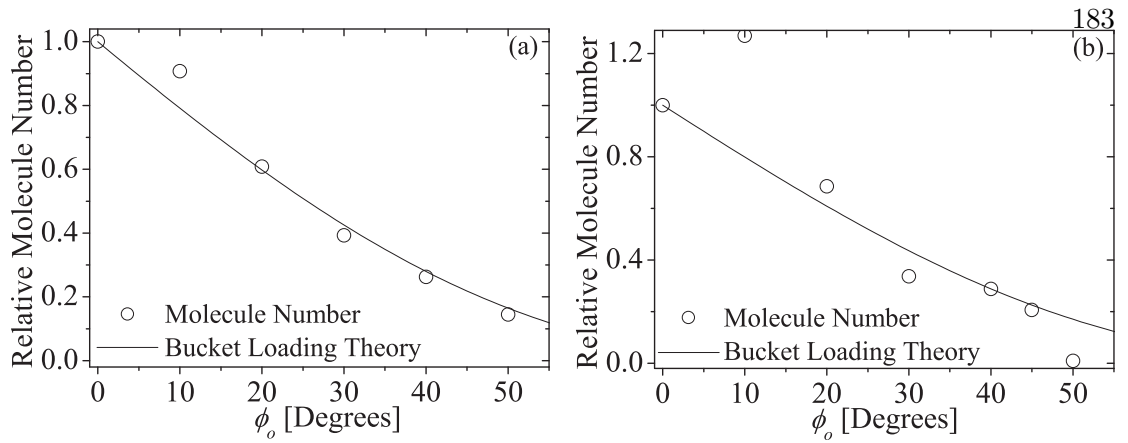
Figure 8.7: Comparison of decelerated packet molecule number to the expected for (a) the current-loop valve and (b) the solenoid valve.

ber than the current-loop valve, it supplies a slower molecular pulse with a mean speed in agreement with a room temperature Xenon expansion. The benefit of the lower initial speed is seen directly in Fig. 8.6(c), where only $\phi_o = 30^o$ is required to decelerate a packet of molecules to after the main pulse. Because of the long pulse from the solenoid valve, the associated ToF structure in Fig. 8.6(c) is more complicated than that of Fig. 8.6(a) due to the loading of many buckets at the beginning of the deceleration sequence. Figure 8.6(d) further demonstrates the advantage of a lower initial speed, which like 8.6(b) shows only the decelerated phase stable molecular packets. As in Fig. 8.6(b) the baseline of the packets varies as they are decelerated off of the main pulse. Here it is seen that with only $\phi_o = 50^o$, the molecular packet is decelerated down to 26 m/s (contrast this with 296 m/s for the current-loop valve). This slowed packet contains a few thousand molecules at a density of $\sim 10^6$ cm^{-3} and a translational temperature of ~ 100 mK as set by the phase space acceptance of the decelerator.

Based on the matching of the molecular phase space at the entrance of the decelerator to the decelerator acceptance, it is possible to predict the molecule number in a given packet. Shown in Fig. 8.7(a,b) as open circles are the ToF-deconvolved, integrated molecular numbers for the decelerated packets relative to operation at $\phi_o = 0^o$ for the

current-loop valve and solenoid valve, respectively. Also, shown in these figures as solid lines are a simple theory for the dependence of the molecule number in a stable packet on ϕ_o taken from Eqn. 9 of Ref. [61]. The agreement of the theory with the experimental data in Fig. 8.7(a) is excellent, with the only noticeable deviation at $\phi_o = 10^o$. This is likely because we have neglected any effects due to the transverse phase space, and because $\phi_o = 10^o$ experiences more of the slowing field than $\phi_o = 0^o$ it has a larger transverse acceptance, while the longitudinal acceptances are similar. The molecule number instability of the solenoid valve is responsible for most of the deviations from the expected behavior in Fig. 8.7(b). For the data point at $\phi_o = 50^o$, however, the low mean speed allows the pulse to expand spatially much more than $\phi_o = 0^o$ to which it is normalized as it exits the decelerator enroute to the detection region. Thus the data point appears below the expected.

To observe the OH-H_2CO collision and reaction dynamics requires monitoring both the OH population and the production of the formyl radical (CHO). The lowest temperature (228 K) measurement [116] of the reaction finds the reaction rate as $10^{-11}\mathrm{cm}^3\mathrm{s}^{-1}$. Since $E_a \sim 0$ the reaction rate at our temperatures of interest will likely be similar. Thus, for a trap volume of 1 cm^3 and reactant densities of 10^6 cm^{-3} we estimate the reaction rate as 10 molecule s^{-1} and the required signal-to-noise ratio for OH detection at 10^5. For cold H_2CO at 25 m/s colliding with a 1 cm long magnetic trap of OH this leads to a production rate of CHO as one molecule per 250 pulses. Clearly, observation of this reaction with current conditions would be heroic, however, further improvements such as multiple trap loading and secondary cooling of the molecular samples, which will increase the sample density, should make these observations possible.

In summary, we have detailed new methods to study interspecies molecular collision and reaction dynamics, and have shown how control of these processes may be achieved. We have also demonstrated experimental preparation of both cold polar

molecules required for these studies.

Chapter 9

High Resolution Microwave Spectroscopy of OH

9.1   Introduction

Current theories that attempt to unify gravity with the other fundamental forces predict spatial and temporal variations in the fundamental constants, including the fine structure constant, α [93]. Compellingly, a space-time varying coupling constant, such as α, implies violation of both Lorentz invariance and CPT symmetry [75]. Comparison of different atomic clock systems [95] has provided tight constraints on the time variation of various fundamental constants, including α, during the modern epoch. While, observation of absorption lines in distant quasars [136, 99] provides conflicting results about possible α variation over cosmological time. Since the largest α variation may have occurred during the early universe [45], the inconsistent conclusions of the quasar measurements are most interesting. Due to the use of spatially diverse absorbers, these measurements are sensitive to relative Doppler shifts, and therefore an independent confirmation of the variation of α is important.

Recently, there has been much interest in using OH megamasers in interstellar space to constrain the evolution of fundamental constants [39, 34, 70] with several key advantages. Most importantly, the multiple lines (that have different dependence on α) arising from one of these localized sources differentiate the relative Doppler shift from true variation in the transition frequency. Furthermore, if it is assumed that the only fundamental constant to vary is α, it can been shown that the sum and difference of the

ΔF = 0 (F is total angular momentum) transition frequencies in the ground Λ-doublet of OH depend on α as $\alpha^{0.4}$ and α^4, respectively [39]. Thus, by comparing these quantities as measured from OH megamasers to laboratory values it is possible to remove the Doppler shift systematic and constrain α over cosmological time. Furthermore, because of the unique properties of the Λ-doublet, the ΔF = 0 transitions are extremely insensitive to magnetic fields. However, as pointed out by Darling [39], for the current limits on $\Delta\alpha/\alpha$ the change in the relevant measurable quantities is on the order of 100 Hz, which prior to this work was the accuracy of the best laboratory based measurement. Moreover, an astrophysical measurement of OH megamasers, scheduled for later this year, expects a resolution better than 100 Hz [8], and thus better laboratory measurements of the OH Λ-doublet microwave transitions are imminently needed to allow for tighter constraints on $\Delta\alpha/\alpha$.

Despite the prominence of the OH radical in molecular physics, the previous best measurement of the OH ground Λ-doublet, performed by ter Meulen and Dymanus [120], has stood for over 30 years. This lack of improvement was due to the relatively slow progress in the center-of-mass motion control of molecules, which limited the maximum field interrogation time, and thus the spectroscopic resolution. The ability of a Stark decelerator [24, 27] to provide slow, cold pulses of molecules makes it an ideal source for molecular spectroscopy [131]. In this work, a Stark decelerator is used along with standard microwave spectroscopy techniques to perform the best measurement to date of the ΔF = 0, Λ-doublet microwave transitions in OH, which along with appropriate astrophysical measurements can be used to constrain $\Delta\alpha/\alpha$ with a sensitivity of 1 ppm over the last $\sim 10^{10}$ years.

9.2   Experiment

In its ro-vibronic ground state OH is a Hund's case (a) molecule with a $^2\Pi$ configuration and total molecule-fixed angular momentum of $\Omega = \frac{3}{2}$. For the most abundant
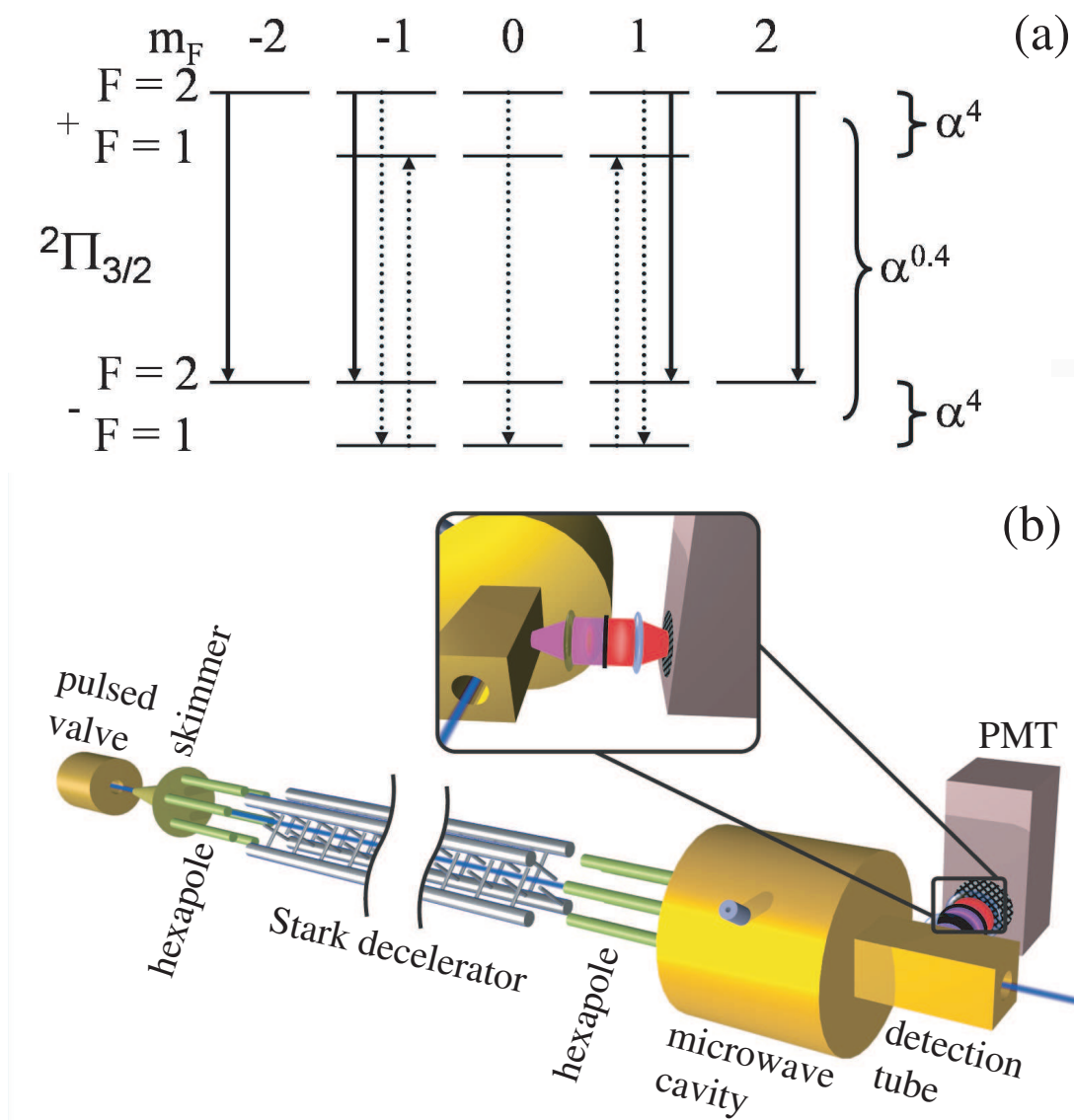
Figure 9.1: (Color online) a) OH ground Λ-doublet state. The arrows represent the effect of the applied microwave pulses for the 2→2 (solid arrows) and 1→1 (dotted arrows) transitions. b) Schematic of experiment (inset depicts detection region).

isotopomer (O^{16}H) the oxygen has no nuclear spin and the hydrogen carries a nuclear spin of $\frac{1}{2}$ leading to two total spin states with F = 1 and 2. Because the unpaired electron in OH has one unit of orbital angular momentum, these ro-vibronic ground states are 'Λ-doubled', leading to the closely spaced opposite parity Λ-doublet states shown in Fig. 9.1(a) labeled as $|F, m_F, \text{parity}\rangle$. Though molecules are decelerated only in the $|2, \pm 2, +\rangle$ and $|2, \pm 1, +\rangle$ states, the field-free region from the hexapole to the microwave cavity leads to an equal redistribution of the population among the five magnetic sub-levels of the F = 2 upper doublet state. In this work, both ΔF = 0 electric dipole transitions between the upper and lower doublet states are studied. Though these transitions exhibit large Stark shifts (as is necessary for Stark deceleration), they show remarkably small Zeeman shifts. In fact, because the magnetic dipole operator respects parity, one expects the ΔF = 0 transitions of a pure case (a) molecule to show no magnetic field dependence. Nonetheless, because the hyperfine splitting differs in the upper and lower doublet, and part of the $|m_F| = 1$ magnetic dipole moment comes from mixing with the other hyperfine component, there is a small quadratic shift of the $|2, \pm 1, +\rangle$ → $|2, \pm 1, -\rangle$ transition frequency (150 Hz/Gauss^2). Furthermore, because OH is not completely case (a) (*i.e.* the electron's orbital angular momentum and spin are slightly decoupled from the axis) the g-factor is slightly larger in the lower doublet [100]. Thus, transitions between the $m_F < 0$ ($m_F > 0$) components are blue-shifted (red-shifted) relative to the zero field value. Hence for experiments probing both positive and negative m_F components such as this work, the g-factor difference leads to a broadening and eventually a bifurcation in the lineshape for increasing magnetic field. This effect, explored at relatively large fields (0.6 - 0.9 T), was found to shift the ΔF = 0 transition frequencies of the $|2, \pm 2, +\rangle, |2, -1, +\rangle$, and $|1, 1, +\rangle$ states at a rate of -sgn(m_F) × 2.7 kHz/Gauss, and the $|1, -1, +\rangle$ and $|2, 1, +\rangle$ states at a rate of -sgn(m_F) × 0.9 kHz/Gauss [100]. For even population distribution this effect leads to a shift of 450 Hz/Gauss and -900 Hz/Gauss for the 2→2 and 1→1 transitions, respectively.
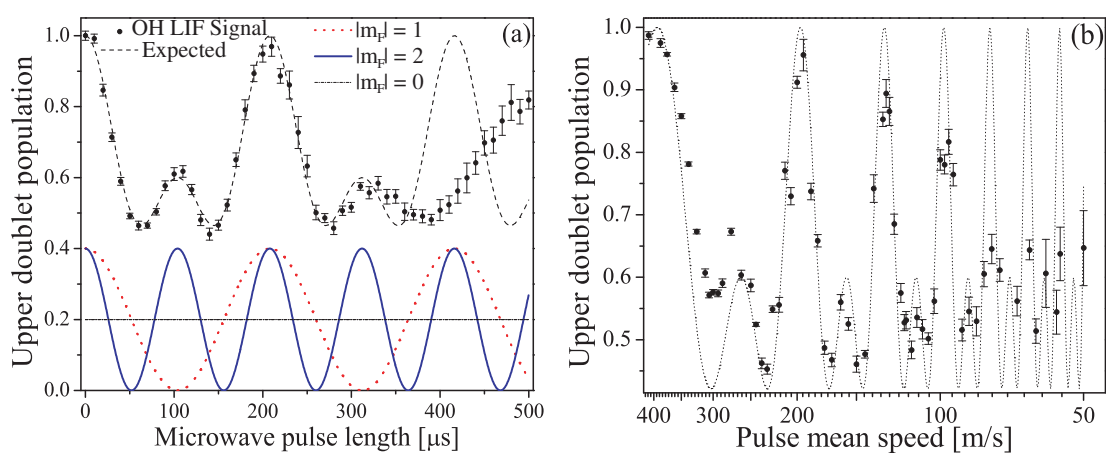
Figure 9.2: (Color online) a) Rabi-flopping as a function of time. The contributions of the individual magnetic sub-levels are shown near the bottom, while the sum is shown as the dashed line. b) Rabi-flopping as a function of velocity for a fixed (spatial) length microwave pulse. The dashed line is the expected.

Shown in Fig. 9.1(b) is a schematic of our experimental setup. OH molecules seeded in Xenon are created in a pulsed discharge [80] producing a molecular pulse with a mean speed of 410 m/s and 10% longitudinal velocity spread. Following a skimmer is an electrostatic hexapole used to transversely couple the molecules into our Stark decelerator, which is described in detail elsewhere [27, 28, 61]. The Stark decelerator is used in a variety of operating conditions, yielding pulses of molecules at a density of 10^6 cm^{-3} with mean speeds chosen between 410 m/s and 50 m/s with longitudinal temperatures between 1 K and 5 mK, respectively. In the current experiment, the present density of the OH beam limits any density related frequency shift to be below 1 mHz. Once the molecular pulse exits the decelerator it is focused by a second hexapole to the detection region. Located between the second hexapole and the detection region is a 10 cm long cylindrical microwave cavity with its axis aligned to the molecular beam. The microwave cavity is operated near the TM$_{010}$ mode, such that the electric field is extremely uniform over the region sampled by the molecules [66]. The microwave cavity is surrounded by highly magnetically permeable material to provide shielding from stray magnetic fields. From measurements of the magnetically sensitive F = 2→F = 1 transition frequency the residual field in the cavity was determined to be < 2 milliGauss. This small field results in an absolute Zeeman shift of < 0.9 Hz and < 1.8 Hz for the 2→2 and 1→1 transitions, respectively. Note that this is a cautious upper-bound on the Zeeman shift, since it is based on work performed at ∼10^7 larger magnetic field where the angular momentum decoupling is enhanced. Furthermore, the use of all metal microwave cavity at the interaction region has removed all electric field related frequency shifts, as an applied external field as large as 700 V/cm resulted in no detectable shift in the measured transition frequencies.

Two independently switchable microwave synthesizers, both referenced to a Cesium standard, are used to provide the microwave radiation for driving the Λ-doublet transitions. For probing the $|2, m_F, +\rangle \rightarrow |2, m_F, -\rangle$ Λ-doublet transition (2→2) only

one synthesizer is needed since the molecules enter the cavity in the F = 2 state. Accordingly, two synthesizers are needed for probing the 1→1 transition. The first synthesizer transfers molecules from the F = 2 upper doublet state to the F = 1 lower doublet state. The second synthesizer then probes the 1→1 transition. After the molecules exit the cavity the population of the upper doublet is probed by laser-induced fluorescence (LIF). For the LIF measurement the molecules are excited along the $^2\Sigma_{1/2}(v = 1) \leftarrow$ $^2\Pi_{3/2}(v = 0)$ line at 282 nm by light produced from a doubled pulsed-dye laser. This excited state decays primarily along $^2\Sigma_{1/2}(v = 1) \rightarrow {}^2\Pi_{3/2}(v = 1)$ at 313 nm. The red-shifted fluorescence is collected and imaged onto a photomultiplier tube coupled to a multi-channel scaler.

To characterize the performance of the microwave cavity the population in the upper doublet was recorded as a function of applied microwave pulse length as shown in Fig. 9.2(a) (so-called Rabi-flopping). For the data shown, the molecules were decelerated to 200 m/s and a microwave pulse resonant with the 2→2 transition was applied such that its midpoint time coincided with the molecules being at the cavity center. Thus, as the pulse length was increased the molecules encountered a pulse that grew symmetrically about the cavity center. Because the LIF detection scheme is sensitive to all molecules in the upper doublet and the applied microwave field simultaneously drives transitions between the different magnetic sub-levels, the Rabi-flopping signal is more complicated than the traditional $\sin^2(\frac{\omega'_R t_p}{2})$. Here ω'_R is the effective Rabi frequency given in terms of the detuning, δ, and Rabi frequency, ω_R, as $\omega'_R = \sqrt{\delta^2 + \omega_R^2}$, and t_p is the microwave pulse length. As shown in Fig. 9.1(a) for the 2→2 transition (solid arrows), both the $|m_F| = 2$ and $|m_F| = 1$ magnetic sub-levels are driven by the microwave field (the $|m_F| = 0$ level has a zero transition moment). Because the electric dipole transition moment of the $|m_F| = 2$ is twice that of $|m_F| = 1$ [18], the Rabi-flopping signal exhibits beating. The calculated individual magnetic sub-level contributions are shown at the bottom of Fig. 9.2(a) with their sum represented by the dashed line plotted over
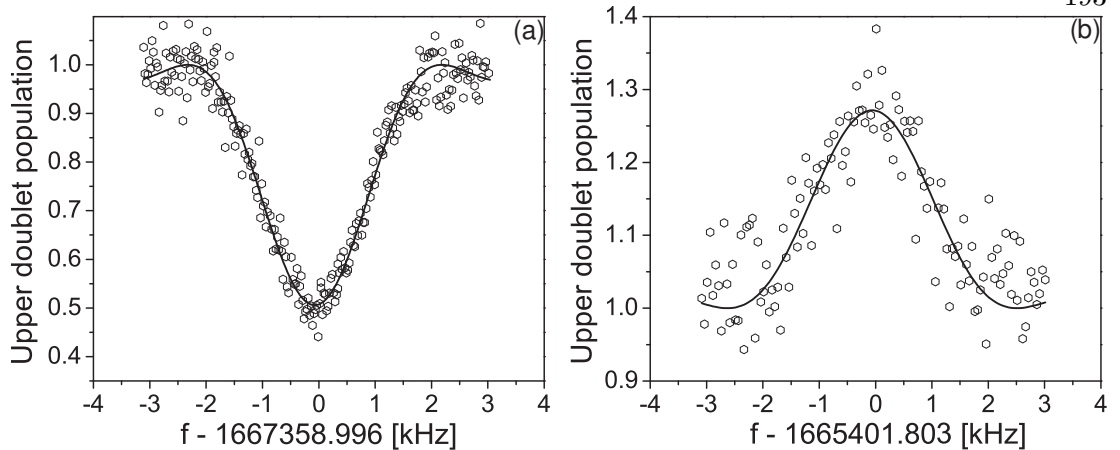
Figure 9.3: Representative line shape of the 2→2 (a) and 1→1 (b) transitions. Both measurements correspond to an interaction time of 0.5 ms (v = 200 m/s). A center frequency is extracted from each fit (solid line).

the data. The data points were determined by comparing the populations in the upper doublet at the detection region with and without the microwave field applied. Clearly, the behavior is exactly as expected until $t_p \geq 300$ μs when ω_R of both the $|m_F| = 2$ and $|m_F| = 1$ transitions appears to decrease. This reduction in ω_R is the result of the electric field diminishing near the cavity end-caps [9].

Alternatively to fixing the molecular velocity, v, and varying t_p, the Stark decelerator allows v to be varied while applying a fixed (spatial) length microwave pulse. This allows a check of systematics associated with beam velocity. Data taken in this manner is shown in Fig. 9.2b, where a microwave pulse resonant with the 2→2 transition was applied for the entire time the molecules were in the cavity. The microwave power for this measurement was chosen such that molecules with a 400 m/s velocity underwent one complete population oscillation (*i.e.* a 2π pulse for the $|m_F| = 1$ and a 4π pulse for the $|m_F| = 2$ transitions). This was done so that population revivals occurred at velocities that were integer sub-multiples of 400 m/s. While the behavior agrees well with the expected (dotted line), there are two noticeable deviations. First, for 270 m/s $\leq v \leq$ 400 m/s the fringe visibility is less than expected. This is because,

as detailed in our earlier work [28, 61], molecules with these relatively high velocities have not been decelerated out of the background molecular pulse. Thus, molecules with a large distribution of speeds (as compared to the decelerated molecules) are detected, leading to reduced contrast. Second, substantial decoherence is observed for $v \leq 130$ m/s. The source of this decoherence has been experimentally determined as the result of microwave radiation leaking from the cavity and being reflected off the decelerator back into the cavity. It is interesting to note that since the metal detection tube acts as a waveguide with a cut-off frequency much higher than that applied, no radiation leaks from the rear of the cavity. Thus, future experiments should include a small waveguide section on both sides of the cavity to prevent leakage. Furthermore, because this decoherence is due to reflected radiation it is microwave power dependent, and presents no problem for the transitions frequency measurements, which use $< 10\%$ of the microwave power used in Fig. 9.2, such that no noticeable decoherence occurs.

9.3   Results

Because two magnetic sub-levels with differing ω_R's undergo the 2→2 transition, the traditional Rabi-spectroscopy method of applying a π pulse over the length of the cavity is not optimal. Thus, for measurements of the 2→2 transition frequency the microwave power was chosen such that for $\delta = 0$ the maximum contrast was produced with as small a microwave power as possible (*i.e.* transfer the molecules to the first dip in Fig. 9.2(a) over the length of the cavity). Representative data for the 2→2 transition is shown in Fig. 9.3(a) where the driving frequency, f, is varied under a fixed microwave power. Data points in this graph were generated by comparing the population in the upper doublet at the detection region with and without the probing microwave field. The fit to the data (solid line) is generated from the typical Rabi lineshape formula except contributions from the different magnetic sub-levels are included. For probing the 1→1 transition it is necessary to prepare the molecules in a F = 1 level since they

originate in the $|2, m_F, +\rangle$ level from the Stark decelerator. This is accomplished by using the first 70 μs the molecules spend in the cavity to drive them on the satellite 2→1 line, yielding molecules in the $|1, \pm 1, -\rangle$ and $|1, 0, -\rangle$ states (downward dotted arrows in Fig. 9.1). The remaining time the molecules spend in the cavity (depending on v) is then used to probe the 1→1 transition frequency by applying a π pulse, which transfers only the $|m_F| = 1$ molecules to the upper doublet (upward dotted arrows in Fig. 9.1). Representative data for the 1→1 transition is shown in Fig. 9.3b. In contrast to the 2→2, line the LIF signal is maximum on resonance because molecules are being transferred into the detected upper doublet. Also, because only 40% of the population participate in the transitions (*i.e.* the $|m_F| = 1$) the contrast between on and off resonance is reduced relative to the 2→2 transition, leading to a slightly larger error for determining the center frequency. For both panels of Fig. 9.3 the molecules were decelerated to 200 m/s yielding linewidths of 2 kHz. A typical fit determines the center frequency within 20 to 50 Hz, depending on the transition. The results of several measurements of both the 2→2 and 1→1 center frequencies are displayed in Fig. 9.4. Each point and its error bar represents the result of a fit to a measured lineshape like those shown in Fig. 9.3. Using the standard error of each fit as a weight the mean and standard error of the transition frequencies are found to be (1 667 358 996 $\pm$ 4) Hz and (1 665 401 803 $\pm$ 12) Hz for the 2→2 and 1→1, respectively. For comparison, the lightly hatched boxes represent the bounds set on the transition frequency by the previous best measurement [120], while the limits produced by this measurement are displayed as darker cross-hatched boxes. The transition frequencies reported here are limited only by statistical uncertainties, as we estimate the uncertainties due to the aforementioned systematic shifts as ($< .001$ (collision shift) + < 2 (magnetic field) + $< .001$ (electric field) + < 1 (doppler shift)) Hz.

The Ramsey technique of separated pulses inside the same microwave cavity was also used to measure the transition frequencies as seen in Fig. 9.5 with a resolution
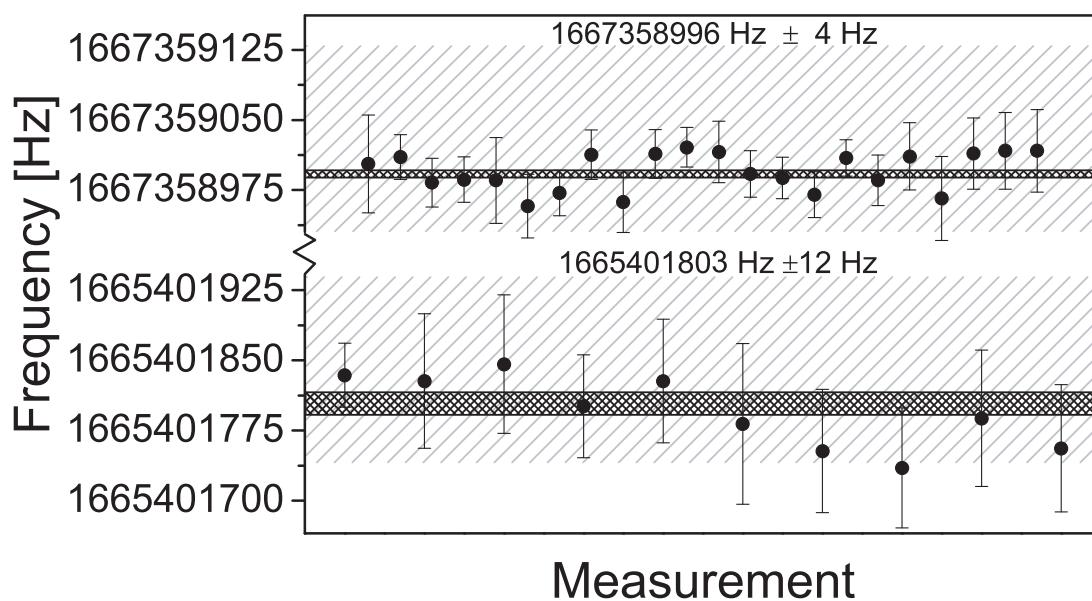
Figure 9.4: Results of multiple measurements of the 2→2 transition (upper) and the 1→1 transition (lower).
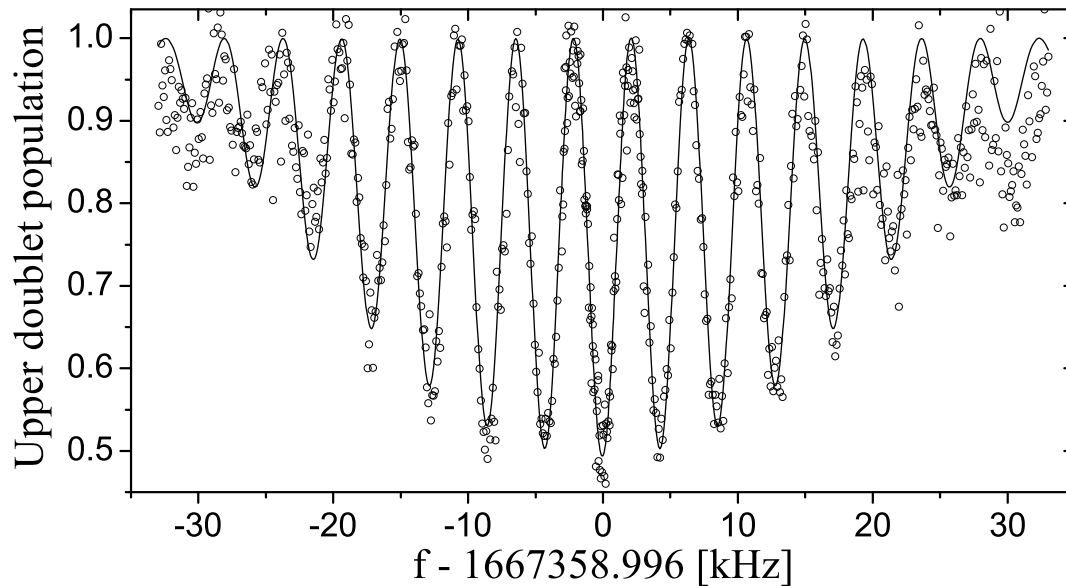
Figure 9.5: Ramsey spectroscopy for the 2→2 transition with 0.2 ms pulse separation time.

comparable to the reported Rabi measurements. However, because the molecular pulses are extremely mono-energetic, minimal gain was observed in the recovered signal-to-noise ratio. This technique will of course be critical for any future molecular fountain clock. The molecular clock could enjoy reduced systematic shifts, such as the magnetic field insensitive transitions demonstrated in this work. It will be most interesting to compare an atomic clock against a molecular one which depends differently on the fine structure constant.

In summary, microwave spectroscopy was performed on slow, cold molecular pulses produced by a Stark decelerator resulting in the most precise measurement of the OH $\Delta F = 0$, Λ-doublet transitions. These results along with appropriate astrophysical measurement of OH megamasers can be used to produce constraints on $\Delta\alpha/\alpha$ with a sensitivity of 1 ppm over the last $\sim 10^{10}$ yr. At the same time the use of cold molecules for the most precise molecular spectroscopy has been demonstrated. Specifically, by producing slow, cold molecular packets the Stark decelerator allows increased interrogation time, while virtually eliminating any velocity broadening. With continued improvement in precision of the astrophysical measurement of the OH megamaser transitions through either long period of data collection/averaging and/or discoveries of new megamaser sources, measurement of this molecular system will provide an important and independent constraint on the variation of fundamental constants that date back to the origin of the universe.

Chapter 10

Not Enough Hours in the Day

This chapter is a collection of several disjoint topics, which we have considered over my stay at JILA. I feel these topics, which do not fit into any of the other chapters, are important enough to future cold molecule work that I have included them here.

10.1   Polar Molecule Collisions

Understanding the collision properties of molecules at cold and ultra-cold is critical to their efficient production and storage. As mentioned in the Introduction, the electric dipole moment possessed by polar molecules fundamentally alters the molecular collision dynamics. Specifically, the long-range dipole-dipole interaction,

$$V_{dd} = \frac{1}{4\pi\epsilon_o r^3} \left(\mu_{\mathbf{1}} \cdot \mu_{\mathbf{2}} - \frac{3(\mu_{\mathbf{1}} \cdot \mathbf{r})(\mu_{\mathbf{2}} \cdot \mathbf{r})}{r^2} \right), \tag{10.1}$$

where μ_i is the electric dipole moment of the colliding molecules and $\mathbf{r}$ is the vector connecting the two molecules, dominates over the other molecule-molecule interaction. The group of John Bohn has pioneered the study of cold polar molecule collisions [18, 19, 122], utilizing carefully calculated potential surfaces and coupled channels calculations. From their calculations, polar molecules are predicted to have elastic and inelastic scattering rates that are large and depend dramatically on electric field. Interestingly, because polar molecule collisions are dominated by the dipole-dipole interaction, it is possible to estimate their elastic collision rates with surprising accuracy from analytical methods.

The next two subsections presents the elastic cross-section predicted by two of these methods, the Born approximation and the Eikonal approximation, and discusses their respective range of validity.

10.1.1   Born Approximation

The exact formulation of the scattering problem, the Lippmann-Schwinger equation, is an integral equation of the scattering particle's wavefunction and impossible to solve. The Born approximation assumes that if the scattering particles' interaction is 'not-too-strong' it is acceptable to replace the wavefunction in the integral with the incoming wavefunction. Doing this results in the famous result for the first-order Born amplitude [108]

$$f(\mathbf{k}, \mathbf{k}') = -\frac{1}{4\pi} \frac{2m}{h^2} \int e^{\imath(\mathbf{k}-\mathbf{k}')\cdot\mathbf{x}'} V(\mathbf{x}') d^3 x, \tag{10.2}$$

where m is the particle mass, $\mathbf{k}$ and $\mathbf{k}'$ are the initial and final momenta, and $V(\mathbf{x}')$ is the scattering potential. The differential cross-section, $\frac{d\sigma}{d\Omega}$, is given as $\frac{d\sigma}{d\Omega} = |f(\mathbf{k}, \mathbf{k}')|^2$.

For scattering via the long range dipole-dipole potential, $V_{dd}(R)$, Eq. 10.2 becomes

$$f(\mathbf{k}, \mathbf{k}') = \frac{m}{\hbar^2} \frac{\mu^2}{4\pi\epsilon_o} \int_0^\infty r^2 dr \int_{-1}^1 e^{\imath qr\cos\theta} \frac{1 - 3\cos^2\theta}{r^3} d(\cos\theta) = \frac{m\mu^2}{3\pi\epsilon_o\hbar^2}, \tag{10.3}$$

where we have used the usual $\vec{q} = \vec{k} - \vec{k}'$, $\vec{q} \parallel \hat{z}$, and taken the molecular dipole moments as a parallel to an electric field pointing at an angle θ reltative to the $\hat{z}$-direction. Finally, we have the cross-section as given by the Born approximation as

$$\sigma_{Born} = \frac{4m^2\mu^4}{9\hbar^4\pi\epsilon_o^2}. \tag{10.4}$$

For OH in the $|2 \pm 2+\rangle$ state, in an external electric field high enough to saturate its dipole moment, we have $\sigma_{Born} = 1.5 \times 10^{-8} cm^2$. Clearly, this large, elastic cross-section is encouraging for the possibility of evaporative cooling, however, before definite predictions can be made the range of validity of the Born approximation must

be understood. The condition that the interaction is 'not-too-strong' means that for the Born approximation to be valid the incoming wavefunction cannot be that different from the true out-going wavefunction. From the Lippmann-Schwinger equation this condition takes the form [108]

$$\left| \int_0^\infty dr r e^{\imath kr} \int_{-1}^1 e^{\imath kr \cos\theta} \frac{1 - 3\cos^2\theta}{r^3} d(\cos\theta) \right| \ll \frac{4\pi\hbar^2}{2m} \frac{4\pi\epsilon_o}{\mu^2}. \tag{10.5}$$

Using, $\hbar k = mv$ and $T = mv^2/3$ we have for the validity of the Born approximation

$$T \ll T_{Upper} = \frac{m}{3k_B} \left(\frac{12\hbar^3 \pi \epsilon_o}{m^2 \mu^2} \right)^2. \tag{10.6}$$

For OH in the $|2 \pm 2+\rangle$ state, in an external electric field high enough to saturate its dipole moment, this constraint reveals that the Born approximation is valid at temperatures less than 150 nK. This small range of validity for the Born approximation is a direct consequence of the strong, long-range nature of the dipole-dipole interaction. Nonetheless, the Born approximation provides a useful upper bound on the elastic collision cross-section of polar molecules. Furthermore, at low temperatures it agrees quite well with the more accurate calculations of the Bohn group.

10.1.2   Eikonal Approximation

The Eikonal approximation is valid when the interaction potential, $V_{dd}(R)$, does not vary considerably over the scale of the deBroglie wavelength of the scattering particle. This approximation complements the Born approximation since it is appropriate as long as the collision energy, E, is much greater than the interaction strength. The basic idea of the Eikonal approximation is that at these energies the idea of a semiclassical path is reasonable and the wavefunction can be replaced by a semiclassical wavefunction. The derivation proceeds using the usual approximations of WKB theory and can be found in most any textbook [108] with the scattering amplitude given as

$$f(\mathbf{k}, \mathbf{k}') = -\imath k \int_0^\infty db b J_o(kb\theta) [e^{2\imath\Delta(b)} - 1] \tag{10.7}$$

with the phase given by

$$\Delta(b) = \frac{-m}{2k\hbar^2} \int_{-\infty}^{\infty} V(\sqrt{b^2 + z^2}) dz, \tag{10.8}$$

where b is the well-known impact parameter and J_o is the zeroth Bessel function of the first kind. Using the optical theorem, the Eikonal scattering cross-section is given as

$$\sigma_{Eik} = \frac{4\pi}{k} Im(f(\mathbf{k}, \mathbf{k})) = 4\pi \int_0^{\infty} dbb(1 - cos(2\Delta(b))). \tag{10.9}$$

In the case of the anisotropic dipole-dipole interaction the integral in Eq. 10.8 is zero if the impact parameter is held constant during integration. While the anisotropic dipole-dipole interaction can be treated with a 'tilted' impact parameter, it is more difficult and the results are very similar to that of the isotropic dipole-dipole interaction ($V_{dd}^{iso} = \frac{1}{4\pi\epsilon_o} \frac{\mu_1 \cdot \mu_2}{r^3}$), which is trivially calculated. Replacing V_{dd} with V_{dd}^{iso}, the integrals of Eqs. 10.8 and 10.9 are straight-forward and yield the Eikonal cross-section as

$$\sigma_{Eik} = \frac{2\pi^2\mu^2}{4\pi\epsilon_o\hbar v}, \tag{10.10}$$

where v is the velocity of the colliding particle. We can make a rough estimate of the range of validity of the Eikonal approximation by defining the length scale of the V_{dd} as equal to the value of r where the dipole-dipole interaction is equation to the incoming kinetic energy

$$\frac{3}{2} k_B T = \frac{\mu^2}{4\pi\epsilon_o r_{Char}^3} \tag{10.11}$$

Note that this is akin to saying for a molecule at temperature T, V_{dd} does not vary appreciable for $r \geq r_{Char}$. The requirement that the deBroglie wavelength be less than this characteristic length scale can be written as

$$\frac{h}{\sqrt{3mk_B T}} < \left(\frac{\mu^2}{6k_B T \pi \epsilon_o} \right)^{1/3}. \tag{10.12}$$

Rearranging this equation leads to a constraint on the temperature, T, for the validity of the Eikonal approximation:

$$T > \frac{4h^6\pi^2\epsilon^2}{k_B m^3 \mu^4}. \tag{10.13}$$

For OH in the $|2 \pm 2+\rangle$ state, in an external electric field high enough to saturate its dipole moment, this leads to the constraint that the Eikonal approximation is valid for T > 1 mK.

The cross-section predicted by the Eikonal approximation for OH in the $|2 \pm 2+\rangle$ state, in an external electric field high enough to saturate its dipole moment,is shown in Fig. 10.1. For comparison the temperature independent Born approximation cross-section is also shown. The vertical blue (left) line denotes the high temperature bound for the range of validity of the Born approximation, while the vertical red (right) line denotes the low temperature bound for the range of validity of the Eikonal approximation. Comparisons of the results of Fig. 10.1 with the more careful calculations [19], show that the Born and Eikonal approximations do a remarkably good job of estimating the cross-section. In fact, the real cross-section essentially follows the Eikonal approximation with temperature until it reaches the value given by the Born approximation. After reaching the Born approximation value, the cross-section levels off and follows the Born approximation at lower temperatures. This behavior is not too surprising, because the lower temperature bound that we have placed on the Eikonal approximation is quite cautious, since on the length scale of r_{Char} the potential is still relatively flat.

Because the electric dipole moment of a polar molecule depends on the electric field, the strength of $V_{dd}(R)$ is also field dependent. Using Eq. 2.21 for the dipole moment as a function of electric field, the cross-section is plotted in Fig. 10.2. In this graph, the Eikonal approximation is used for $T > 150nK$ and the Born approximation is used for $T < 150nK$. As the field is initially increased the dipole moment increases and consequently, so does the cross-section. Likewise, once the dipole moment is saturated the cross-section no longer increases with field. For temperatures where the Born approximation is valid, the cross-section does not depend on temperature and follows the top-most curve.
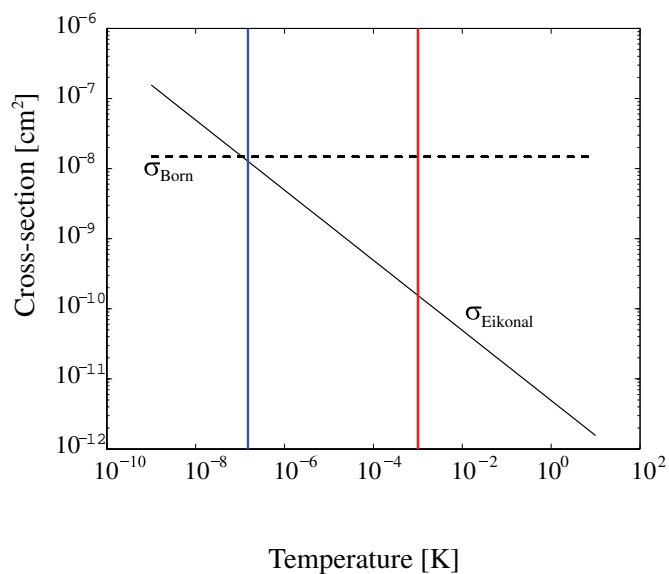
Figure 10.1: The Born and Eikonal approximations for OH-OH dipole-dipole collisions, in an external electric field high enough to saturate the OH dipole. The Born approximation is valid to the left of the blue (left) vertical line, while the Eikonal approximation, strictly speaking, is valid to the right of the red (right) vertical line. Comparison, with more careful calculations show the predictions of the Eikonal approximation are actually quite good down to the temperature at which the cross-section of the Born and Eikonal approximation are comparable.
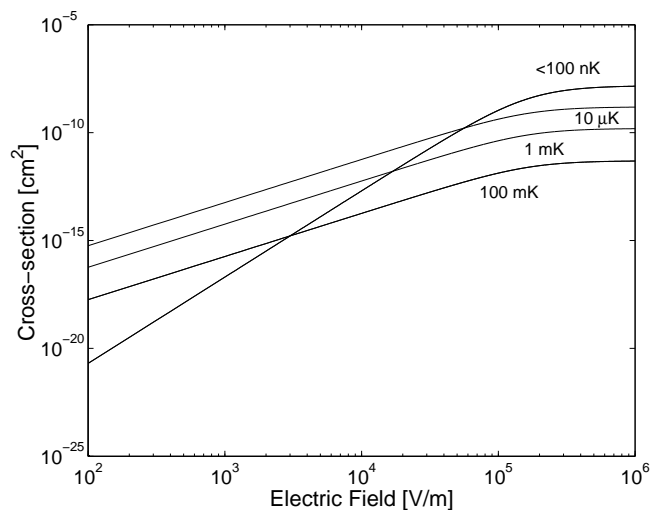
Figure 10.2: OH-OH cross-sections as a function of electric field for several temperatures.

10.2   Sympathetic Cooling

One possibility for further cooling of polar molecules is by elastic collisions with a colder gas, so-called sympathetic cooling. Like the buffer gas cooling described in Chap. 1, sympathetic cooling of polar molecules would be performed by trapping the polar molecule in a region of high density cold gas. Since current molecule production techniques already produce molecules around 1 mK, and the cold gas for sympathetic cooling must be colder than this, laser cooled atoms seem the only viable choice for the buffer gas. Experimentally, sympathetic cooling with laser cooled atoms may be implemented by co-trapping the laser cooled atoms with the polar molecules. Since radical molecules, like OH, have large magnetic moments the simplest sympathetic cooling scheme would be to confine both the polar molecule and laser cooled atom in a single magnetic trap and allow them to thermalize. However, the laser cooled atom will fill a much smaller volume in this trap than the warmer polar molecules, and thus, the probability for cooling collisions is reduced. As such, it will likely be better to trap the polar molecules in an electric field. The strength of the confining electric field can then be used to match the polar molecule volume to the volume of the magnetically trapped laser cooled atoms. Furthermore, by trapping the polar molecules in their absolute ground state (in an AC Stark trap [130]) inelastic collisions are removed, making each collision a cooling collision. Therefore, the only limit to the sympathetic cooling process is the trap lifetime. And for successful sympathetic cooling, we require the elastic collision rate to be sufficiently greater than the inverse trap lifetime, such that the cooling can be completed before the molecules are lost from the trap.

The van der Waals interaction will be the dominant potential between a polar molecule and a laser cooled atom. To zeroth order this can be approximated as the result of the polar molecule polarizing the atom and then interacting with the induced
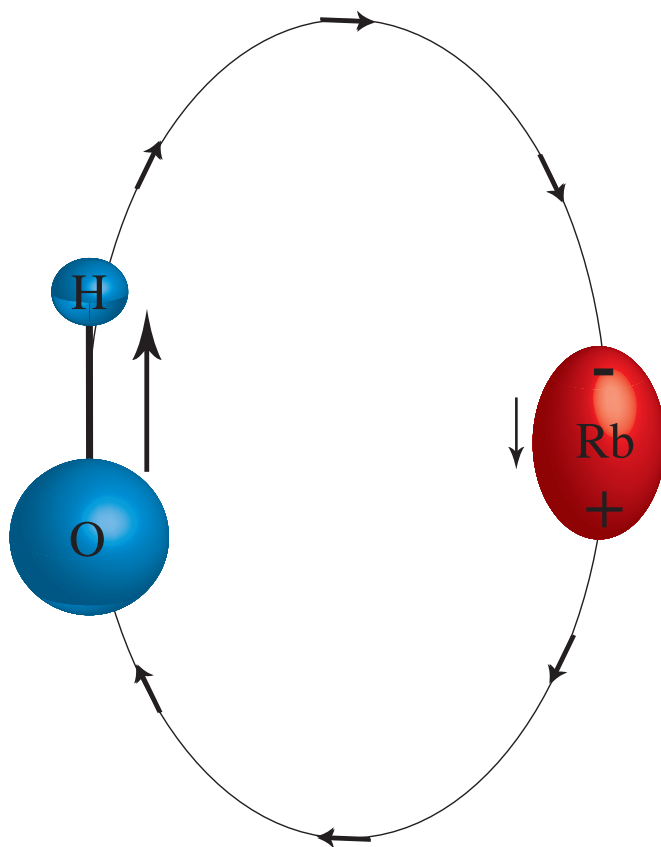
Figure 10.3: Schematic of the OH-Rb collision interaction.
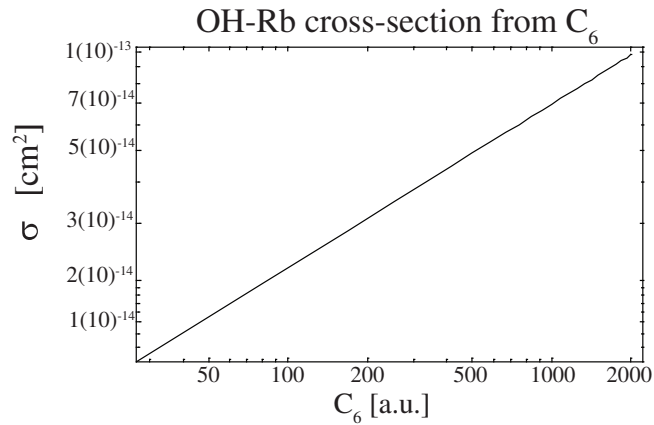
Figure 10.4: OH-Rb collision cross-section versus C_6.

dipole moment, as shown in Fig. 10.3 for the case of OH and Rb,

$$V_6 = \frac{-\mu_{pm}\mu_{atom}}{2\pi\epsilon_o r^3} = \frac{-\mu_{pm}\left(\alpha_{atom}\frac{\mu_{pm}}{4\pi\epsilon_o r^3}\right)}{2\pi\epsilon_o r^3} = \frac{C_6}{r^6}, \tag{10.14}$$

where μ_{pm} and μ_{atom} are the dipole moments of the polar molecule and the atom, respectively, α_{atom} is the polarizability of the atom, and C_6 is the van der Waals coefficient. From this simple estimation, we find $C_6 = 50$ a.u for OH-Rb collisions.

A better estimation of C_6 can be made from second-order perturbation theory with the dynamic polarizability integral [44, 43]

$$C_6 = \frac{3}{\pi} \int_0^\infty \alpha_{pm}(\omega)\alpha_{atom}(\omega)d\omega \tag{10.15}$$

with

$$\alpha_i(\omega) = \sum_n \frac{\delta_{n,i}\mu_{n,i}^2}{\delta_{n,i}^2 + \omega^2}, \tag{10.16}$$

where $\mu_{n,i}$ and $\delta_{n,i}$ are the is the transition dipole moment and transition frequency, respectively, of the nth transition in particle i. This method is quite accurate, and for comparison it gives a C_6 value for Rb-Rb collisions that is 90% of the measured value. The extra 10% comes from atom core effects, which are clearly not accounted for in this approximation. In the case of OH-Rb collisions this method gives $C_6 = 282$ a.u. [10]. From the C_6 constant it is trivial to estimate the scattering cross-section from the

theory of Gribakin and Flambaum [54]. It should be noted that this theory is valid only in the semi-classical limit, where the idea of a trajectory is still a decent approximations, and may fail when the molecules are sufficiently cooled by the buffer gas. A graph of this result for the cross-section is shown in Fig. 10.4. From this graph, we see the cross-section for the range of predictions of C_6 is around 4×10^{-14} cm^2. From Eq. 1.3 with 100 μK buffer gas and 100 mK molecular gas, 40 collisions are required to bring the molecular gas temperature within 2% of the buffer gas. Using a buffer gas density of $\rho = 10^{10}$ cm^{-3} and 10 mK as the average temperature of molecular gas (calculated from Eq. 1.3 for 40 collisions), and our estimated value of the cross-section, we have the collision rate as $\Gamma = \rho \sigma v = 0.002$ Hz. And thus, the molecules would need to be trapped for sim6 hours to come into thermal equilibrium with the cold buffer gas.

Though the outlook seems grim for sympathetic cooling of polar molecules there may still be some possibilities. For example, using large electric fields to polarize the laser cooled atoms would increase the collision rate (though simple estimates show only a 10$\times$ increase in the cross-section). Furthermore, it is expected that the cross-section increases with decreasing collision energy [69], which would make the estimations given here a little cautious. Perhaps the best chance at sympathetic cooling is to use metastable laser cooled nobel gases like xenon or cold Rydberg atoms. These particles are easily polarized and would have a larger collision cross-section with polar molecules, however, their large internal energies may present a problem if inelastic collisions are prominent.

10.3   Para-electric Cooling

Because the entropy of a collection of polar molecules depends on the polarization of the sample, para-electric cooling (PEC), an analog to adiabatic demagnetization refrigeration (ADR) [97], is possible. PEC would proceed by using an external electric field to polarize a sample of polar molecules in the presence of a thermal reservoir.
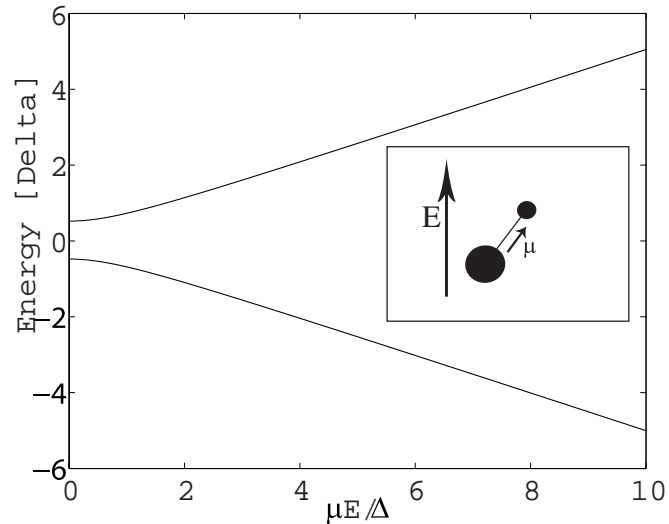
Figure 10.5: Simple model for describing the features of para-electric cooling.

The entropy of this sample, polarized at temperature T_i, is equal to the entropy of an unpolarized sample at temperature, $T < T_i$. Thus, by removing the electric field and allowing the spin degree of freedom to equilibrate with the thermal degrees of freedom the sample cools to temperature T.

The essential features of PEC can be described by the toy-model presented in Fig. 10.5, where the energy difference between states due to the Stark shift is simply given as

$$E = 2\epsilon\sqrt{\frac{\Delta}{2} + (\mu E)^2} = \Delta\epsilon\sqrt{1 + \left(\frac{2\mu E}{\Delta}\right)^2}. \tag{10.17}$$

As seen in the above equation, the key difference between PEC and ADR is that the Stark shift couples opposite parity states, which can be degenerate only for symmetric top molecules. Thus, even at low-field, the states representing parallel (strong-field seeking) and anti-parallel (weak-field seeking) to the electric field are usually not degenerate, which leads to a limit to the ultimate temperature. If interactions between molecules are neglected, the behavior of a sample of these polar molecules is given by

the one-particle partition function

$$Q = \sum_{\epsilon=-}^{+} e^{\beta E(\epsilon,|\vec{E}|)} = \left(1 + e^{-\beta\Delta\sqrt{1+\left(\frac{2\mu E}{\Delta}\right)^2}}\right), \qquad (10.18)$$

where $\beta = 1/(k_B T)$. From the partition function we have the entropy, S, and polarization, P, as

$$\frac{S}{R} = \frac{\delta T \ln(Q)}{\delta T} = \ln(Q) + \beta\Delta\sqrt{1+\left(\frac{2\mu E}{\Delta}\right)^2}\frac{Q-1}{Q} \qquad (10.19)$$

$$\frac{P}{R} = \frac{1}{Q}\sum_{\epsilon=-}^{+} \mu\epsilon e^{\beta E(\epsilon,|\vec{E}|)} = \mu\frac{1 - e^{-\beta\Delta\sqrt{1+\left(\frac{2\mu E}{\Delta}\right)^2}}}{1 - e^{-\beta\Delta\sqrt{1+\left(\frac{2\mu E}{\Delta}\right)^2}}} = \mu\tanh\left(\beta\Delta\sqrt{1+\left(\frac{2\mu E}{\Delta}\right)^2}\right), \qquad (10.20)$$

where R is the universal gas constant and thus these quantities are per mole.

The basic scheme of PEC is shown in Fig. 10.6(a). Starting with a 'warm' sample in zero field (circle #1) an electric field is applied that polarizes the molecules. Depending on the strength of the field the entropy is lowered (circle #2 or #2'). Because the molecules are in contact with a thermal reservoir, *e.g.* a cloud of laser cooled atoms, their temperature is not increased since any liberated energy from the dipole is absorbed by the reservoir. Next, the thermal bath and the electric field is removed, allowing the polar molecule sample to depolarize, leading to a lower temperature. Effectively, the extra thermal energy has went into depolarizing the molecules, *i.e.* internal energy. From the two possible paths in Fig. 10.6(a) and (b) it is seen that the degree of initial polarization (or reduction in entropy) sets the final temperature. Furthermore, it is seen from the $|\vec{E}| = 0$ trace in Fig. 10.6(a) that it is impossible to get below a certain temperature. This is feature is specific to PEC and is a direct result of the non-degeneracy at zero-field of weak- and strong-field seeking states. Because the cooling of the translational degrees of freedom comes from putting energy in the internal degrees of freedom, once the translational energy falls below the zero-field energy splitting the depolarization ceases since there is not enough energy to flip a strong-field seeking
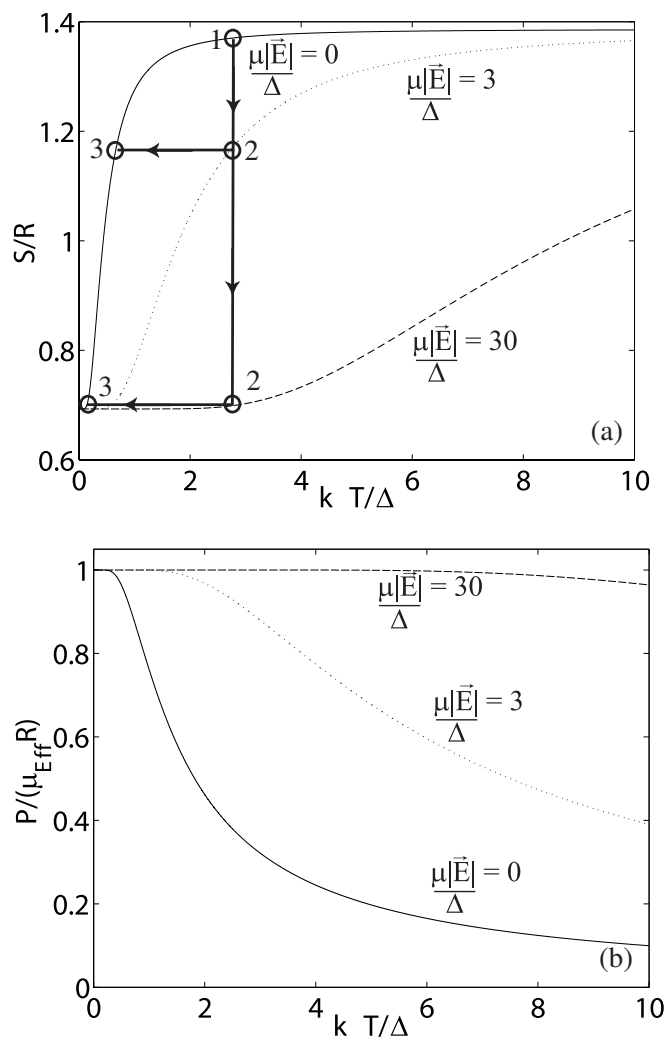
Figure 10.6: (a) Entropy per unit mole of a sample of polar molecules. (b) Polarization per unit mole of a sample of polar molecules.

Table 10.1: Minimum attainable temperatures using para-electric cooling.

Molecule	Minimum PEC Temperature
OH	16 mK
NH	1 μK
ND$_3$	16 mK
H$_2$CO	46 mK
Symmetric Top	$\sim$0

molecule to the weak-field seeking state. Because at a finite temperature there is a velocity distribution this minimum temperature can be significantly less than the zero-field energy splitting and from Fig. 10.6(a) is found to be around $\Delta/5$. This minimum temperature for a few important molecules is given in Tab. 10.1.

From this table it is clear that PEC may have limited usefulness for molecules like OH and H$_2$CO, which have large zero-field energy splittings. However, the process could be very useful for molecule like NH, which have a very small zero-field energy splitting. Furthermore, symmetric top molecules, like CH$_3$CN, which can be degenerate in zero field could be cooled to extremely low temperatures. In ADR, the only limit to the final temperature is the second order phase transition of spontaneous magnetization. Once the magnetic dipoles spontaneously align they generate a magnetic field, which limits the final temperature. For electric dipole moments at low energies the dipoles will want to be anti-parallel and this limit should not exist. Therefore, this technique could be used to get to extremely low temperatures, and perhaps, is a likely road to a degenerate gas.

It is worth noting that several assumptions have been made in the previous analysis. First, by dealing with thermodynamical properties we have assumed that the gases have reached equilibrium. Second, the gases move towards equilibrium through collisions. Thus, we require that collision rate between the polar molecules and the laser cooled atoms, serving as a temperature reservoir, be large enough to reach equilibrium

within the trap lifetime. Furthermore, the polarizing and depolarizing collisions are by definition inelastic and we thus require a state insensitive trap. From the previous section on sympathetic cooling we note that the collision rates for current densities and temperatures is probably too small for efficient PEC. Nonetheless, PEC may still be useful for two reasons. First, since Stark decelerated molecules are in the weak-field seeking state, the first step in PEC of polarizing the molecules along the field could be replaced by a microwave pulse, which transfers the molecules to the strong-field seeking state with unit efficiency. Second, it may be that PEC can be used after some other type of cooling has produced molecules in the microKelvin regime to reach even lower temperatures, since in the microKelvin regime collisions should be much more efficient at depolarizing the sample.

10.4   Cavity-Assisted Doppler Cooling

While various forms of cavity-cooling for a single atom trapped in a cavity [142] have existed for some time [128, 85], recently a proposal for cavity-assisted Doppler cooling by the Vuletic group has appeared [133, 132] that may hold promise for cooling large numbers of molecules. A schematic of the implementation of this method is shown in Fig. 10.7(a), where a cloud of molecules held at the center of a cavity (by some trapping force) is irradiated with laser-light that is far detuned from any transition. By sufficient detuning of the incident light, the probability of a molecule being in the excited state is exceedingly small, and thus the problem of finding a closed transition for molecular laser cooling is avoided. At these large detunings the time-scale on which conservation of energy can be violated is small, and thus the scattering of photons is best described by two-photon processes, *i.e.* Rayleigh scattering. The basic idea of cavity-assisted Doppler cooling is that for a molecule cloud with finite temperature the Rayleigh scattered light will be Doppler shifted to the red and blue of the incident laser-light at ω (see Fig. 10.7(b)). Thus, if a cavity is placed around the molecules that

sufficiently modifies the electromagnetic mode density and its resonance is tuned to the blue of ω, the molecules will preferentially scatter blue-shifted Rayleigh light and will be cooled (see Fig. 10.7(c)).

Of course, before definitive predictions can be made about the feasibility of cavity-assisted Doppler cooling a detailed analysis of the scattering rates involved must be done. We analyze the situation for the case of a 3-level molecule as shown in Fig. 10.8. The molecules start in the ground state, **a**, and can scatter photons from the laser at ω via the excited state **b**. Depending on detuning and saturation, there are several possibilities for the atom-photon interaction; absorption followed by spontaneous emission, Rayleigh scattering through **b** back to **a**, and Raman scattering through **b** to state **c**. Note that a scattering event that leaves the molecule in state **c** is undesirable since state **c** will no longer interact appropriately with the cooling laser and will likely be ejected from any trap. In the far detuned limit, we need only worry about the two-photon analog to spontaneous emission, spontaneous Raman scattering. Raman scattering occurs via the same process as Rayleigh scattering, and thus, depends on the laser detuning in the same way. The Raman and Rayleigh rates are easily derived from Fermi's golden rule. Starting from Eq. 5 on page 525 of Ref. [35], where the Born expansion has been used to evaluate the transition matrix to second order, we find the Rayleigh and Raman rates as

$$\Gamma_{aa} = \frac{8\pi}{3} \frac{I}{\hbar\omega} \frac{2\pi}{\hbar} |T_{aa}|^2 \frac{(\hbar\omega)^2}{\hbar^3 c^3} \tag{10.21}$$

$$\Gamma_{ac} = \frac{8\pi}{3} \frac{I}{\hbar\omega} \frac{2\pi}{\hbar} |T_{ac}|^2 \frac{(\hbar\omega')^2}{\hbar^3 c^3} \tag{10.22}$$

with

$$T_{ai} = \frac{\mu_{ab}\mu_{bi}}{2\epsilon_o} \frac{(2\omega_{ab} + \omega' - \omega)\sqrt{\omega\omega'}}{(\omega_{ab} + \omega)(\omega_{ab} - \omega')} \tag{10.23}$$

where Γ_{aa} is the Rayleigh scattering rate, Γ_{ac} is the Raman scattering rate, I is the laser intensity, μ_{xy} is the transition dipole moment between states **x** and **y**, ω is the laser and Rayleigh photon frequency, ω_{ab} is the resonance frequency between states **a**
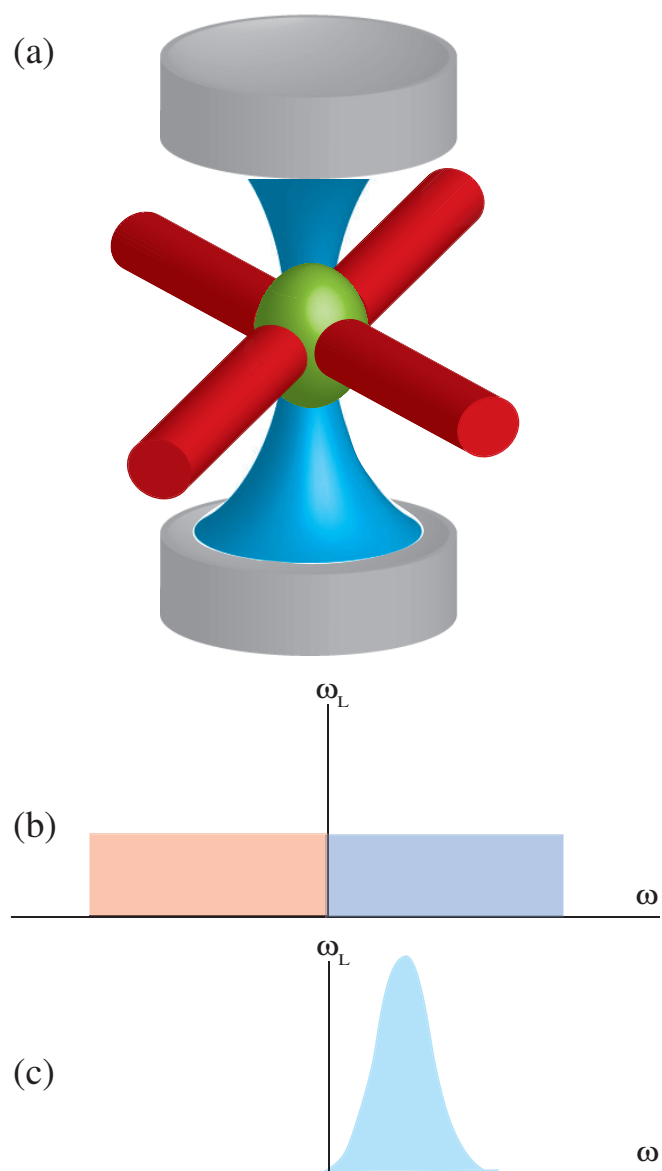
Figure 10.7: (a) Schematic of cavity cooling set-up. (b) Rayleigh scattered spectra of molecules with a finite temperature. (c) The Rayleigh scattered spectra of (b) in the presence of a high finesse optical cavity.

and **b**, ω' is the Raman photon frequency, and for $i = a$ ω' is replaced by ω. Thus, we have the Rayleigh and Raman scattering rates as

$$\Gamma_{aa} = \frac{I}{\hbar\omega}\frac{\omega^4}{6\pi\hbar^2\epsilon_o^2 c^4}\mu_{ab}^4\left(\frac{2\omega_{ab}}{\omega_{ab}^2 - \omega^2}\right)^2 \tag{10.24}$$

$$\Gamma_{ac} = \frac{I}{\hbar\omega}\frac{\omega\omega'^3}{6\pi\hbar^2\epsilon_o^2 c^4}\mu_{ab}^2\mu_{bc}^2\left(\frac{(2\omega_{ab} + \omega' - \omega)}{(\omega_{ab} - \omega)(\omega_{ab} + \omega')}\right)^2. \tag{10.25}$$

Since Raman scattering pumps the molecule to a dark state, we require $\Gamma_{aa} \gg \Gamma_{ac}$ for cavity-assisted doppler cooling to work as proposed in Ref. [132].

For a real molecule, the complex ro-vibrational structure means there are many states accessible by Raman scattering. This can be accounted for in the above picture by replacing the properties of state **c** by the net properties of all the Raman accessible final states, that is

$$\widetilde{\mu}_{bc} = \sum_{i=1}^{N}\mu_{bi} \tag{10.26}$$

$$\widetilde{\omega}' = \frac{1}{N}\sum_{i=1}^{N}\omega_i' \tag{10.27}$$

$$\tag{10.28}$$

In the case of the OH radical, the significant allowed Raman transition are to several rotational components of the ground and first-excited vibrational states. Since scattering through the first electronic excited state requires a laser photon in the ultra-violet (308 nm) and the ro-vibration spacings are at most in the infrared, one can assume $\omega = \omega'$ without loss of accuracy. With this assumption, the ratio of Raman and Rayleigh scattering rates becomes[1]

$$\frac{\Gamma_{ac}}{\Gamma_{aa}} = \left(\frac{\widetilde{\mu}_{bc}}{\mu_{ac}}\right)^2 = 6.5. \tag{10.29}$$

Clearly, our requirement that the Rayleigh rate dominate over the Raman rate is not met, and cavity-assisted doppler cooling as proposed in Ref. [132] will not work for OH. In fact, this result should be quite general for most molecules since there are typically

---

[1] This ration is calculate for the R3/2 line, which is the lowest frequency stretched transition from the OH ground state.
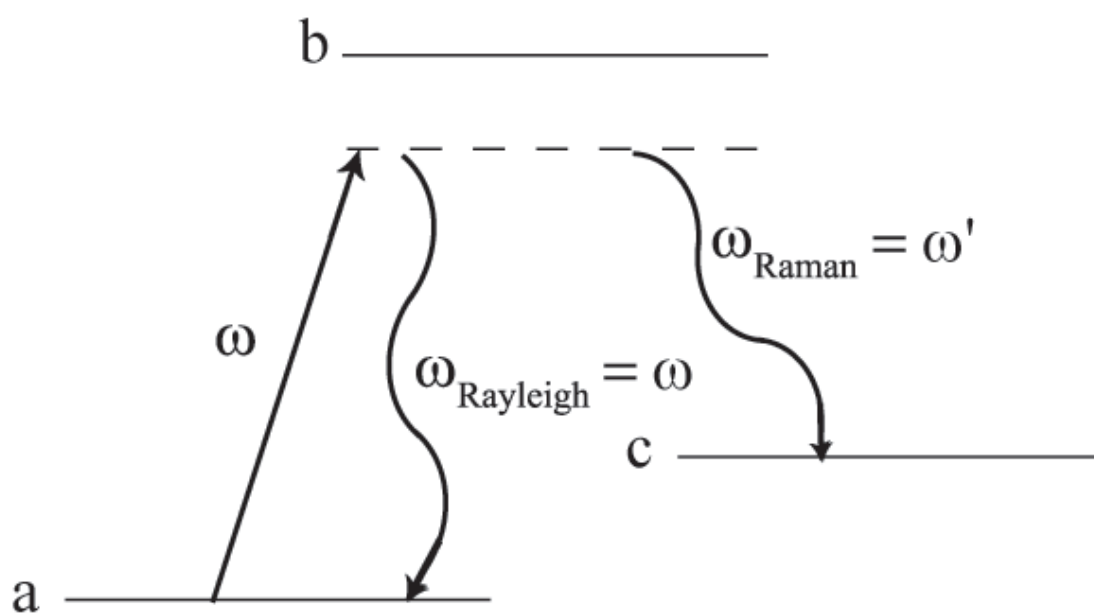
Figure 10.8: 3-level atom system. By letting state **c** have the properties of Raman accessible final states, this simple model sufficiently represents a real molecule.

many final states (other than **a**) to scatter into and the transition moment for each of these final states is usually comparable to μ_{ab}.

Nonetheless, there is still some promise for cavity-assisted Doppler cooling of a molecular gas. This hope lies in the so-called 'collective effects' observed in the cavity-assisted Doppler cooling of cold cesium atoms [26, 33]. In these experiments, two distinct types of collective effects were observed. For smaller detunings, a non-negligible intra-cavity photon number of blue-shifted Rayleigh light stimulated the molecules to emit into the cavity mode. For larger detunings (>1 GHz detuned), the cold cesium atoms self-organized, under the intra-cavity field, into a regular lattice structure that Bragg-scattered from the incident beams into the cavity. In both of these regimes, the collective effects worked to increase the Rayleigh scattering rate significantly over other scattering processes – though in the latter case only center of mass damping is observed, *i.e.* the atoms are only slowed, not cooled. A rule-of-thumb from the cold atom work is that for collective effects to occur $N\eta$ must be approximately one, where N is the number of molecules in the cavity mode and η is the ratio of scattering into free space versus scattering into the cavity mode. For a Gaussian transverse mode with waist w_o and finesse F and cavity light with wave vector $k = 2\pi/\lambda$, η is given as $\eta = 12F/(\pi(kw_o)^2)$ and is a measure of how strongly the cavity has influenced the local electromagnetic mode density. For a molecule density in the range of 10^7 cm^{-3}, $w_o =$ 100 μm, and 1 cm spacing, N $\approx$ 1000. Thus, one needs $\eta \approx 10^{-3}$, which requires a finesse of approximately 1000 at 308 nm (for OH). While a cavity with finesse of 1000 in the ultra-violet is non-trivial, it can be made with careful coatings, and the possibility of seeing collective effects seem very real. Of course several factors such as, starting with a warmer gas (the molecule temperature will be $\sim$ 100 mK, while the cesium work started around 100 μK) and the effect of molecules moving in and out of the cavity mode (any current molecule trap will be of order 1 cm, while the cavity waist is of order 100 μm), may work against the onset of the collective effects. For this reason detailed

quantum Monte-Carlo simulations are currently underway by Josh Dunn of the Chris Greene group here at JILA that account for all of these effects, and we can hope for a reasonable prediction for the onset of collective dynamics in the near future.

10.5   Capacitive Detection of Polar Molecules

The most serious challenge facing all of cold molecule research is the lack of a sensitive, non-destructive detection technique. Currently, most molecule detection schemes utilize laser-induced fluorescence or ionization detection. Typically, both of these schemes leave the molecule in a final state that differs from the initial state, *i.e.* destructive detection, and are quite insensitive when compared with traditional atomic fluorescence detection techniques. The reason for the lack of sensitivity is simple, in molecular fluorescence detection the lack of a cycling transition means that with a typical solid-angle-of-collection one expects to collect on order 1 photon from every 1000 excited molecules, where atomic experiments expect roughly 1000 photons from each atom. It should be noted that, while ionization detection can be quite sensitive, small ionization cross-sections usually translate to long integration times.

Techniques, like phase-contrast imaging [17], hold much promise for detection of cold trapped samples of molecules. However, these techniques may not be suitable for detecting a moving molecular beam. Here we present a new technique, capacitive detection of polar molecules, which works by detecting the induced charge on a capacitor when the dielectric constant of the space between the capacitor plates is changed, *i.e.* when polar molecules fly between the plates. This technique is particularly amenable to supersonic beam experiments, where the molecules are all moving with roughly the same velocity.

A schematic of the detector is shown in Fig. 10.9(a). It consists of two parallel stainless-steel plates held at constant voltage, V, 'sandwiched' around a Boron Nitride spacer. The polar molecules pass through a hole drilled in the Boron nitride spacer and

(a)

Stainless Steel

Boron Nitride

Stainless Steel

Molecular propagation axis

(b)

9.00 pm

9.25 pm

9.50 pm
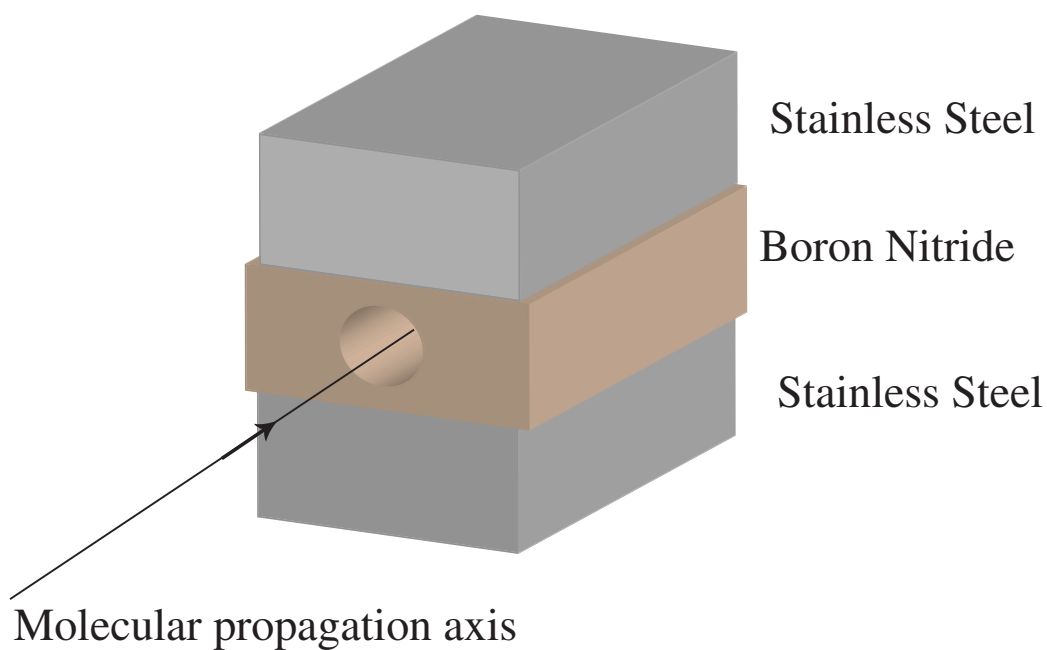
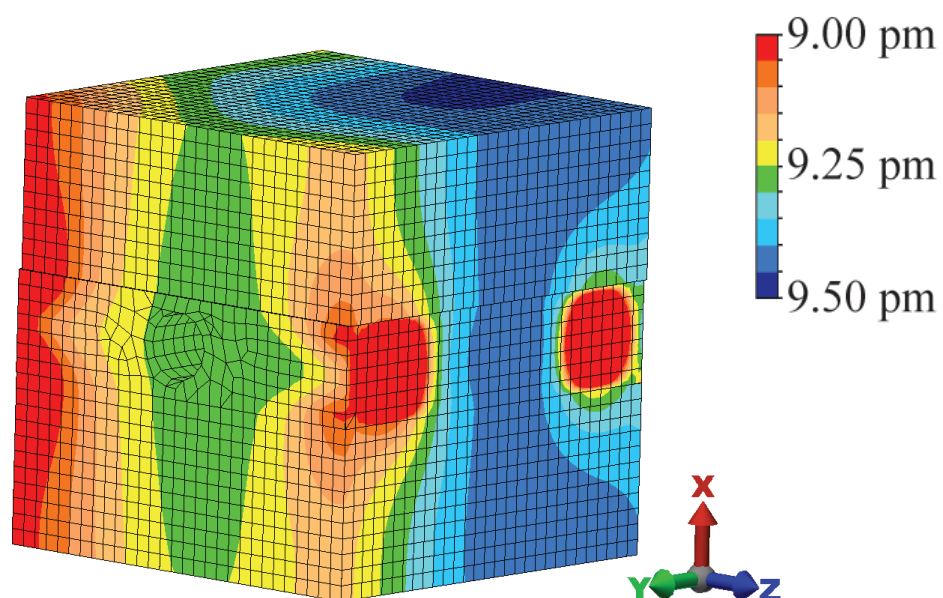Figure 10.9: (a) Capacitive detector assembly. (b) Results of a finite-element analysis of the deformation of the parallel plate capacitor for 5mG acceleration in the $-\hat{x}$ direction. For this analysis, the detector assembly is held at four points along its midplane. This mounting scheme reduces relative vibration between the plates, since most of the acceleration results in a common-mode movement of the plates.

cause current to flow in the leads connected to the plates since the plates are held at constant voltage. The amount of induced current is easily calculated by considering the extra amount of potential energy, ΔU, stored in the capacitive field due to the presence of the polar molecules

$$\Delta U = \frac{1}{2}\Delta Q V = N \left(\sqrt{\left(\frac{\Delta}{2}\right)^2 + (\mu E)^2} - \frac{\Delta}{2} \right), \tag{10.30}$$

where N is the number of polar molecules, ΔQ is the charged induced by the presence of the polar molecules, Δ is the energy separation between the states mixed by the Stark interaction (see Chapter 2), μ is the expectation value of the dipole moment of the polar molecule, and E is the electric field magnitude. Note that the right most term in Eq. 10.30 is simply the energy of the N polar molecules in an electric field of strength, E. Solving for the induced charge, we have

$$\Delta Q = \frac{2N \left(\sqrt{\left(\frac{\Delta}{2}\right)^2 + (\mu E)^2} - \frac{\Delta}{2} \right)}{V}. \tag{10.31}$$

The predictions of this equation are shown in Fig. 10.10 for the case of OH molecules flying through two parallel plates spaced by 1 cm. The induced charge reaches a maximum equal to $2\mu/d$, where d is the plate separation. This maximum represents the induced charge for a linear Stark shift, μE, and is recovered in Eq. 10.31 in the limit $V \to \infty$.

Near the supersonic nozzle one can expect on order of $N = 10^{12}$ cm^{-3}, and thus the total induced charge in a 10 kV/cm field is $\Delta Q = 0.6$ fC. Since this charge is induced in the time it takes a molecular packet to fly into the capacitor, which is ~ 100 μs at this beam location, we have the induced current as $I = 6$ pA. Detection of current at this level is certainly possible (commercial ammeters with fA resolution are available), though not trivial. Several techniques, such as applying a voltage ripple to the capacitor and using lock-in detection techniques, using the knowledge of the molecular velocity to gate the detection in time, and using the fact that when the
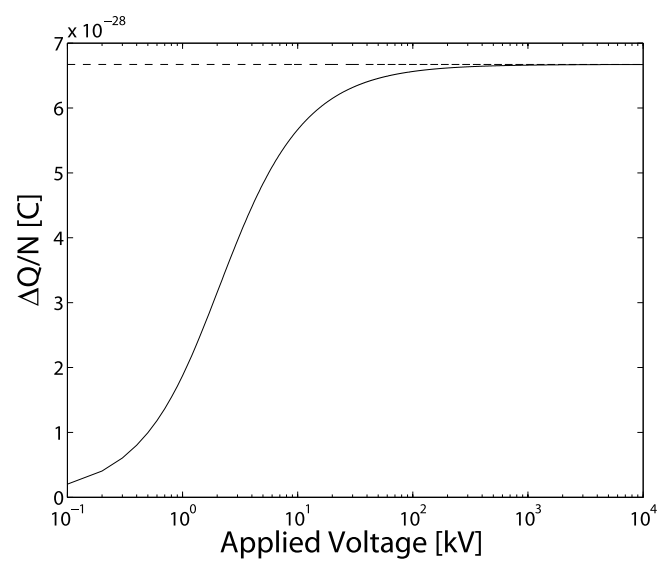
Figure 10.10: The induced charge on a parallel plate capacitor spaced by 1 cm.

molecules exit the capacitor there should be an equal-magnitude, opposite-sign current pulse relative to the current pulse that occurred when they entered, may make high signal-to-noise ratio detection of these pulses easier. Furthermore, with ever increasing current measurement capabilities, detection of these currents and lower may soon make this all-electronic detection technique trivial.

Voltage instability and mechanical vibration present the largest sources of noise for these measurements. While time-gating will virtually eliminate them for measurements in a beam, where the signal persists for ~ 100 μs, the eventual goal, measuring the current in a capacitor situated around a trap of polar molecules as a means to monitor the trap dynamics (lifetime, etc.), will require low DC noise. Since voltage lock-in detection should circumvent any voltage instability problems, mechanical vibration is the most serious problem. Specifically, if the distance between the capacitor plates moves by an amount δ, due to vibrations, it generates a noise current of

$$I_{Noise} \approx \frac{f \Delta Q_{Noise}}{2} = \left(\frac{f C_o V}{2} \right) \frac{\delta}{d}, \tag{10.32}$$

where C_o is the vibration free capacitance and f is the frequency of the vibration. Depending on the speed of the signal, low-pass electronic filters can be used to remove a large portion of the vibration-induced current spectrum. Nonetheless, if one desires to monitor trap dynamics, say trap lifetime in a mixed molecule trap where chemical reactions may occur, a bandwidth of several kHz may be required. Shown in Fig. 10.11 is the acceleration spectrum of our second-generation decelerator taken by a piezo-electric accelerometer. As expected, the largest vibrations are due to the turbo-molecular pumps and constitute ~ 5 mG acceleration. From a static finite-element analysis of our prototype design, we find this vibration produces ~ 0.5 pm plate displacement (see Fig. 10.9(b)). Which, produces a noise current of 0.1 fA. While this value is well below the expected current for measurement near the beam source, it will be the limiting factor for measurements in a trap where the density can be as much as 5 orders of magnitude
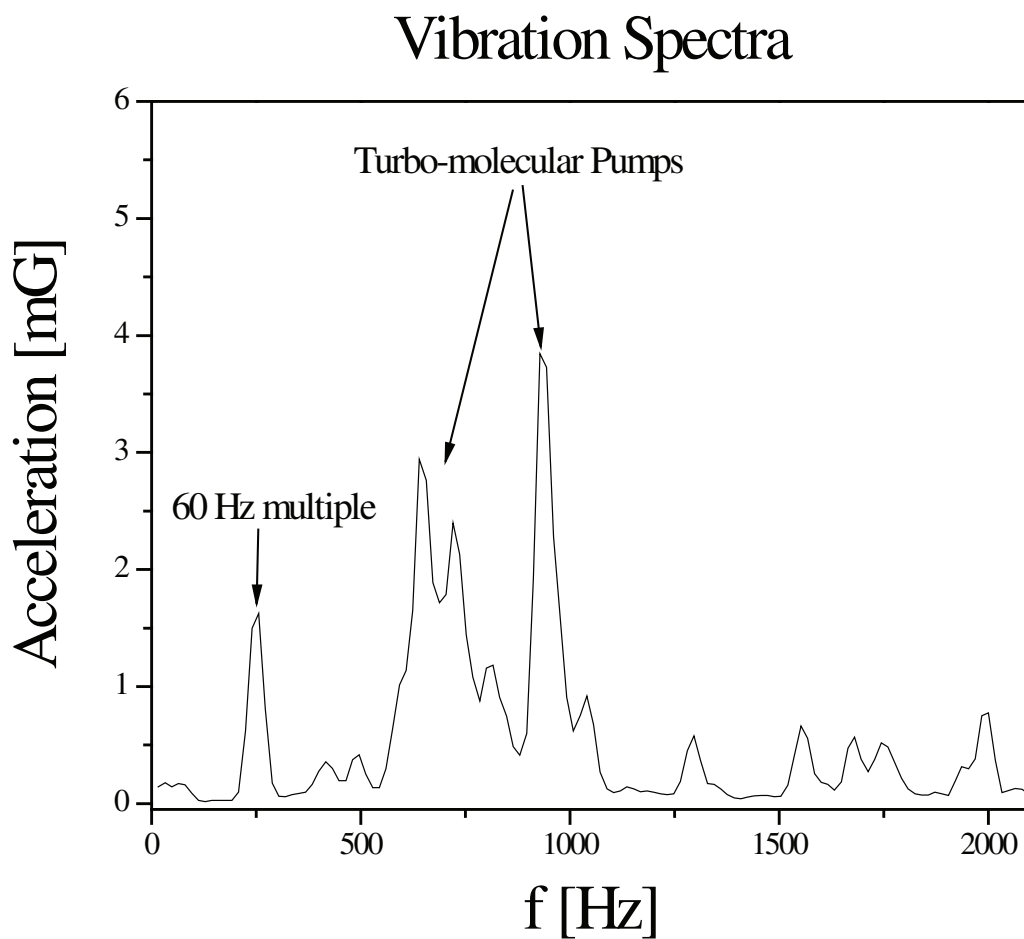
Vibration Spectra

Figure 10.11: Vibration spectrum of second-generation Stark decelerator. The vibration due to the turbo-molecular pumps is clearly visible, as is a harmonic of the 60 Hz line frequency.

smaller. However, with careful vibration isolation and mounting, as in the work of Ref. [92], it appears this systematic can be controlled.

Bibliography

[1] J. R. Bochinski, private communication.

[2] AZ Technology Inc., www.aztechnology.com.

[3] Sebastiaan Y. T. van de Meerakker, Private Communication.

[4] M. Greiner, C. A. Regal, and D. S. Jin, Nature **426**, 537 (2003); M. W. Zwierlein et al., Phys. Rev. Lett. **91**, 250401 (2003); S. Jochim et al., Science **302**, 2101 (2003); T. Bourdel et al., Phys. Rev. Lett. **93**, 050401 (2003).

[5] Magnetic dipoles and electric quadrupoles also present anisotropic interactions. See A. Griesmaier et al., Phys. Rev. Lett. **94**, 160401 (2005) and R. Santra and C. H. Greene, Phys. Rev. A **67**, 062713 (2003), respectively.

[6] A. V. Avdeenkov and J. L. Bohn, Phys. Rev. A **66**, 052718 (2002); *ibid.* Phys. Rev. Lett. **90**, 043006 (2003).

[7] E. R. Meyer and J. L. Bohn, in preparation.

[8] N. Kanekar, private communication.

[9] For the TM_{010} mode the electric field is uniform along the cavity axis. However, due to the use of multiple frequencies, we work below the TM_{010} cavity resonance leading to the observed electric field decay.

[10] J. Hutson, private communication.

[11] The use of optical cavities for modern atomic, molecular, and optical physics. In G. Scoles, editor, <u>Atomic and Molecular Beam Methods</u>, volume 1. Oxford University Press, New York, 1988.

[12] E. R. I. Abraham et al. <u>J. Chem. Phys.</u>, 103:7773, 1995.

[13] M. Alagia, N. Balucani, P. Casavecchia, D. Stranges, and G.G. Volpi. <u>J. Chem. Phys.</u>, 98:2459, 1993.

[14] J. R. Alvarez-Idaboy et al. <u>J. Amer. Chem. Soc.</u>, 123:2018–2024, 2001.

[15] P. Anderson, N. Aristov, D. Beushausen, and H.W. Lülf. <u>J. Chem. Phys.</u>, 95:5763, 1991.

[16] Roger W. Anderson. <u>J. Phys. Chem A</u>, 101:7664, 1997.

[17] M. R. Andrews, M.-O. Mewes, N. J. van Druten, D. S. Durfee, D. M. Kurn, and W. Ketterle. <u>Science</u>, 273:84, 1996.

[18] A. V. Avdeenkov and J. L. Bohn. <u>Phys. Rev. A</u>, 66:052718, 2002.

[19] A. V. Avdeenkov and J. L. Bohn. <u>Phys. Rev. Lett.</u>, 90:043006, 2003.

[20] Y. B. Band and P. S. Julienne. <u>Phys. Rev. A</u>, 51:R4317, 1995.

[21] K. Bergmann, H. Theuer, and Shore B. W. <u>Rev. Mod. Phys.</u>, 70:1003, 1998.

[22] R.B. Bernstein. <u>Chemical dynamics via Molecular Beam and Laser Techniques</u>. Oxford University Press, New York, 1982.

[23] H. L. Bethlem, G. Berden, F. M. H. Crompvoets, R. T. Jongma, A. J. A. van Roij, and G. Meijer. <u>Nature</u>, 406:491, 2000.

[24] H. L. Bethlem, G. Berden, and G. Meijer. <u>Phys. Rev. Lett.</u>, 83:1558, 1999.

[25] H. L. Bethlem et al. <u>Phys. Rev. A</u>, 65:053416, 2002.

[26] A. T. Black, H. W. Chan, and V. Vuletic. <u>Phys. Rev. Lett.</u>, 91:203001, 2003.

[27] J. R. Bochinski et al. <u>Phys. Rev. Lett.</u>, 91:243001, 2003.

[28] J. R. Bochinski et al. <u>Phys. Rev. A</u>, 70:043410, 2004.

[29] J. L. Bohn and P. S. Julienne. <u>Phys. Rev. A</u>, 54:R4637, 1996.

[30] B. Borca et al. <u>Phys. Rev. Lett.</u>, 91:070404, 2003.

[31] D. M. Brink and G. R. Satchler. <u>Angular Momentum</u>. Clarendon Press, Oxford, third edition, 1993.

[32] Benjamin L. Brown, Alexander J. Dicks, and Ian A. Walmsley. <u>Phys. Rev. Lett.</u>, 96:173002, 2006.

[33] H. W. Chan, A. T. Black, and V. Vuletic. <u>Phys. Rev. Lett.</u>, 90:063003, 2003.

[34] J. N. Chengalur and N. Kanekar. <u>Phys. Rev. Lett.</u>, 91:241302, 2003.

[35] C. Cohen-Tannoudji, J. Duport-Roc, and G. Grynberg. <u>Atom-Photon Interactions</u>. Wiley, New York, 1998.

[36] J. A. Coxon. <u>Can. J. Phys.</u>, 58:933, 1980.

[37] F. M. H. Crompvoets, H. L. Bethlem, J. Kupper, A.J.A. van Roij, and G. Meijer. <u>Phys. Rev. A</u>, 69:063406, 2004.

[38] B. D'Anna et al. <u>Phys. Chem. Chem. Phys.</u>, 5:1790, 2003.

[39] J. Darling. <u>Phys. Rev. Lett.</u>, 91:011301, 2003.

[40] Ch. Daussy et al. Phys. Rev. Lett., 83:1554, 1999.

[41] R. de Carvallo et al. Eur. Phys. J. D, 7:289, 1999.

[42] D. DeMille. Phys. Rev. Lett., 88:067901, 2002.

[43] A. Derevianko, J.F. Babb., and A. Dalgarno. Phys. Rev. A, 63:052704, 2001.

[44] A. Derevianko, W. R. Johnson, M. S. Safronova, and J. F. Babb. Phys. Rev. Lett., 82:3589, 1999.

[45] P. A. M. Dirac. Nature, 139:323, 1937.

[46] E. A. Donley et al. Nature, 417:529, 2002.

[47] R. O. Doyle. J. Quant. Spectrosc. Radiat. Transfer, 8:1555, 1968.

[48] M. Dupuis and W. A. Lester. J. Chem. Phys., 81:847, 1984.

[49] E. Egorov et al. Phys. Rev. A, 63:030501, 2001.

[50] M.S. Elioff, J.J. Valentini, and D.W. Chandler. Science, 302:1940, 2003.

[51] A. Fioretti, D. Comparat, A. Crubellier, O. Dulieu, F. Masnou-Seeuws, and P. Pillet. Phys. Rev. Lett., 80:4402, 1998.

[52] R. H. Fowler and L. Nordheim. Proc. R. Soc. Lond., A, 119:1733878, 1928.

[53] B. Gaffari et al. Phys. Rev. A, 60:3878, 1999.

[54] G.F. Gribakin and V.V. Flambaum. Phys. Rev. A, 48:546, Year = 1993.

[55] C. Haimberger, J. Kleinert, M. Bhattacharya, and N. P. Bigelow. Phys. Rev. A, 70:021402, 2004.

[56] T. D. Hain, R. M. Moision, and T. J. Curtiss. J. Chem. Phys., 111:6797–6806, 1999.

[57] W. E. Henke et al. J. Chem. Phys., 76:1327–1334, 1982.

[58] Jens Herbig et al. Science, 301:1510, 2003.

[59] G. Herzberg. Molecular Spectra and Molecular Structure. Krieger Publishing Company, Malabar, Florida, second edition, 1989.

[60] M. Hillenkamp, K. Sharon, and U. Even. J. Chem. Phys., 118:8699, 2003.

[61] Eric R. Hudson et al. Eur. Phys. J. D, 31:351, 2004.

[62] Eric R. Hudson et al. Phys. Rev. A, in press, 2006.

[63] J. J. Hudson et al. Phys. Rev. Lett., 89:023002, 2002.

[64] K. Ikejiri, H. Ohoyama, Y. Nagamachi, T. Teramoto, and T. Kasia. Chem. Phys. Lett., 379:255, 2003.

[65] S. Inouye, J. Goldwin, M. L. Olsen, C. Ticknor, J. L. Bohn, and D. S. Jin. Phys. Rev. Lett., 93:183201, 2004.

[66] J. D. Jackson. Classical Electrodynamics. John Wiley and Sons, Inc., New York, third edition, 1998.

[67] P. S. Julienne and Jacques Vigue. Phys. Rev. A, 44:4464, 1991.

[68] T. Junglen, T. Rieger, S. A. Rangwala, P. W. H. Pinkse, and G. Rempe. Phys. Rev. Lett., 92:223001, 2004.

[69] M. Kajita. Eur. Phys. J. D, 20:55, 2002.

[70] N. Kanekar, J. N. Chengalur, and T. Ghosh. Phys. Rev. Lett., 93:051302, 2004.

[71] W. Kanzig, H.R. Hart Jr, and S. Roberts. Phys. Rev. Lett., 13:543, 1964.

[72] A. J. Kerman, J. M. Sage, S. Sainis, T. Bergeman, and D. DeMille. Phys. Rev. Lett., 92:153001, 2004.

[73] A. J. Kerman et al. Phys. Rev. Lett., 92:033004, 2004.

[74] I. B. Khriplovich and S. K. Lamoreaux. CP Violation Without Strangeness: Electric Dipole Moments of Particles, Atoms, and Molecules. Springer, New York, 1997.

[75] V. Alan Kostelecky, R. Lehnert, and Malcolm J. Perry. Phys. Rev. D, 68:123511, 2003.

[76] B Kuhn. J. Chem. Phys., 111:2565, 1999.

[77] Jon K. Laerdahl and Peter Schwerdtfeger. Phys. Rev. A, 60:4439, 1999.

[78] R. Latham. High Voltage Vacuum Insulation. Academic Press, London, 1995.

[79] P. D. Lett et al. Phys. Rev. Lett., 71:2200, 1993.

[80] H. J. Lewandowski et al. Chem. Phys. Lett., 395:53, 2004.

[81] H. Y. Li et al. Chem. Phys., 307:35, 2004.

[82] Matt Mackie, Ryan Kowalski, and Juha Javanainen. Phys. Rev. Lett., 84:3803, 2000.

[83] J. P. Maillard, J. Chauville, and A. W. Mantz. J. Mol. Spectrosc., 63:120, 1976.

[84] M. W. Mancini et al. Phys. Rev. Lett., 92:133203, 2004.

[85] P. Maunz, T. Puppe, I. Schuster, N. Syassen, P.W.H. Pinske, and G. Rempe. Nature, 428:50, 2004.

[86] J. D. Miller et al. Phys. Rev. Lett., 71:2204, 1993.

[87] M. Mizushima. The Theory of Rotating Diatomic Molecules. Wiley, New York, 1975.

[88] E. D. Morris and H. Niki. J. Chem. Phys., 55:1991, 1971.

[89] S. B. Nagel et al. Phys. Rev. Lett., 94:083004, 2005.

[90] H. Niki et al. J. Phys. Chem., 88:5342, 1984.

[91] A. N. Nikolov et al. Phys. Rev. Lett., 84:246, 2000.

[92] Mark Notcutt, Long-Sheng Ma, Andrew D. Ludlow, Seth M. Foreman, Jun Ye, and John L. Hall. Phys. Rev. A, 73:031804, 2006.

[93] K.A. Olive and Y.Z. Qian. Phys. Today, 57:40, 2004.

[94] R. K. Pathria. Statistical Mechanics. Butterworth-Heinemann, Oxford, 2nd edition, 1996.

[95] E. Peik et al. Phys. Rev. Lett., 93(17):170801, 2004.

[96] P. Pillet et al. J. Phys. B: At. Mol. Opt. Phys., 30:2801, 1997.

[97] F. Pobell. Matter and Methods at Low Temperature. Springer, Berlin, 2nd edition.

[98] D Proch and T Trickl. Rev. Sci. Instrum., 60:713, 1989.

[99] R. Quast, D. Reimers, and S.A. Levshakov. Astron. Astrophys., 415:L7, 2004.

[100] H. E. Radford. Phys. Rev., 122:114, 1961.

[101] N.F. Ramsey. Molecular Beams. Oxford University Press, Oxford, 1956.

[102] N.F.A. Ramsey. Phys. Rev., 78:695, 1950.

[103] S. A. Rangwala, T. Junglen, T. Rieger, P. W. H. Pinkse, and G. Rempe. Phys. Rev. A, 67:043406, 2003.

[104] C. A. Regal, C. Ticknor, J. L. Bohn, and D. S. Jin. Nature, 424:47, 2003.

[105] B. C. Regan et al. Phys. Rev. Lett., 88:071805, 2002.

[106] D.W. Rein. J. Mol. Evol., 4:15, 1974.

[107] T. Rieger, T. Junglen, S. A. Rangwala, P. W. H. Pinkse, and G. Rempe. Phys. Rev. Lett., 95:173002, 2005.

[108] J.J. Sakurai. Modern Quantum Mechanics. Addison-Wesley, Reading, Massachussets.

[109] K. Shibuya et al. J. Phys. Chem., 83:940, 1979.

[110] V. Sivakumaran et al. Phys. Chem. Chem. Phys., 5:4821, 2003.

[111] P. Soldan and J. M. Hutson. Phys. Rev. Lett., 92:163202, 2004.

[112] D.M. Sonnenforh, R.G. Macdonald, and K. Liu. J. Chem. Phys., 93:1478, 1991.

[113] M. R. Soto and M. Page. J. Phys. Chem., 94:3242–3246, 1990.

[114] R. Spence and W. Wild. J. Chem. Soc., 1:338, 1935.

[115] C. A. Stan, M. W. Zwierlein, C. H. Schunck, S. M. F. Raupach, and W. Ketterle. Phys. Rev. Lett., 93:143001, 2004.

[116] L. J. Stief et al. Rate-constant for the reaction of hydroxyl radical with formalde-hyde over the temperature-range 228-362-k. J. Chem. Phys., 73(5):2254–2258, 1980.

[117] Kevin. E. Strecker et al. Phys. Rev. Lett., 91:080406, 2003.

[118] T. Takekoshi, B. M. Patterson, and R. J. Knize. Phys. Rev. Lett., 81:5105, 1998.

[119] M.R. Tarbutt, H.L. Bethlem, J.J. Hudson, V.L. Ryabov, V.A. Ryzhov, B.E. Sauer, G. Meijer, and E.A. Hinds. Phys. Rev. Lett., 92:173002, 2004.

[120] J. J. ter Meulen and A. Dymanus. Astrophys. J., 172:L21–L23, 1971.

[121] J.J. ter Meulen, W.L. Meerts, G.W.M. van Mierlo, and A. Dymanus. Phys. Rev. Lett., 36:1031, 1976.

[122] C. Ticknor and John L. Bohn. Phys. Rev. A, 71:022709, 2005.

[123] C.H. Townes and A.L. Schawlow. Microwave Spectroscopy. Dover, New York, 1975.

[124] M. C. van Beek and J. J. ter Meulen. Chemical Physics Letters, 337:237, 2001.

[125] Sebastiaan Y. T. van de Meerakker, Nicolas Vanhaecke, Hendrick L. Bethlem, and Gerard Meijer. Phys. Rev. A, 71:053409, 2005.

[126] Sebastiaan Y. T. van de Meerakker, Nicolas Vanhaecke, Hendrick L. Bethlem, and Gerard Meijer. Phys. Rev. A, 73:023401, 2006.

[127] S. Y. T. van de Meerakker et al. Phys. Rev. Lett., 94:023004, 2005.

[128] S.J. van Enk, J. McKeever, H.J. Kimble, and J. Ye. Phys. Rev. A, 64, 2001.

[129] J. van Veldhoven, H. L. Bethlem, and G. Meijer. Phys. Rev. Lett., 94:083001, 2005.

[130] J. van Veldhoven, H. L. Bethlem, and G. Meijer. Phys. Rev. Lett., 94, 2005.

[131] J. van Veldhoven, J. Kupper, H. L. Bethlem, B. Sartakov, A. J. A. van Roij, and G. Meijer. Eur. Phys. J. D, 31:337–349, 2004.

[132] V. Vuletic, H. W. Chan, and A. T. Black. Phys. Rev. A, 6403, 2001.

[133] V. Vuletic and S. Chu. Phys. Rev. Lett., 84:3787, 2000.

[134] D. Wang et al. Phys. Rev. Lett., 93:243005, 2003.

[135] H. Wang et al. Phys. Rev. A, 53:R1216, 1996.

[136] J. K. Webb, M. T. Murphy, V. V. Flambaum, V. A. Dzuba, J. D. Barrow, C. W. Churchill, J. X. Prochaska, and A. M. Wolfe. Phys. Rev. Lett., 87:091301, 2001.

[137] J. D. Weinstein, R. deCarvalho, K. Amar, A. Boca, B. C. Odom, B. Friedrich, and J. M. Doyle. J. Chem. Phys., 109:2656, 1998.

[138] J. D. Weinstein, R. deCarvalho, T. Guillet, B. Friedrich, and J. M. Doyle. Nature, 395:148, 1998.

[139] H. Wiedemann. Particle Accelerator Physics I: Basic Principles and Linear Beam Dynamics. Berlin, 2nd edition.

[140] K. Xu, T. Mukaiyama, J. R. Abo-Shaeer, J. K. Chin, D. E. Miller, and W. Ketterle. Phys. Rev. Lett., 91:210402, 2003.

[141] J. Ye, L. S. Ma, and J. L. Hall. IEEE Trans. Instrum. Meas., 46:178, 1997.

[142] J. Ye, D. W. Vernooy, and H.J. Kimble. Phys. Rev. Lett., 83:4987, 1999.

[143] R. A. Yetter et al. J. Chem. Phys., 91:4088, 1989.

[144] R.N. Zare, A.L. Smeltekopf, W.J. Harrop, and D.L. Albritton. J. Mol. Spectrosc., 46:37, 1973.

[145] Tanya Zelevinsky et al. Phys. Rev. Lett., 96:203201, 2006.

[146] Gotz Zinner et al. Phys. Rev. Lett., 85:2292, 2000.